Evaluation of Generic EBS Design Concepts and Process Models: Implications to EBS Design Optimization

(FCRD-USED-2012-000140)

Fuel Cycle Research & Development

Carlos F. Jové Colón, Jeffrey A. Greathouse, Stephanie Teich-McGoldrick, Randall T. Cygan, Teklu Hadgu, James E. Bean, Mario J. Martinez, Polly L. Hopkins, José G. Argüello, Francis D. Hansen (SNL)

Florie A. Caporuscio, Michael Cheshire, Schön S. Levy, Mary K. McCarney (LANL)

Harris R. Greenberg, Thomas J. Wolery, Mark Sutton (LLNL)

Jonny Rutqvist, Carl I. Steefel, Jens Birkholzer, Hui-Hai Liu, James A. Davis, Ruth Tinnacher, Ian Bourg, Michael Holmboe, Juan Galindez (LBNL)

June 15th, 2012

SAND 2012-5083 P

Prepared by:

Sandia National Laboratories

Albuquerque, New Mexico 87185

U.S. DEPARTMENT OF ENERGY

Sandia National Laboratories
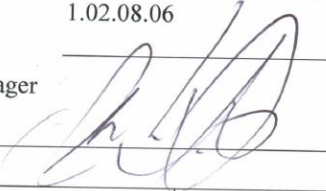
FCT Document Cover Sheet

Name/Title of Deliverable/Milestone	Evaluation of Generic EBS Design Concepts and Process Models: Implications to EBS Design Optimization
Work Package Title and Number	Engineered Barrier Systems (EBS) Evaluations - SNL (FT-12SN080606)
Work Package WBS Number	1.02.08.06
	Milestone Number M2FT-12SN0806061
Responsible Work Package Manager	
Carlos F. Jove Colon *(signature)* (Name/Signature)	06/15/2012 (Date Submitted)

Quality Rigor Level for Deliverable/Milestone	☒ QRL-3	☐ QRL-2	☐ QRL-1 ☐ Nuclear Data	☐ N/A*

This deliverable was prepared in accordance with   Sandia National Laboratories
_____
(Participant/National Laboratory Name)

QA program which meets the requirements of
☐ DOE Order 414.1   ☐ NQA-1-2000   ☒ Other: DOE QA Order

This Deliverable was subjected to:
☒ Technical Review   ☐ Peer Review

Technical Review (TR)	**Peer Review (PR)**
Review Documentation Provided	**Review Documentation Provided**
☐ Signed TR Report, or	☐ Signed PR Report, or
TR Report No.: _____	PR Report No.: _____
☐ Signed TR Concurrence Sheet (attached), or	☐ Signed PR Concurrence Sheet (attached), or
☒ Signature of TR Reviewer(s) below	☐ Signature of PR Reviewers below

Name and Signature of Reviewers
Andrew W. Miller */(signature)*   06/13/2012

_____   _____

_____   _____
(Name/Signature)   (Date)

*Note: In some cases there may be a milestone where an item is being fabricated, maintenance is being performed on a facility, or a document is being issued through a formal document control process where it specifically calls out a formal review of the document. In these cases, documentation (e.g., inspection report, maintenance request, work planning package documentation, or the documented review of the issued document through the document control process) of the completion of the activity along with the Document Cover Sheet is sufficient to demonstrate achieving the milestone. QRL for such milestones may also be marked N/A in the work package provided the work package clearly specifies the requirement to use the Document Cover Sheet and provide supporting documentation.

FCRD-TIO-2011-000050, Rev. 0

AKNOWLEDGEMENTS

SUMMARY

The assessment of generic EBS concepts and design optimization to harbor various disposal configurations and waste types needs advanced approaches and methods to analyze barrier performance. To accomplish this, the advancement of sophisticated approaches to the evaluation of EBS processes should result in the development of modeling tools to evaluate EBS coupled physico-chemical phenomena at various scales. Further, experimental investigations need to be conducted in parallel to provide essential information that serve not only as model input but also as a testing and validation platform to these models resulting in enhanced confidence and uncertainty reduction. These process and/or sub-process model representations will then provide valuable information about EBS responses to disposal conditions that then feed into the system performance assessment of the generic repository system. The focus of this report is on the development and exploitation of theoretical approaches and their implementation into modeling tools to evaluate key processes to barrier performance. It also describes important accomplishments in experimental investigations essential to fill knowledge gaps on key processes to clay barriers such as radionuclide sorption, reactive diffusion, and clay phase interactions. Significant progress has been attained in all these activities demonstrated by the superb level of fruitful results obtained in many areas within a wide range of EBS tasks encompassed within this UFDC activity.

This report is a collaborative contribution of multiple DOE labs: Sandia National Laboratories (SNL), Lawrence Berkeley National Laboratory (LBNL), Lawrence Livermore National Laboratory (LLNL), and Los Alamos National Laboratory (LANL). The content of this report is organized as follows:

- (Part I) Overview of the importance of THMC processes to barrier performance and a high level analysis of a two-domain multi-barrier EBS design concept with the DSEF thermal analysis. Such an example illustrates the usefulness of thermal analysis to repository design optimization (RDO) when interfaced with multiple sources of information that include barrier thermal properties, EBS geometry, waste decay heat, and storage time. The results of this high level analysis can be used to evaluate the extent of the *sacrificial barrier* in the layered EBS on the basis of scientific knowledge describing clay phase stability and behavior at elevated temperatures. It also discusses current and potential international collaborations related to EBS activities such as DECOVALEX 2015 and the ROK – US Joint Fuel Cycle Study among others.

- (Part II) THMC processes in clay barriers:

  o Modeling of THM processes within bentonite and the interaction between the EBS and a clay disposal formation in the near field through the expansion and refinement of the TOUGH-FLAC coupling and the implementation of the dual-structure representation in the Barcelona Basic Model (BBM). Such an extension of the BBM provides for a more accurate representation of expansive clay behavior capturing dependencies on swelling strain and pressure during suction cycles which are attributed chemo-mechanical couplings.

  o Reactive-diffusive transport modeling approaches for radionuclide migration in bentonite. This work describes the theoretical description and implementation of the Poisson-Nernst-Planck approach to represent reactive diffusion compacted

clay. The model allows for the treatment of medium pore size as a fractal distribution. Ion diffusion in the highly confined clay interlayer was modeled using molecular dynamics (MD) simulations of H_2O self-diffusion and sodium. Experimental investigations were conducted to study U(VI) sorption onto clay and implications to reactive diffusive transport in bentonite. These sorption experiments comprised batch and kinetic studies to accurately evaluate equilibration times.

- (Part III) Experimental studies of clay stability and clay-metal interactions at high temperatures and pressures. This work presents experimental results on the high temperature conversion of bentonite clay to other phases like chlorite and also changes in solution chemistry. These experimental work provide important information on the clay degradation under hydrothermal conditions and the fate of silica in the system. Moreover, it provides key information to the evaluation of the technical basis for the advancement of thermal constraints which is crucial to the description of barrier performance.

- (Part IV) This effort involves two topics on thermodynamic modeling and database development :

    o Thermodynamic database development of clay phases for 23 compositions at various hydration states using algorithms implemented in MS Excel spreadsheets. Such implementation allows for transparency, ease of usage, and potential for model expansion.

    o Thermodynamic modeling of C-S-H cement leaching and clay hydration (swelling). Thermodynamic methods to represent non-ideal solid solutions (Margules type) and computation of chemical equilibrium using a Gibbs energy minimization (GEM) were used to describe the incongruent dissolution of C-S-H cement and Na-beidellite hydration as a function of relative humidity (RH). These methods were implemented in the form of C++ code using the open-source Cantera constitutive modeling toolkit. This model implementation allows the use of a flexible and agile platform to model fluid-solid interactions using robust thermodynamic relations.

- (Part V) Molecular Dynamics (MD) study of clay hydration at ambient and elevated temperatures. Provides results of atomistic calculations using advanced computational methods and approaches to characterize clay swelling behavior through molecular properties of the interlayer structure as a function of interlayer cation hydration for various clay compositions (Mg, Ca, Na, Cs).

- (Part VI) Coupled thermal-mechanical (TM) and thermo-hydrological (TH) modeling in salt. Results are shown of 3D modeling of TM and TH processes in a salt repository using SNL Sierra Codes to describe the effects of crushed salt consolidation in the presence of moisture for a single heat-generating waste package disposal room configuration. The constitutive model of Callahan is used to describe crush salt consolidation with and without moisture. Also advances a 3D two-phase modeling of H_2O transport through crushed salt in response to the waste thermal load. This model also accounts for H_2O transport in various domains (intact and crushed salt, excavated rock zone – ERZ) and its hydrological properties.

CONTENTS

8

FIGURES

<u>Part I - Overview of Engineered Barrier System (EBS) Concept Evaluation</u>

Part II - Investigation of Reactive Transport and Coupled THM Processes in EBS

Part III - Clay Stability and Clay – Metal Interactions

13

Part IV - Thermodynamic Database and Model Development: Cement Leaching and Clay Hydration Properties

Part V - Molecular Dynamic (MD) Study of Clay Hydration

Part VI - Coupled Thermal-Mechanical (TM) and Thermo-hydrological (TH) Modeling in Salt

TABLES

ACRONYMS

1D	One Dimensional
2D	Two Dimensional
3D	Three Dimensional
ANDRA	Agence Nationale pour la gestion des Déchets RAdioactifs
BBM	Barcelona Basic Model
CEC	Cation Exchange Capacity
CI	Cement – (clay) Interactions
CPU	Central Processing Unit
C-S-H	Calcium-Silica-Hydrate
DECOVALEX	DEvelopment of COupled Models and their VALidation against EXperiments
DOE	Department of Energy
DSEF	Disposal Systems Evaluation Framework
EBS	Engineered Barrier System
EC	European Community
EDZ	Excavated Disturbed Zone
ENRESA	Empresa Nacional de Residuos Radiactivos
EoS	Equation of State
ESDRED	Engineering Studies and Demonstrations of Repository Designs
ERZ	Excavated Rock Zone
FCAWG	Fuel Cycle Alternative Working Group
FCRD	Fuel Cycle Research and Development
FEBEX	Full-scale Engineered Barriers Experiment
FEP	Features, Events, and Processes
GCMC	Grand Canonical Monte Carlo
GDSM	Generic Disposal System Model
GEM	Gibbs Energy Minimization
GWd	Gigawatt days
GWd/MT	Gigawatt (thermal) - days per Metric Ton
HKF	Helgeson-Kirkham-Flowers
HLW	High-Level nuclear Waste
HM	Heavy Metal

IAEA	International Atomic Energy Agency
IAPWS	International Association for the Properties of Water and Steam
IGD-TP	Implementing Geological Disposal of Radioactive Waste Technology Platform
IGSC	Integration Group for the Safety Case
LAMMPS	Large-scale Atomic/Molecular Massively Parallel Simulator
LANL	Los Alamos National Laboratory
LBNL	Lawrence Berkeley National Laboratory
LLNL	Lawrence Livermore National Laboratory
MD	Molecular Dynamics
MOC	Modified Open Cycle
MT	Metric Ton
MTHM	Metric Tons of Heavy Metal
NAGRA	National Cooperative for the Disposal of Radioactive Waste
NAWRA	Radioactive Waste Management Authority of the Czech Republic
NBS	Natural Barrier System
NE	DOE-Nuclear Energy
NEA	Nuclear Energy Agency
NW	Nuclear Waste
OECD	Organization for Economic Co-operation and Development
PA	Performance Assessment
RD&D	Research, Development, and Demonstration
R&D	Research and Development
RDO	Repository Design Optimization
RH	Relative Humidity
ROK	Republic of Korea (South Korea)
SEM	Scanning Electron Microscopy
SNL	Sandia National Laboratories
SRA	Strategic Research Agenda
TEM	Transmission Electron Microscopy
THM	Thermal-Hydrological-Mechanical
TM	Thermal-Mechanical

THMC	Thermal-Hydrological-Mechanical-Chemical
UFDC	Used Fuel Disposition Campaign
UOX	Uranium Oxide Fuel
URL	Underground Research Laboratory
VCS	Villars-Cruise-Smith
WIPP	Waste Isolation Pilot Plant
XRD	X-ray Diffraction
YMP	Yucca Mountain Project

Overview of Engineered Barrier System (EBS) Concept Evaluation
(Part I)

1. Overview of Engineered Barrier System (EBS) Concept Evaluation

1.1 Introduction

Engineered Barrier System (EBS) design concepts are a key component of the safe containment and long-term isolation of nuclear waste in geological repositories. The generic assessment of EBS requires a comprehensive understanding of important processes (and sub-processes) intrinsic to barrier domains, in many cases almost irrespective of the geologic host media (e.g., clay and crystalline rock) when applied to backfilled disposal concepts. For example, the EBS design concepts for clay and granite host rock media are very similar in terms of barrier materials and their potential interactions with the repository environment. Crushed salt backfill as barrier material in salt media is of course different from that envisioned for clay and crystalline rock. However, all these EBS buffer/backfill materials are exposed to Thermal-Hydrological-Mechanical-Chemical (THMC) processes that are coupled and common to these materials regardless of their type (see Fig. 1.1). These processes can also manifest in various spatial and time scales in the disposal environment. A discussion on the type and key features of various EBS design concepts were discussed in The UFDC report "Disposal Systems Evaluations and Tool Development - Engineered Barrier System (EBS) Evaluation" (Jové Colón et al., 2011) consistent with R&D needs and priorities described in the Used Fuel Disposition campaign (UFDC) R&D Roadmap report (Nutt et al., 2011). The above-mentioned UFDC report emphasized the important need for a flexible and agile approach to the study of generic EBS design concepts in various host-rock media using sophisticated computational tools and methods. *The current effort focuses on the development and application of such tools to examine important processes on barrier materials that can determine EBS performance*. The idea of "optimization" in the assessment of generic EBS design concepts involves the evaluation of various configurations stemming from the assessment of THMC coupled process models and information from experimental activities. Such global evaluation of the composite nature of the EBS allows for the examination of the collective functional structure of the barriers and their waste isolation capacity. This report is a collaborative contribution of multiple DOE labs: Sandia National Laboratories (SNL), Lawrence Berkeley National Laboratory (LBNL), Lawrence Livermore National Laboratory (LLNL), and Los Alamos National Laboratory (LANL). It encompasses a wide range of topics relevant to EBS processes described in the Summary section. Planned work for the rest of FY12 and FY13 on these research activities are given at the end of each part.

Jové Colón et al. (2011) summarized some of the characteristics of the proposed variants of multi-layered barrier configurations envisioned for backfilled disposal environments. The goal was to describe EBS design concepts having various levels of complexity from the number of barrier layers/domains and material types. This evaluation provides the basis for EBS design concept optimization in the analysis of compliance with performance and/or functional requirements of the EBS. These concepts were based on idealized waste package/canister geometries, barrier materials, and disposal configurations. There is a wide range of candidate materials for EBS concepts that includes metallic phases for canister and overpack materials for various types of steels (carbon, stainless steel), cast iron, and copper (Bennett and Gens, 2008). These authors describe the general characteristics of the metallic waste barrier and buffer materials for various European disposal concepts and waste types. An important aspect of barrier materials is that they can be tailored to fill an engineered role. For example, the addition

of graphite or quartz to clays can enhance thermal or mechanical properties (Beziat et al., 1992; Geneste et al., 1990; Jobmann and Buntebarth, 2009; Westerman, 1979). In addition to enhancements in thermal conductivity, the inclusion of graphite as part of the buffer / backfill admixtures can also offer some advantages such as contributing to lowering bulk permeability, mechanical strength, reduced conditions, and it's relatively inexpensive (Beziat et al., 1992; Geneste et al., 1990). The next section provides a general description of the important applications of tools and methods to evaluate EBS performance.
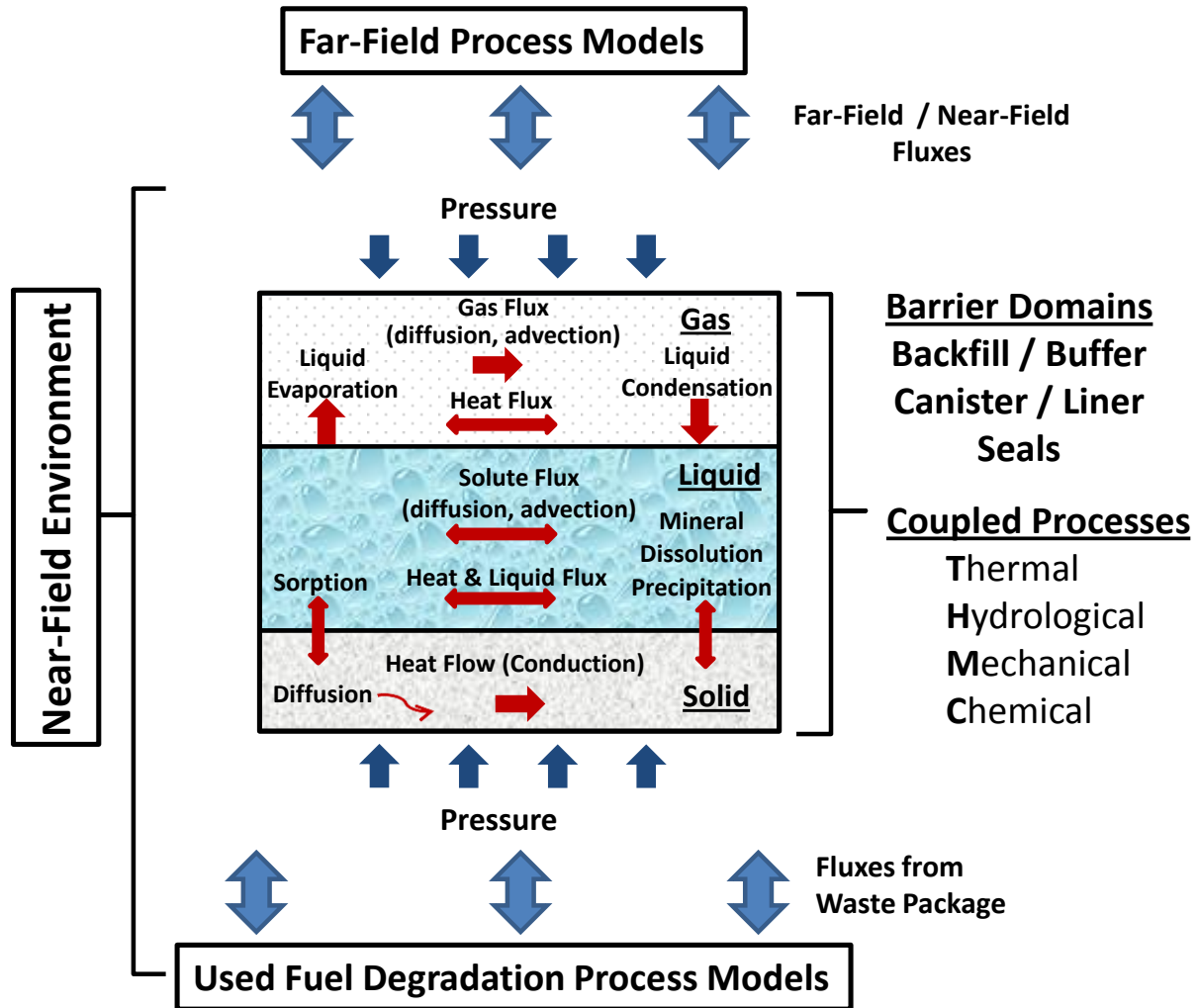
Figure 1.1. EBS coupled process phenomena (center) and interrelations between process models from other domains (modified after Olivella et al. 2011)

1.2 Optimization of EBS Design Concepts

The concept of repository design optimization (RDO) has been central in the use of site characterization data in repository programs such as the Deaf Smith County, Texas (DOE, 1988). The rationale for the technical basis of RDO encompasses various aspects of repository performance and safety analysis such as pre-closure operations to post-closure performance. The various forms of site characterization data, whether site specific or not, are crucial to the conception of design options, assessment of design performance, evaluation of disposal activities, waste canister and EBS emplacement, and cost analysis. The strategy of RDO relies on comprehensive characterization of the host-rock media underground structures, THMC phenomena and process model development, and EBS materials to be considered at the disposal galleries, for example:

1) Investigations of the underground environment to obtain data on the construction of shafts for the ventilation system.

2) Thermal, hydrological, and mechanical (THM) investigations of the underground environment:

   a) Evaluation of the stability of underground openings and excavations including the extent of the excavated rock zone (ERZ) and the selection of ground support systems for construction operations.

   b) Thermal, hydrological and mechanical studies to analyze these responses in rock and EBS materials. Such studies at the scale of underground research laboratories (URLs) provide key information used in the validation of coupled process models used to evaluate the design of the underground facilities and emplacement geometries of the disposal galleries.

3) Laboratory-scale experiments – Thermomechanical, thermal conductivity, transport, and fluid/solid interaction and phase stability studies. These studies provide key parameter data to models and the analysis of phase stability as a function of intensive variables such as temperature and pressure. Generation of data on processes covering phase solubility, sorption, fluid-solid interactions under various chemical conditions is crucial to the understanding of interactions at EBS interfaces as a function of pressure and temperature.

4) Together with items (2) and (3) above, development and application of modeling approaches is crucial to evaluate THMC phenomena in the EBS. Figure 1.1 (center) depicts the main processes affecting EBS materials in the near-field along with information interfacing between far-field and waste package process models for these domains.

Post-closure analysis and development of long-term repository design concepts is an iterative process that combines the results of field, laboratory, and modeling studies. This information is fundamental for the adequate evaluation of predictive methods and approaches when analyzing responses to model input parameters affecting the performance of repository key elements such as the EBS. For this reason, the importance of evaluating the predictive capability of THMC process models based on information gathered from engineered barrier experiments has been emphasized by researchers in European and USA nuclear waste repository programs (Gens et al., 2010; Gens et al., 2009; Guimaraes et al., 2007; Guimaraes et al., 2006, 2010; Olivella et al., 2011; Rutqvist et al., 2009a; Rutqvist et al., 2008; Rutqvist et al., 2009b; Rutqvist et al., 2011; Rutqvist et al., 1991). Another important aspect is the passing of information between the near-

field and process models from other domains such as the far-field. Figure 1.1 illustrates this importance when quantifying fluxes between the near- and far-field domains. Figure 1.1 also summarizes some of the key EBS processes and their couplings investigated in this report which are an integral part of an RDO strategy.

It should be noted that EBS processes and their potential interplay on radionuclide transport are among the highest ranked topics in the UFDC Disposal R&D Roadmap that includes waste form, THM processes, waste container, radionuclide speciation and solubility, and buffer/backfill material. Table 1.1 summarizes the priority ranking for the EBS for buffer/backfill and seal/liner materials after Nutt et al. (2011).

Table 1.1. Summary of the priority ranking for the EBS for buffer/backfill and seal/liner materials with associated FEPs (Nutt et al., 2011).

BUFFER / BACKFILL (media type) →	Clay	Salt	Crystalline	Mixed Materials
2.1.04.01: BUFFER/BACKFILL	High	Medium	Medium	Medium
2.1.07.02, .03, .04, 09: MECHANICAL PROCESSES	Medium	Medium	Medium	Medium
2.1.08.03, .07, .08: HYDROLOGIC PROCESSES	Medium	Medium	Medium	Medium
2.1.09.01, .03, .07, .09, .13: CHEMICAL PROCESSES - CHEMISTRY	Medium	Medium	Medium	Medium
- Radionuclide speciation/solubility	High	High	High	High
2.1.09.51, .52, .53, .54, .55, .56, .57, .58, .59, .61: CHEMICAL PROCESSES – TRANSPORT	Medium	Medium	Medium	Medium
- Colloid facilitated transport	Low	Low	Low	Low
2.1.11.04: THERMAL PROCESSES	Medium	Medium	Medium	Medium
2.1.12.01, .02, .03: GAS SOURCES AND EFFECTS	Medium	Medium	Low	Low
SEAL / LINER MATERIALS →	Cement	Asphalt	Metal	Polymer
2.1.05.01: SEALS	Medium	Medium	Medium	Medium
2.1.07.02, .08, .09: MECHANICAL PROCESSES	Medium	Medium	Medium	Medium
2.1.08.04, .05, .07, .08, .09: HYDROLOGIC PROCESSES	Low	Low	Low	Low
- Flow through seals	Medium	Medium	Medium	Medium
2.1.09.01, .04, .07, .09, .13: CHEMICAL PROCESSES – CHEMISTRY	Medium	Medium	Medium	Medium
- Radionuclide speciation/solubility	High	High	High	High
- Advection, diffusion, and sorption	Medium	Medium	Medium	Medium
2.1.11.04: THERMAL PROCESSES	Medium	Medium	Medium	Medium

Note:

1. FEP number lists delimited by commas show only the change in the fourth field of the FEP

The Strategic Research Agenda (SRA) report (SRA, 2011; www.igdtp.eu) for Implementing Geological Disposal of Radioactive Waste Technology Platform (IGD-TP) developed by the European Community (EC) framework programme provides a description of the research, development, and demonstration (RD&D) topics and priorities for geological disposal of nuclear waste. This report identifies with a high level of importance (to receive a license) in the safety case the need for "increase confidence in, and testing and further refinement of the tools (concepts, definition of scenarios and computer codes) used in safety assessments". Such a high prioritization ranking for increased confidence in process knowledge, methods, and tools is consistent with that UFDC Disposal R&D Roadmap report (Nutt et al. 2011).

1.2.1   Thermal Analysis for Layered EBS

Sacrificial Barrier and Thermal Constraints

THMC processes central to performance of barrier materials and their interactions with the surrounding environment are thermally driven. Postclosure repository performance assessment as described in DOE (1988) for nuclear waste disposal in salt focuses on coupled thermally-driven effects like compaction which then affects porosity and permeability. Dissolution and precipitation phenomena also affect permeability and fluid flow which in combination with mechanical processes can affect fluid fluxes in the EBS. Similarly, clay phase changes and mineral degradation as a result of thermal effects is considered an important aspect of long-term barrier performance. Barrier material stability and potential geochemical interactions with fluids have been considered a central aspect in the constraint of thermal limits in the EBS. However, some investigators argue that such constraints should be imposed on a rigorous scientific basis that in many cases is lacking (Wersin et al., 2007).

One strategy in analyzing the thermal effects is to study temperature profiles reaching from the waste canister surface toward the EBS outer boundaries in the near-field environment. Such analysis, although theoretical, can serve as an initial assessment of the fraction of *sacrificial* barrier material affected by elevated temperatures. For example, montmorillonite clay phase transformation induced by temperature can be used as an indicator of the barrier *sacrificial* domain to be substantially affected by temperature. It should be noted that that the term *sacrificial* doesn't necessarily means the destruction or complete compromise of the barrier isolation capability at a particular spatial location. It denotes the barrier region experiencing the most significant changes in response to thermal effects. An example of this is described in NAGRA (2002) for the Swiss repository concept where attainment of clay barrier temperatures below the purported thermal limit of 100°C is not possible because of waste thermal loads and low thermal conductivity of the unsaturated bentonite. Given the disposal design of the NAGRA Swiss concept, the thermal constraints considered applies to the half of the clay-ring outer domain of the bentonite barrier at a temperature that does not exceed 125°C (Johnson and King, 2003). Such rationale is based on the temperatures at which silica cementation and phase transformation of smectite to illite have been observed and can affect clay swelling properties. However, it should be noted that experimental observations indicate that clay material may be stable at temperatures in excess of 150°C in the absence of pervasive interactions with aqueous fluids. As discussed in Wersin et al. (2007) and Jové Colón et al. (2011), loosening temperature constraints in the clay barrier could liberate design options s to potentially more cost-effective and flexible repository design diminishing spatial requirements at the site and accommodating a wider range of waste types with higher burnup rates and heat loads. In conclusion, the

establishment of EBS thermal constraints requires a comprehensive assessment of barrier material stability and behavior under a wide range of conditions. The current UFDC EBS task is conducting research activities with the goals of obtaining wide-ranging and yet detailed information of EBS processes and their accurate description in modeling tools and methods.

DSEF Thermal Analysis of Layered EBS Using the Disposal System Evaluation Framework (DSEF)

As described above, thermally-driven processes drive the evaluation of THMC processes. The Disposal System Evaluation Framework (DSEF) is a tool developed by LLNL to evaluate repository design concepts and options through information links on waste form type and repository environments; see Hardin et al. (2011) and Jové Colón et al. (2011) for more details. DSEF also interfaces with sophisticated tools and methods used in thermal analysis of the EBS. As an example, the DSEF thermal analysis tool has been used to evaluate peak temperature profiles for a two-domain clay barrier EBS concept in clay host media. Jové Colón et al. (2011) describes the basic characteristics of backfilled EBS design ranging from single-domain (layer) buffer to more complex multi-layered barrier domain concepts (see for example Figure 1.2). DSEF allows for rapid evaluation of thermal behavior in the EBS on the basis of geometric, waste form type, and barrier material properties. DSEF also allows for designation of radial dimensions to define barrier thickness according to the EBS circular concentric geometry as depicted in Figure 1.2. The dimensions of the layered EBS configuration are given in Figure 1.3. The waste type and configuration considered in this example is a 12-assembly UOX fuel with burnup rates of 40 and 60 GWd/MT to represent alternate waste forms. Two types of clay barrier types were evaluated: (1) 80/20 bentonite clay and graphite mixture (inner) and dry benonite (outer); (2) 80/20 bentonite clay and graphite mixture (inner); (2) 85/15 bentonite clay and graphite mixture (outer). Thermal conductivities for the bentonite/graphite mixture were obtained from Jobmann and Buntebarth (2009). For each of these two combinations of barrier types, four cases with varying burnup rates and storage times were examined for a total of eight cases. DSEF uses pre-defined waste form decay heat data, geometry, and material properties. The thermal analysis calculations in DSEF were performed by Harris Greenberg (LLNL) using analytical formulations implemented in the Mathcad software package as described in Hardin et al. (2011) and Jové Colón et al. (2011). More details on DSEF Version 2.0 will be described in the LLNL milestone report M4FT-12LL0806043 to be submitted in July 2012.

Figure 1.4 illustrates the resulting thermal resistance profile of the various barrier domains from the waste package surface to the cement lining. In all cases, the thermal conductivity for the cement lining is 1.7 W/ m K. Table 1.2 describes the input parameter and results for each case. The results are presented in the form of peak temperatures and the time of occurrence after storage. These results show the interrelationships and importance between barrier material thermal properties, fuel burnup rates, and storage time while retaining the same EBS geometric configuration. It shows that in cases 1 through 4, the use of dry bentonite (unmixed) in the outer barrier layer leads to higher peak temperatures than in cases 5 through 8 where a mixed bentonite/graphite buffer is considered for the outer barrier. Such analysis, albeit high level, exemplifies the importance of thermal regimes and other key variables to RDO that can determine EBS design performance. Thermal constraints, however, need to be evaluated comprehensively in parallel with other determining factors to EBS performance.
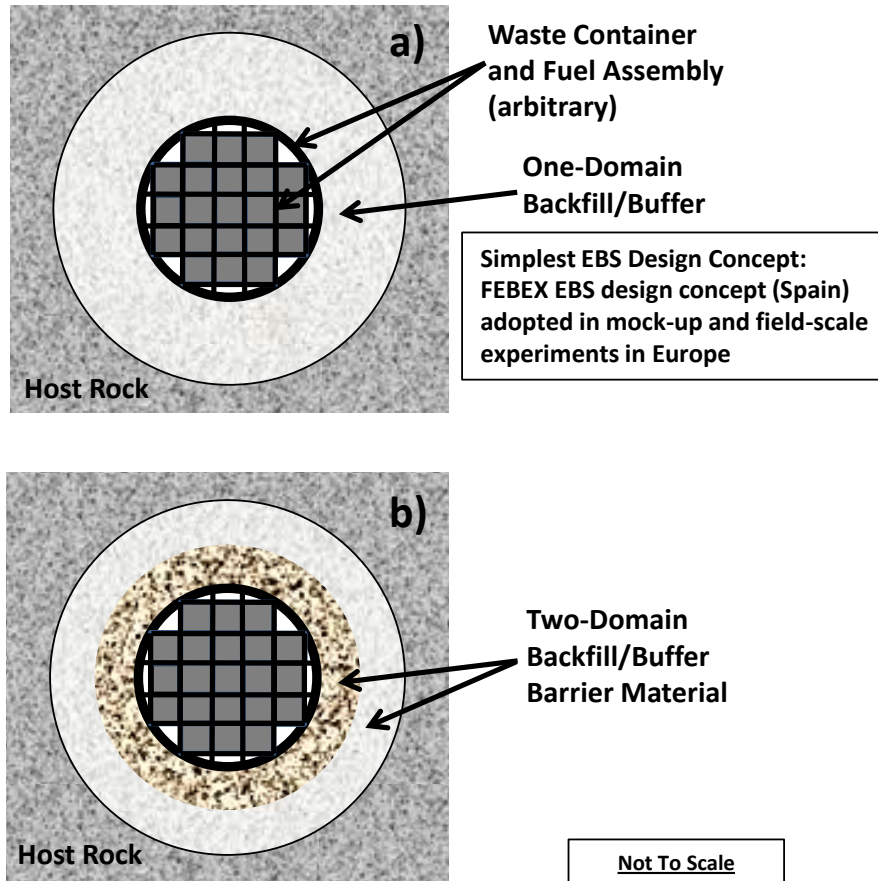
Figure 1.2. Generalized backfilled multi-layered EBS design for one- and two-domain backfill/buffer barriers: a) single-domain and b) two-domain.

	EBS Component	Component Thickness m	Inner Radius m	Outer Radius m	Material Type	Material Type	Thermal Conductivity W/m-K
	Waste Form Outer R	0.475	N/A	0.475	UOX SNF Fuel Assembly	UOX SNF Fuel Assembly	N/A
	Canister	0	0.475	0.475	Steel	Steel	46
	Waste Package	0.1	0.475	0.575	Steel	Steel	46
These names can be changed below	Buffer Layer 1	1.2375	0.575	1.8125	Other	Bentonite-Graphite Mix	3.3
	Buffer Layer 2	1.2375	1.8125	3.05	Bentonite - Dry	Bentonite - Dry	0.6
	Backfill	0	3.05	3.05	Not in EBS for this Case	Not in EBS for this Case	N/A
	Liner	0.75	3.05	3.8	Cementitious Material	Cementitious Material	1.7
	Host Rock Inner Radius, m ---->		3.8				

Figure 1.3. Snapshot of DSEF spreadsheet section summarizing dimensions and properties EBS components for cases 1 through 4 (see Table 1.2).

29
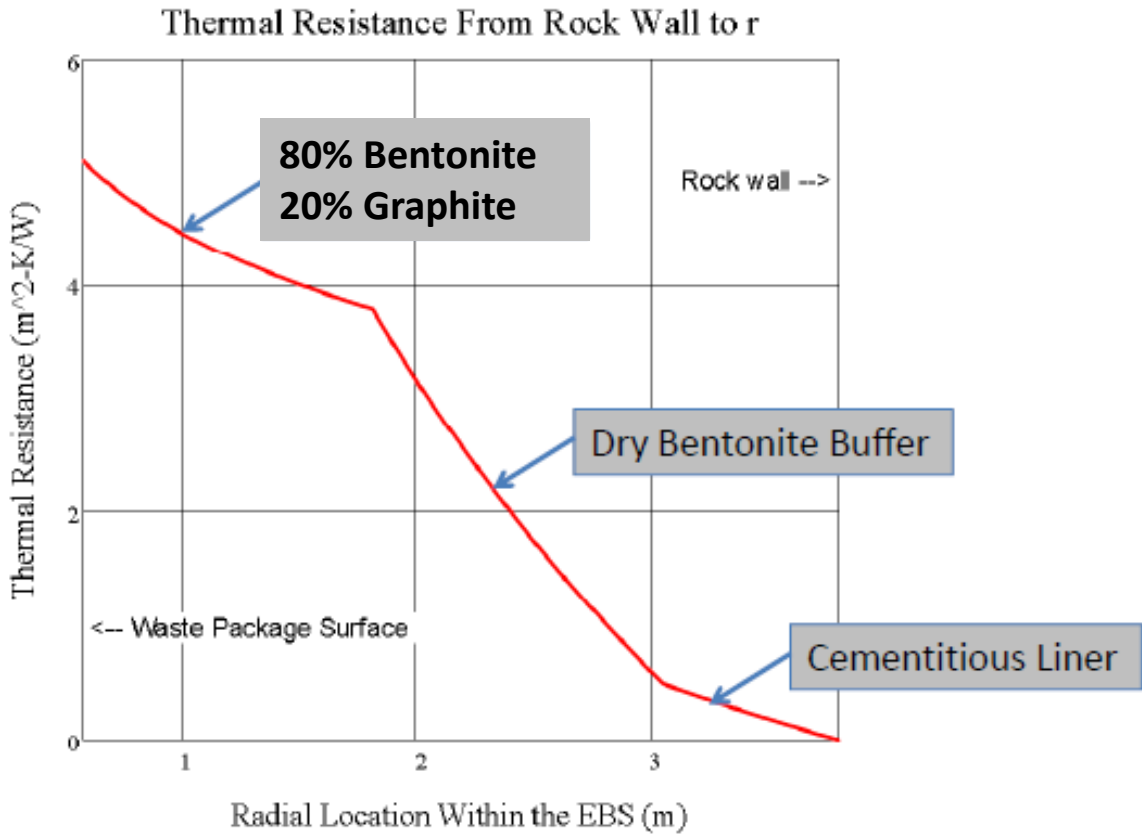
Figure 1.4. Thermal resistance profile of the layered EBS with respect to radial location.

Table 1.2. EBS input parameters and results for the eight cases considered in the thermal analysis.

Case	Inner Buffer Layer	Thermal conductivity (W/m K)	Outer Buffer Layer	Thermal conductivity (W/m K)	Burnup (GWd/MT UOX)	Storage Time (years)	Case Number	Waste Pkg Surface — Outer r (0.575 m)		Inner Buffer Layer — Outer r (1.8125 m)		Outer Buffer Layer — Outer r (3.05 m)		Host Rock Wall — (Liner Outer r) Wall Inner (r = 3.8 m)	
								Peak Temp. (°C)	Time of Peak Temp. (yr)	Peak Temp. (°C)	Time of Peak Temp. (yr)	Peak Temp (°C)	Time of Peak Temp. (yr)	Peak Temp (°C)	Time of Peak Temp. (yr)
Base EBS Design plus alternate Waste Forms and Storage Times	80% Bentonite, 20% Graphite	3.3	Dry Bentonite	0.6	60	40	1	404.5	47	335.3	51	195.5	87	181.4	101
					60	100	2	205.8	120	177.8	132	127.8	256	122.8	299
					40	40	3	268.6	48	225.3	53	138.5	96	130.0	112
					40	100	4	151.2	126	133.1	152	103.8	345	100.4	371
Alternate EBS Design Case plus Waste Form and Storage Time Variations	80% Bentonite, 20% Graphite	3.3	85% Bentonite, 15% Graphite	2.2	60	40	5	283.1	57	226.7	69	195.5	87	181.4	101
					60	100	6	157.7	152	138.2	225	127.8	256	122.8	299
					40	40	7	192.8	59	157.7	76	138.5	96	130.0	112
					40	100	8	121.5	226	110.5	299	103.8	345	100.4	371

Color Coding: Yellow (100°C<T<120°C), Brown (120°C<T<140°C); Red (T>140°C)

The entire thermal analysis just presented is inherently constrained by a set of assumptions, for example, constant thermal conductivity within the barrier layers. Although this assumption is valid in many cases, thermal conductivity of porous granular material can be highly susceptible to porosity and saturation levels, temperature, and compaction. Therefore, detailed analysis of the barrier thermal behavior are needed to systematically assess its performance and other couplings. Still, DSEF provides a high level description of EBS thermal behavior with a knowledge base approach that links various categories of important information relevant to the evaluation of EBS performance.

1.3 International Collaboration on EBS

Recommended international collaborations relevant to the study of EBS were described in Jové Colón et al. (2011). The recent DECOVALEX 2015 project kick-off meeting held at LBNL (April, 2012) outlined the collaborations and engagements in this phase of the project:

- **HE-E Heater Test**: Studies of bentonite/rock interaction to evaluate sealing and clay barrier performance, in a micro-tunnel at the Mont Terri URL, proposed by ENRESA (Spain). Details about this collaboration are given in Section 2.3 of Part II of this report.

- **Bedrichov Tunnel Experiment**: Interpretation of inflow patterns and tracer transport behavior in fractured granite, proposed by NAWRA (Radioactive Waste Management Authority of the Czech Republic). This engagement with DECOVALEX is more aligned with the natural system (NS) activity but some level of integration with EBS is anticipated.

Other international collaborations relevant to EBS:

Republic of Korea (ROK) – US Joint Fuel Cycle Study: Task 2 – Engineered and Natural Barrier Systems databases – UFDC contacts: Yifeng Wang (SNL) and Carlos F. Jové Colón (SNL). This collaboration activity involves the sharing of thermodynamic and sorption databases from the UFDC program. UFDC reviewed the literature on radionuclide interactions with clay materials and SNL published a the peer-reviewed journal article in Environmental Science and Technology Miller and Wang (2012) in a March 2012 meeting. The ROK allows UFDC members of this task access to their web-based sorption database. Presentations describing each task were given at the recent Fuel Cycle Alternative Working Group (FCAWG) meeting held at SNL (June 2012). This meeting allowed participants from both countries to exchange views and information about this collaboration.

Collaborations on Salt Disposal R&D: The Nuclear Energy Agency (NEA) Integration Group for the Safety Case (IGSC) recently sanctioned a Salt Club for advancing salt repository options for member states and the USA. Collaborations with German researchers to leverage their considerable expertise while enhancing our generic salt program. This alliance will have the goal of advancing the science and technology on key issues such as seal strategy, constitutive modeling, and granular salt consolidation:

Collaborate on a state-of-the-art paper on reconsolidation of granular salt. (September 2012.)

Support review and concurrence on a catalogue of potentially relevant features, events, and processes (FEPs) for high-level waste disposal in salt, consistent with the conclusions of the 2nd US/German workshop participants.

Planning participation in the Implementing Geological Disposal of Radioactive Waste Technology Platform (IGD-TP) strategic initiative on seal systems for generic repositories.

Cement-Clay Interactions (CI) experiments at Mt. Terri: Initial contact has been established with Dr. Urs Mäder (Univ. of Bern, Switzerland) regarding participation in this activity. The focus of this cement-clay interaction (CI) activity in the current phase is on analytical characterization of sampled material at the clay-cement interface. There is also a planned activity on reactive transport modeling of interest to UFDC EBS evaluation. This modeling activity is current planned for a subsequent phase of this project. According to Dr. Mäder, there is an interest from various international groups on the modeling aspects of cement-clay interactions.

1.4   References

Bennett, D. G., and Gens, R., 2008, Overview of European concepts for high-level waste and spent fuel disposal with special reference waste container corrosion: Journal of Nuclear Materials, v. 379, no. 1-3, p. 1-8.

Beziat, A., Dardaine, M., and Mouche, E., 1992, Measurements of the thermal conductivity of clay-sand and clay-graphite mixtures used as engineered barriers for high-level radioactive waste disposal: Applied Clay Science, v. 6, p. 245-263.

DOE, 1988, Consultation Draft - Site Characterization Plan Deaf Smith County, Texas; Volumes 7, Volume 7, Office of Civilian Radioactive Waste Management Salt Repository Project Office U.S. Department of Energy, p. 208-249.

Geneste, P., Raynal, M., Atabek, R., Dardaine, M., and Oliver, J., 1990, Characterization of a French Clay Barrier and Outline of the Experimental Program: Engineering Geology, v. 28, no. 3-4, p. 443-454.

Gens, A., Guimaraes, L. D., Olivella, S., and Sanchez, M., 2010, Modelling thermo-hydro-mechano-chemical interactions for nuclear waste disposal: Journal of Rock Mechanics and Geotechnical Engineering, v. 2, no. 2, p. 97–102.

Gens, A., Sanchez, M., Guimaraes, L. D., Alonso, E. E., Lloret, A., Olivella, S., Villar, M. V., and Huertas, F., 2009, A full-scale in situ heating test for high-level nuclear waste disposal: observations, analysis and interpretation: Geotechnique, v. 59, no. 4, p. 377-399.

Guimaraes, L. D., Gens, A., and Olivella, S., 2007, Coupled thermo-hydro-mechanical and chemical analysis of expansive clay subjected to heating and hydration: Transport in Porous Media, v. 66, no. 3, p. 341-372.

Guimaraes, L. D., Gens, A., Sanchez, M., and Olivella, S., 2006, THM and reactive transport analysis of expansive clay barrier in radioactive waste isolation: Communications in Numerical Methods in Engineering, v. 22, no. 8, p. 849-859.

-, 2010, Coupled THMC modeling of unsaturated swelling clays: Constitutive formulation and boundary value problems: Unsaturated Soils: Theoretical and Numerical Advances in Unsaturated Soil Mechanics, p. 515-529.

Hardin, E., Blink, J. A., Greenberg, H. R., Sutton, M., Fratoni, M., Carter, J., Dupont, M., and Howard, R., 2011, Generic Repository Design Concepts and Thermal Analysis (FY11) (SAND2011-6202): Sandia National Laboratories, Albuquerque, New Mexico, 278 pp.

Jobmann, M., and Buntebarth, G., 2009, Influence of graphite and quartz addition on the thermo-physical properties of bentonite for sealing heat-generating radioactive waste: Applied Clay Science, v. 44, no. 3-4, p. 206-210.

Johnson, L. H., and King, F., 2003, Technical Report 02-11: Canister Options for the Disposal of Spent Fuel, NAGRA: Wettingen, Switzerland, p. 57 pp.

Jové Colón, C. F., Caporuscio, F. A., Levy, S. S., Blink, J. A., Greenberg, H. R., Halsey, W. G., Fratoni, M., Sutton, M., Wolery, T. J., Rutqvist, J., Liu, H. H., Birkholzer, J., Steefel, C. I., and Galindez, J., 2011, Disposal Systems Evaluations and Tool Development - Engineered Barrier System (EBS) Evaluation, p. 1-192.

Miller, A. W., and Wang, Y., 2012, Radionuclide Interaction with Clays in Dilute and Heavily Compacted Systems: Environmental Science and Technology, v. 46, no. 4, p. 1981-1994.

NAGRA, 2002, Demonstration of disposal feasibility for spent fuel, vitrified high-level waste and long-lived intermediate-level waste, Technical Report 02-05, NAGRA: Wettingen, Switzerland, 472 pp.

Nutt, M., Voegele, M., Jove-Colon, C., Wang, Y., Howard, R., Blink, J., Liu, H.-H., Hardin, E., and Jenni, K., 2011, Used Fuel Disposition Campaign Disposal Research and Development Roadmap (Fuel Cycle Research and Development), Prepared for U.S. Department of Energy Used Fuel Disposition Campaign FCR&D-USED-2011-000065

Olivella, S., Castagna, S., Alonso, E. E., and Lloret, A., 2011, Porosity Variations in Saline Media Induced by Temperature Gradients: Experimental Evidences and Modelling: Transport in Porous Media, v. 90, no. 3, p. 763-777.

Rutqvist, J., Backstrom, A., Chijimatsu, M., Feng, X. T., Pan, P. Z., Hudson, J., Jing, L., Kobayashi, A., Koyama, T., Lee, H. S., Huang, X. H., Rinne, M., and Shen, B. T., 2009a, A multiple-code simulation study of the long-term EDZ evolution of geological nuclear waste repositories: Environmental Geology, v. 57, no. 6, p. 1313-1324.

Rutqvist, J., Barr, D., Birkholzer, J. T., Chijimatsu, M., Kolditz, O., Liu, Q. S., Oda, Y., Wang, W. Q., and Zhang, C. Y., 2008, Results from an international simulation study on coupled thermal, hydrological, and mechanical processes near geological nuclear waste repositories: Nuclear Technology, v. 163, no. 1, p. 101-109.

Rutqvist, J., Barr, D., Birkholzer, J. T., Fujisaki, K., Kolditz, O., Liu, Q. S., Fujita, T., Wang, W. Q., and Zhang, C. Y., 2009b, A comparative simulation study of coupled THM processes and their effect on fractured rock permeability around nuclear waste repositories: Environmental Geology, v. 57, no. 6, p. 1347-1360.

Rutqvist, J., Ijiri, Y., and Yamamoto, H., 2011, Implementation of the Barcelona Basic Model into TOUGH-FLAC for simulations of the geomechanical behavior of unsaturated soils: Computers & Geosciences, v. 37, no. 6, p. 751-762.

Rutqvist, J., Stephansson, O., Noorishad, J., and Tsang, C. F., 1991, Modeling of Hydro-Thermo-Mechanical Effects in a Fracture Intersecting a Nuclear Waste Deposition Hole: High Level Radioactive Waste Management, Vols 1 and 2, p. 547-554.

SRA, 2011, Implementing Geological Disposal of Radioactive Waste Technology Platform Strategic Research Agenda 2011 (IGD-TP), European Community (EC) Euratom framework programme, 63 pp. (ISBN 978-91-979786-0-6) (www.igdtp.eu)

Wersin, P., Johnson, L. H., and McKinley, I. G., 2007, Performance of the bentonite barrier at temperatures beyond $100^{o}C$: A critical review: Physics and Chemistry of the Earth, v. 32, no. 8-14, p. 780-788.

Westerman, R. E., 1979, Preliminary Conceptual Designs for Advanced Packages for the Geological Disposal of Spent Fuel, PNNL-2990: Richland, Washington, Pacific Northwest Laboratory, 109 pp.

Investigation of Reactive Transport and Coupled THM Processes in EBS

(Part II)

1. INTRODUCTION

Geological repositories for disposal of high-level nuclear waste generally rely on a multibarrier system to isolate radioactive waste from the biosphere. The multibarrier system typically consists of the natural barrier system (NBS), which includes the repository host rock and its surrounding subsurface environment, and the engineered barrier system (EBS). The EBS represents the man-made, engineered materials placed within a repository, including the waste form, waste canisters, buffer materials, backfill, and seals (OECD, 2003). The EBS plays a significant role in the containment and long-term retardation of radionuclide release.

During the lifespan of a geologic repository, the performance of the EBS is affected by complex thermal, hydrogeological, mechanical, chemical and biological processes, such as heat release due to radionuclide decay, multiphase flow (including gas release due to canister corrosion), swelling of buffer materials, radionuclide diffusive transport, waste dissolution, and chemical reactions. All these processes are related to each other. An in-depth understanding of these coupled processes is critical for the performance assessment (PA) of an EBS and the entire repository. Within the EBS work package of the Used Fuel Disposition (UFD) Campaign, LBNL's research is currently focused on two relevant areas, namely (1) the thermal-hydrological-mechanical-chemical (THMC) processes in buffer materials (bentonite), and (2) the diffusive transport in the EBS associated with clay host rock, with the long-term goal of developing a full understanding of (and verified modeling capabilities to simulate) the impact of coupled processes on radionuclide transport in different components of EBS, as well as the interaction between the EBS components and the near-field host rock (e.g., clay/shale)—and how these processes affect radionuclide release.

LBNL's focus areas address key Features, Events and Processes (FEPs), which have been ranked in importance from medium to high, as listed in Tables 7 and 8 of the *Used Fuel Disposition Campaign Disposal Research and Development Roadmap* (FCR&D-USED-2011-000065 REV0) (Nutt, 2011). Specifically, they address FEP 2.2.01, Excavation Disturbed Zone (EDZ), for shale by investigating the effects of coupled processes on interactions between shale (clay) disposal formations and the EBS; FEPs 2.1.04.01, Buffer/Backfill; FEPs 2.1.07.02, 03, 04, 09, Mechanical Processes; FEPs 2.1.08.03, 07, 08, Hydrologic Processes; and FEP 2.1.11.04, Thermal Processes, by studying coupled processes in the EBS; and FEPs 2.1.09.52, 53, 54, Chemical Processes—Transport, by investigating reactive-diffusive radionuclide transport in bentonite.

This report documents the progress that LBNL has made in its two R&D focus areas in FY12. Section 2 presents the modeling results of THM processes within bentonite and the interaction between the EBS and a clay disposal formation in the near field. Sections 3 and 4 document the development of reactive-diffusive transport modeling approaches for radionuclide migration in bentonite, supported by molecular dynamics simulations of ion diffusion. Section 5 reports on experimental studies on sorption and reactive diffusive transport of U(VI) in bentonite. Work activities in the remaining months of FY12 and proposed activities in FY13 are presented in Section 6.

2.   MODELING COUPLED THM PROCESSES IN EBS

The long-term chemical and mechanical stability of protective bentonite buffers and tunnel backfill is a key issue in the long-term performance of backfilled, multiple barrier nuclear waste repositories. For example, a certain swelling pressure should be maintained to keep the buffer homogenous, to prevent canister sinking, to prevent the adverse effect of external rock shear movements, to limit colloid transport, and to prevent the buffer from being a preferred pathway of radionuclide transport. The long-term stability of the buffer is governed by coupled thermal-hydrological-mechanical and chemical (THMC) processes. These coupled THMC processes can be simulated by numerical modeling, e.g., by a coupling of LBNL's TOUGHREACT reactive transport simulator to a geomechanical code such as FLAC3D. However, this requires appropriate constitutive models describing couplings between the different processes.

In this section, we describe our ongoing work on developing and applying such models for the analysis of EBS coupled processes. We have previously implemented the Barcelona Basic Model (BBM) into the TOUGH-FLAC simulator in FY11 and currently are expanding this to a dual-structure model for expansive clay, such as bentonite. A dual-structure model has important features for modeling the mechanical behavior of a bentonite buffer, such as irreversible strain during suction cycles. However, most importantly, a dual-structure model provides the necessary link between chemistry and mechanics, enabling us to develop a fully coupled THMC model for the analysis of long-term EBS behavior.

In FY11, we focused on using TOUGH-FLAC with the newly implemented Barcelona Basic Model (BBM) for simulating coupled THM processes within a generic bentonite-backfilled emplacement tunnel and its interactions with the natural system (clay formations). In FY12, we are continuing such analysis, including more parameter studies, with the aim of summarizing this work in a journal paper. A substantial amount of FY12 work is being devoted to implementing a dual-structure model into TOUGH-FLAC for more rigorous modeling of expansive clay and potential coupling to chemistry. In addition, we are initiating modeling of the HE-heater test at the Mont Terri underground research laboratory, as a participant in the international DECOVALEX project. The HE-heater test is an ongoing half-scale heater experiment for EBS and near-field behavior; the measurements on coupled processes parameters will help validate the ongoing model development.

2.1   Sensitivity Studies Related to EBS THM Modeling of a Generic Repository

In FY12, we have continued EBS modeling using the newly implemented BBM model in TOUGH-FLAC for parameter study and scenario analysis. This work is being summarized in a journal paper related to a presentation made at the international TIMODAZ project workshop at Mont Terri, Switzerland, February 7 and 8, 2012. The journal paper describes the new code developments for EBS and their applications to a generic repository in a clay host rock.

In these simulations, we considered clay host-rock properties derived from the Opalinus clay at Mont Terri, Switzerland (Gens et al., 2007). The EBS design featured waste emplacement in horizontal tunnels back-filled with bentonite-based swelling clays as a protective buffer (Figure 2.1).
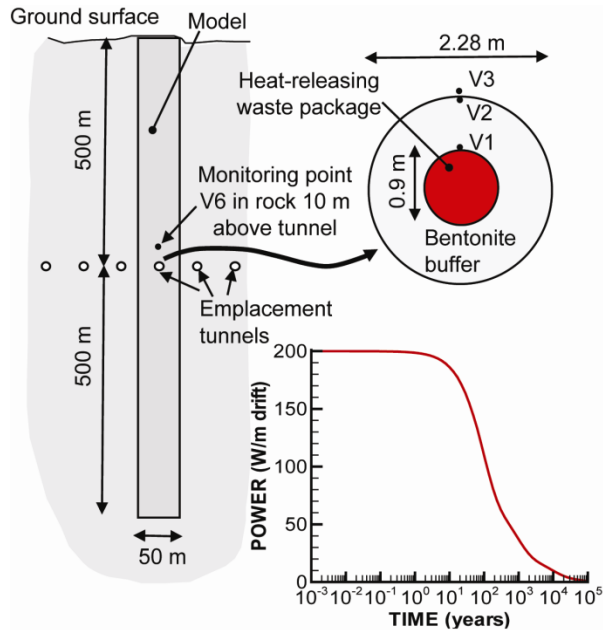
Figure 2.1. Model domain for an assumed bentonite back-filled horizontal emplacement drift at 500 m depth in clay host rock.

In FY11, a comprehensive sensitivity study was completed related to (1) thermal management and peak temperature, (2) resaturation time and buffer swelling, and (3) rock failure for layered rock. The FY11 modeling included extreme temperature conditions, leading to very high temperature in the buffer, slow buffer resaturation, and strong thermal pressurization. The thermal pressurization was related to thermal expansion of fluids in the pores of the low permeability clay host rock, leading to pore-pressure increases around the repository horizon lasting for thousands of years.

In FY12, we made additional simulations considering more realistic conditions and properties than what were assumed in some of the FY11 simulations:

1) In the case of the buffer consisting of bentonite pellets (rather than bentonite blocks), the initial water saturation of 1% considered in the FY11 modeling study was deemed unrealistic, based on observations in field tests at the Mont Terri underground laboratory. Even though the saturation could be a few percent during emplacement, the pellets will quickly equilibrate with the relative humidity in the air, and therefore an initial saturation around 20 to 25% would be realistic. In FY12, we conducted additional simulations in which the initial saturation was set to 20% in the case of a bentonite pellet.

2) In the extreme case of low rock thermal conductivity, a low initial buffer saturation, and a high thermal line load, a peak temperature up to 150°C was achieved in the FY11 sensitivity study. The justification for such a high peak temperature was based on early thermal simulations within the Swiss nuclear waste program, where such a high temperature was considered. However, the current concept targets the temperature at the canister-bentonite interface to be between 125°C and 135°C. This is also what is being considered as the upper target temperature at the planned full scale demonstration heater test at Mont Terri, although the scientific basis for this is not yet fully established. Thus, in FY12, we conducted simulations for peak temperatures up to 135°C.

39

3) In the FY11 model simulations, a layered rock formation was considered corresponding to that of the Opalinus clay observed at the Mont Terri rock laboratory. However, Mont Terri is relatively shallow, in a sloping part of the Opalinus clay, with a layering dipping at an angle of 45°. A repository would likely be placed at deeper locations, where the target repository units would be horizontal, with horizontal beddings, and with relatively stiffer geomechanical properties as a result of compaction. In FY12, we therefore conducted simulations for the case of horizontal bedding planes.

Figure 2.2 shows an example of simulation results for a bentonite buffer made of dry pellets having an initial saturation of 20%. The peak temperature is 118°C at 40 years, whereas the peak temperature in the Opalinus clay is less than 100°C (Figure 2.2a). Time to complete saturation of the buffer is 100 years, and there is significant thermal pressurization. When the layers of the Opalinus clay are horizontal, the potential for shear failure along bedding planes is much less, since no significant thermally induced shear stress develops along the beddings in such a case.
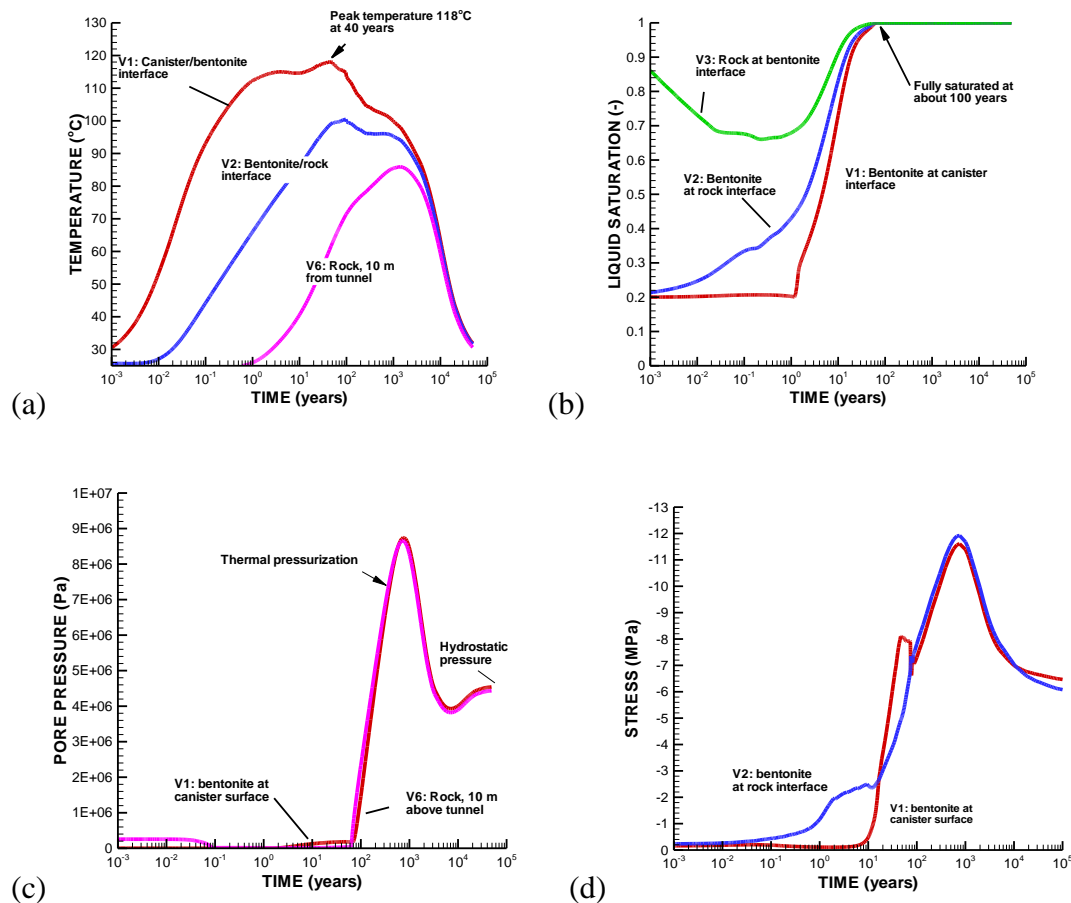
Figure 2.2. Simulated evolution of THM processes in buffer: (a) temperature, (b) liquid saturation, (c) fluid pressure, and (d) total radial stress (σx). See Figure 2.1 for locations of V1, V2, V3, and V6.

40

2.2 Implementation of a Dual-Structure Bentonite Model into TOUGH-FLAC

In this section, we present the development and implementation of a dual-structure material model of expansive clay into TOUGH-FLAC. In such a model, the material consists of two structural levels: a microstructure in which the interactions occur at the particle level, and a macrostructure that accounts for the overall fabric arrangement of the material comprising aggregates and macropores (Figure 2.3) (Gens et al., 2006, Sánchez et al., 2005, Gens and Alonso, 1992). The dual-structure (or double-structure) model approach is especially useful when trying to incorporate the effects of chemical variables on the mechanical behavior of expansive clays. Because they contain large amounts of active clay minerals, those materials are especially susceptible to changes in the geochemical environment. Thus, the double structure model can provided the link between mechanical and chemical processes modeling, which enables mechanistic modeling of processes important for long-term buffer stability, including:

- Effect of pore water salinity on swelling (loss of swelling?)
- Conversion of smectite to non-expansive mineral forms (loss of swelling?)
- Cementation by precipitation of silica (buffer becomes brittle?)

In this section, we first present an overview of the basic equations in the dual-structure model following (in part) the developments by Alonso et al. (1999) and Sánchez et al. (2005). We then summarize the implementation of this model into TOUGH-FLAC.
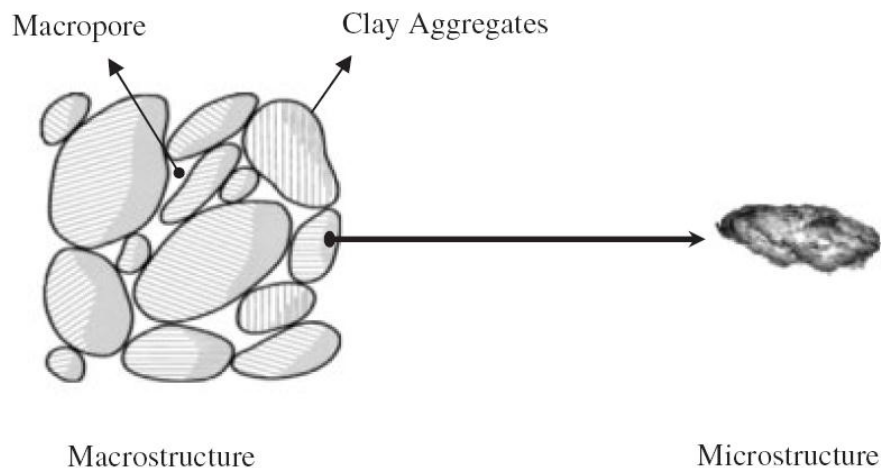
Figure 2.3. Schematic representation of the two structural levels considered (Sánchez et al., 2005).

2.2.1 The Dual-Structure Approach and Barcelona Expansive Model

Alonso et al. (1999), in their presentation of the Barcelona Expansive Model (BExM), provide a suitable mathematical formulation for implementation of a dual structure model into TOUGH-FLAC. Sánchez et al. (2005) provide another comprehensive description and mathematical formulation in terms of generalized elastoplasticity and implementation into a finite element code. The implementation of the BExM into TOUGH-FLAC is done as an extension of the existing TOUGH-FLAC implementation of the BBM, adding the microstructural level. The

BBM model can describe many typical features of unsaturated-soil mechanical behavior, including wetting-induced swelling or collapse strains, depending on the magnitude of applied stress, as well as the increase in shear strength and apparent preconsolidation stress with suction (Gens et al., 2006). The extension to dual-structure behavior enables modeling of more expansive soils, including dependency of swelling strains and swelling pressures on the initial state and on the stress path, strain accumulation during suction cycles, as well as secondary swelling. It is believed that such behavioral features are mainly related to the existence of coupled chemo-hydro-mechanical phenomena between distinct levels of structure within the material (Alonso et al., 1999).

Conceptually, in a dual-structure model as described by Alonso et al., (1999) and Sánchez et al., (2005), the total volume, V, of the material consists of the solid phase, V_s, the microstructural voids V_{vm}, and the macrostructure voids V_{vM}:

$$V = V_s + V_{vm} + V_{vM} = V_m + V_{vM} \tag{2.1}$$

with the total void ratio and porosity being the sum of microstructural and macrostructural components according to

$$e = \frac{V_v}{V_s} = e_M + e_m = \frac{V_{vM}}{V_s} + \frac{V_{vm}}{V_s} \tag{2.2}$$

$$\phi = \frac{V_v}{V} = \phi_M + \phi_m = \frac{V_{vM}}{V_s} + \frac{V_{vm}}{V_s} \tag{2.3}$$

The microstructure can swell to invade the macroporosity, depending on the mechanical confinement and load level. This is relevant when considering permeability changes during bentonite swelling, because fluid movement takes place through the macroporosity, which is not proportional to the total strain and deformation of the bentonite.

2.2.1.1   Macrostructural Level

The macrostructural behavior is modeled based on the BBM, in which the mechanical behavior depends on a three-dimensional yield surface in p'-q-s space (Figure 2.4), where p' is net mean stress (i.e., total stress minus gas-phase pressure), q is deviatoric stress (or shear stress), and s is suction. The size of the elastic domain increases as suction increases. The rate of increase, represented by the loading-collapse (LC) curve, is one of the fundamental characteristics of the BBM (Gens et al., 2006).

The suction-dependent loading collapse (LC) yield surface (Figure 2.4) bounds the elastic region according to

$$f_{LC} = \frac{q^2}{g_y(\theta)^2} - \frac{M^2}{g_y(\theta = 0)^2}(p' + p_s)(p_0 - p') = 0 \tag{2.4}$$

where θ is the Lode's angle and the function $g_y(\theta)$ describes the shape of the yield surface in the deviatoric plane. M is the constant slope of the critical state line (Figure 2.4), whereas p_s represents the increase in cohesion with suction and the function

$$p_0 = p^c \left(\frac{p_0^*}{p^c} \right)^{[\lambda_{Ps0} - \kappa_{Ps0}]/[\lambda_{Ps} - \kappa_{Ps0}]} \qquad (2.5)$$

is the net mean yield stress (or apparent pre-consolidation stress) at current suction, where P_0^* is the net mean yield stress (or pre-consolidation stress) at full saturation and λ_{PS} is a compressibility parameter in virgin soil states at suction s.

$$g_{LC} = \frac{\alpha_a q^2}{g_y(\theta)^2} - \frac{M^2}{g_y(\theta = 0)^2} (p' + p_s)(P_0 - p') \qquad (2.6)$$

where α_a is a parameter that gives rise to the nonassociative model, i.e., $g_{LC} \neq f_{LC}$.
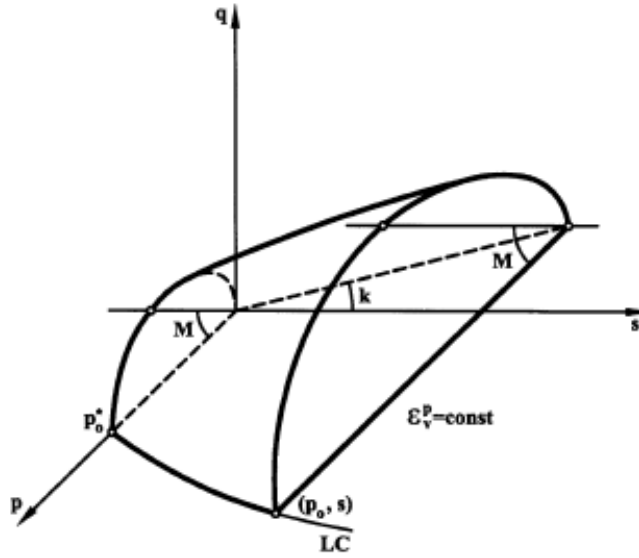
Figure 2.4. Three-dimensional representation of the yield surface in the BBM (Gens et al. 2006).

2.2.1.2 Microstructural Level

In the BExM, the following assumptions are adopted related to microstructural behavior and its interaction with the macrostructure:

- The microstructure is mainly saturated and the effective stress concept holds.
- The microstructural behavior is elastic and volumetric.
- Mechanical, hydraulic, and chemical equilibrium exists between microstructure and macrostructure.
- Coupling between microstructure and macrostructure results in a possible buildup of macrostructural elastoplastic strains when elastic microstructural strains occur.

With these assumptions, the increment of volumetric microstructural strain increment $d\varepsilon_{vm}^e$ depends exclusively on the increment of mean effective stress $dp' = d(p - p^l) = d(p - p^g + p^g - p^l) = d(p+s)$, where p is mean stress (or mean pressure), p^l is liquid phase pressure, p^g is gas

phase pressure as *s* is suction. Therefore, a straight line p + s = constant can be drawn around the current state of stress and suction along which no microstructural strain takes place. This line, called Neutral Line (NL), moves with the current stress state (C) and separates at each instant the zone of microstructural swelling from the zone of microstructural shrinkage in the p-s planes (Figure 2.5).
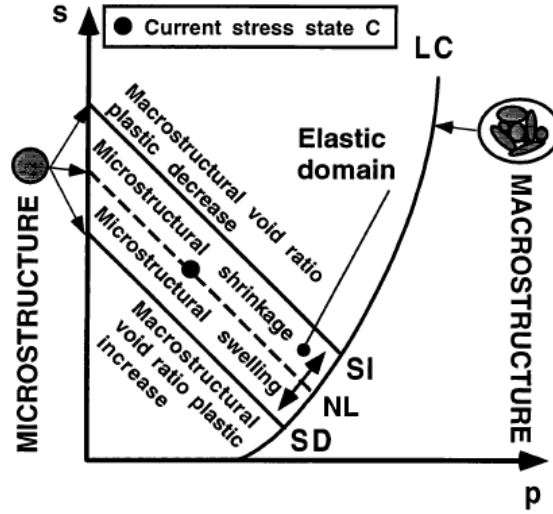
Figure 2.5. Microstructural and macrostructural elastoplastic responses in a double-structure model equivalent to the Barcelona Expansive Model.

2.2.1.3   Interaction between Structural Levels

Microstructural swelling affects the structural arrangement of the macrostructure, inducing an irreversible increase of the macroporosity. Reciprocally, microstructural shrinkage induces an irreversible decrease of the macroporosity. In BExM, the irreversible macrostructural deformations induced by microstructural effects are considered proportional to the microstructural strain according to interaction functions with the general form:

$$d\varepsilon_{v\beta}^{p} = f d\varepsilon_{vm}^{e} \tag{2.7}$$

where $\varepsilon_{v\beta}^{p}$ is the macrostructural plastic strain arising from the interaction between both structures. Two interaction functions are defined; f_c for MC (microstructural contraction) path and f_s for MS (microstructural swelling) paths (Sánchez et al., 2005). Alonso et al. (1990) proposed the following possible interaction functions, in which case for isotropic loading, f_c and f_s depend on the ratio p/p_o (Figure 2.6).

$$f_c = f_{c0} + f_{c1}(p/p_0)^{n_c} \text{ and } f_s = f_{s0} + f_{s1}(p/p_0)^{n_s} \tag{2.8}$$

The ratio p/p_o is a measure of the distance from the current stress state to the yield locus for the macrostructure *LC* and has the same meaning as the overconsolidation ratio for an isotropically consolidated soil. A low p/p_o implies a dense packing of the material. It is expected that under such dense packing (dense macrostructure), the microstructural swelling strongly affects the global arrangement of clay aggregates, which becomes more open, resulting in a softening of the macrostructure. This also means that the macrostructural yield surface *LC* shrinks. On the other

44

hand, when the microstructure contracts, macrostructural plastic strain can occur under the conditions of an open macrostructure, which tends to a more dense state. In such a case, the elastic domain increases and *LC* expands (Alonso et al. 1999; Sánchez et al., 2005).
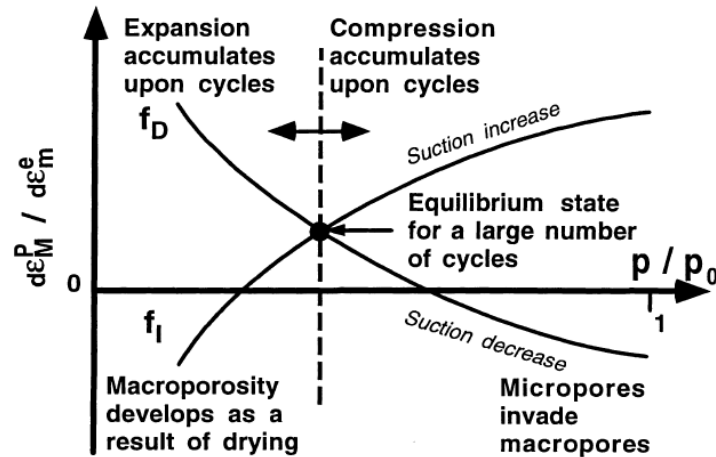
Figure 2.6. Summary of micro–macropore interaction mechanisms.
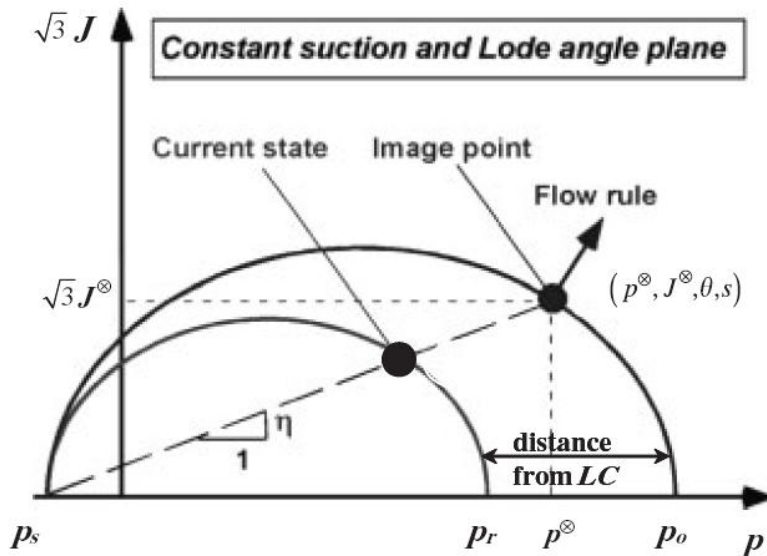
Figure 2.7. Reference pressure and plastic flow direction (Sánchez et al. 2005).

Elastic Strain

Equivalent to the BBM model, the macrostructural volumetric elastic strain increment for the BExM model is associated with changes in net mean stress dp' and suction ds (Alonso et al., 1999)

$$d\varepsilon_{vM}^e = \frac{1}{K_M}dp' + \frac{1}{K_s}ds \qquad (2.10)$$

where K_M is the macrostructural bulk modulus and K_s is the modulus associated with suction strain. K_M and K_s are defined as

$$K_M = \frac{(1+e)p'}{\kappa_{ps}(s)} \qquad (2.11)$$

$$K_s = \frac{(1+e)(s+p_{atm})}{\kappa_{sp}(p',s)} \qquad (2.12)$$

where κ_{ps} and κ_{SP} are compressibility parameters.

In BExM, the microstructural volumetric strain depends on the change in the microstructural effective stress

$$d\varepsilon_{vm}^e = \frac{1}{K_m}d\hat{p} \qquad (2.13)$$

where K_m is the microstructural bulk modulus for change in mean effective stress. Alonso et al. (1999) define two alternative laws for the microstructural behavior through two alternative expression for the microstructural modulus

$$K_m = \frac{(1+e)\hat{p}}{\kappa_{ps}(s)} \qquad (2.14)$$

$$K_m = \frac{e^{-\alpha_m \hat{p}}}{\beta_m} \qquad (2.15)$$

The deviatoric elastic strain increment is defined as

$$d\varepsilon_q^e = \frac{1}{3G}dq \qquad (2.16)$$

where G may be obtained using a constant Poisson's ratio υ in

$$G = \frac{3(1-2\upsilon)}{2(1+\upsilon)}K \qquad (2.17)$$

Thus, the equations for elastic mechanical strain indicate the dependency of bulk modulus on suction (and hence fluid saturation), which in a dry clay can be significantly stiffer than in a water-saturated clay.

Plastic Strain

Macrostructural plastic strain occurs by two plastic mechanisms: either when the stress lies on the LC yield surface, or as a result of microstructural contraction/swelling (MC and MS path). The increment of volumetric macrostructural strain is described as a result of microstructural contraction/swelling

$$d\varepsilon_{v\beta}^{p} = f d\varepsilon_{vm}^{e} \qquad (2.18)$$

where $d\varepsilon_{v\beta}^{p}$ is macrostructural strain as a result of microstructural contraction (MC or MS path).

The coupling between both plastic mechanisms is considered mathematically assuming that:

$$d\varepsilon_{v}^{p} = d\varepsilon_{vLC}^{p} + d\varepsilon_{v\beta}^{p} \qquad (2.19)$$

Then the hardening variable of the macrostructure—the pre-consolidation pressure p_0^*—depends on the total plastic volumetric strain ε_v^p, which is the sum of the plastic strain induced by LC yielding (ε_{LC}^p) and plastic strain induced by microstructural strain impact on the macrostructure $\varepsilon_{v\beta}^p$. That is,

$$\frac{dp_0^*}{p_0^*} = \frac{(1 + e_M) d\varepsilon_v^p}{\lambda_{ps0} - \kappa} \qquad (2.20)$$

When the stress state is on the LC yield surface, the plastic strains are obtained from the plastic flow rule

$$d\varepsilon_{vLC}^{P} = d\Lambda \frac{\partial g}{\partial p'} \qquad (2.21)$$

$$d\varepsilon_{qLC}^{P} = d\Lambda \frac{\partial g}{\partial q} \qquad (2.22)$$

where $d\Lambda$ is the plastic multiplier obtained from the consistency condition $df_{LC} = 0$.

The macrostructure plastic strain induced by microstructure volumetric strain is given by the flow rule at the image point on the LC yield surface. The coordinates of the image point (P^*, q^*, s^*) are given by (Alonso et al., 1999)

$$p^* = \frac{\eta^2 k_s s - M^2 p_0}{\eta^2 - M^2}, \ q^* = \eta(p + k_s s), \ s^* = s$$

where

$$\eta = \frac{q}{p + k_s s} \qquad (2.23)$$

2.2.2   Implementation of BExM into TOUGH-FLAC

We implemented the BExM in FLAC[3D], by extending our previous implementation of the BBM to include the microstructure level and its interactions with macrostructure. This is done using the User Defined constitutive Model (UDM) option in FLAC3D, including C++ coding and dynamic link libraries. Specifically, the following calculation items were added

1) Microstructural strain and effective stress

2) Micro/macrostructural interaction functions
3) Plastic macrostructural strain from structural interactions
4) Plastic corrections in the FLAC3D elastoplastic algorithm
5) Plastic hardening/softening factors
6) Global elastic tensor depending on microscopic and macroscopic structural compliances

Implementation of the first three items is straightforward, whereas items 4 and 5 are related to the FLAC3D elastoplastic algorithm and involve calculation of the plastic multiplier $d\Lambda$ associated with the elastic predictor-plastic corrector algorithm in FLAC3D. In this algorithm, current stress increments are estimated (by Hooke's law) and added to the stresses from the previous time step, and then corrected back to the yield surface if the calculated principal stresses violate the yield criterion. Using such an approach the current stress is calculated as

$$p' = p'_{est} + Kd\Lambda c_a \qquad (2.24a)$$

$$q = q_{est} + Kd\Lambda c_b \qquad (2.24b)$$

where p'_{est} and q_{est} are the estimated stresses obtained in the previous step, plus the current incremental elastic estimates, and constants c_a and c_b are the components normal to the plastic potential calculated as (Rutqvist et al., 2011):

$$c_a = M^2(2p' - p_c + p_s) \qquad (2.25a)$$

$$c_b = \alpha_a 2q \qquad (2.25b)$$

The value of the plastic multiplier $d\Lambda$ is defined by substituting Equations (2.25a) and (2.25b) in Equation (2.4), requiring that the new stress point be located on the yield surface ($f_{LC}(q, p') = 0$). Then,

$$a(d\Lambda)^2 + bd\Lambda + c = 0 \qquad (2.26)$$

where

$$a = (MKc_a)^2 + (3Gc_b)^2 \qquad (2.27a)$$

$$b = -\left[Kc_a c_a^e + \frac{3}{\alpha_a} Gc_b c_b^e \right] \qquad (2.27b)$$

$$c = f(q_{est}, p'_{est}) \qquad (2.27c)$$

Finally, FLAC^{3D} evaluates new stresses p' and q from Equations (2.24a) and (2.24b) using the expression for $d\Lambda$ corresponding to the root of Equations (2.26) and (2.27) with smallest magnitude (Rutqvist et al., 2011). In the case of microstructural contraction or swelling (i.e., MC or MS path), the components normal to the plastic potential are given by substituting p and q with $p*$ and q^* into (2.25a) and (2.25b). In the case of simultaneous LC yield and microstructural contraction or swelling, the stress state will be on the LC surface, and therefore $p = p^*$ and $q = q^*$, and Equations 2.24–2.27 are still valid.

48

Finally, in at the end of each FLAC3D step, the hardening parameter, i.e., the pre-consolidation pressure P_0 and the tangential bulk modulus, are updated based on the total volumetric strain and stress state, and these are stored for use in the next step.

2.2.3   Testing and Verification of Implementation

The implementation will be tested by comparison of TOUGH-FLAC simulation results to published experimental results such as those provided in Sánchez et al. (2005). In fact, the numerical results by Sánchez et al. (2005) using their implementation into CODE_BRIGHT are to our knowledge the only existing numerical results using this type of dual-structure modeling of unsaturated clay. The implementation and testing will be further documented in a scientific paper and in the next progress report.

2.3   Modeling of the Mont Terri HE-Heater Test

We are initiating modeling of the Mont Terri HE-heater test as a participating research team in the newly launched international DECOVALEX-2015 project. DECOVALEX-2015 is the next project phase of the DECOVALEX Project, which is a unique international research collaboration, initiated in 1992 for advancing the understanding and mathematical modeling of coupled thermo-hydro-mechanical (THM) and thermo-hydro-mechanical-chemical (THMC) processes in geological systems—subjects of importance for performance assessment of radioactive waste repositories in geological formations.

The HE-E Heater Test focuses on the THM behavior of bentonite barriers in the early nonisothermal resaturation stage and their THM interaction with Opalinus clay (Figure 2.8). The objective is to better understand the evolution of a disposal system of high level waste in the early post-closure period with emphasis on the thermal evolution, buffer resaturation (*in situ* determination of the thermal conductivity of bentonite and its dependency on saturation), pore water pressure in the near field, and the evolution of swelling pressures in the buffer. Because the test is conducted in a micro-tunnel (at 1:2 scale), it is considered a validation, not a demonstration experiment. The heating test involves two types of bentonite buffer materials. The heater-buffer interface will be heated to a maximum of 135^oC and a temperature of 60–70°C is expected at the buffer-rock interface. A dense instrumentation network is already in place in the host rock surrounding the micro-tunnel (from a previous experiment testing the impact of ventilation on the clay host rock) and will be improved (up to 40 piezometers in total); various sensors will also be placed in the buffer material. The heating phase has started in late summer of 2011 and is being continued for at least three years.

A proposed task description and plans for the DECOVALEX 2015 were presented at the 1st DECOVALEX-2015 workshop in Berkeley, April 17–19, 2012. It was decided that the final task description, including all necessary data to begin the modeling activities, will be distributed to the research teams in June 2012. The first task will be to model a previous single heater experiment (HE-D heater test) for determination and calibration of *in situ* properties related to the coupled THM behavior of the Opalinus clay host rock. This includes parameters governing heat transfer and thermal expansion, as well as hydraulic and mechanical coupling parameters. The modeling of the HE-D heater experiment should be completed by October 2012, before the next DECOVALEX Workshop.
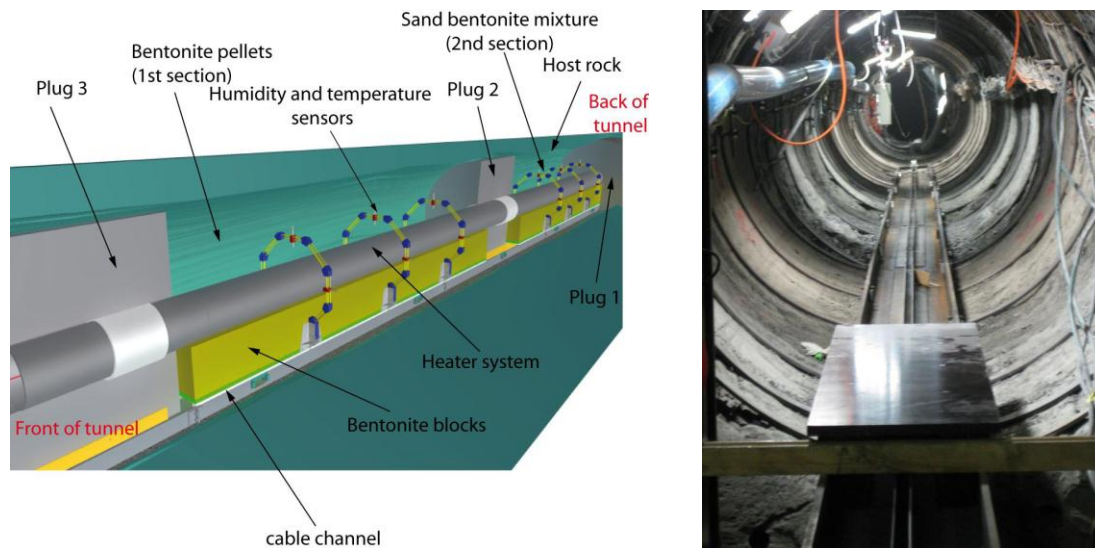
Figure 2.8. Schematic setup of HE-E heater test at Mont Terri and photo of micro-tunnel (Garritte et al. 2012).

2.4   Conclusions

We are developing and applying coupled THMC models for the analysis of EBS coupled processes in bentonite-backfilled repositories. In FY11, we developed an advanced modeling capability by implementing the Barcelona Basic Model into the TOUGH-FLAC simulator. In FY12, we have further improved our modeling capability and initiated a modeling validation study using international data sets. We expanded the Barcelona Basic Model to a dual-structure model for expansive clay, such as bentonite. We are currently testing and verifying this implementation against published numerical modeling and experimental data. The next step will be to link the dual-structure model with the diffuse double layer theory for the coupling between chemistry and mechanics, resulting in a coupled THMC model for the analysis of long-term EBS behavior. We have also initiated work on the modeling of the HE-E heater test, along with our participation in the DECOVALEX project. The first phase will involve modeling of a previous HE-D heater test for calibration and validation of the rock-mass model related to THM processes under heating of the Opalinus clay.

3. MODELING REACTIVE DIFFUSIVE TRANSPORT

Diffusion is one of the key transport processes that needs to be considered when studying radionuclide transport in the EBS. While it is possible to estimate diffusion coefficients for single species/contaminants in specific media (such as compacted bentonite and clay-rich rock) based on experiments, such an approach does not generally provide a robust predictive capability for diffusion rates across a range of physical and chemical conditions. It would be advantageous, therefore, to develop a more general model that could be used in the context of both mechanistic- and performance-assessment-style simulation tools for geological nuclear waste repositories. In the case of compacted bentonite in particular—but also for clay-rich rocks of the kind considered as host rocks for geological waste repositories in France and Switzerland (e.g., Bure in France and Mt. Terri in Switzerland)—there is a need to include the effect of electrical double layers around the clay in modeling ion transport through the EBS. Electrical double layers affect sorption, but perhaps more importantly, they affect transport. The negatively charged clay particles develop electrical double layers that will be balanced by a cation-enriched double layer. While anions are likely to be excluded completely only at very high degrees of compaction (e.g., a dry density of 1.9 g/cm^3—see Tournassat and Appelo, 2011), their concentration is decreased in the double layer even at lower degrees of compaction, and the tortuosity of the compacted clay with respect to chloride changes as well. Both of these contribute to slower diffusive transport rates through the clay (Bourg et al., 2003; Bourg et al., 2006; Leroy et al., 2006; Gonçalvès et al., 2007). These effects become increasingly important as the compaction increases, since this decreases the volume (or porosity) of bulk water at the expense of either the double layer or the clay interlamellar water.

Three types of water presence are recognized in compacted bentonite (Bourg et al, 2003; Wersin et al, 2004):

1. Interlayer water (ϕ_{IL}) with only water and cations within the Tetrahedral-Octahedral-Tetrahedral (TOT) layers of the montmorillonite. Here, the cations balance the fixed charge of the TOT layers;

2. Diffuse double layer (ϕ_{DDL}) containing cations and anions, but with an excess of ions (normally cations) to balance the charge of the clay surface;

3. Bulk or free pore water (ϕ_B), which is charge balanced.

The proportions of each kind of water depend on the compaction of the bentonite, but also on the ionic strength of the solution through its effect on the width of the diffuse double layer (DDL).

We are pursuing two separate but related approaches to modeling ion diffusion through clays. The first makes use of a Donnan equilibrium approach, in which a mean electrostatic potential is defined for the electrical double layer that balances the fixed negative charge of the clays. In this approach, the electrical double layer is treated as a single continuum (no discretization within it) in chemical equilibrium with the bulk water. The second approach involves the use of the Nernst-Planck and Poisson-Boltzmann equation (often referred to as the Poisson-Nernst-Planck or P-N-P equation). In this second approach (which is ultimately what the Donnan equilibrium or mean electrostatic approach is based on), the electrical potential as a function of distance from the charged clay surfaces is resolved. Thus, the concentration of anions and cations varies continuously. In the case of overlapping double layers, as between two clay interlamellae or closely spaced clay particles, the electrical potential does not decay to zero, with the result that

the aqueous solution in the center of the space or pore cannot be described as corresponding to "bulk water."

3.1   Mean Electrostatic Approach for Diffuse Double Layer

Initially at least, the mean electrostatic or Donnan Equilibrium approach to describing the diffuse electrical double layer balancing the negatively charged clay surfaces is based on the Poisson-Boltzmann equation, a full treatment of which is provided in the next section. A rigorous model for the diffuse layer could be derived from the combination of several equations, including the Poisson equation that describes the distribution of electrical potential, φ, in water

$$\frac{\partial^2 \varphi}{\partial x^2} = -\frac{\rho_z}{\varepsilon},$$

(3.1)

where ε is the permittivity and ρ_z is the volumetric charge density given by

$$\rho_z = e \sum_i z_i C_i$$

(3.2)

where e is the elementary charge of an ion, z_i is the charge of the ion, and C_i is its concentration. The Boltzmann distribution gives an expression for the concentration $\overline{C_i(x)}$ in the diffuse layer:

$$\overline{C_i(x)} = C_i \exp\left(\frac{-z_i e \varphi(x)}{k_B T}\right)$$

(3.3)

where C_i is the concentration in the bulk solution, k_B is the Boltzmann constant, and T is the absolute temperature. By combining Equation 3.3 with the Poisson equation (Eqn. 3.2) yields the Poisson-Boltzmann equation

$$\frac{\partial^2 \varphi}{\partial x^2} = \frac{-e}{\varepsilon} \sum_i z_i C_i \exp\left(\frac{-z_i e \varphi(x)}{k_B T}\right)$$

(3.4)

which can be solved exactly for various simple formulations (e.g., the Gouy-Chapman model). For an arbitrary multicomponent system, Equation 3.4 needs to be solved numerically along with the diffusion equations for the various species.

The approach adopted here treats a porous medium as consisting of three kinds of porosity, corresponding to the kinds of water described above for compacted bentonite. For the Diffuse Double Layer, this involves defining a mean potential for the diffuse layer, the thickness of which will depend on the ionic strength of the solution. Its volume is given by the total surface area of charged mineral multiplied by the diffuse layer thickness:

$$\phi_{DDL} = \tau_{DDL} A_{ext} w_{mont} \rho_{dry}$$

(3.5)

where A_{ext} is the external surface area of the montmorillonite, τ_{DDL} is the thickness of the diffuse layer, w_{mont} is the weight fraction of montmorillonite in the bentonite, and ρ_{dry} is the dry density of the compacted bentonite. At 25°C, the thickness of the diffuse layer can be approximated by the Debye length (κ^{-1}, the distance over which the potential in the diffuse layer drops by e)

$$\tau_{DDL} \cong \kappa^{-1} = \frac{3.04 \times 10^{-10}}{\sqrt{I}} \tag{3.6}$$

where I is the ionic strength (Stumm, 1992; Schoch et al., 2006). In some cases, the diffuse layers may overlap, resulting in a smaller volume for the total diffuse layer per unit volume of porous medium.

3.1.1   Donnan Equilibrium Model

Several treatments of an explicit diffuse layer calculation based on a Donnan Equilibrium assumption have been presented in the literature (Wersin et al., 2004; Appelo et al., 2007; Leroy et al., 2007; Appelo et al., 2008). Typically, this involves an assumption that the Donnan Equilibrium condition applies, which equates the chemical potentials of the species in the diffuse layer and the bulk solution. Writing equations for the chemical potentials of the species i in the macroporosity (superscript "B") and microporosity (superscript "DDL") respectively, we have

$$\mu_i^B = \mu_i^{B,0} + k_B T \ln a_i^B \tag{3.7}$$

$$\mu_i^{DDL} = \mu_i^{DDL,0} + k_B T \ln a_i^{DDL} + q_i \varphi_m \tag{3.8}$$

where the superscript 0 (first term on the right-hand side) refers to the chemical potential at the reference state, a_i are the species activities, q_i, is the charge of an ion (the elementary charge of a particle, e, multiplied by the valence of the ion, z_i), k_B is the Boltzmann constant, and φ_m is the mean electrical potential in the diffuse layer. The condition of Donnan Equilibrium implies that

$$\mu_i^{DDL} = \mu_i^B \tag{3.9}$$

$$\mu_i^{DDL,0} = \mu_i^{B,0} \tag{3.10}$$

Combining Equations 3.7 through 3.10 gives the Boltzmann distribution for the ion activities in the diffuse layer:

$$a_i^{DDL} = a_i^B \exp\left(\frac{-z_i e \varphi_m}{k_B T}\right) \tag{3.11}$$

If the activity coefficients for the ions are assumed to be the same in the diffuse layer and the bulk water (probably not strictly true, but we would need a much more sophisticated model to improve on this assumption), then one can use Equation 3.11 to calculate concentrations in the diffuse layer as well

$$C_i^{DDL} = C_i^B \exp\left(\frac{-z_i e \varphi_m}{k_B T}\right) \tag{3.12}$$

Note that from Equation 3.12, it is possible to calculate all of the concentrations in the diffuse layer once its mean potential is determined numerically. The mean potential of the diffuse layer can be calculated with an additional charge balance equation:

$$\phi^{DDL} \sum_i z_i C_i^{DDL} = Q^{SL} \tag{3.13}$$

where Q^{SL} is the total charge in the Stern Layer calculated with the surface complexation model, ϕ^{DDL} is again the volume of the diffuse layer, and C_i^{DDL} is the concentration in mol m^{-3}. The left-hand side of Equation 3.13 gives a volumetric charge density in units of charge equivalents per unit volume porous medium. The surface charge is given by

$$Q^{SL} = \sum_k^{Ns} z_k \Gamma_k \tag{3.14}$$

where Γ_k is the concentration in units of moles sorbed species per unit volume porous medium and z_k is the valence of the surface complex. By combining the Boltzmann equation (Eqn. 3.12), and the charge balance (Equation 3.13), it is possible to calculate the mean potential of the diffuse layer, φ_m, along with the total concentrations of the primary species partitioned between the mineral surfaces (the Stern Layer), the diffuse layer, and the bulk solution. Since Equation 3.12 provides an algebraic relationship between the primary species in the bulk water and diffuse layer, it is not necessary to introduce the primary species in the diffuse layer as independent unknowns. In contrast, a kinetic treatment of the exchange between the two domains would require that the primary species in the diffuse layer be considered as independent unknowns.

3.1.2 Dynamic Calculation of Double Layer Width

Previously, the volume corresponding to the "microporosity" or electrical double layer sub-continuum was calculated in advance using Eqn. 3.4. During FY12, we have added the capability to calculate this quantity dynamically at initialization, although update of the double layer thickness (on input, as some fraction or multiple of the Debye Length defined in Eqn. 3.4) is not yet possible. It turns out that an update of the diffuse layer volume (or porosity) requires appropriately weighting both the old and the new concentrations in the accumulation term within an individual time step, or a significant mass-balance error develops. Adding this feature is planned for the continuing FY12 work. When this is complete, it will be possible to simulate the effects of a changing double layer volume as a result of a propagating ionic strength (or salinity) wave. Currently, this option is now available only during the initialization—the user specifies multiples of the Debye length to be considered, and this is multiplied by the total surface area of the clay (typically bentonite) specified in the input. This also makes it possible for the DDL volume to be spatially variable.

Figure 3.1 shows the results of two calculations of the same 25 cm clay domain that use the same surface area of illitic clay (200 m^2/g) present at 20% of the rock volume. A site density of 5.88×10^{-6} mol sites/m^2 illite is used to determine the fixed mineral charge, which is variable in this case because of the inclusion of pH-dependent surface complexation. A no-flux boundary is used at 25 cm (on the right side of the domain), while the left boundary is treated as a Dirichlet (fixed concentration) boundary condition. At pH 7.5, two cases are considered: (1) a case in which the bulk water ionic strength is 0.04M, and (2) a case in which the bulk water ionic strength is 0.4M. The cations in the initial domain (Na$^+$, Ca^{2+}, and Mg^{2+} at 0.1M, 0.05M, and 0.05M in the higher ionic strength case and 0.01M, 0.005M, and 0.005M respectively in the lower ionic strength case) are balanced by bromide. In the 0.4 M ionic strength case, a total site

density of 1.509 moles sites/L solution is calculated, with 82% of the sites negatively charged. A diffuse layer microporosity of 1% is calculated. In the 0.04 M case, nearly the same percentage of negatively charged sites (82%) is calculated, resulting in 1.238 moles negatively charged sites per liter solution. A microporosity of 3.3% is calculated in the 0.04 M ionic strength case. The boundary condition consists of K^+ at either 0.1M (high ionic strength) or 0.01M (lower ionic strength) in place of Na^+ and chloride rather than bromide as the balancing anion. Solving for the Nernst-Planck equation, the range of diffusivities in the bulk water porosity (12%) is assumed to be representative of bulk water without a tortuosity connection such that the values range from 8.37 x 10^{-5} cm^2/s for H^+ to 7.3 x 10^{-6} cm^2/s in the case of Ca^{2+} and Mg^{2+}. Diffusivities in the electrical double layer are assumed to be an order of magnitude lower than in the bulk water macroporosity. In both cases, potassium diffuses into the domain while sodium diffuses out. Chloride also diffuses into the domain, replacing bromide as the balancing anion.

Figure 3.1 shows the results of the simulation after 10 days over the 10 cm close to the fixed concentration (Dirichlet) boundary on the left. Chloride is suppressed (partially excluded) in both cases, but the difference between the double layer porosity and the bulk water porosity is more pronounced at lower ionic strength. Sodium is strongly enriched in the diffuse layer at lower ionic strength (0.04M), although the gap between diffuse layer and bulk water porosity is equally pronounced at high ionic strength because of the presence of the divalent cations, which tend to balance the charge in this case.
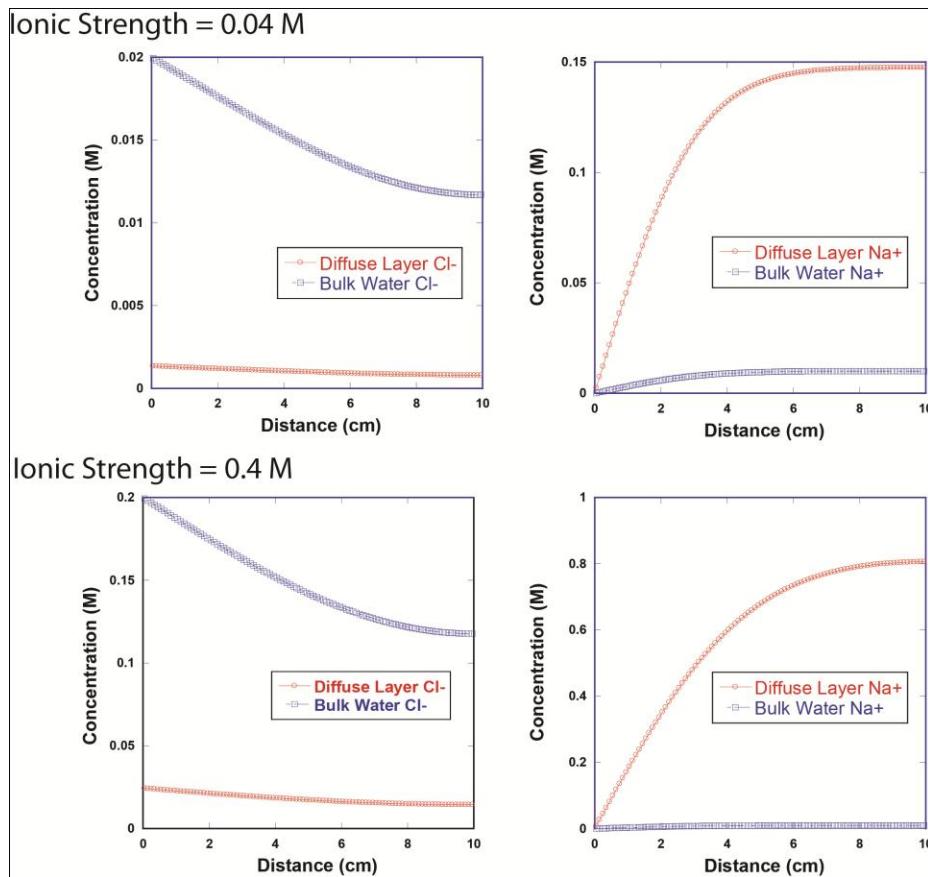
Figure 3.1. Effect of ionic strength on the anion (chloride) and cation (sodium) concentrations in the diffuse double layer compared to the bulk water.

3.1.3   Alternative Models for Montmorillonite Surface Charge

The classical surface complexation model considers the possibility of cations being added to the Stern layer, thus changing the net charge that needs to be balanced by the diffuse layer. In some clays, protonation and deprotonation reactions can change the charge—at the pH corresponding to the Zero Point of Charge (ZPC), in fact, the net charge of the surface in these clays is zero. In the case of the planar sites on montmorillonite, the clay making up most of the bentonite, the sites are not easily protonated or deprotonated. As a result, ion exchange models that do not consider protonation are often considered. In the case of the mean electrostatic diffuse layer model described here, it is now possible to consider either completely fixed mineral surface charge, in which case all of the charge is accommodated by the diffuse layer, or a case in which only cation (exclusive of protons) sorption in the Stern layer is included. The latter case has been investigated by using surface complexation reactions that do not include H^+, but allow for Stern layer sorption of Ca^{2+}, Mg^{2+}, Na^+, and K^+.

When modeling experimental data like that presented in Fernández and Mäder (2011), the ability to partition between the Stern layer (which is assumed to be largely immobile) and the diffuse layer itself is an advantage for achieving the best possible fit with the experimental data. Here we present the initial speciation of the initial conditions for a column experiment conducted over a period of 300 days by Fernández and Mäder (2011).

Table 3.1. Initial and boundary conditions for the column experiment conducted by Fernández and Mäder (2011).

Component	Initial Condition
pH	8.5
Na^+	400
Ca^{2+}	23
Mg^{2+}	15
K^+	2.7
Cl^-	362
SO_4^{2-}	58

The non-electrostatic surface complexation constants used in the speciation calculations are given in Table 3.2. The simulations indicate that only 0.265% of the sites are filled by cations, leaving the rest of the montmorillonite surface as negatively charged. For the initial conditions in Table 3.1, the computed percentages are 0.263%, 0.0012%, and 0.00068% for Na^+, Ca^{2+}, and Mg^{2+}, respectively, while the coverage by K^+ is insignificant. The remainder of the 9.32 moles site/liter will be unfilled, negatively charged hydroxyl sites that are balanced by cation enrichment in the diffuse layer.

Table 3.2. Surface complexation constants (non-electrostatic) used in speciation calculations for initial condition (from Fernández and Mäder, 2011)

Reaction	Log Keq
>Montmor-Ca^{2+} → Ca^{2+} + 2 >Montmor-	3.58
>Montmor-Mg^{2+} → Mg^{2+} + 2 >Montmor-	3.64
>Montmor-Na^{+} → Na^{+} + >Montmor-	5.99
>Montmor-K^{+} → K^{+} + >Montmor-	1.99

3.2   Poisson-Nernst-Planck Approach

Surface phenomena in the clay pore space gain relevance as the level of compaction increases and the dimensions of the space confined between clay layers shifts towards the range of nanometers. At such scales, solute transport can no longer be explained by concentration gradients alone. In fact, DDL develops in the neighborhood of the negatively charged clay surfaces can extend well into the aqueous phase, effectively constraining the space available to anions (an event known as anion exclusion) and, in general, distorting the spatial distribution of ionic species in solution. This can be addressed by solving the Poisson-Nernst-Planck (PNP) set of equations, which allows for the determination of the electric potential over the entire domain, along with the spatial distribution of the concentration of ionic species. Although this approach has been taken for some time in the field of nanofluidic dynamics, it has largely been neglected in clay science.

In this sense, the model that has been developed here may constitute a significant step forward towards the understanding of solute transport in highly compacted clays, because it makes it possible to avoid the simplifying assumptions that pervade previous modeling efforts, and perhaps most importantly, that limit the extension of results to differing conditions.

A brief review of the commonly used simplifications include:

a) Treatment of molecular diffusion as described by Fick's law, where the diffusion rate is linearly proportional to the concentration gradient alone;

b) Surface complexation models, whether of the double- (e.g., Avena and De Pauli, 1998) or triple-layer (e.g., Leroy and Revil, 2004) type, relying on the assumption that counter-ions swarming in a fully developed DDL would neutralize the charge density of the clay surface. From a mathematical standpoint, that implies that the set of equations is closed by the following additional expression:

$$Q_d = -\varepsilon \frac{\partial \varphi}{\partial n} = \operatorname{sgn} \varphi_0 \left\{ 2\varepsilon RTI_c \sum_i C_i^* \left[\exp\left(-\frac{z_i F \varphi_0}{RT} \right) - 1 \right] \right\}^{1/2} \tag{3.15}$$

where Q_d is the electrical charge as integrated over the whole extension of the DDL and φ_0 is the electrical potential at the shear plane.

c) Anion exclusion effects (which entail an effective reduction of the anion-accessible porosity) being explained in terms of a Donnan equilibrium between pore and external solutions (see

Section 3.1 above), along with charge-balance considerations, as in Birgersson and Karnland (2009).

As the mean pore size decreases, e.g., as a result of compaction, DDL developing on opposite clay surfaces may overlap (Gonçalvès et al., 2007). On the one hand, this increases the relative weight of migration into solute transport, as diffusing ions are subjected to non-negligible electrical forces. On the other hand, this dilutes the independence of surface complexation reactions with respect to solute transport, as the evolving ion spatial distribution influences the charge of the DDL, Q_d. Finally, by allowing for a continuous spatial distribution of ionic species both along and transversally to the direction of the pore axis, the PNP set of equations suggests that it is not possible to discretize the pore space in a nonphysical way (e.g., micro- and macroporosity, total and anion-accessible porosity, etc.).

3.2.1   Conceptual Model

The present PNP model relies on the following set of statements:

a. Solutes may be either adsorbed to the clay surface or remain mobile in the pore space;
b. These two distinctly different behaviors correspond to the two domains on either side of the so-called shear plane;
c. Double- or triple-layer models can be used in simulating surface complexation reactions;
d. On the diffuse layer side of the shear plane, diffusion of ionic species is simulated by means of the PNP set of equations;
e. Continuity of mass and electric potential should hold at the Stern layer, which implies a permanent feedback between both domains.

Figure 3.2 shows a sketch of the triple layer model and its related electric potential profiles for the cases of fully developed and truncated (overlapping) diffuse layers.
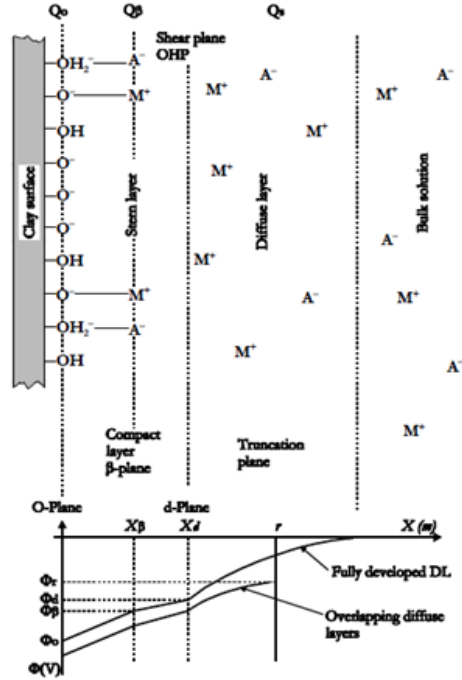
Figure 3.2. Sketch of the triple-layer model at clay surface (top) and its related electrical potential in the cases of truncated and untruncated diffuse layers (bottom). M+ represents a metal cation (e.g., Na+) and A− an anion (e.g., Cl−). OHP is the outer Helmholtz plane. The d-plane is associated with the shear plane; i.e., φd ~ξ, where ξ is the zeta potential arising in electrokinetic phenomena. The β-plane and 0-plane are respectively the mean plane in of Stern layer and the surface of the clay particle. After Gonçalvès et al. (2007).

3.2.2   Surface Complexation

While ample literature exists on this particular topic, a surface complexation model of Avena and Pauli (1998), developed specifically for clays, is worth looking at as potentially useful for the present research.

The following cation exchange reactions are considered in the model:

$$X + H^+ \rightleftharpoons XH^+$$
$$X + Na^+ \rightleftharpoons XNa^+$$

(3.16)

along with protonation/deprotonation reactions:

$$SOH_2^+ \rightleftharpoons SOH + H^+$$
$$SOH \rightleftharpoons SO^- + H^+$$

(3.17)

whose reaction constants are, respectively:

$$K_1 = \frac{\{XH^+\}}{\{X\}[H^+]} \exp\left(\frac{F\varphi_0}{RT}\right)$$

(3.18)

59

$$K_2 = \frac{\{XNa^+\}}{\{X\}[Na^+]} \exp\left(\frac{F\varphi_0}{RT}\right) \tag{3.19}$$

$$K_3 = \frac{\{SOH_2^+\}}{\{SOH\}[H^+]} \exp\left(\frac{F\varphi_0}{RT}\right) \tag{3.20}$$

$$K_4 = \frac{\{SOH\}}{\{SO^-\}[H^+]} \exp\left(\frac{F\varphi_0}{RT}\right) \tag{3.21}$$

Mass-balance equations are:

$$N_1 = \{X\} + \{XNa^+\} + \{XH^+\} \tag{3.22}$$

$$N_2 = \{SOH_2^+\} + \{SO^-\} + \{SOH\} \tag{3.23}$$

where N_1 and N_2 are the surface densities of variable charged sites, and are given in mol/m^2.

The structural surface charge density is defined as:

$$Q_i = -FN_1 = -F\left(\{X\} + \{XNa^+\} + \{XH^+\}\right) \tag{3.24}$$

where F is the Faraday constant, given in C/mol, and the surface charge density is:

$$Q_s = F\left(\{SOH_2^+\} - \{SO^-\} + \{XNa^+\} + \{XH^+\}\right) \tag{3.25}$$

As a consequence, the total surface charge density is the net sum of the two:

$$Q_0 = Q_s + Q_i = F\left(\{SOH_2^+\} - \{SO^-\} - \{X\}\right) \tag{3.26}$$

Finally, for surface charge to be balanced by the DDL, the following identity must be met:

$$Q_d = -Q_0 \tag{3.27}$$

where Q_d is derived by the Gouy–Chapman theory:

$$Q_d = -(8000\varepsilon RT)^{1/2} I^{1/2} \sinh\left(\frac{F\varphi_d}{2RT}\right) \tag{3.28}$$

As discussed above, Equation 3.28 is only valid when the DDL is fully developed, i.e., there is no overlapping between DDLs surrounding opposite clay surfaces. The model also assumes that the surface plane and the diffuse layer plane are separated by a region of constant capacitance; thus:

$$\varphi_0 - \varphi_d = \frac{1}{C_{Str}} Q_0 \qquad (3.29)$$

The set of Equations 3.18-3.25 is solved with the sorption sites as unknowns, along with Equation 3.26, 3.28, and 3.29 for Q_0, Q_d, φ_0, and φ_d, respectively

The set of equations above (3.18 through 3.29) can be solved for the case where Equation 3.28 applies. Unfortunately, Equation 3.28 holds whenever the DDL occupies a small portion of the pore space such that the bulk water properties ($\varphi = 0$) are present between the charged surfaces of the clay. That is not necessarily the case for highly compacted clays; on the contrary, the EDL affects concentrations and transport in the pore space in the case of the compacted clays and its geometry is in turn affected by the geometry of the pore structure.

The preceding paragraphs hint at the need for coupling the modules of solute transport and surface complexation reactions into a single, holistic model. As described above, such a model discretizes the pore space in terms of the predictable behavior ionic species, DDL, and pore architecture and is therefore more physically based than the somewhat ad hoc Donnan schemes.

From a mathematical standpoint, continuity should be assured for mass, namely, C_i, and the electric properties, Q_d and φ_d, at the interface between the two domains (i.e., the so-called shear plane, which is the outer confine of the Stern layer), so that a constant feedback from one sub-domain (DDL, Stern layer) to the other is accounted for. This particular feature of the model is currently under development.

3.2.3   The Poisson–Nernst–Planck set of equations

3.2.3.1   Background

The Poisson–Nernst–Planck set of equations is given by:

$$\left\{ \begin{array}{l} \dfrac{\partial C_1}{\partial t} + \nabla \bullet \left(D_1 \nabla C_1 + D_1 \dfrac{F z_1}{RT} C_1 \nabla \varphi \right) = 0 \\[2ex] \dfrac{\partial C_2}{\partial t} + \nabla \bullet \left(D_2 \nabla C_2 + D_2 \dfrac{F z_2}{RT} C_2 \nabla \varphi \right) = 0 \\[1ex] \qquad\qquad\qquad \vdots \\[1ex] \dfrac{\partial C_N}{\partial t} + \nabla \bullet \left(D_N \nabla C_N + D_N \dfrac{F z_N}{RT} C_N \nabla \varphi \right) = 0 \\[2ex] \dfrac{F}{\varepsilon} \left(z_1 C_1 + z_2 C_2 + \ldots + z_N C_N \right) + \nabla^2 \varphi = 0 \end{array} \right. \qquad (3.30)$$

where C_i, z_i, and D_i, for $i = 1, 2, \ldots, N$ (number of species), are, respectively, the concentration, valence and diffusion coefficient of the i-th ionic species, φ is the electrical potential, R is the universal gas constant, ε is the permittivity of the medium, and T is the temperature.

The finite element scheme adopted in this work makes use of the variational approach, namely the Galerkin weighted residual method, of establishing the governing equilibrium equations of a system. Let w be a weighting function; then the Nernst–Planck set of equations becomes:

$$\frac{\partial C_i}{\partial t} + D_i \frac{\partial^2 C_i}{\partial x^2} + D_i \frac{Fz_i}{RT} C_i \frac{\partial^2 \varphi}{\partial x^2} = 0 \Rightarrow$$

$$\int w \frac{\partial C_i}{\partial t} dx + D_i \int w \frac{\partial^2 C_i}{\partial x^2} dx + D_i \frac{Fz_i}{RT} \int w C_i \frac{\partial^2 \varphi}{\partial x^2} dx = 0 \Rightarrow \tag{3.31}$$

$$\int w \frac{\partial C_i}{\partial t} dx - D_i \int \frac{\partial w}{\partial x} \frac{\partial C_i}{\partial x} dx - D_i \frac{Fz_i}{RT} \int \frac{\partial w C_i}{\partial x} \frac{\partial \varphi}{\partial x} dx = -D_i \int w \frac{\partial C_i}{\partial n} d\Gamma - D_i \frac{Fz_i}{RT} \int w C_i \frac{\partial \varphi}{\partial n} d\Gamma$$

where, for the sake of simplicity, a one-dimensional case was considered.

Given that φ and $\dfrac{\partial \varphi}{\partial n}$ are non–zero at the same boundary, namely the clay surface, then both terms on the right–hand side of the equation can be merged together. Therefore:

$$\int w \frac{\partial C_i}{\partial t} dx - D_i \int \frac{\partial w}{\partial x} \frac{\partial C_i}{\partial x} dx - D_i \frac{Fz_i}{RT} \int \frac{\partial w C_i}{\partial x} \frac{\partial \varphi}{\partial x} dx = -D_i \int w \left(\frac{\partial C_i}{\partial n} + \frac{Fz_i}{RT} C_i \frac{\partial \varphi}{\partial n} \right) d\Gamma \tag{3.32}$$

At the boundary the flux, J, is equal to zero, that is:

$$J_\Gamma = D_i \frac{\partial C_i}{\partial n} + D_i \frac{Fz_i}{RT} C_i \frac{\partial \varphi}{\partial n} \bigg|_\Gamma = 0 \Rightarrow D_i \left(\frac{\partial C_i}{\partial n} + \frac{Fz_i}{RT} C_i \frac{\partial \varphi}{\partial n} \right) \bigg|_\Gamma = 0 \tag{3.33}$$

As a consequence, when substituting into the Nernst–Planck set of equations, one obtains:

$$\int w \frac{\partial C_i}{\partial t} dx - D_i \int \frac{\partial w}{\partial x} \frac{\partial C_i}{\partial x} dx - D_i \frac{Fz_i}{RT} \int \frac{\partial w C_i}{\partial x} \frac{\partial \varphi}{\partial x} dx = 0 \tag{3.34}$$

as the right–hand side of the equation vanishes.

Analogously, for the one-dimensional form of the Poisson equation:

$$\frac{\partial^2 \varphi}{\partial x^2} = -\frac{F}{\varepsilon} \sum_i z_i C_i \Rightarrow$$

$$\int w \frac{\partial^2 \varphi}{\partial x^2} dx = -\frac{F}{\varepsilon} \sum_i z_i \int w C_i dx \Rightarrow \tag{3.35}$$

$$\int \frac{\partial w}{\partial x} \frac{\partial \varphi}{\partial x} dx - \frac{F}{\varepsilon} \sum_i z_i \int w C_i dx = \int w \frac{\partial \varphi}{\partial n} d\Gamma$$

At the boundary, both the electrical potential and the surface charge are non-zero and interdependent. It can be assumed that a linear relationship exists between the potential and its gradient, namely:

$$\alpha \frac{\partial \varphi}{\partial n} = \varphi - \varphi_0 \tag{3.36}$$

for a given value of φ.

Substituting into the Poisson equation yields:

$$\int \frac{\partial w}{\partial x} \frac{\partial \varphi}{\partial x} dx - \frac{F}{\varepsilon} \sum_i z_i \int w C_i dx = \frac{1}{\alpha} \int w \varphi d\Gamma - \frac{1}{\alpha} \int w \varphi_0 d\Gamma \tag{3.37}$$

3.2.3.2   *Finite Element Formulation*

Using a finite element approach, the Nernst–Planck set of equations becomes:

$$\int w \frac{\partial C_i}{\partial t} dx - D_i \int \frac{\partial w}{\partial x} \frac{\partial C_i}{\partial x} dx - D_i \frac{F z_i}{RT} \int \frac{\partial w C_i}{\partial x} \frac{\partial \varphi}{\partial x} dx =$$

$$-D_i \int w \left(\frac{\partial C_i}{\partial n} + \frac{F z_i}{RT} C_i \frac{\partial \varphi}{\partial n} \right) d\Gamma \Rightarrow$$

$$\left(\int \underline{H}^T \underline{H} dx \right) \frac{\partial \underline{C}_i}{\partial t} - D_i \left(\int \underline{B}^T \underline{B} dx \right) \underline{C}_i - 2D_i \frac{F z_i}{RT} \left(\int \underline{H}^T \underline{C}_i \underline{B}^T \underline{B} dx \right) \underline{\varphi} =$$

$$-D_i \int \underline{H}^T \left(\frac{\partial \underline{H}}{\partial n} \underline{C}_i + \frac{F z_i}{RT} \underline{H}^T \underline{C}_i \frac{\partial \underline{H}}{\partial n} \underline{\varphi} \right) d\Gamma \tag{3.38}$$

which for both off– and on–boundary nodes results in:

$$\left(\int \underline{H}^T \underline{H} dx \right) \frac{\partial \underline{C}_i}{\partial t} - D_i \left(\int \underline{B}^T \underline{B} dx \right) \underline{C}_i - 2D_i \frac{F z_i}{RT} \left(\int \underline{H}^T \underline{C}_i \underline{B}^T \underline{B} dx \right) \underline{\varphi} = \underline{0} \tag{3.39}$$

Similarly, the Poisson equation takes the following form:

$$\left(\int \underline{B}^T \underline{B} dx \right) \underline{\varphi} - \frac{F}{\varepsilon} \sum_i z_i \left(\int \underline{H}^T \underline{H} dx \right) \underline{C}_i = \left(\int \underline{H}^T \frac{\partial \underline{H}}{\partial n} d\Gamma \right) \underline{\varphi} \tag{3.40}$$

So, for all off–boundary nodes:

$$\left(\int \underline{B}^T \underline{B} dx \right) \underline{\varphi} - \frac{F}{\varepsilon} \sum_i z_i \left(\int \underline{H}^T \underline{H} dx \right) \underline{C}_i = \underline{0} \tag{3.41}$$

and for on-boundary nodes:

$$\left(\int \underline{B}^T \underline{B} dx \right) \underline{\varphi} - \frac{F}{\varepsilon} \sum_i z_i \left(\int \underline{H}^T \underline{H} dx \right) \underline{C}_i = \frac{1}{\alpha} \left(\int \frac{\partial \underline{H}^T}{\partial n} d\Gamma \right) \underline{\varphi} - \frac{1}{\alpha} \left(\int \frac{\partial \underline{H}^T}{\partial n} d\Gamma \right) \varphi_0 \tag{3.42}$$

and regrouping:

$$\left[\left(\int \underline{B}^T \underline{B} dx\right) - \frac{1}{\alpha}\left(\int \underline{H}^T \frac{\partial \underline{H}}{\partial n} d\Gamma\right)\right]\underline{\varphi} - \frac{F}{\varepsilon}\sum_i z_i \left(\int \underline{H}^T \underline{H} dx\right)\underline{C}_i = -\frac{1}{\alpha}\left(\int \underline{H}^T \frac{\partial \underline{H}}{\partial n} d\Gamma\right)\varphi_0$$

(3.43)

So, in matrix notation:

$$\underline{\underline{M}} = \int \underline{H}^T \underline{H} dx$$

(3.44)

$$\underline{\underline{K}}_{D_i} = -D_i \int \underline{B}^T \underline{B} dx$$

(3.45)

$$\underline{\underline{K}}_{D_i nl} = -2D_i \frac{F z_i}{RT}\left(\int \underline{H}^T \underline{C}_i \underline{B}^T \underline{B} dx\right)$$

(3.46)

$$\underline{\underline{K}} = \int \underline{B}^T \underline{B} dx$$

(3.47)

$$\underline{\underline{M}}_{z_i} = -\frac{F}{\varepsilon} z_i \int \underline{H}^T \underline{H} dx$$

(3.48)

$$\underline{\underline{B}} = -\left(\int \underline{H}^T \frac{\partial \underline{H}}{\partial n} d\Gamma\right)$$

(3.49)

$$\left[\left(\int \underline{B}^T \underline{B} dx\right) - \frac{1}{\alpha}\left(\int \frac{\partial \underline{H}^T}{\partial n} d\Gamma\right)\right]\underline{\varphi} - \frac{F}{\varepsilon}\sum_i z_i \left(\int \underline{H}^T \underline{H} dx\right)\underline{C}_i = -\frac{1}{\alpha}\left(\int \frac{\partial \underline{H}^T}{\partial n} d\Gamma\right)\varphi_0$$

(3.50)

For off–boundary nodes, this yields:

$$\begin{pmatrix} M & 0 & \cdots & 0 & 0 \\ 0 & M & \cdots & 0 & 0 \\ \vdots & \vdots & \ddots & 0 & \vdots \\ 0 & 0 & \cdots & M & 0 \\ 0 & 0 & \cdots & 0 & 0 \end{pmatrix}\frac{1}{\Delta t}\left(C^{t+\Delta t} - C^t\right) + \begin{pmatrix} K_{D_1} & 0 & \cdots & 0 & K_{D_1 nl} \\ 0 & K_{D_2} & \cdots & 0 & K_{D_2 nl} \\ \vdots & \vdots & \ddots & 0 & \vdots \\ 0 & 0 & \cdots & K_{D_N} & K_{D_N nl} \\ M_{z_1} & M_{z_2} & \cdots & M_{z_N} & K \end{pmatrix}C^{t+\Delta t} = \begin{pmatrix} 0 \\ 0 \\ \vdots \\ 0 \\ 0 \end{pmatrix}$$

(3.51)

For on–boundary nodes, this yields:

$$
\begin{pmatrix}
M & 0 & \cdots & 0 & 0 \\
0 & M & \cdots & 0 & 0 \\
\vdots & \vdots & \ddots & \vdots & \vdots \\
0 & 0 & \cdots & M & 0 \\
0 & 0 & \cdots & 0 & 0
\end{pmatrix}
\frac{1}{\Delta t}\left(C^{t+\Delta t}-C^{t}\right)+
\begin{pmatrix}
K_{D_1} & 0 & \cdots & 0 & K_{D_1 nl} \\
0 & K_{D_2} & \cdots & 0 & K_{D_2 nl} \\
\vdots & \vdots & \ddots & 0 & \vdots \\
0 & 0 & \cdots & K_{D_N} & K_{D_N nl} \\
M_{z_1} & M_{z_2} & \cdots & M_{z_N} & \left(K+\dfrac{1}{\alpha}B\right)
\end{pmatrix}
C^{t+\Delta t}=
\begin{pmatrix}
0 \\
0 \\
\vdots \\
0 \\
\dfrac{1}{\alpha}B\varphi_0
\end{pmatrix}
\tag{3.52}
$$

so that when α is small, $\underline{\underline{B}}$ becomes dominant over the remaining elements of the equation, with the result that $\varphi = \varphi_0$, i.e., it becomes a Dirichlet type boundary condition. On the other hand, when α is large, then $\dfrac{\partial \varphi}{\partial n}$ tends progressively towards 0, which is a boundary condition of the Neumann type:

$$
\begin{pmatrix}
K_{D_1} & 0 & \cdots & 0 & K_{D_1 nl} \\
0 & K_{D_2} & \cdots & 0 & K_{D_2 nl} \\
\vdots & \vdots & \ddots & 0 & \vdots \\
0 & 0 & \cdots & K_{D_N} & K_{D_N nl} \\
M_{z_1} & M_{z_2} & \cdots & M_{z_N} & \left(K+\dfrac{1}{\alpha}B\right)
\end{pmatrix}
C^{t+\Delta t}=
\begin{pmatrix}
0 \\
0 \\
\vdots \\
0 \\
\dfrac{1}{\alpha}B\varphi_0
\end{pmatrix}
\tag{3.53}
$$

3.2.3.3 *Calibration*

A code was developed for the resolution of the PNP set of equations under a two-dimensional finite-element framework. To evaluate its performance, a relatively simple 1D case was chosen for which other numerical solutions are known.

Figure 3.3 shows the results provided by the code along with those obtained by CrunchFlow (Steefel, 2009) for a simple one-dimensional problem developed originally by Lichtner (1998). In this problem, Na^+ and Cl^- are present at 0.1 mM in both the internal domain and at the boundary on the left. However, the concentrations of H^+ and $NO3^-$ are different between the boundary (0.001 mM and pH 6) and the internal domain (0.1 mM and pH 4). Without coupling and using only Fick's Law, the sodium and chloride profile should remain flat, but the electrochemical migration flux (Steefel and Maher, 2009) causes fluxes of both of these as the hydrogen ion diffuses more rapidly than the nitrate out of the system. As can be seen, the agreement is excellent, as the code reproduces the electrical interaction of ionic species induced by the differing diffusion coefficients once a concentration gradient is introduced.
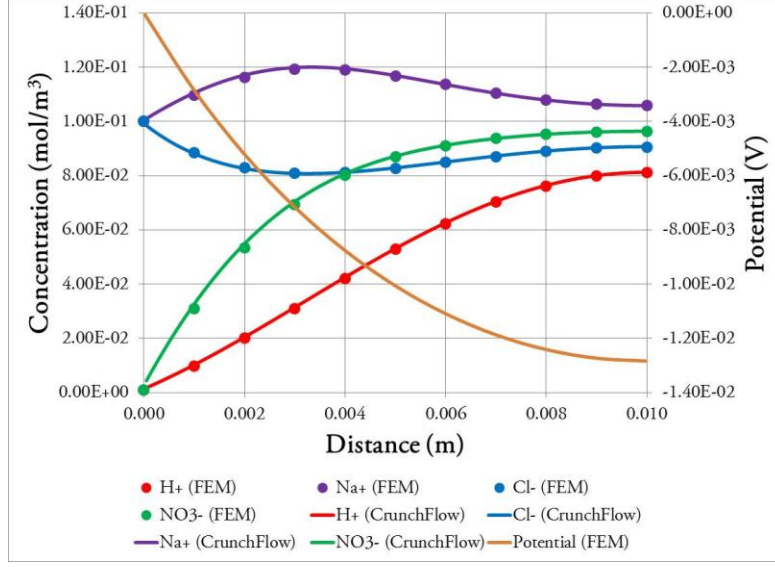
Figure 3.3. Results obtained by the PNP set of equations under a 2D finite element scheme (dotted lines), as compared to those provided by CrunchFlow (solid lines).

3.2.3.4 Special Case: The Poisson–Boltzmann equation

Let us consider a binary solution under steady-state conditions. Then, the system can be described by the following set of equations:

$$\begin{cases} \dfrac{\partial C_1}{\partial x} + \dfrac{F}{RT} z_1 C_1 \dfrac{\partial \varphi}{\partial x} = 0 \\[2mm] \dfrac{\partial C_2}{\partial x} + \dfrac{F}{RT} z_2 C_2 \dfrac{\partial \varphi}{\partial x} = 0 \\[2mm] \dfrac{\partial^2 \varphi}{\partial x^2} + \dfrac{F}{\varepsilon}\left(z_1 C_1 + z_2 C_2 \right) = 0 \end{cases} \tag{3.54}$$

as the partial time derivatives go to zero.

Assuming that the solution to the set of equations is

$$C_1 = C_{1,\infty} \exp\left(-z_1 \frac{F\varphi}{RT} \right)$$

$$C_2 = C_{2,\infty} \exp\left(-z_2 \frac{F\varphi}{RT} \right) \tag{3.55}$$

then

$$\frac{\partial C_1}{\partial x} = \frac{\partial C_1}{\partial \varphi}\frac{\partial \varphi}{\partial x} = -z_1 \frac{F}{RT} C_{1,\infty} \exp\left(-z_1 \frac{F\varphi}{RT} \right)\frac{\partial \varphi}{\partial x}$$

$$\frac{\partial C_2}{\partial x} = -z_2 \frac{F}{RT} C_{2,\infty} \exp\left(-z_2 \frac{F\varphi}{RT} \right)\frac{\partial \varphi}{\partial x} \tag{3.56}$$

66

Substituting into the set of equations yields:

$$\left\{ \begin{array}{l} -z_1 \dfrac{F}{RT} C_{1,\infty} \exp\left(-z_1 \dfrac{F\varphi}{RT}\right)\dfrac{\partial\varphi}{\partial x} + \dfrac{F}{RT} z_1 C_{1,\infty} \exp\left(-z_1 \dfrac{F\varphi}{RT}\right)\dfrac{\partial\varphi}{\partial x} = 0 \\[2ex] -z_2 \dfrac{F}{RT} C_{2,\infty} \exp\left(-z_2 \dfrac{F\varphi}{RT}\right)\dfrac{\partial\varphi}{\partial x} + \dfrac{F}{RT} z_2 C_{2,\infty} \exp\left(-z_2 \dfrac{F\varphi}{RT}\right)\dfrac{\partial\varphi}{\partial x} = 0 \\[2ex] \dfrac{\partial^2\varphi}{\partial x^2} + \dfrac{F}{\varepsilon}\left[z_1 C_{1,\infty} \exp\left(-z_1 \dfrac{F\varphi}{RT}\right) + z_2 C_{2,\infty} \exp\left(-z_2 \dfrac{F\varphi}{RT}\right)\right] = 0 \end{array} \right. \tag{3.57}$$

The first two identities are true, whereas the third one is the Poisson–Boltzmann equation. As a consequence, it can be stated that, under a consistent set of boundary conditions, the Poisson–Boltzmann equation represents the solution of the PNP set of equations for the steady state. This is relevant for the determination of the initial conditions of a given problem, since even before a concentration gradient is introduced, a pre-existing, non-uniform spatial distribution of the species should be observable by virtue of the electric potential emanating from the charged clay surfaces.

In keeping with the notation of the preceding section, the determination of the initial conditions entails that the Poisson–Boltzmann equation has to be solved. That means that a solution has to be found for the set of equations given by:

$$\begin{pmatrix} K_{D_1} & 0 & \cdots & 0 & K_{D_1 nl} \\ 0 & K_{D_2} & \cdots & 0 & K_{D_2 nl} \\ \vdots & \vdots & \ddots & 0 & \vdots \\ 0 & 0 & \cdots & K_{D_N} & K_{D_N nl} \\ M_{z_1} & M_{z_2} & \cdots & M_{z_N} & K \end{pmatrix} C = \begin{pmatrix} 0 \\ 0 \\ \vdots \\ 0 \\ 0 \end{pmatrix} \tag{3.58}$$

which is valid for off–boundary nodes. And for on–boundary nodes:

$$\begin{pmatrix} K_{D_1} & 0 & \cdots & 0 & K_{D_1 nl} \\ 0 & K_{D_2} & \cdots & 0 & K_{D_2 nl} \\ \vdots & \vdots & \ddots & 0 & \vdots \\ 0 & 0 & \cdots & K_{D_N} & K_{D_N nl} \\ M_{z_1} & M_{z_2} & \cdots & M_{z_N} & \left(K + \dfrac{1}{\alpha} B\right) \end{pmatrix} C = \begin{pmatrix} 0 \\ 0 \\ \vdots \\ 0 \\ \dfrac{1}{\alpha} B\varphi_0 \end{pmatrix} \tag{3.59}$$

In the following, a simple case of a binary solution in compacted clay will be considered with the aim of demonstrating the applicability of the Poisson–Boltzmann equation (and, by extension, of the PNP set of equations) for the description of the spatial distribution ionic species concentrations in the pore space.

Figure 3.4 shows an example 2D calculation with the electrical potential field using the numerical PNP approach in which the differing diffusion rates of the ionic species is combined

with a transverse (perpendicular to the charged clay surfaces) calculation of the electrical potential and flux. The boundary conditions at the clay surfaces are no-flux for the species concentrations and Dirichlet for the electrical potential, with a value of -0.12 Volts assumed. After ten days of diffusion down the length of the clay interlamellae (X-coordinate), the electrical potential shows a curved front due to the effects of the negatively charged clay surface at the top and bottom.
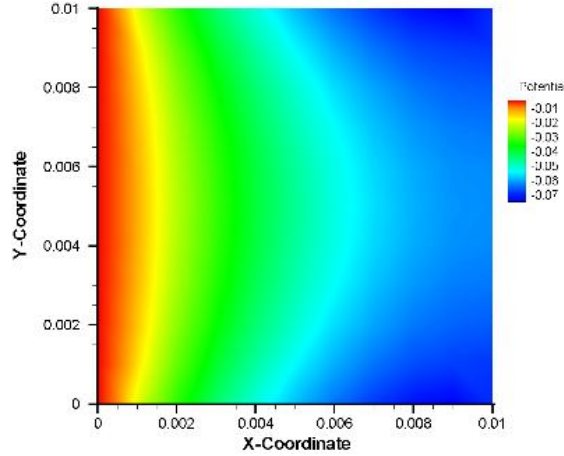
Figure 3.4. Example 2D calculation of electrical potential field for the case where the charged clay surfaces (top and bottom) have a -0.12 V charge.

3.2.4   Comparison to Van Loon et al. (2007) Diffusion Data

For such a case, it should be proved that the anion concentration, $C(x, y, z)$ integrated over the pore space should equal that measured experimentally:

$$\int_{V_P} C(x, y, z) dV = \left[A^-\right] \varepsilon_{A^-} V_T \tag{3.60}$$

where V_T is the total volume of a given clay sample whose porosity is ϕ, $V_P = \phi V_T$ is its volume of pores, $\left[A^-\right]$ is the concentration of anions in solution at the outlet of the sample, and ε_{A^-} is the so-called anion-accessible porosity (Van Loon et al., 2007).

Considering the case of a solution confined between two parallel charged walls, the Poisson–Boltzmann equation takes the following form:

$$\frac{d^2\varphi}{dy^2} = \frac{2FC_\infty}{\varepsilon} \sinh\left(\frac{F\varphi}{RT}\right) \tag{3.61}$$

Incorporating the steric correction, which accounts for the constraint to the space physically available to ions in highly concentrated solutions, the expression above becomes:

$$\frac{d^2\varphi}{dy^2} = \frac{2FC_\infty}{\varepsilon} \frac{\sinh\left(\dfrac{F\varphi}{RT}\right)}{1 + 4\dfrac{C_\infty}{C_{max}} \sinh^2\left(\dfrac{F\varphi}{2RT}\right)} \tag{3.62}$$

68

where C_{max} represents the maximum possible concentration for a given ion size in solution. It becomes apparent that this equation recovers its original form when $C_{max} \to \infty$.

Under the hypothesis that the pore space is constituted by a number of layers of thickness h, the total amount of anions in one such layer is:

$$Total\ mass\ per\ layer = \int_0^h C(r)\,dr = C_\infty \int_0^h \exp\left(\frac{F\varphi(r)}{RT}\right)dr = G(h) \tag{3.63}$$

where $\varphi(r)$ is the solution of the Poisson–Boltzmann equation (r is a dummy variable), and the total mass is written explicitly as a function of h.

It is worth pointing out that $G(h)$ equals zero when h is less than the threshold marking the transition between innercrystalline and interlamellar water, which is on the order of 0.94 nm (Tournassat and Appelo, 2011).

Assuming that the sizes of clay pores are uniform, then the anion concentration is simply:

$$\left[A^-\right]_{calc} = \frac{G(h_{med})}{h_{med}} \tag{3.64}$$

where h_{med} is the average pore thickness.

Numerical results were compared to experimental data provided by Van Loon et al. (2007). In the process, the values of the surface electrical potential, the average pore thickness, and the effective hard-sphere packing length were adjusted to obtain the best fit (Table 3.3). Results obtained for best-fit values are shown in Figure 3.5

Table 3.3. Parameters used during the fitting of Van Loon et al (2007) data.

Dry density (kg/m^3)	Surface potential (V)	Effective hard-sphere packing length (m)	Pore thickness (m)
1300	-0.12	5.00E-10	3.00E-09
1600	-0.12	5.00E-10	1.40E-09
1900	-0.12	5.00E-10	1.00E-09
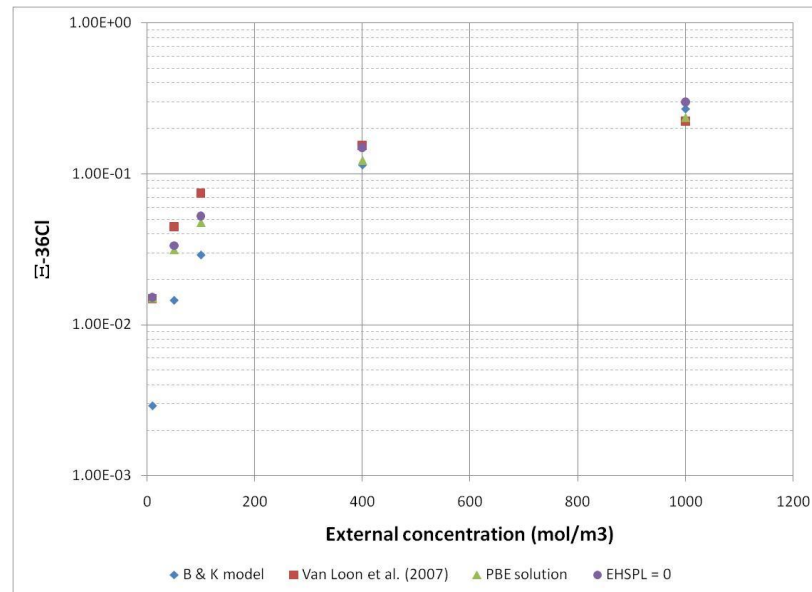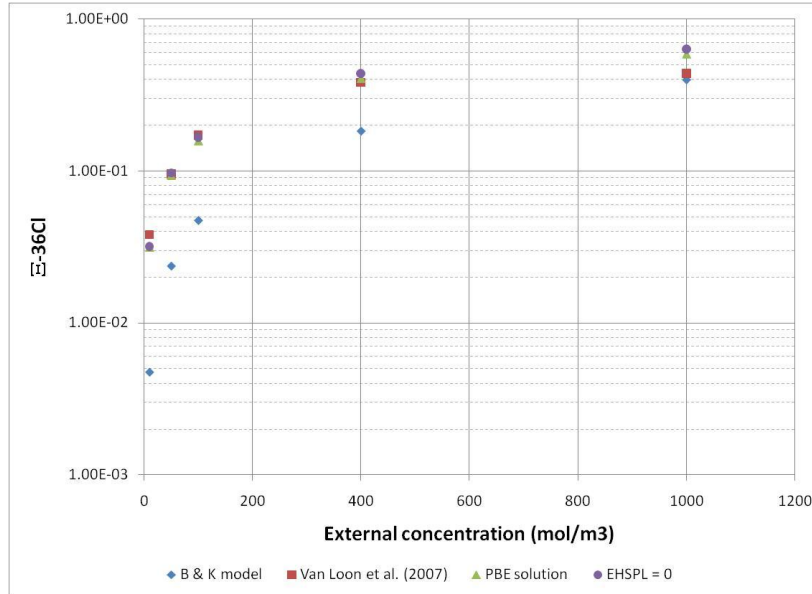
Figure 3.5. Chloride concentration ratios as a function of dry density and ionic strength of the external solution (from top to bottom: results obtained for dry density equal to 1300 kg/m³, 1600 kg/m³ and 1900 kg/m³)

70
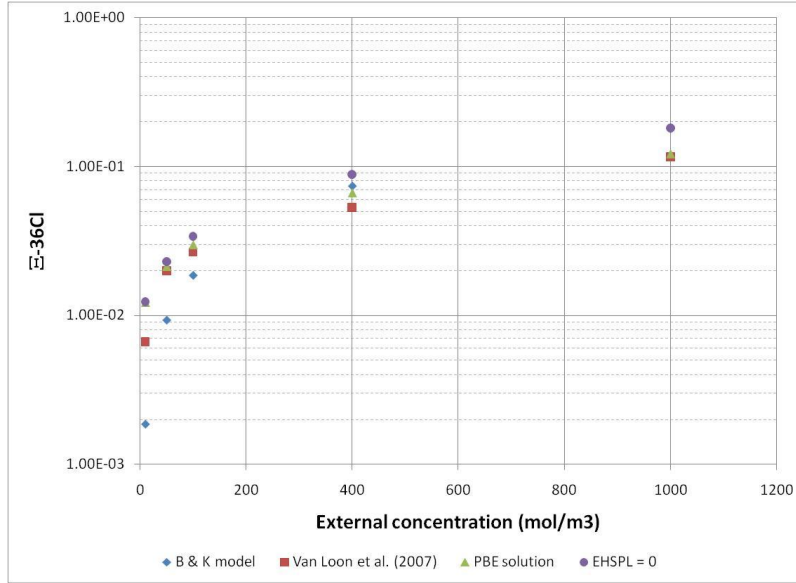
Figure 3.5 (Cont.) Chloride concentration ratios as a function of dry density and ionic strength of the external solution (from top to bottom: results obtained for dry density equal to 1300 kg/m³, 1600 kg/m³ and 1900 kg/m³)

As can be seen, the results obtained provide a good approximation to experimental data for all the dry density values considered. They even improve upon the predictions of the Birgersson and Karnland model, as shown in the diagram above. Moreover, the calculated average pore thickness is consistent with the values calculated by Tournassat and Appelo (2011) for the range of dry density values below approximately 1600 kg/m³. For higher dry density values, however, the total pore volume is reduced to such an extent that the calculated average interlamellar distance is less than the fitted h_{med} that is shown in the table above and, in fact, even less than the maximum innercrystalline spacing (the above-mentioned threshold of 0.94 nm). Since anions are completely excluded from the innercrystalline pore space, it follows that for dry densities higher than 1600 kg/m³, the concentration of anions in clay should be nil. As noted by Tournassat and Appelo (2011), this contradicts experimental evidence. Based on this, it is suggested that the assumption of the pore space being uniformly distributed is not correct.

In contrast to the assumption of a uniform pore distribution, we assume in what follows that the pore size distribution of clays obeys a fractal law, such that the following number-size relationship holds (Mandelbrot, 1999):

$$N(L) = kL^{-D} \tag{3.65}$$

where $N(L)$ is the number of elements of size equal to or less than a given characteristic length L, D is the fractal dimension and k is a constant of proportionality.

Fractal theory has been used for the description of the pore-size distribution of soils and its related hydraulic, mechanical, and surface properties (Xu, 2004; Xu et al., 2004; Xu and Xia, 2006; Ersahin et al., 2006, among others). In most cases, however, the characteristic length considered was the radius of pores. An original contribution of the present study is to insert the interlamellar distance into the relationship above, namely:

$$N(L) = kL^{-D} \tag{3.66}$$

where h varies between 0 and a maximum thickness, h_{max}, which corresponds to the total porosity of the sample.

If one further assumes that, as Viani et al. (1983) put it, "Clay minerals normally occur as crystals of colloidal size in which parallel silicate layers are stacked one above the other like the leaves of a book" (which in itself supports the hypothesis of h being described as a fractal, since a fractal is a shape made of parts similar to the whole in some way), then it becomes apparent that the total pore space should be proportional to the number of spaces between those leaves and to the distance between them, which means that:

$$V_P \, \alpha \sum_{i=1}^{N} N_i h_i \tag{3.67}$$

Let us assume a parallelepipedic sample of perfectly flat layered clay whose sides in the x- and y-directions are B and L, respectively. For such a case, the total pore space is given by:

$$V_P = BL \sum_{i=1}^{N} N_i h_i \tag{3.68}$$

In a more general, less restrictive, case, we suggest here that the factor BL can be replaced by a shape factor, ξ, which condenses the information related not only to the geometrical shape of the sample, but also (in keeping with the image depicted by Viani et al., 1983) the information about how flat or bent the leaves are.

The number of layers being continuous rather than discrete, then the summation becomes an integral:

$$V_P = \xi \int_{0}^{\infty} h dN \tag{3.69}$$

Differentiating N from the number-size relationship and performing the integral, one obtains:

$$V_P = \xi \int_{0}^{\infty} h dN = -\xi Dk \int_{h_{max}}^{0} h^{-D} dh = \xi Dk \frac{1}{1-D} h_{max}^{1-D} \Rightarrow$$

$$h_{max} = \left[(1-D) \frac{\phi V_T}{\xi Dk} \right]^{\frac{1}{1-D}} \tag{3.70}$$

Analogously, the total amount of anions in the clay sample can be calculated in terms of the mass of each interlamellar space, as shown above:

$$Total\ mass = \xi \int_{0}^{\infty} G(h) dN = -\xi \int_{h_{max}}^{0} G(h) Dkh^{-D-1} dh =$$

$$-\xi \int_{h_{min}}^{0} G(h) Dkh^{-D-1} dh - \xi \int_{h_{max}}^{h_{min}} G(h) Dkh^{-D-1} dh = \xi \int_{h_{min}}^{h_{max}} G(h) Dkh^{-D-1} dh \tag{3.71}$$

because, as discussed above, the integral vanishes between 0 and $h_{min} = 0.94$ nm.

The integral can be calculated numerically by making use of a Gaussian quadrature rule, according to which the following equation is valid:

$$\xi \int_{h_{min}}^{h_{max}} G(h) Dkh^{-D-1} dh = \sum_{j=1}^{n} w_i \xi G(h_i) Dkh_i^{-D-1} \tag{3.72}$$

where n is the number of integration points and w_i are the corresponding weighting factors.

Several simulations were performed in order to find the combination of the factor ξk and the fractal dimension D that minimizes the error made with respect to the total amount of anions measured experimentally. Let the error be defined as:

$$Error = \sum_{i=1}^{5} \left(\frac{CalcMass_i - ExpMass_i}{ExpMass_i} \right)^2 \tag{3.73}$$

where $CalcMass_i$ and $ExpMass_i$ represent the total amount of anions calculated and experimentally measured, respectively, for a given value of the ionic strength of the external solution. The summation has as many terms as ionic strength values considered.

Figure 3.6 display the error made as a function of the fractal dimension and the shape factor (assuming k is equal to one).
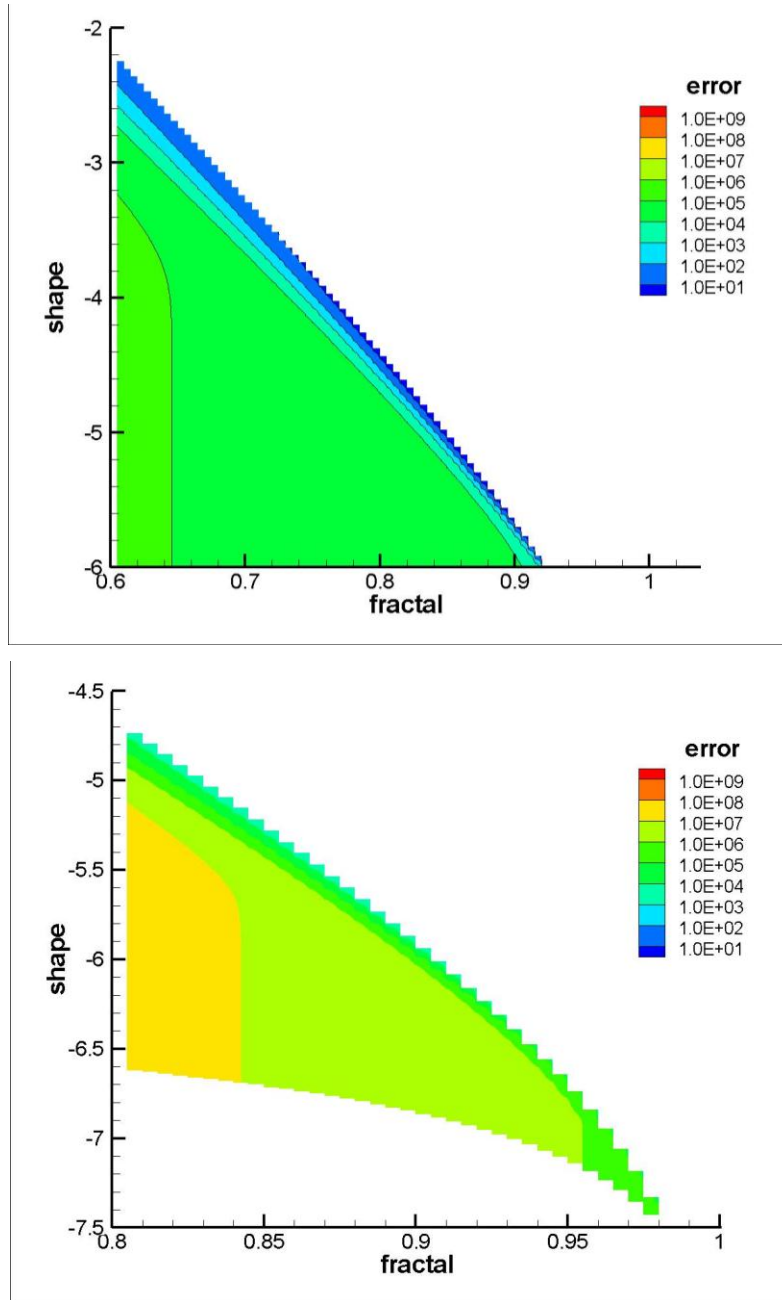
Figure 3.6. Error as a function of the combination of the fractal dimension and the shape factor

Some comments are worth making concerning Figure 3.6. The values of h_{max} calculated increase from the upper right towards the lower left of the diagrams, so that the points of that region correspond to the case where the calculated h_{max} is less than h_{min} and thus were thus deemed irrelevant. Furthermore, the minimum errors are confined to a very small range of h_{max} very

close in value to $h_{\min}$, but this is perhaps what might be expected when dealing with highly compacted clays. Best-fit values are summarized in Table 3.4.

Table 3.4. Parameters used during the fitting procedure of fractal behavior

Dry density (kg/m^3)	Fractal dimension	Log(ξ)
1300	0.875	-5.400
1600	0.960	-6.730
1900	0.980	-7.330

Results that take into account the values listed in Table 3.4 with a non-uniform clay interlamellae spacing are shown in the following figures.
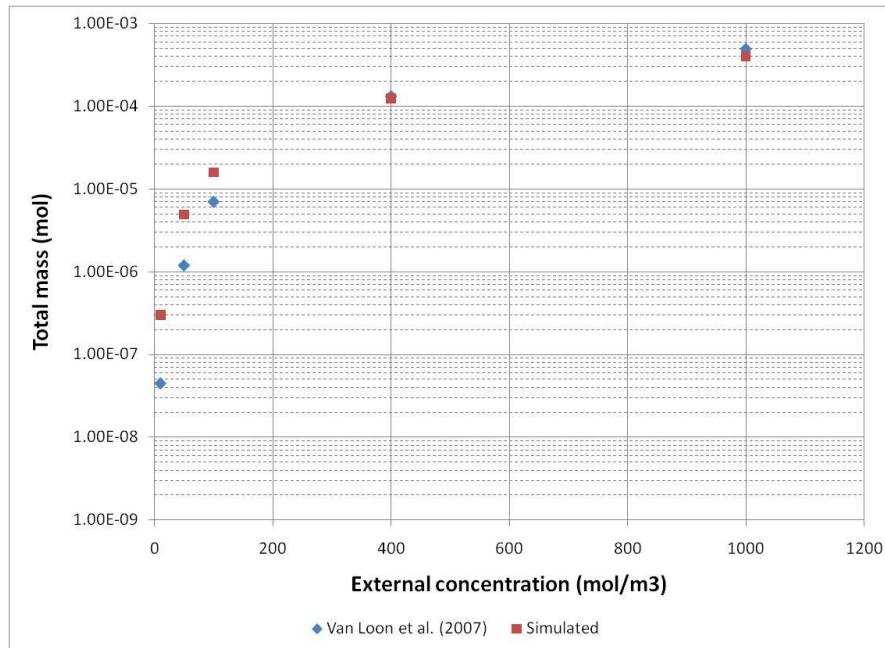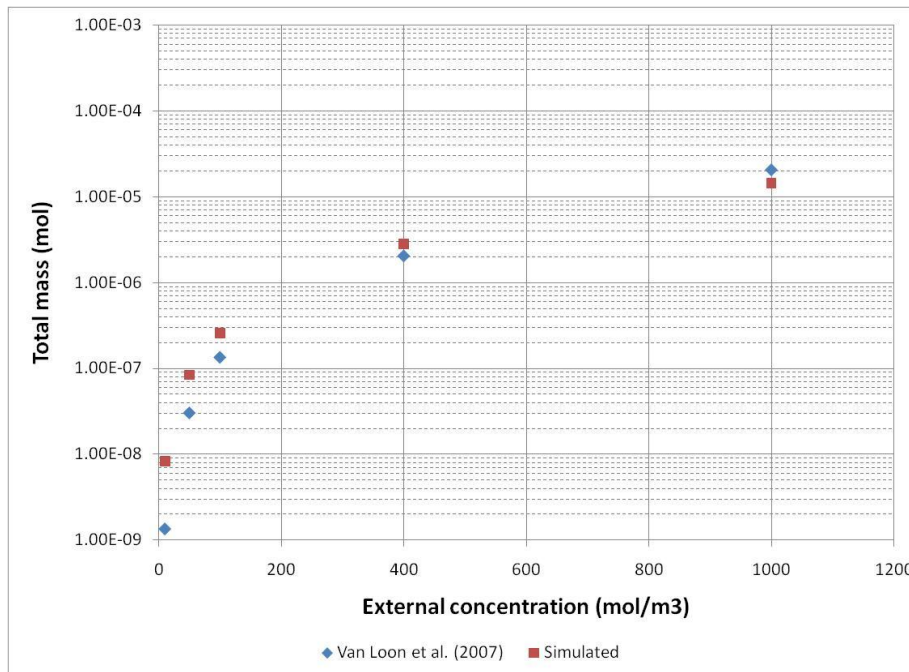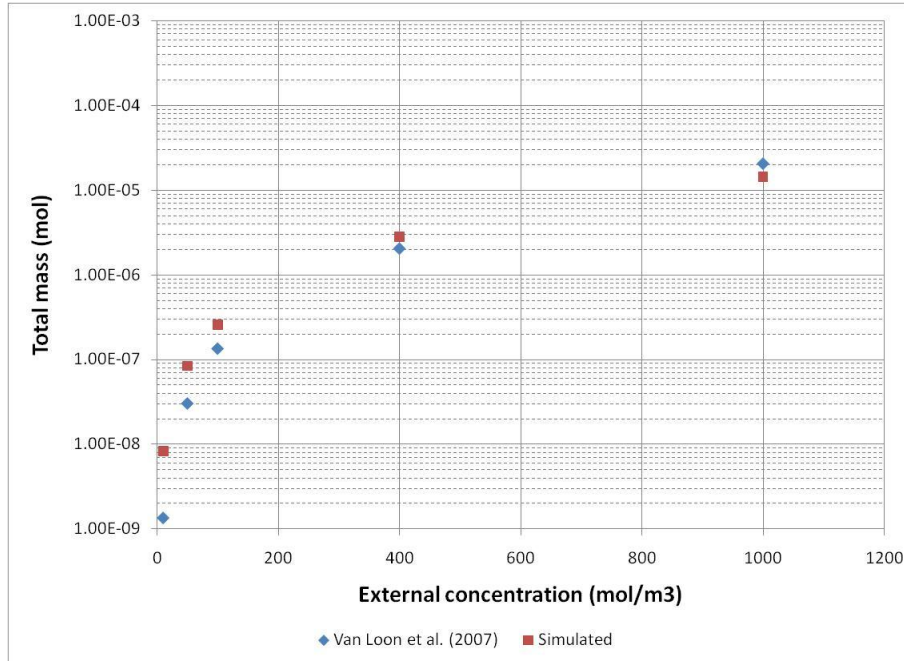
Figure 3.7. Chloride total mass as a function of dry density and ionic strength of the external solution (from top to bottom: Results obtained for dry density equal to 1300 kg/m³, 1600 kg/m³ and 1900 kg/m³), based on fractal values in Table 3.4

As Figure 3.7 demonstrates, the agreement with experimental data is satisfactory even though values of D and $\text{Log}(\xi)$ that were tested were restricted to rational numbers. The solutions shown above, however, may not be unique, which suggests that an additional constraint may be required. In this regard, the analysis of swelling pressure might provide the needed constraint. Unfortunately, Van Loon et al. (2007) do not provide such data.

76

3.3 Conclusions

A conceptual model involving the coupling of the Poisson-Nernst-Planck set of equations with a suitable surface complexation model was presented as an attempt to bridge the gap between nanofluidic dynamics and clay science.

Even though the practical features of the model are currently under development, the evidence collected so far allows us to state that it has great potential for the simulation of solute transport in such media because it is more physically grounded than previous models. Good agreement with available experimental data gives further support to such a claim. Indeed, the spatial distribution of the electric potential and the concentration of every species of the geochemical system were simulated, and a good fit of experimental data was found over a wider range of external conditions than is possible with the Donnan-based models.

In addition, the present study is able to reconcile the theory of the Poisson–Boltzmann equation with seemingly conflicting experimental evidence of non-zero anion concentrations found in highly compacted clays by making use of the theory of fractals. If proved suitable, that would have relevant implications for the process of upscaling results from the nano- up to macro-scales based on the self-similarity of the fractal structure of clays.

4. MOLECULAR DYNAMICS (MD) SIMULATIONS OF ION DIFFUSION IN MONTMORILLONITE INTERLAYER NANOPORES

Considering that EBS is subject to substantial temperature variations, the objective of our MD simulations is to predict the temperature dependence of water and solute diffusion coefficients (D) in clay interlayer nanopores as characterized by the phenomenological activation energy E_A (kJ mol^{-1}) of the Arrhenius relation: $\ln D \propto -E_A/RT$, where R is the ideal gas constant and T is absolute temperature. We aim to predict E_A in *individual nanopores* with sufficient accuracy to aid in the interpretation of experimental data on E_A in *macroscopic* (cm-scale) samples of compacted montmorillonite (MMT) (Kozaki et al., 1996,1998,1999,2005,2008). For a variety of ionic solutes (Na$^+$, Ca^{2+}, Cs$^+$, Cl$^-$) diffusing in macroscopic (cm-scale) samples of compacted Na-MMT, E_A takes three distinct values, suggestive of three distinct diffusion pathways or mechanisms, with increasing compaction. In the case of Na$^+$, for example, E_A equals ~18.5 ± 1.5 kJ mol^{-1} (consistent with the value in bulk liquid water) at low dry bulk densities ($\leq$ 0.8 kg dm^{-3}), decreases to ~15.5 ± 1.5 kJ mol^{-1} at intermediate dry bulk densities (0.9 to 1.2 kg dm^{-3}), and increases to ~25 ± 2 kJ mol^{-1} at high dry bulk densities ($\geq$ 1.6 kg dm^{-3}) (Kozaki et al., 2005). It will be possible to use these results to determine activation energies for diffusion through the compacted bentonite in larger (repository) scale models as a function of the evolving temperature field. In the nearer term, these activation energies will be used as input for microscopic continuum models of the kind described in Section 3.

As a necessary first step of our simulations, we conducted a series of simulations of the three-layer hydrate of Na-MMT (Figure 4.1) aimed at developing a best-practice methodology for predicting D and E_A values of interlayer solutes in smectite interlayers using MD simulations. A thorough sensitivity analysis was found necessary in order to accurately predict self-diffusion coefficients over a wide range of temperatures, i.e., to accurately mimic the temperature dependence of experimental self-diffusion coefficients. For our sensitivity analysis, we investigated the influence of three methodological choices (the rigidity of the clay structure, the size of the simulated system, and the water content per clay unit cell) as described in the next

paragraph. At each condition, we investigated four temperatures (278 to 353 K) to determine the activation energy of sodium and water diffusion. In order to determine the accuracy of our predicted self-diffusion coefficients, we also simulated "homogenous" systems without smectite, i.e., Na^+ ions in bulk water.
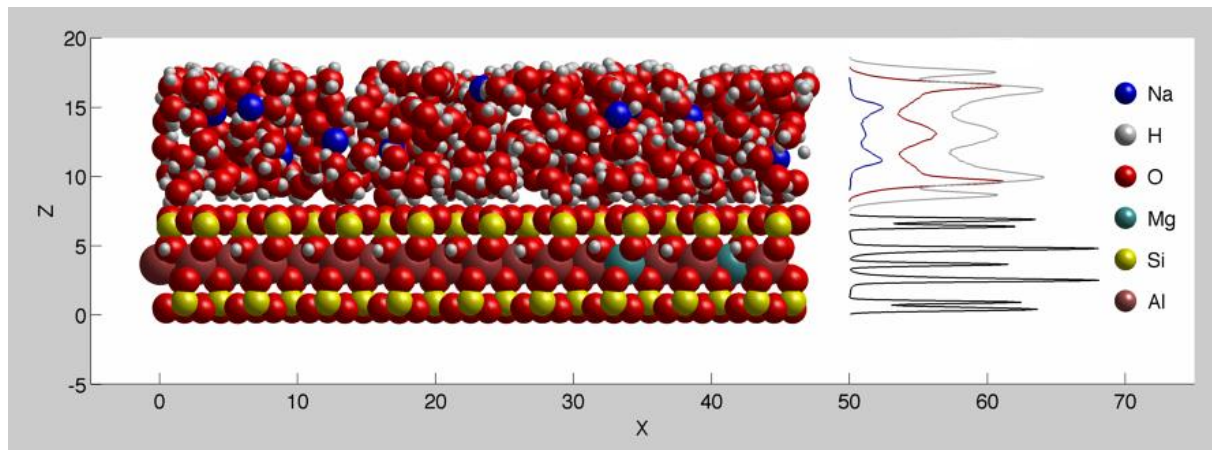
Figure 4.1. Illustration showing a typical MMT lamella of size ~45×45×1 nm in the three-layer hydrate (expected to be the predominant hydration state in the bentonite barrier in different concepts of geological nuclear waste disposal, such as the Swedish KBS-3 concept (Holmboe et al., 2012) with a basal spacing (total MMT + H₂O thickness) of 1.89 nm. The figure shows a "snapshot" of the interlayer water and sodium, whereas clay atoms (Al, Si, Mg, O, H) are displayed at their time-averaged coordinates. The curves on the right side of the figure show the average z-direction density distributions of the different types of atoms present in the system (scaled independently for clarity): Na⁺ (blue), water oxygen (red), water hydrogen (gray) as well as all MMT atoms (black).

Our decision to investigate the influence of clay structure rigidity was motivated by the fact that most previous MD simulation studies of clay interlayer nanopores probed relatively small smectite-water systems ($< 10^4$ atoms) using rigid smectite clay structures. The use of fully flexible clay layers has been advocated by several authors (Kalinichev et al., 2000; Cygan et al., 2004), but data comparing systems with rigid and flexible clay structures have not been published. To fully evaluate the influence of clay flexibility, we modeled systems where the clay lamellae were either fully rigid, fully flexible, or semi-flexible (i.e., all atoms were fixed except the structural H atoms). To probe the influence of simulation cell size, we simulated clay-water systems with one, two, three, or four clay lamellae (denoted MMTx1-4), as shown in Figure 4.2, and homogeneous systems (bulk water with dissolved Na⁺) with 512, 2778, or 22,224 water molecules. Simulation cell size is known to influence diffusion coefficients predicted by MD simulations, but this artifact has only been studied in simulations of bulk fluids (Yeh and Hummer, 2004), never in simulations of porous media. Finally, we simulated systems with a range of water contents (12, 15, and 18 H₂O molecules per unit cell) because although the basal spacing of the three-layer hydrate [1.89 nm (Kozaki et al., 1998; Chen et al., 2009)] is relatively well known from XRD data, the exact water content of the three-layer hydrate is less precisely known.
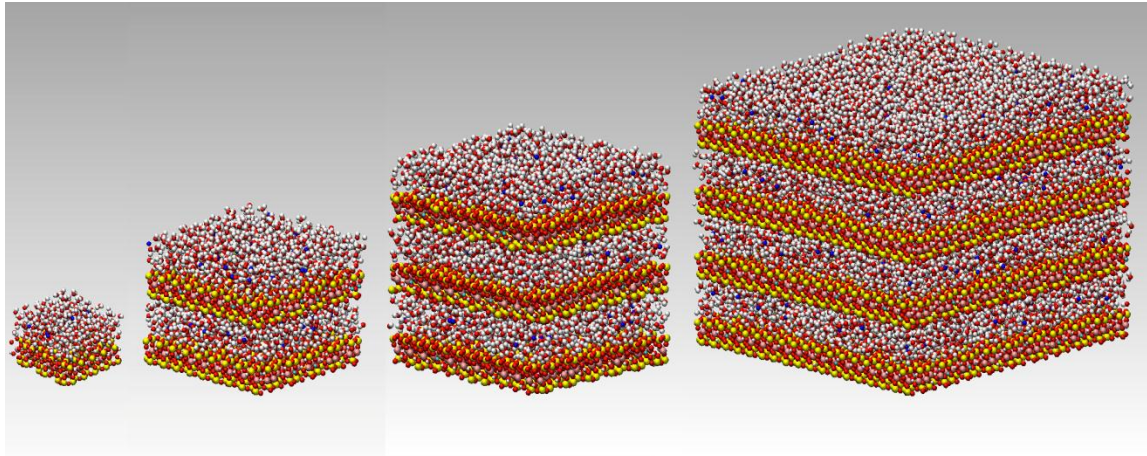
Figure 4.2. MD simulation snapshots showing the four different sizes of MMT/H$_2$O/Na$^+$ systems simulated in this work, hereafter designated as MMTx1-4 (from left to right).

4.1   Simulation Methodology

In brief, our methodology uses the versatile MD code LAMMPS (Plimpton, 1995) with a rigid SPC/E water model and the CLAYFF force field (Cygan et al., 2004), which is known to correctly predict a range of structural and thermodynamical properties of smectite interlayer water and exchangeable cations (Bourg and Sposito, 2010; Ferrage et al., 2011) The CLAYFF force field includes atomic partial charges and van der Waals parameters for all clay structural atoms along with bond stretch parameters for structural OH groups. The clay investigated in this study was a typical 2:1 Na$^+$-exchanged smectite (Wyoming montmorillonite) with the unit cell structural formula of (Al$_{3.33}$Mg$_{0.66}$)Si$_8$O$_{20}$(OH)$_4$Na$_{0.66}$, i.e., containing a negative structural charge of 0.66/unit cell, created by Al to Mg substitutions in the octahedral sheet. Clay atomic coordinates were taken from Bickmore et al. (2003) and relaxed during an initial equilibration in the NVT ensemble (constant number of particles, volume and temperature) followed by a volume optimization in the NPT ensemble (constant number of particles, pressure and temperature), resulting in equilibration runs of > 500 ps in fully flexible configurations at the corresponding sizes and temperatures. Production runs were then carried out for a total duration of 10 ns for each simulated system. In total, close to 300,000 CPU hours were used on the Hopper NERSC cluster, a Cray XE6 with 153,216 compute cores. For each simulated system, we determined the self-diffusion coefficient of water and sodium (hereafter we focus primarily on the sodium results) from the slope of the mean square displacement of the simulated particles using the well-known Einstein relation,

$$D = \frac{1}{2n} \lim_{\tau \to \infty} \frac{d\langle l^2 \rangle}{d\tau}$$

(4.1)

where *n* is the dimensionality of the system and $\langle l^2 \rangle = \langle |r(t) - r(t + \tau)|^2 \rangle$ is the mean square displacement.

4.2   Results

Interlayer water content: Our simulations with different water contents showed that an interlayer water content of 14.5 ± 0.5 water molecules per unit cell is consistent with experimental data on the basal spacing of the three-layer hydrate of Na-MMT. Within this range,

79

uncertainty regarding the interlayer water content has a negligible influence on the overall uncertainty of predicted E_A values. Therefore, we focus hereafter on results obtained at the interlayer water content of 15 water molecules per unit cell.

Flexibility of the clay structure: Figure 4.3 shows the D values of Na^+ in the three-layer hydrate of Na-MMT for different degrees of flexibility of the MMT structure. Similar data were obtained for H_2O. In general, although clay flexibility had a small influence on the self-diffusion coefficients of Na^+ and H_2O, the influence on E_A was substantial, with a difference of 2.5 kJ/mol when comparing the fully flexible and fully rigid systems. The semi-flexible system yielded essentially the same E_A values as the fully flexible system, suggesting that most of the impact of clay flexibility on the dynamics of interlayer water and sodium results from the motion of H atoms in the clay structure. This finding is quite remarkable in view of the fact that the clay H atoms are not in direct contact with the interlayer water (Figure 4.1).
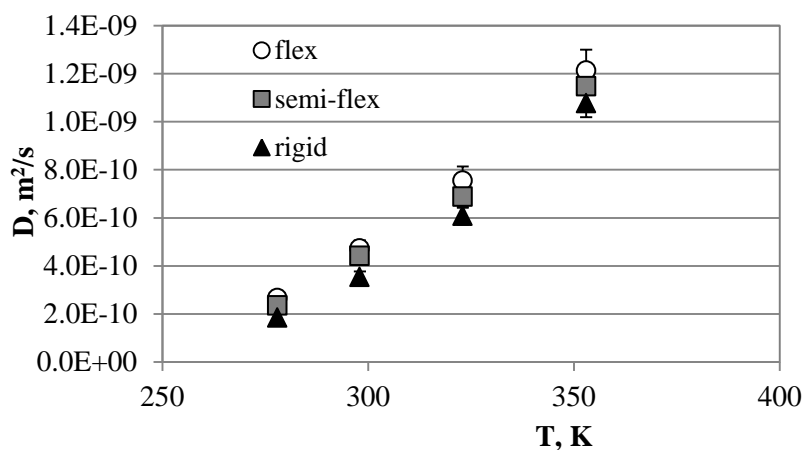
Figure 4.3. MD simulation predictions of the self-diffusion coefficient of Na^+ as a function of temperature for different degrees of flexibility of the MMT structure from fully flexible or semi-flexible (with flexible structural hydroxyl groups) to fully rigid.

Simulation cell size: Our results on the size-dependence of D are shown in Figures 4.4 and 4.5 for the systems with a fully flexible clay structure and a water content of 15 water molecules per unit cell. In general, we find that D decreases linearly with the inverse of the simulation cell size ($1/L$) as expected from simulations of bulk liquid water (Yeh and Hummer, 2004). Interestingly, for Na^+ (but not for H_2O) the smallest system deviates from the expected trend, perhaps because the arrangement of structural charge sites in a system with a single clay sheet creates unrealistic charge and electric field environments.
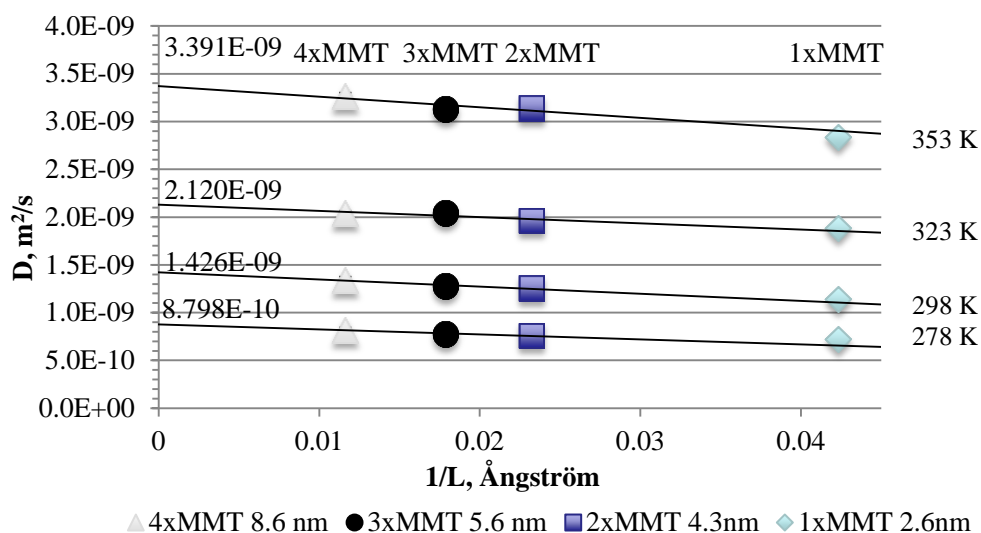
Figure 4.4. Self-diffusion coefficients of H$_2$O plotted vs. the inverse of system size.
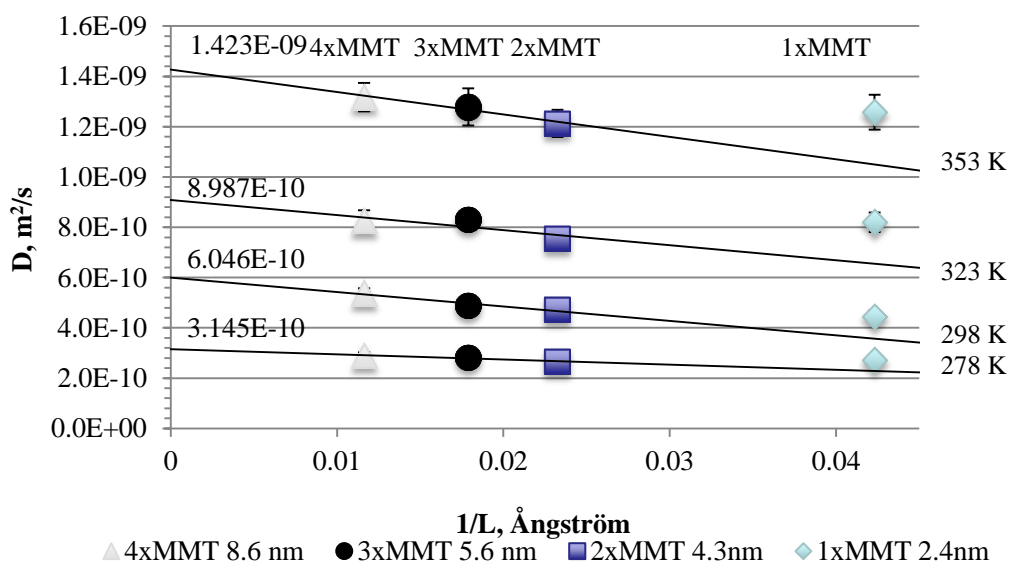
Figure 4.5. Self-diffusion coefficients of Na$^+$ plotted vs. the inverse of system size.

Prediction of E_A values: Figure 4.6 summarizes the E_A values obtained for Na$^+$ (data for water are not shown) in bulk liquid water and in clay interlayer water. The green column on the left side of the figure shows the measured E_A value for sodium diffusion in bulk liquid water (18.43 kJ/mol). The second set of columns (denoted "D SPC/E") shows E_A values calculated from sodium diffusion coefficient in bulk liquid water and in the three-layer hydrate of Na-MMT (reported for the fully flexible clay system). The third set of columns (denoted "Ds SPC/E") shows E_A values calculated from MD simulation D values *extrapolated to an infinitely large simulation cell*. This third set of colums (our best estimates of the E_A values of sodium) shows that our MD simulations closely approximate the experimental E_A value for sodium diffusion in bulk liquid water (green bar). This third set of columns also shows that sodium diffusion in the

81

three-layer hydrate of Na-MMT has a E_A value roughly 2 kJ/mol lower than sodium diffusion in bulk liquid water. Longer simulations will be required to precisely quantify this difference.
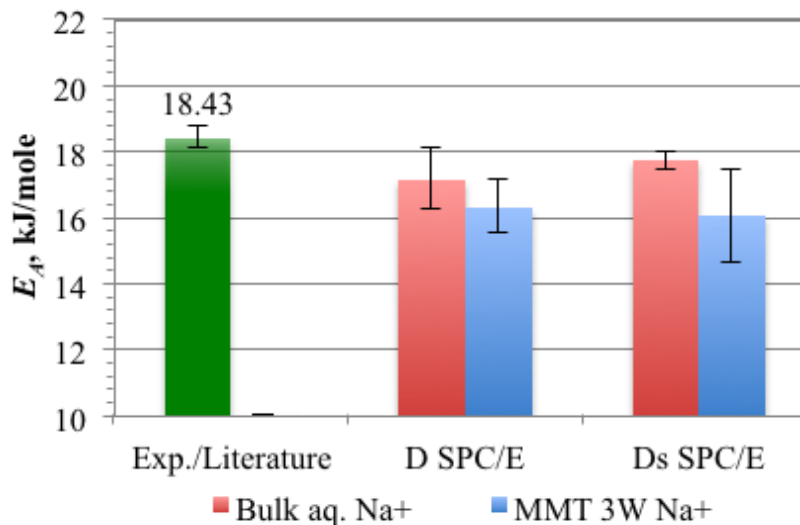
Figure 4.6. Comparison of our predicted E_A values for Na$^+$ diffusion in bulk liquid water (red bars) and in 3-layer hydrate of Na-MMT (blue bars). The experimental value for Na$^+$ in bulk liquid water is displayed on the left (green bar).

4.3   Conclusions

From molecular dynamics simulations we determined the influence of temperature, clay structure flexibility, simulation cell size, and water content on water and sodium diffusion in the three-layer hydrate of Na-montmorillonite. Our simulations led to the development of a robust MD simulation methodology that correctly predicts the temperature dependence of sodium diffusion in bulk liquid water. This methodology predicts that sodium diffusion has a lower activation energy (E_A) in the three-layer hydrate of Na-montmorillonite than in bulk liquid water. These results open up a promising avenue for explaining experimental results on the activation energy of diffusion of ionic solutes in macroscopic samples of compacted montmorillonite. It will be possible to use these results to determine activation energies for diffusion through the compacted bentonite in larger (repository) scale models as a function of the evolving temperature field. In the nearer term, these activation energies will be used as input for microscopic continuum models of the kind described in Section 3.

5.   EXPERIMENTAL STUDIES OF THE REACTIVE DIFFUSIVE TRANSPORT OF U(VI) IN BENTONITE

Bentonite backfill/buffer is proposed as part of EBS around nuclear wastes disposed in deep underground disposal sites. An important aspect of repository performance for an EBS is the capacity of the barrier to limit the radionuclide flux to the biosphere to acceptably low levels. Montmorillonite is the dominant mineral phase present in bentonites. In current models for radionuclide diffusion through bentonite in an EBS, the apparent and effective diffusion coefficients are linked through a K_d value, a sorption partitioning coefficient that is often believed to be a constant value for a particular radionuclide and solid phase sample. In the case of U(VI), however, this s unlikely to be true because of the very high sensitivity of the K_d value

to pH and bicarbonate and calcium concentrations. By extension to the aqueous chemistry of other actinides, we can expect the K_d values of Np(V), Am, and Pu(VI) to be also sensitive to pH and bicarbonate concentrations. It should be noted that waste forms, and possibly concrete in the vicinity of an EBS, are likely to create gradients in these chemical variables (pH, HCO_3^-, Ca^{2+}) within the EBS. Therefore, it is important to represent U(VI) (and other actinides) partitioning within an EBS with a *surface complexation model* rather than a constant K_d value. This will have a significant impact on the conceptual model that describes U(VI) diffusion through an EBS.

5.1   Background

5.1.1   Diffusion of Radionuclides

The state of knowledge with respect to diffusion-driven flux shows that there are large differences in the measured diffusion behavior of various radionuclides, e.g. between halides (^{36}Cl, ^{129}I) and actinides ($^{238,235}U$, ^{237}Np, ^{232}Th). The differing behaviors are a result of the two major processes that have important effects on macroscopic diffusive transport, i.e. *molecular diffusion* and *sorption.* The research effort described in this section is an effort to describe these two processes for U(VI) in fundamental terms and to develop a conceptual model that can be used in numerical, diffusion-driven transport models (Sections 3 and 4 of this report).

Generally speaking, the mineralogical composition of bentonites is nearly all montmorillonite. Varying amounts of carbonate minerals (calcite, dolomite), quartz, accessory minerals (pyrite, feldspar), other clay minerals, and organic matter are typically present at low concentrations. For an experimental study of fundamental processes, these other minerals present serious difficulties in the maintenance of aqueous chemical conditions and in constraining U(VI) processes to only diffusion and sorption. For example, the presence of calcite makes it extremely difficult to control pH and dissolved calcium and bicarbonate concentrations by experimental design, and each of these variables has a significant impact on U(VI) sorption (Davis et al., 2004; Fox et al., 2006). Furthermore, the presence of pyrite may cause reduction of U(VI) to U(IV). U(IV) would be present almost completely in the solid phase, either precipitated as UO_2 or very strongly sorbed, to a different extent than U(VI), thus complicating the quantification of U(VI) sorption. Because of the experimental difficulties introduced by such impurities and the objective of understanding the *fundamental processes* that control macroscopic diffusion, the experimental program in this research effort is composed of two parts, studies of U(VI) sorption and diffusion in: 1) pure montmorillonite, and 2) bentonite. The pure montmorillonite studied in this research is a purified sample of Wyoming Swy-2, Na-montmorillonite, as obtained from the Clay Minerals Society. The bentonite sample has not yet been selected, but will be chosen in consultation with other DOE laboratories.

Montmorillonite is composed of particles made up of positive charge-deficient alumino-silicate lamellae stacked one above the other (Figure 4.1). The net negative structural charge is compensated by cations located in the interlamellar space and adjacent to the external stack surfaces. These characteristics explain the substantial cation exchange capacities (CEC) and high specific surface areas of montmorillonite.

Two factors are known to be particularly important in controlling macroscopic diffusion: 1) the charge of the diffusing species (anion, cation, neutral), and 2) the degree to which the diffusing species adsorbs onto the mineral surface contacting the aqueous solution, commonly quantified in terms of the sorption distribution coefficient, K_d (Bourg et al, 2003; 2006). Generally

speaking, the interaction of these factors leads to the classification of radionuclides into two groups: one for elements relatively unaffected by sorption ($K_d \sim 0$), which are generally anionic, and a second group for which sorption is important ($K_d > 100$).

Macroscopic diffusion has been classically evaluated based on Fick's laws for one dimensional diffusion in a saturated, homogeneous porous material, adapted to take into account "simple" effects of sorption on radionuclide flux through the material. These laws are as follows:

- *Fick's first law* (for steady state flux in one dimension) is given by $J = -D_e \frac{dC}{dx}$ where J is the solute flux (mol·s^{-1}·m^{-2}), D_e the so-called 'effective' diffusion coefficient, and dC/dx the gradient in radionuclide concentration (C, mol·m^{-3}) resulting from conditions imposed at the boundaries of the system (separated by a distance, dx (m)). The expression is then adapted to account for the effects of material porosity and pore space geometry by defining $D_e = D_0 \left(\frac{\delta}{\tau^2}\right) \omega$, where D_0 is the solute diffusion coefficient in free solution, ω is the total porosity, δ is a 'constrictivity' factor, and τ is a 'tortuosity' factor (≥ 1), representing the average length of the diffusion paths effectively linking the boundaries of the system relative to the distance dx.

- *Fick's second law* (for flux time dependence) is given by $\frac{\partial C}{\partial t} = D_a \frac{\partial^2 C}{\partial x^2}$, where D_a is the 'apparent' diffusion coefficient, given by $D_a = \frac{D_e}{(\omega + \rho K_d)}$, where ρ is the clay density (kg·m^{-3}), and K_d (m^3·kg) is a constant representing the partitioning of the radionuclide between total mobile dissolved species and total immobilized sorbed species. Note here that the word, total, refers to the fact that the dissolved and sorbed radionuclide may have several species in aqueous solution and sorbed to the clay. K_d is generally determined experimentally. If needed, K_d can be replaced in numerical macrodiffusion models by more complex representations (isotherms, surface complexation models) capable of taking into consideration variable sorption as a function of system composition. It is the intent of this research to determine a surface complexation model and conceptual model for U(VI) sorption on montmorillonite that would replace K_d in the expressions above.

Values for diffusion and sorption parameters have been measured for a variety of radiotracers in montmorillonites and bentonites (van Loon et al., 2007; Glaus et al., 2007; Bradbury and Baeyens, 2000, 2002, 2005). The vast majority of the experimental data measured the flux through a mass of clay material compacted to a given density and equilibrated with an electrolyte solution of known composition. Most data have been collected for non-sorbing anions (e.g. ^{36}Cl$^-$, ^{129}I$^-$), tritium, i.e., the water tracer (HTO), and alkali (Cs$^+$, Na$^+$, K$^+$, Rb$^+$, Li$^+$) and alkaline earth (Sr^{2+}, Ca^{2+}) cations. Several interesting trends have been observed:

1) D_e and associated 'accessible porosity' values for anionic tracers are generally much smaller than corresponding values for HTO,

2) D_e for anions has been observed to *decrease* with decreasing solution ionic strength (van Loon et al., 2007)

3) D_e values for certain cations (Na$^+$, K$^+$, Rb$^+$, Cs$^+$) have been found to be significantly higher than D_e for tritium (HTO) and *increases* with decreasing solution ionic strength.

4) D_e for any given tracer type (anion, HTO, cation) tends to decrease with increasing material density.

The current conceptual model for radionuclide (and U(VI)) diffusive transport in clay and bentonites has the following features:

- U(VI) dissolved speciation is determined by the bentonite porewater composition. Thus, understanding the macroscopic diffusive transport of U(VI) requires a thorough characterization of the composition of aqueous solutions, as this determines the solubility and speciation of U(VI). U(VI) is known to form strong ternary aqueous complexes with CO_3^{2-} and Ca^{2+} (Fox et al., 2006).

- The majority of connected porosity is associated with the clay mineral fraction of a bentonite, a major proportion of which is made up of the permanent negative charge clay mineral, montomorillonite.

- U(VI) solid-solution partitioning in bentonites is dominated by sorption on montmorillonite minerals, although there could be exceptions for unusual bentonite samples, in which other minerals contribute to U(VI) sorption, or for systems in which U(VI) is reduced to U(IV).

- U(VI) sorption on bentonites and montmorillonites can be described using surface complexation models that divide U(VI) sorption between ion exchange sites and complexation by edge sites.

- Accessible porosities differ depending on radionuclide species net charge, with cations and neutral species accessing most if not all of the total connected porosity, while anions are excluded from clay interlayer volumes and the solution immediately adjacent to external basal surfaces – anion accessible porosity is therefore less than the total porosity.

5.1.2   Surface Complexation Models for U(VI) Sorption on Montmorillonite

Several models have been developed to describe surface complexation on montmorillonite. However, there is a lack of consistency among these models and large differences in the conceptual development. For example, some of the models have been developed with an electrical double layer model (generally the diffuse double layer model) to provide an electrostatic energy correction term to the mass laws for surface complexation. Others have been developed without electrostatic potential correction terms. Most differentiate between binding within the interlamellar space (called ion exchange, and believed to be dominated by electrostatic energy) and binding at the edge sites of the alumino-silicate layers, where the layer structures are terminated (surface complexation, dominated by covalent chemical bonds). Some differentiate between aluminol and silanol groups that are present at the edge sites.

A classic paper in the field is that of McKinley et al. (1995), who studied U(VI) sorption to montmorillonite in $NaClO_4$ solutions as a function of ionic strength and pH under a $N_2(g)$ atmosphere. The authors developed a surface complexation model that described their experimental U(VI) sorption data. The model included fixed-charge (ion exchange sites) and aluminol and silanol edge sites similar to those on gibbsite and quartz. At low pH and low ionic strength, U(VI) was bound predominantly to the ion exchange sites; the concentration of ion exchange sites was determined experimentally. The concentration of edge sites was estimated by image analysis from a transmission electron microscope (TEM). The binding constants for surface complexation of U(VI) at aluminol and silanol sites, and for $UO_2^{2+}/2Na^+$ ion exchange, was determined by fitting to the experimental U(VI) sorption data. The triple layer electrical double layer (EDL) model was used to correct for electrostatic energy terms associated with U(VI) binding to the edge sites. The EDL properties of the aluminol sites were based on fitting

acid-base titration data for gibbsite and for the silanol sites using data from the literature. A half-reaction approach was used for the ion exchange reactions.

Important new data that impact conceptual model development were collected in the paper of Catalano and Brown (2005). Extended X-ray absorption fine structure (EXAFS) spectroscopy was performed for samples with sorbed U(VI) at various pH values and ionic strengths. Solutions reacted with the montmorillonite samples were in equilibrium with partial pressure of $CO_2(g)$ in air. The spectroscopic results at low pH (about 4) and low ionic strength (0.001M) agree with the conclusion of McKinley et al. (1995) that U(VI) sorption was dominated by ion exchange. At pH 7 and at high ionic strength (1M), spectroscopic results indicate covalent surface complexation binding of U(VI) species. For conditions between these two extremes, both ion exchange and surface complexation binding of U(VI) was indicated, and the general results suggested that ion exchange was likely more important under these conditions than was previously thought by McKinley et al. (1995). Furthermore, the authors concluded that the covalent surface complexation binding on montmorillonite occurred at iron (Fe) octahedral edge sites rather than at aluminol and silanol sites as had been previously thought. The Fe atoms to which U(VI) was bonded (through oxygen atoms) was not thought to be present as contaminant iron nanoparticles, but instead to uncommon Fe atoms that had substituted for Al atoms in the octahedral sheets that make up the montmorillonite mineral structure. The spectroscopic results also led to a conclusion that a significant fraction of the U(VI) bound at edge sites was also bound with one or two carbonate molecules, a so-called ternary surface complex (Bargar et al., 2000). No sorbed U(VI) dimers or polymers were observed, suggesting that the U(VI) multimeric surface species assumed to exist at the montmorillonite by McKinley et al. (1995) did not occur. This study has important implications for the development of a surface complexation model for U(VI) sorption on montmorillonite, especially the evidence for the speciation of sorbed U(VI).

Bourg et al. (2007) reviewed the surface chemistry of montmorillonite and an important new interpretation of acid-base titration data for montmorillonite/solution suspensions and the estimation of surface potentials at edge sites, with special influences from the work of Tournassat et al (2004) and Bickmore et al. (2003). Along with the paper by Catalano and Brown (2005), this work should have a major impact on the development of new surface complexation models for U(VI) sorption on montmorillonite. Tournassat et al. (2004) developed an edge surface structure and reactivity model that explicitly includes edge sites that arise from the isomorphic substitution of Fe(III) for Al, based on the chemical composition of the bentonite sample, MX-80. The total number of Fe-substituted sites in MX-80 is equal to 0.68 sites/nm^2, divided among three site types, Fe(III)-hydroxyls, Fe-Si bridging hydroxyls, and Fe-Al bridging hydroxyls. Ten types of edge site hydroxyls were identified, each with its own acidity constant, and it was argued that the electrical potential related to the constant charge deficiency of the mineral structure has an influence on edge site electrical potential. These interactions result in a complex electrical double layer model for the edge sites.

In conclusion, a conceptual model for the binding of U(VI) to montmorillonite exists but a surface complexation model has not been carefully calibrated over a wide range of chemical conditions. In addition, the complexities of the electrical double layer at edge sites have not yet been incorporated in any surface complexation model. Moreover, new thermodynamic data are available for the U(VI) system that indicate that uranyl-calcium-carbonate ternary aqueous complexes dominate U(VI) speciation and affect its sorption behavior (Fox et al., 2006;

Bradbury and Baeyens, 2011). A systematic study of sorption as a function of U(VI) aqueous speciation for variable pH, bicarbonate, and Ca concentrations is needed. Surface species need to be selected for a new surface complexation model that are consistent with bond valence calculations and spectroscopic results (Arai et al., 2006; Catalano and Brown, 2005) and the acid-base chemistry model of Bourg et al. (2007).

5.2   Materials and Methods

Our research goal is to gain a detailed understanding of U(VI) sorption characteristics onto clay minerals as a function of U(VI) solution speciation. A mechanistic understanding of U(VI) sorption behavior is required for the interpretation of apparent diffusion coefficients, and the decoupling of U(VI)-mineral interactions from apparent metal diffusion rates. U(VI) sorption data are needed for the successful design of U(VI) diffusion experiments, e.g. in terms of expected U(VI) concentrations in the solid phase, the duration of experiments, and appropriate sampling intervals. Our research approach includes a variety of experiments as well as the development of U(VI) surface complexation models.

First, typical batch sorption envelope experiments were performed to characterize U(VI) sorption onto a pretreated clay mineral (Na-montmorillonite) over a range of pH conditions and atmospheric CO_2 concentrations, using specific sorption equilibration times. The partial pressure of carbon dioxide in equilibrium with the solution phase was varied in order to study the role of U(VI)-carbonate solution complexes on U(VI) sorption. The experiments described in this report had the goal to minimize calcium solution concentrations, and hence, the influence of ternary aqueous U(VI)-Ca-carbonato complexes. However, future experiments will also include calcium at various, controlled solution concentrations. The resulting batch sorption data are used in the development of U(VI)-Na-montmorillonite surface complexation models (SCMs), which are able to link U(VI) sorption behavior with U(VI) solution speciation based on existing thermodynamic data.

Second, batch kinetic studies were performed to investigate U(VI) sorption kinetics at various ionic strength conditions, which is motivated by the following reasons. First, kinetic data are needed for the selection of appropriate sorption equilibration times in lab-scale experiments, which aim to characterize U(VI) sorption under equilibrium conditions. For instance, substantial errors may be introduced into model-based predictions of U(VI) mobility if experimentally-determined K_d values do not represent equilibrium values. Second, U(VI) contact times with the solid phase are expected to be substantially longer in diffusion experiments than in typical batch sorption studies. Therefore, kinetic data over extended sorption times are needed to ensure that metal sorption characteristics are comparable between these systems. Finally, it is well understood that differences in the series of elemental reactions comprising a reaction pathway can lead to changes in the overall reaction rate (Stone and Morgan, 1990). Hence, kinetic sorption studies provide a useful tool to indicate potential changes in the dominant, underlying processes responsible for U(VI) sorption, e.g. as a function of chemical solution composition. For instance, Nagasaki reported fast ('outer' surface) and slow ('interlayer' surface) steps for U(VI) sorption to montmorillonite in the absence of organic ligands (Nagasaki, 2001), while in the presence of U(VI)-humic acid complexes only the fast metal sorption step was observed. Kinetic results do not allow any conclusions about the formation of specific surface complexes, in contrast to spectroscopic data. However, they provide first indications of potential changes in

sorption mechanisms over a range of environmentally relevant U(VI) concentrations, which are typically far below the concentration limits accessible by spectroscopic techniques.

5.2.1 Materials

All chemicals used in this study were reagent grade or better. Acids, bases and salt solutions used in equilibrium and kinetic batch experiments were of TraceSelect grade (Sigma Aldrich) in order to minimize calcium background concentrations. Aqueous solutions were prepared with Nanopure water (Barnstead ultrapure water system). Glassware was cleaned by soaking in acid (10 % (v/v) HCl) over 12 to 24 hours, followed by thorough rinsing with Nanopure water and air-drying.

U(VI) solutions contained ^{238}U from a 1.299 mM uranyl nitrate stock solution, provided by Dr. David Singer and originally obtained from Wayne Lukens (both, Lawrence Berkeley National Laboratory). Uranium solution concentrations were quantified by ICP-MS after acidification with TraceSelect grade HNO_3. All samples from batch sorption studies were analyzed for U solution concentrations; selected samples were analyzed for calcium background concentrations and for elements that could indicate clay dissolution or insufficient solid-liquid separations (Si, Al, Fe, etc.).

A commercially available, well-characterized, standardized Source Clay (Na-montmorillonite, SWy-2, Clay Minerals Society) was selected for experimental study. This material is known to contain considerable impurities of quartz (8 %) and feldspars (16 %) as well as calcite (Costanzo and Guggenheim, 2001; Chipera and Bish, 2001; Mermut and Cano, 2001). This required a purification procedure in order to ensure that U(VI) sorption is investigated for a (reasonably) pure clay mineral. Hence, prior to its use in experiments, the clay was pretreated to remove mineral impurities and minimize calcium release from the mineral due to Ca-carbonate dissolution during experiments (see 5.2.2 Clay Pretreatment). Treatment methods were selected with the goal to effectively remove mineral impurities while preserving the original clay characteristics as much as possible. After mineral pretreatment, a clay stock suspension of 10 g/L was prepared in Nanopure water, and its exact solid concentration determined by weighing two 10 mL volume fractions before and after drying at 45 °C. A solid concentration of 0.5 g/L was selected for all batch sorption studies, in order to cover a range of U surface concentrations while avoiding complete (i.e. 100%) U(VI) sorption.

5.2.2 Clay Pretreatment

The steps for the pretreatment of Na-montmorillonite (SWy-2, Clay Minerals Society) included: (1) the removal of calcite impurities using a sodium acetate/acetic acid solution, (2) the clean-up of acetate from the clay suspension with Nanopure water, (3) transforming the clay into its sodium-form by equilibration with a Na-salt solution, (4) the removal of excess Na-salts from suspended clay, (5) the separation of quartz and feldspar impurities from clay particles by centrifugation and (6) oven-drying of the clay mineral phase. We decided to first treat a small batch (approximately 20 grams) of the Source Clay according to this procedure, to monitor relevant solutes over the course of this pretreatment process, and to use this clay material for a first set of batch sorption envelope and batch kinetic experiments. Then, the results from the monitoring of the purification process combined with data describing the release of calcium in batch experiments will allow us to decide if the selected pretreatment methods are sufficient for our experimental needs. Pretreatment steps were performed using dialysis membranes, since it is

possible to efficiently 'up-scale' this set-up for the purification of larger mineral quantities later on.

At the beginning of the pretreatment, dialysis membranes (SpectraPor #6, 8kDa MWCO, regenerated cellulose, 40 mm flat width) were cleaned by soaking (15-30 minutes) and thorough rinsing in Nanopure water for three times. In the meantime, four liters of extractant solution of 1 M sodium-acetate/glacial acetic acid (0.5635 M), buffered at pH=5, were prepared. Aliquots of the extraction solution and all other solutions used as dialysis buffers subsequently were collected for ICP-MS (Ca, Mg, Mn, Ti, Si, Al, K, Fe) and IC (acetate, nitrate) analysis blanks, and the original conductivity of the solution was determined. Then, approximately 20 grams of the original Source Clay (as received) were weighed into a glass beaker, and 40 mL of extractant solution added. After stirring the suspension with a disposable transfer pipette for about one minute, the suspension was filled into two 13-cm long, pre-cleaned dialysis bags using a glass funnel.

Then, the clay contained in the dialysis bags was dialyzed against approximately 950 mL of the extractant solution in a glass beaker over 3.5 hours. Afterwards, the buffer solution was sampled for ICP-MS and IC analysis and the conductivity of the solution recorded. Dialysis bags were brought into contact with a fresh sodium acetate/glacial acetic acid buffer solution of the same volume, and the dialysis continued over another 43.6 hours. Again, at the end of this dialysis step, the buffer solution was sampled for ICP-MS and IC analysis of metals and salts, and its conductivity measured. This procedure was continued, for a total of four dialysis steps with acetate extractant solutions over various individual dialysis time-frames (3.5, 43.6, 5.7 and 15.2 hours). Then, the buffer solution composition was changed to a 1 M $NaNO_3$ solution in order to bring the clay into its Na-form, again following a similar buffer exchange and sampling procedure. Overall, four buffer exchanges with nitrate solutions were performed using individual dialysis times of 4.4, 4.5, 15.3 and 3.5 hours. Finally, excess salts were removed from the clay by dialysis against Nanopure water over a series of five buffer exchanges with dialysis times of 2.8, 16.7, 2.8, 6.8 and 13.2 hours.

In the next step, the clay was removed from the dialysis bags and re-suspended in Nanopure water. In order to fully re-suspend the solid, the suspensions were sonicated, stirred in glass beakers and shaken up by hand after transfer into 250 mL Corning glass bottles. Then, the clay suspension (2 x 600 mL) was poured into centrifugation liners and centrifuged on a Beckman Avanti J-25 centrifuge at 1000 g over 7 minutes. This centrifugation time was calculated (based on Stokes law) to effectively remove particles of an average particle size > 2 µm from suspension, which is believed to be an appropriate size cut-off for quartz and feldspar impurities. After centrifugation, the supernatant solutions were transferred into glass beakers and dried in a VWR convection oven set at 45 °C , which resulted in a temperature of 42-43 °C inside the oven. The larger size fraction produced in the centrifugation step, which was characterized by a darker sediment color, was discarded. Depending on the beaker size used during drying, the clay suspensions took 6-13 days to reach apparent dryness.

The dried clay was recovered from the glass beakers using Teflon rods. Then, the mineral was milled in 10 mL capsules using a Retsch MM 400 ball mill at a frequency of 30/sec over two minutes. After milling of several clay batches, all of the material was combined in one glass beaker and thoroughly homogenized. Last, a 10 g/L stock suspension was prepared and its exact solid concentration determined by drying as described above.

5.2.3   Batch Sorption Equilibrium Experiments

All batch sorption experiments were set up at room temperature (22.5 – 23.5 °C), with a nominal total U(VI) concentration of 10^{-6} M, a Na-montmorillonite concentration of 0.5 g/L, and a total ionic strength of 0.1 M. Target pH values ranged from 4.0 to 10.0; the sorption equilibration time was set at 48.5 hours. Solutions were equilibrated with three different gas phases varying in terms of their CO_2 partial pressures: (1) atmospheric CO_2 in air (0.039%, 390 ppm), (2) CO_2-free atmosphere (glove box, filled with 93.3% N_2/5.7% H_2 gas mixture) (3) ~1% CO_2 atmosphere (disposable Sigma Aldrich glove bag purged with certified 2% CO_2/balance nitrogen gas mixture; Praxair P/N: NI CD2C-K). In experiments performed under atmospheric or elevated CO_2 levels, additions of sodium bicarbonate buffer were used to facilitate solution equilibration with the gas phase for samples with target pH values of 7.0 or greater. Fifty-mL polycarbonate centrifuge vials ('Oakridge centrifuge tubes') were used as sample vials to minimize U(VI) wall sorption effects. In addition to samples containing Na-montmorillonite and U(VI) (1 replicate per pH condition), each experiment also included experimental standards (in duplicate). These standards represented 100% of the U(VI) solution concentration in the absence of a mineral phase and at pH conditions selected for minimization of wall sorption effects (pH=2). In addition, electrolyte blanks containing 0.1 M NaCl but no U(VI) or solid were used in order to provide blank values (in duplicate) for calcium concentrations.

At the beginning of batch sorption experiments, aliquots of Nanopure water, the Na-montmorillonite stock suspension and a 1M NaCl solution were transferred into sample vials to give the desired solid concentration and ionic strength in the final sample volume of 40 mL. For samples with target pH values at or above 7.0, increasing amounts of 1M or 0.1M $NaHCO_3$ buffer solution were added. Solution pH values were adjusted with small volumes of 1, 0.1, 0.01 and 0.001M HCl or NaOH solutions, and closed sample vials pre-equilibrated with shaking over 12 to 24 hours. On the next day, aliquots of the U(VI) stock solution were added to obtain the final desired concentrations. After re-adjustment of solution pH, U(VI) sorption equilibration was allowed to take place during shaking over 48.5 hours. Afterwards, final pH values were recorded while minimizing gas exchange during the pH measurements. Then, a 13-mL aliquot of the sample suspension was removed by pipetting in order to decrease the liquid mass of the suspensions, and decrease sample centrifugation times. The remaining 27 mL of the sample suspensions were centrifuged to remove >50 nm particles from solution, as calculated based on Stokes law (Beckman Coulter Allegra 64R, F0850 rotor, centrifugation at 26,900 g over 61 minutes). Afterwards, 1.5 mL and 20 mL aliquots of supernatant solution were collected to analyze for metal concentrations by ICP-MS, and carbonate concentrations by Total Inorganic Carbon (TIC) analysis on a Shimadzu TOC-V.

For the correction of U(VI) wall sorption effects, solid phases and remaining sample solutions were discarded, and vials briefly rinsed with UV-water. In the process, some clay was re-mobilized from the container vials by vigorous shaking by hand, or if necessary, by using disposable, plastic transfer pipettes. Sample vials were then filled with 40 mL of 2% nitric acid solutions (TraceSelect grade) in order to facilitate U(VI) desorption from container walls during shaking over approximately 60 hr. Washing solutions were analyzed for concentrations of desorbed U(VI) as described above.

Experimental results for batch sorption envelope experiments are reported in terms of distribution coefficients (K_d values) and fractions of U(VI) sorbed. Distribution coefficients, with units of L/kg, represent the ratio of sorbed (e.g., in mol/kg) over dissolved (e.g., in mol/L) U

concentrations after sorption reaction for 48.5 hours. Sorbed U(VI) fractions were calculated based on concentration differences in supernatant and acid-wash solutions:

$$f_{U(VI)_{sorbed}} = \frac{\left([U]_{Std,supernat.} + [U]_{Std,wash}\right) - \left([U]_{Sample,supernat.} + [U]_{Sample,wash}\right)}{\left([U]_{Std,supernat.} + [U]_{Std,wash}\right)} \times 100\% \qquad (5.1)$$

where $[U]_{supernat.}$ and $[U]_{wash}$ represent U(VI) concentrations in supernatant and acid-wash solutions for standards (subscript *Std*) and individual sample vials (subscript *Sample*) respectively.

5.2.4   Batch Kinetic Experiments

In order to allow for a direct comparison, kinetic studies were also set up at room temperature (22.5 – 23.5 °C), with a nominal total U(VI) concentration of 10^{-6} M and a Na-montmorillonite concentration of 0.5 g/L. All kinetic samples were in contact with atmospheric CO_2 in air (0.039%, 390 ppm). Total ionic strengths were varied between the values of 0.002, 0.01, and 0.1M; pH conditions were set up at target values of pH=5.

In kinetic experiments, U(VI) sorption behavior was characterized as a function of time based on the repeated sampling of the same sample suspension at specified time-points. Hence, larger, initial sample volumes (100 mL) were needed. Furthermore, standard concentrations representing 100% of U(VI) in solution in the absence of a mineral phase were calculated based on direct ICP-MS analysis of 5 µL aliquots of the U(VI) stock solution. No wall sorption corrections were performed in these experiments. However, due to the use of larger suspension volumes and sample vials compared to the batch equilibration experiments, we assume that the total mineral surface area may largely exceed the total surface area of container walls. This would lead to even lower wall sorption effects than observed in batch equilibration experiments.

Kinetic sorption experiments consisted of two main steps: (1) pre-equilibration of U(VI) solutions and Na-montmorillonite suspensions at the specified pH and ionic strength conditions; and (2) time-dependent sorption of U(VI) onto the clay, which is characterized by repeated sampling of sample suspensions. On the first day, we prepared 43.8 mL U(VI)-electrolyte solutions and clay-electrolyte suspensions in 125 mL Nalgene bottles and 50 mL Corning centrifuge tubes, respectively. In the process, we combined Nanopure water with 1M NaCl, and an aliquot of either the U(VI) stock solution or Na-montmorillonite stock suspension. Addition volumes were selected in order to give the desired final concentrations in a total suspension volume of 100 mL. The pH values of solutions were adjusted with small volumes of HCl and NaOH (1, 0.1, 0.01, 0.001M; $V_{pH,1}$ = 3.75 mL). Then, sample vials were set up on a shaking table for pre-equilibration overnight.

On the next day, a second pH check/adjustment was performed ($V_{pH,2}$ = 2.5 mL). Then, the kinetic experiment and recording of time was started by pouring the individual clay suspensions into the Nalgene bottles containing U(VI) solutions at the same pH and ionic strength. After brief mixing of suspensions by hand, four 1-mL volume fractions were transferred into four 2-mL centrifugation vials. (Suspension volumes of 1 mL in 2-mL centrifugation vials were selected in order to minimize the height of liquid levels, sample centrifugation times, and hence, the time-frames needed in between sampling events.) The remaining sample suspensions were set up for sorption equilibration under continuous shaking. Sampled suspensions were centrifuged in order to remove >50 nm clay particles, based on calculations using Stokes law

(Beckman Coulter Allegra 64R, F3602 rotor, 11 minutes at 26,000 g / 16,335 rpm). After centrifugation, two 0.75 mL supernatant fractions were combined twice to give two 1.5-mL sample solutions for ICP-MS analysis.

After sampling the first time-point, basically the same sampling/centrifugation procedure was followed for the rest of the kinetic experiment. However, for the remaining time-points only one 1.5 mL ICP-MS sample was created per sampling event. In addition, the same procedure was applied to collect supernatant solutions for TIC analysis on the first and last day of the kinetic experiment. TIC measurements allow us to determine if potential changes in dissolved carbonate concentrations occurred over time. Last, the pH-values of sample suspensions were determined every couple of days in order to monitor for any potential pH-shifts over the course of the experiment.

5.3   Results and Discussion

5.3.1   Clay Pretreatment

An overview of the conductivity measurements over the course of dialysis steps using different types of buffer solutions is given in Figure 5.1. In the following figures, all of the measurements represent values determined in buffer solutions at the end of individual dialysis steps; the switching to different, initial buffer solution compositions, from Na-acetate/acetic acid to sodium nitrate and Nanopure water, are indicated by dashed lines in the diagrams. First, conductivity measurements (Figure 5.1) show fairly constant values for the dialysis steps with extractant and 1 M $NaNO_3$ solutions. This is followed by a sharp drop with the use of Nanopure water as dialysis buffer, and is continued with increasingly lower conductivity values due to the repeated exchange of Nanopure water (lowest conductivity value measured: 151 µS/cm). For comparison, the fractions of Na, acetate and nitrate remaining in the buffer solutions over time (Figure 5.2) show similar trends. Hence, conductivity measurements are a useful tool to monitor clay dialysis in 'real-time'. In addition, the dialysis procedure appears to effectively remove excess salts from the pretreated clay.

Furthermore, Ca solution concentrations in the extractant buffer solutions during Ca removal steps are shown in Figure 5.3. These measured concentrations were further used in a mass balance calculation in order to estimate (1) the efficiency of the Ca removal process, and (2) the maximum Ca concentrations potentially released from pretreated Na-montmorillonite in later batch sorption experiments. In this calculation, we used the CaO content provided for SWy-2 by the Clay Minerals Society (1.68% (w/w)), and assumed a solid concentration of 0.5 g/L in batch experiments. We determined that the Ca purification steps removed 84.8% of total Ca found in the original Source Clay material. Furthermore, maximum Ca solution concentrations in batch sorption experiments were estimated at 2.3 x 10^{-5} mol/L. Actual measurements of calcium concentrations released over the course of batch sorption envelope experiments are provided in the "Results and Discussion" section for batch sorption equilibrium experiments. Overall, Ca concentrations measured in batch experiments agree well with the upper limit estimated based on mass balance considerations. Furthermore, our data indicate that Ca concentrations released from the clay in batch sorption experiments are not high enough to affect U(VI) solution speciation in terms of the formation of ternary U(VI)-Ca-carbonato species in these systems.
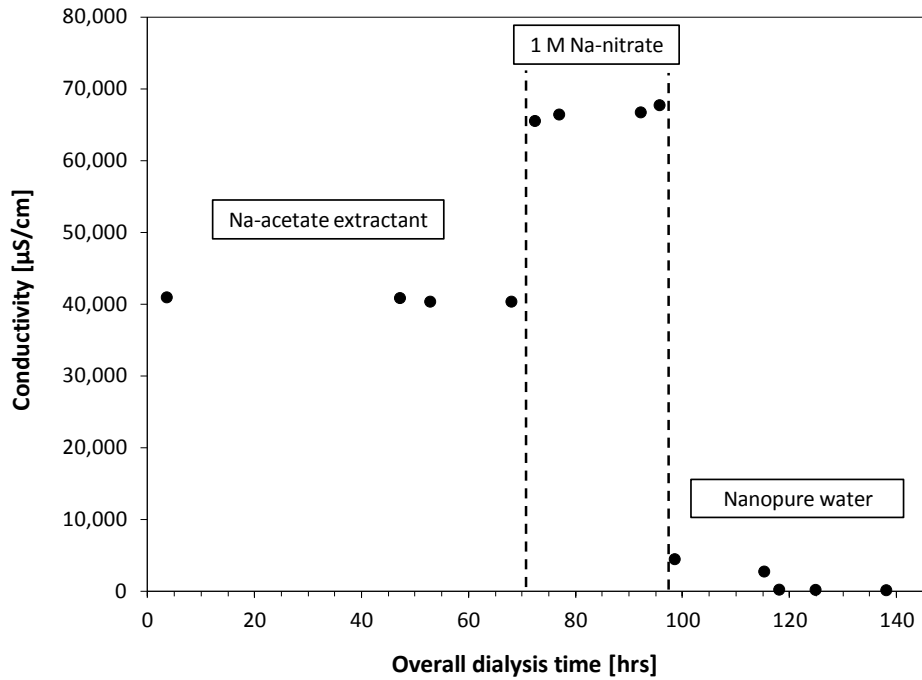
Figure 5.1. Results of conductivity measurements of dialysis buffer solutions over the course of clay pretreatment steps. (Dashed lines indicate changes in buffer compositions.)
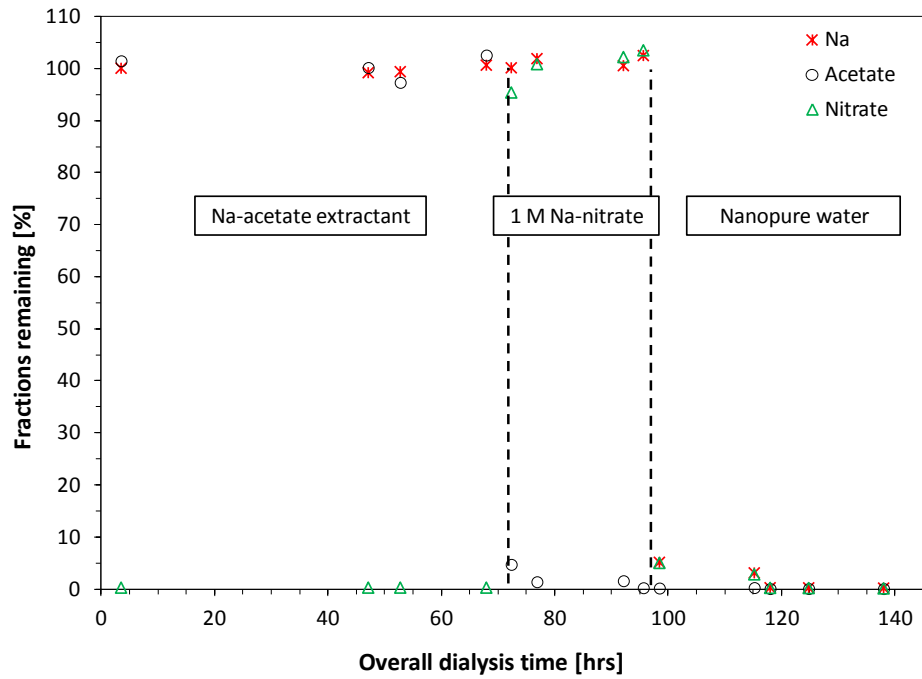
Figure 5.2. Fractions of sodium (Na), acetate and nitrate remaining in dialysis buffer solutions over the course of clay pretreatment.
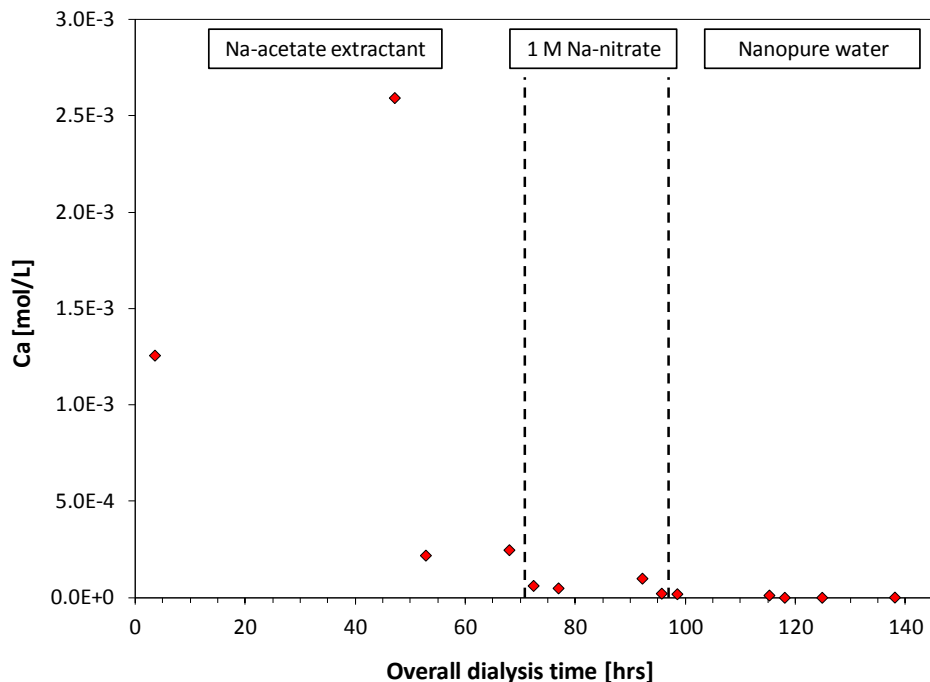
Figure 5.3. Calcium concentrations measured in dialysis buffer solutions over the course of clay pretreatment.

5.3.2   Batch Sorption Equilibrium Experiments

The results from the batch U(VI) sorption equilibrium experiments will be the basis for the development of U(VI)-montmorillonite surface complexation models. They provide important input parameters in terms of total and dissolved U(VI), dissolved inorganic carbon (TIC), and calcium concentrations, equilibrated with the mineral phase at various pH conditions and partial pressures of $CO_2(g)$. In the following, we describe and compare the data for all experiments in terms of uranium, TIC and Ca concentrations. Throughout this report, error bars for ICP-MS and TIC data represent 95% confidence intervals of analytical errors.

5.3.2.1   Uranium(VI) Sorption

In Figs. 5.4 to 5.6, U(VI) sorption onto Na-montmorillonite is illustrated for three different CO_2 gas compositions: (1) atmospheric CO_2 (0.039% CO_2), (2) CO_2-free atmosphere, and (3) ~1% CO_2 atmosphere. Each figure describes U(VI) sorption data in terms of percent U(VI) sorbed (primary y-axis) and log K_d values (secondary y-axis). In addition, in Figures 5.7 and 5.8, all U(VI) sorption data are shown for visual comparison; Table 5.1 provides a detailed overview of all values.

94
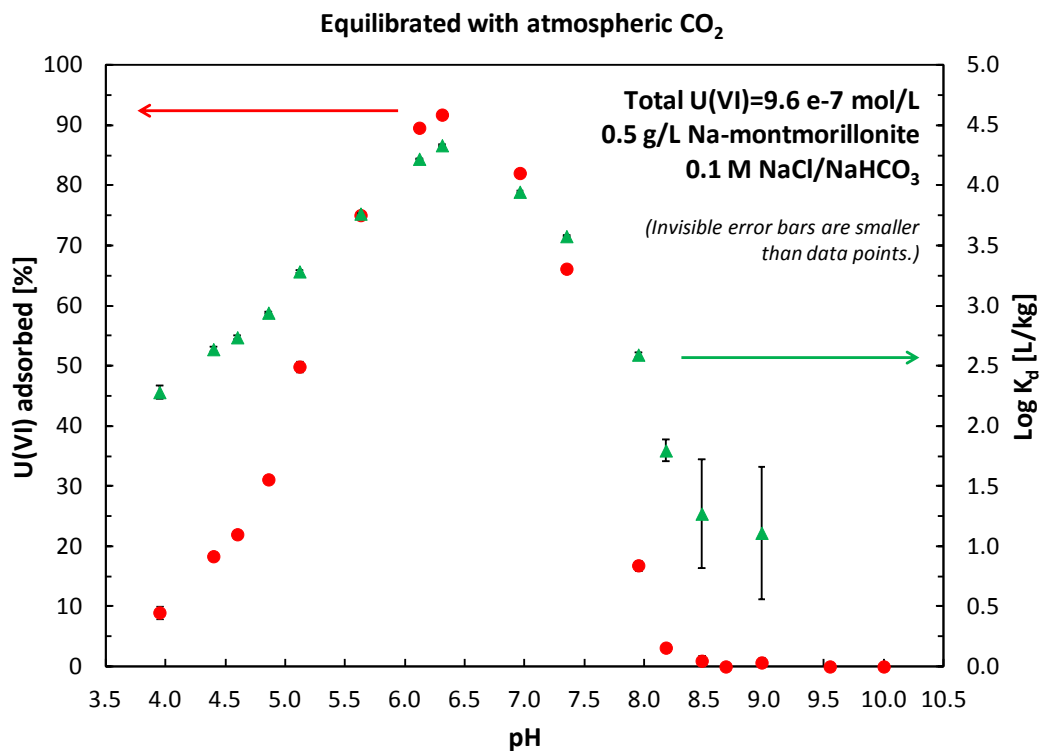
Figure 5.4. U(VI) adsorption onto Na-montmorillonite under atmospheric CO₂ conditions.
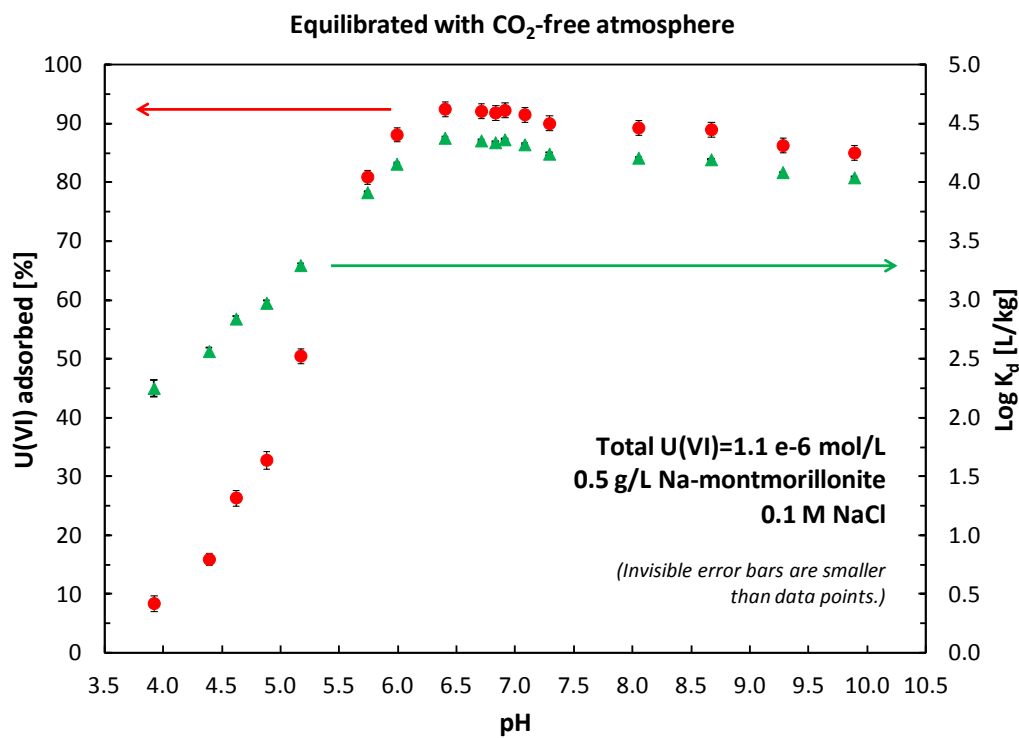
Figure 5.5. U(VI) adsorption onto Na-montmorillonite under an atmosphere free of CO₂ and O₂ gases.
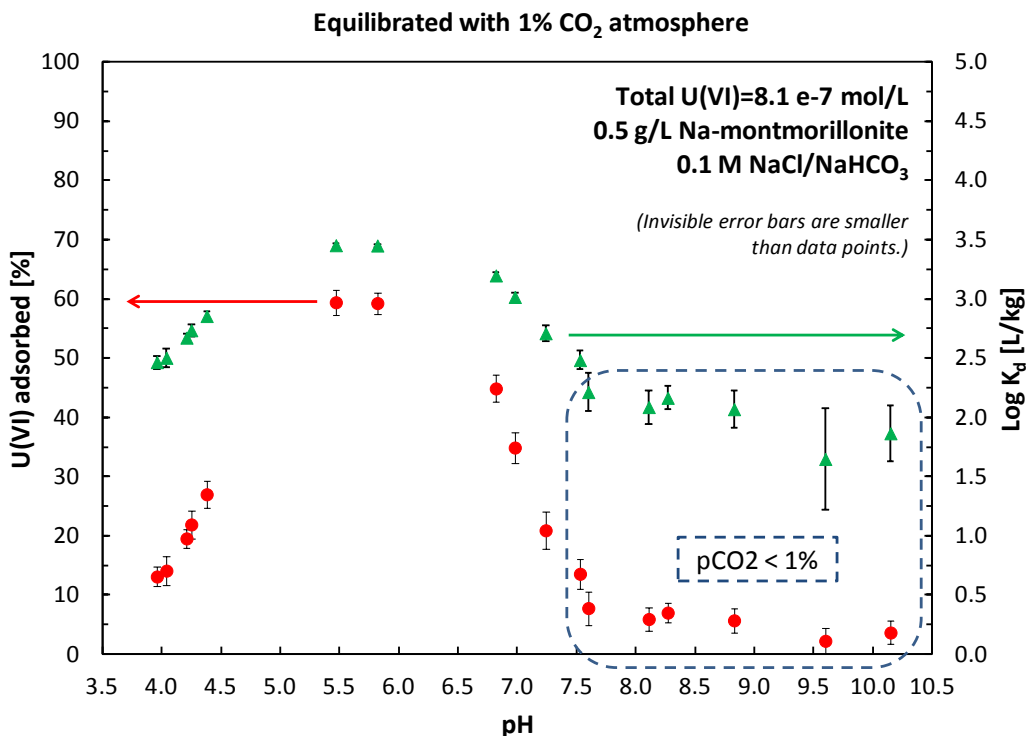
Figure 5.6. U(VI) adsorption onto Na-montmorillonite after equilibration with a ~1% CO$_2$ atmosphere.

Table 5.1. Summary of U(VI) adsorption data in batch sorption envelope experiments

Atmospheric CO$_2$				CO$_2$-free atmosphere				~1% CO$_2$ atmosphere			
Final pH	U(VI) sorbed	Kd	log Kd	Final pH	U(VI) sorbed	Kd	log Kd	Final pH	U(VI) sorbed	Kd	log Kd
[ ]	[%]	[L/kg]	[L/kg]	[ ]	[%]	[L/kg]	[L/kg]	[ ]	[%]	[L/kg]	[L/kg]
3.95	8.98	191	2.28	3.92	8.46	179	2.25	4.04	14.09	318	2.50
4.40	18.33	434	2.64	4.39	15.96	367	2.57	3.96	13.10	292	2.47
4.60	21.98	545	2.74	4.62	26.42	695	2.84	4.21	19.53	470	2.67
4.86	31.10	874	2.94	4.88	32.83	946	2.98	4.25	21.89	543	2.73
5.12	49.86	1,925	3.28	5.17	50.54	1,978	3.30	4.38	26.99	715	2.85
5.63	75.04	5,820	3.76	5.74	80.98	8,239	3.92	5.47	59.41	2,833	3.45
6.12	89.57	16,624	4.22	5.99	88.15	14,403	4.16	5.82	59.27	2,817	3.45
6.31	91.75	21,533	4.33	6.40	92.52	23,945	4.38	6.82	44.86	1,575	3.20
6.96	82.05	8,845	3.95	6.71	92.15	22,712	4.36	6.98	34.88	1,037	3.02
7.35	66.13	3,780	3.58	6.83	91.89	21,917	4.34	7.24	20.91	512	2.71
7.95	16.82	391	2.59	6.91	92.30	23,211	4.37	7.53	13.56	304	2.48
8.18	3.13	63	1.80	7.08	91.58	21,049	4.32	7.60	7.77	163	2.21
8.48	0.95	19	1.27	7.29	90.06	17,528	4.24	8.11	5.92	122	2.09
8.68	n.d.	n/a	n/a	8.05	89.33	16,212	4.21	8.27	7.01	146	2.16
8.98	0.66	13	1.11	8.67	89.03	15,703	4.20	8.83	5.70	117	2.07
9.55	n.d.	n/a	n/a	9.28	86.32	12,216	4.09	9.60	2.24	44	1.65
10.00	n.d.	n/a	n/a	9.89	85.07	11,027	4.04	10.15	3.64	73	1.86

Under atmospheric CO$_2$ conditions, U(VI) sorption onto Na-montmorillonite is characterized by relatively low sorption in low and high pH regions, and a sorption maximum at around pH 6.3 (Figure 5.4). At low pH, U(VI) sorption is assumed to be limited due to its competition with protons for the same reactive surface/ion exchange sites (Stumm, 1992). At high pH, low uranium sorption is attributed to increasing carbonate concentrations leading to weakly or non-

sorbing aqueous U(VI)-carbonato complexes (Davis et al., 2004; Hsi and Langmuir, 1985). Highest and lowest U(VI) K_d values ranged from K_d = 21,533 L/kg (92% U(VI) sorbed) at pH=6.3 to K_d = 13 L/kg (0.7% U(VI) sorbed) at pH=9. At pH=4, the K_d value was determined at 191 L/kg (9% U(VI) sorbed). Hence, under atmospheric CO_2 conditions, U(VI)-montmorillonite distribution coefficients vary over three orders of magnitude as a function of pH.

In CO_2-free systems (Figure 5.5), the shape of the U(VI) batch sorption envelope is different compared to the atmospheric CO_2 system. In the low-pH region, U(VI) sorption characteristics remain similar with comparable K_d values in the pH range from 4 to 6. Above pH 7, however, U(VI) sorption is much stronger in the absence of CO_2. The increase in U(VI) sorption at high pH values is attributed to the lack of aqueous U(VI)-carbonato complexes in the $N_2(g)$ environment. As a result, K_d values varied from a lowest value of 179 L/kg (8.5% U(VI) sorbed) at pH = 3.9 to a high of 23,945 L/kg (93% U(VI) sorbed) at pH = 6.4. From pH = 6.7 to pH = 9.9, K_d values decreased only by a factor of around 2 (from 22,712 to 11,027 L/kg).

The effect of carbonato solution complexes on U(VI) sorption characteristics is also demonstrated by U(VI) sorption results for the system with elevated CO_2 concentrations (~1% CO_2 atmosphere). In this case, the shape of the sorption envelope is similar to the one determined under atmospheric carbon dioxide conditions. However, U(VI) sorption decreased at pH values greater than 5.8 (K_d = 2,817 L/kg, 59% U(VI) sorbed). Due to an error in the experimental set up and problems with a disposable glove bag, only solutions up to a pH of 7.24 were equilibrated with the ~1% CO_2 atmosphere; solutions at higher pH values had lower inorganic carbon concentrations than would be expected for a 1% atmosphere (for details, see TIC results). Hence, only the experimental data points up to pH = 7.24 were included in the visual comparison (Figures 5.7 and 5.8). However, it can be assumed that at ~1% CO_2, U(VI) sorption would be similar or lower at the higher pH value, again due to the influence of carbonate solution species. The experiment with the 1% CO_2 atmosphere is being repeated to overcome the experimental error.

5.3.2.2   Uranium Wall Sorption

A comparison of U(VI) sorption onto container wall surfaces was determined for all three types of batch sorption experiments in Figure 5.9. In general, U(VI) wall sorption was low, with less than 2% of the total U(VI) solution concentrations lost onto container walls. U(VI) wall sorption exhibits a similar pH dependence to U(VI) sorption on montmorillonite under atmospheric CO_2 conditions. Interestingly, the data from the ~1% CO_2 experiment suggest that higher amounts of U(VI) were sorbed onto container walls at elevated carbonate concentrations.

5.3.2.3   Total Inorganic Carbon (TIC)

A comparison of TIC data for all types of batch sorption envelope experiments is provided in Figure 5.10. The TIC results for the experiment performed under atmospheric CO_2 conditions generally follow the values expected from the literature. For the CO_2-free glove box experiment, we see a slight increase in TIC concentrations with increasing pH. This is an indication that the glove bag is not able to exclude carbon dioxide completely; however, CO_2 contamination was fairly minor.
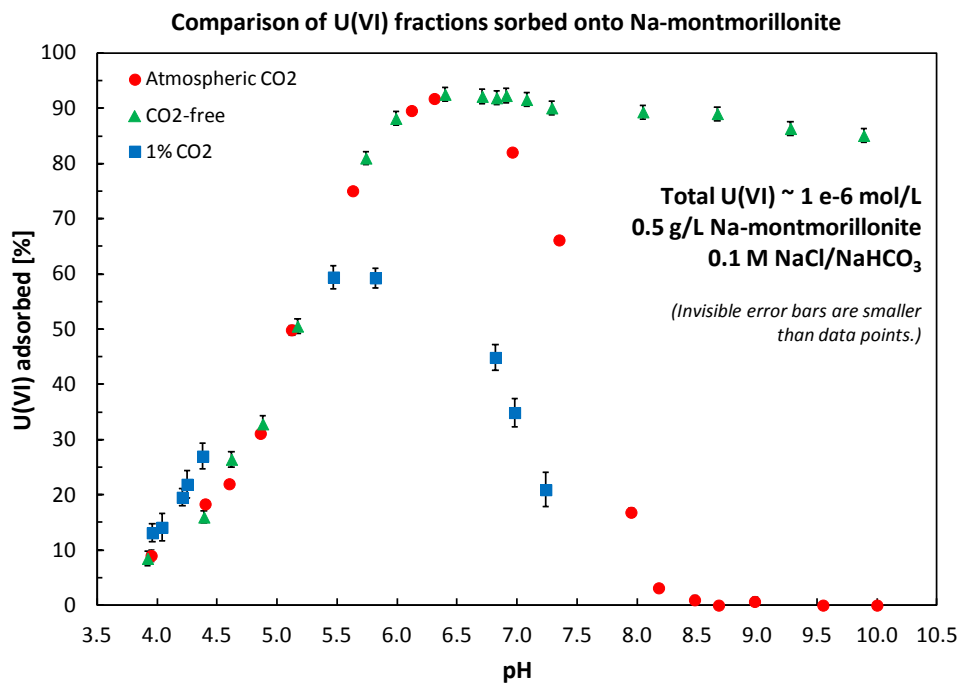
Figure 5.7. Comparison of U(VI) sorbed onto Na-montmorillonite in batch sorption equilibrium experiments.
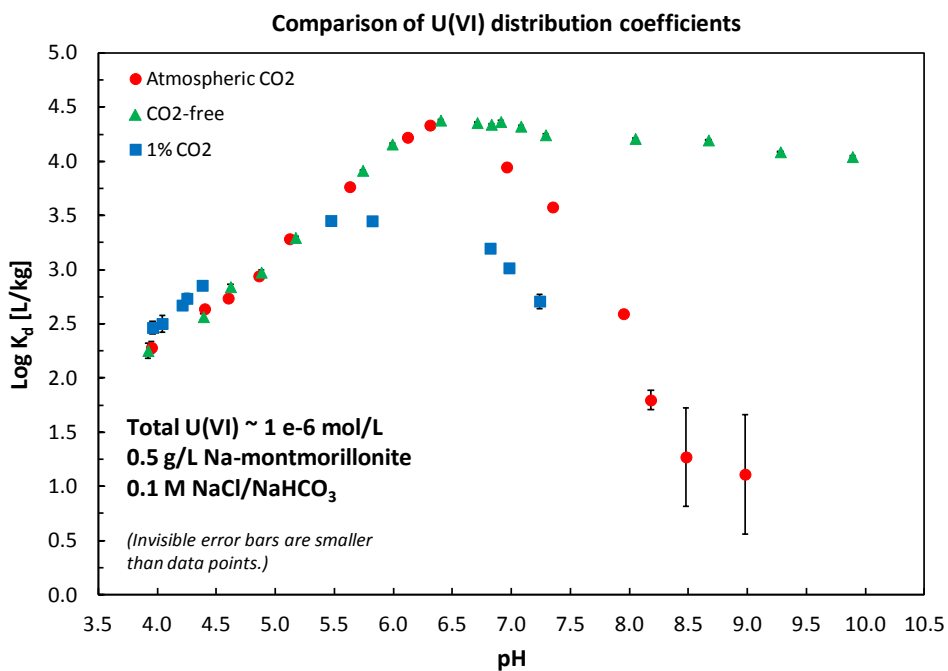
Figure 5.8. Comparison of U(VI)-montmorillonite K_d values determined in batch sorption equilibrium experiments.
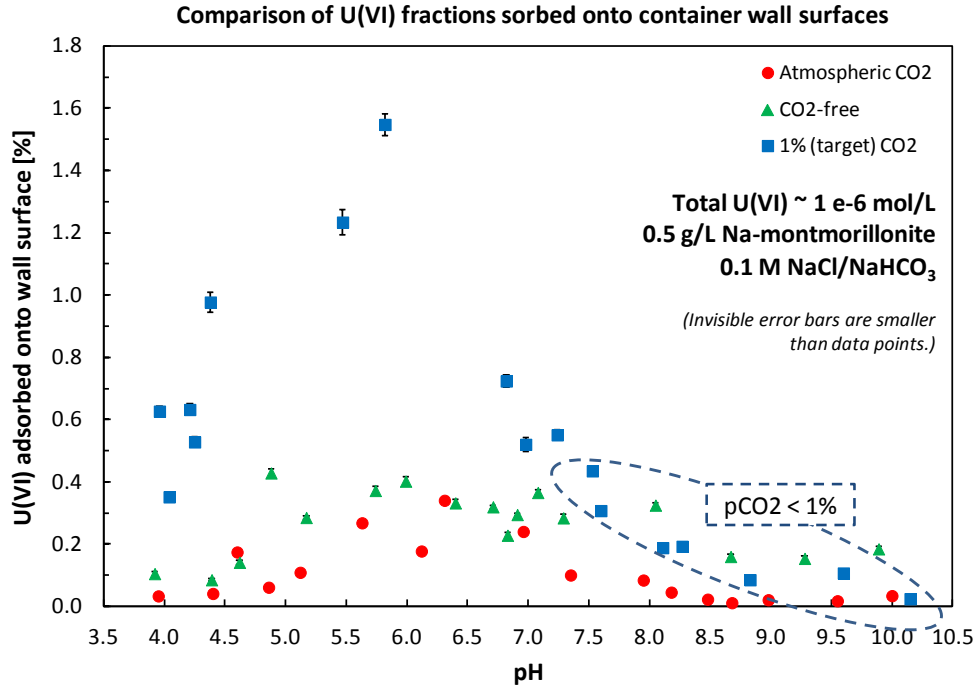
Figure 5.9. U(VI) container wall sorption determined in batch sorption envelope experiments.
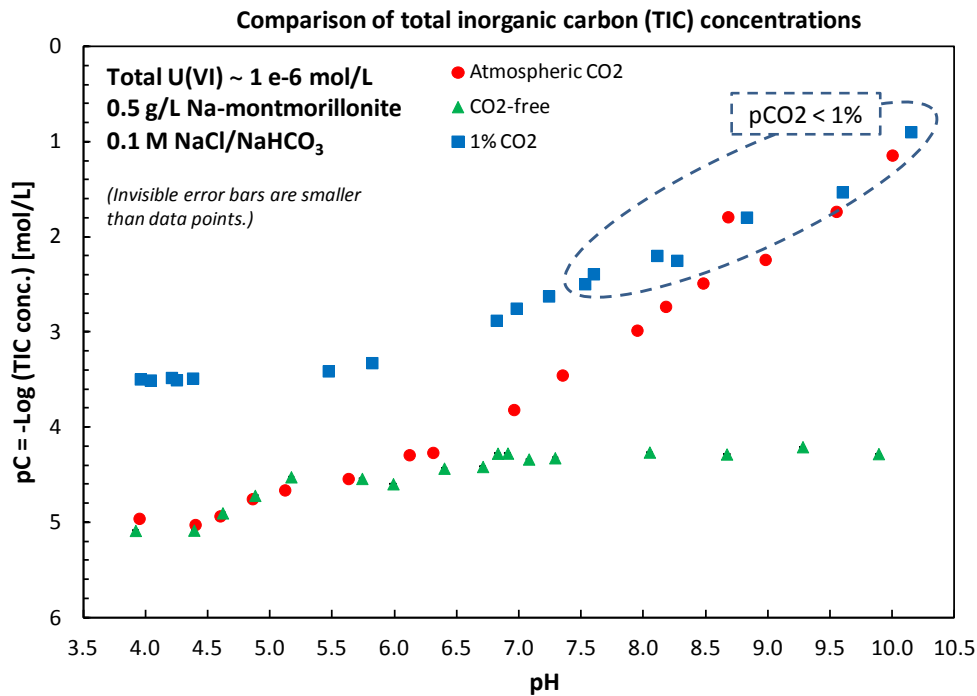
Figure 5.10. Total inorganic carbon (TIC) concentrations measured in batch sorption envelope experiments.

For the experiment set up at elevated (2%) CO_2, the TIC results suggest some experimental problems. Using these data, we back-calculated the atmospheric CO_2 concentrations equilibrated with the measured total carbonate concentrations in solution. We determined that solutions up to a pH of 7.24 were equilibrated with ~1% CO_2, while solutions at higher pH values showed lower dissolved carbonate contents than expected. First, this indicates that the purging of solutions and of the disposable glove bag with 2% CO_2/N_2 gas was insufficient. In addition, it was found that the amounts of sodium bicarbonate buffer added to solutions at higher target pH values were not high enough. Based on these results, the latter data points were excluded from comparisons of U(VI) sorption data determined in other carbon dioxide environments (Figures 5.7 and 5.8). However, data points in the lower pH region are still representative for a 1% CO_2 atmosphere.

5.3.2.4 *Calcium*

Total calcium concentration data are shown in Figure 5.11, and as Ca released from the clay mineral in Figure 5.12. The latter was calculated based on the subtraction of Ca contents in blanks containing no mineral phase. Blank values ranged from 42 to 109 µg/L Ca in the experiments, and contributed between 5.6% and 25% of total Ca concentrations in solution. The addition of sodium bicarbonate buffer solutions at elevated pH values may also slightly add to Ca background concentrations. For instance, if we assume that the degree of purity of $NaHCO_3$ given by the manufacturer (99.998%) is accurate, and all buffer impurities are due to Ca, the buffer addition to a pH = 10 sample at atmospheric CO_2 levels would increase the Ca background by around 3×10^{-6} mol/L Ca (128 µg/L Ca). Hence, Ca background concentrations in the added $NaHCO_3$ buffer cannot fully explain the increase in Ca levels with higher pH values. Instead, this trend may indicate that carbonate ligands in solution may enhance Ca release from the clay mineral. This hypothesis is further supported by lower Ca concentrations found in solutions in contact with atmospheric/CO_2-free gas phases in comparison to the Ca levels found in solutions in contact with the ~1% CO_2 atmosphere. Overall, in these systems the determined Ca background concentration levels are not high enough to affect U(VI) solution speciation in terms of the formation of ternary U(VI)-Ca-carbonato solution complexes. Typical Ca concentrations with relevant effects on U(VI) speciation are at millimolar concentrations (Fox, et al., 2006).

100
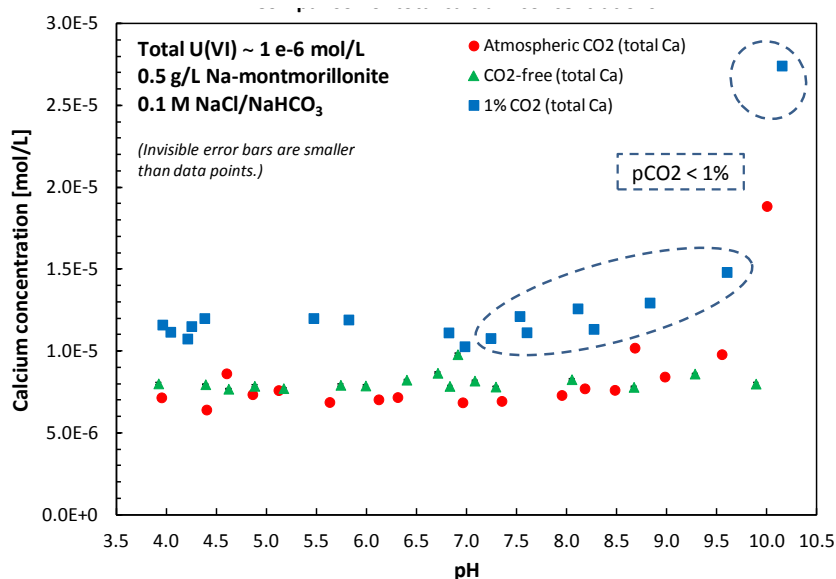
Figure 5.11. Total calcium concentrations measured in U(VI) batch equilibrium experiments.
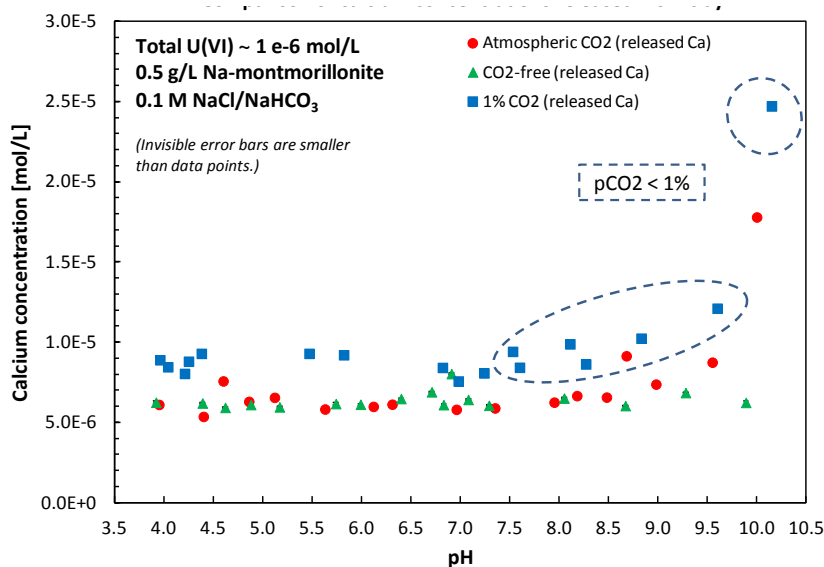
Figure 5.12. Ca concentrations released from Na-montmorillonite in batch experiments, corrected for background Ca.

5.3.3   Batch Sorption Kinetic Experiments

In experiments conducted at a (target) pH value of 5.0, U(VI) shows an initial fast uptake, followed by slower sorption kinetics (Figure 5.13). As a result, U(VI) K_d values (Figure 5.14) slightly increase over time. For instance, for an ionic strength of 0.002 M, K_d values increased from 12,700 L/kg (2 days) to 23,100 L/kg (13 days), for I=0.01 M, from 8,350 L/kg to 10,200 L/kg, and for I=0.1 M from 1,710 L/kg to 2,480 L/kg. Hence, distribution coefficients determined at sorption equilibration times of 2 days are slightly lower than those determined under full steady-state conditions. Furthermore, it appears that these slower, long-term sorption processes may be affected by the ionic strength conditions in sample solutions. Increasing ionic strength seems to cause slower overall sorption reactions in comparison to lower salt contents. However, based on the data depicted in Figures 5.13 and 5.14, the potential influence of ionic strength on U(VI) sorption kinetics is difficult to judge.

Figure 5.15 shows the results normalized to the final values of U(VI) surface concentrations reached in kinetic experiments, assuming for now that these concentrations represent steady-state values. Assuming pseudo-first order reversible sorption kinetics and constant chemical conditions, two systems should show the same kinetic sorption behavior if they reach their individual equilibrium surface concentrations at the same rate (Espenson, 1995). In other words, systems with the same pseudo-first order sorption kinetics show the same fractional approach to equilibrium at any given point in time, independent of the individual equilibrium surface concentrations reached. Typically, reaction kinetics are compared between systems using a 'characteristic time' where 50% of equilibrium concentrations have been approached (Espenson, 1995; Stone and Morgan, 1990). However, due to the fast sorption rates observed for the lowest ionic strength conditions, we decided to evaluate potential differences in U(VI) sorption kinetics due to ionic strength for time-points where 95% of the U(VI) equilibrium surface concentrations have been reached. The 95% limit is indicated as a horizontal, green line in Figure 5.15. Based on this interpretation, the time-frames needed to the reach the same fraction of the U(VI)

101

sorption equilibrium is longer with increasing ionic strength, given that other chemical conditions were constant. Figure 5.16 illustrates that dissolved inorganic carbon remained fairly constant throughout the experiments. On the other hand, pH values seemed to consistently increase in all samples over time (Figure 5.17). In the near future, we will use surface complexation modeling as a tool to determine if these pH changes had a significant impact on the kinetic behavior observed.

The results suggest the possibility that different sorption mechanisms were dominant at various ionic strength conditions. For instance, it might be possible that at low ionic strength (fast) ion exchange reactions drive the overall sorption kinetics at pH 5 (McKinley et al., 1995). At higher ionic strengths, surface complexation reactions at clay edge sites might gain importance due to the increased competition between U(VI) ions and other cations for ion exchange sites. Therefore, (possibly slower) surface complexation reactions may become more and more relevant under these conditions. However, other explanations for this behavior are also possible, and will be evaluated in further detail in the future.
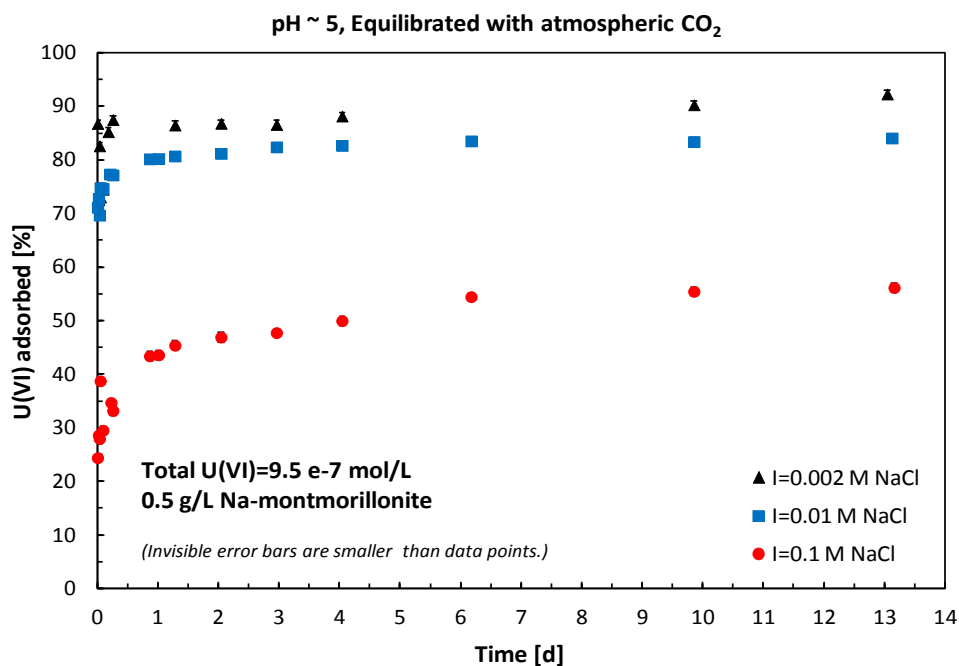
Figure 5.13. U(VI) sorption as a function of time at pH=5, equilibrated with air.
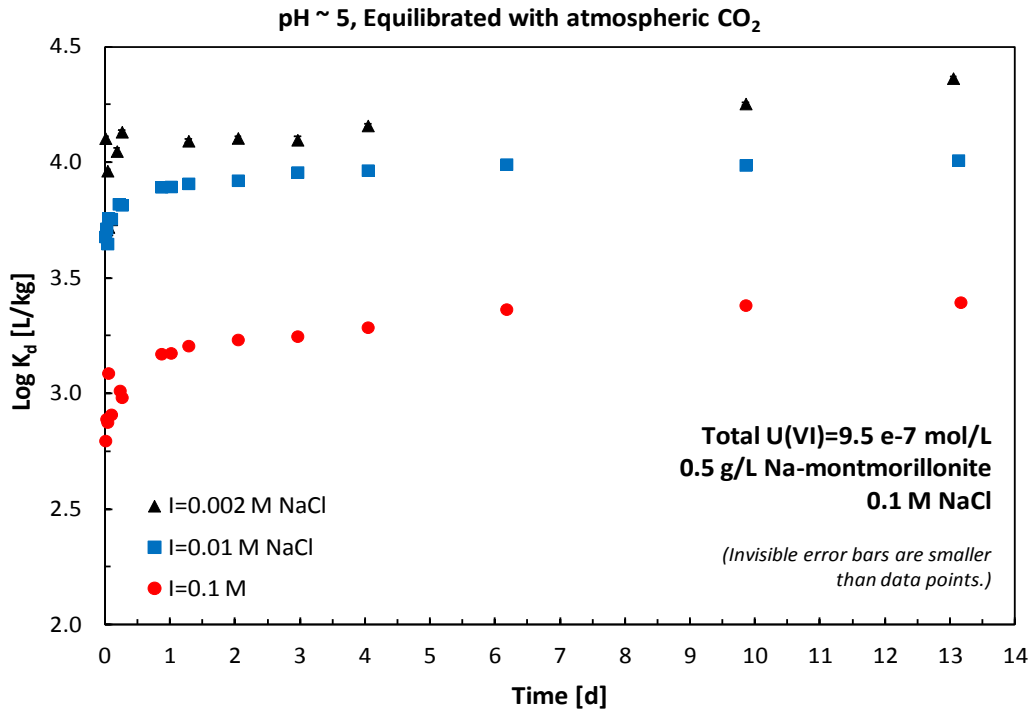
Figure 5.14. U(VI) K$_d$ values with time at pH=5, equilibrated with air.
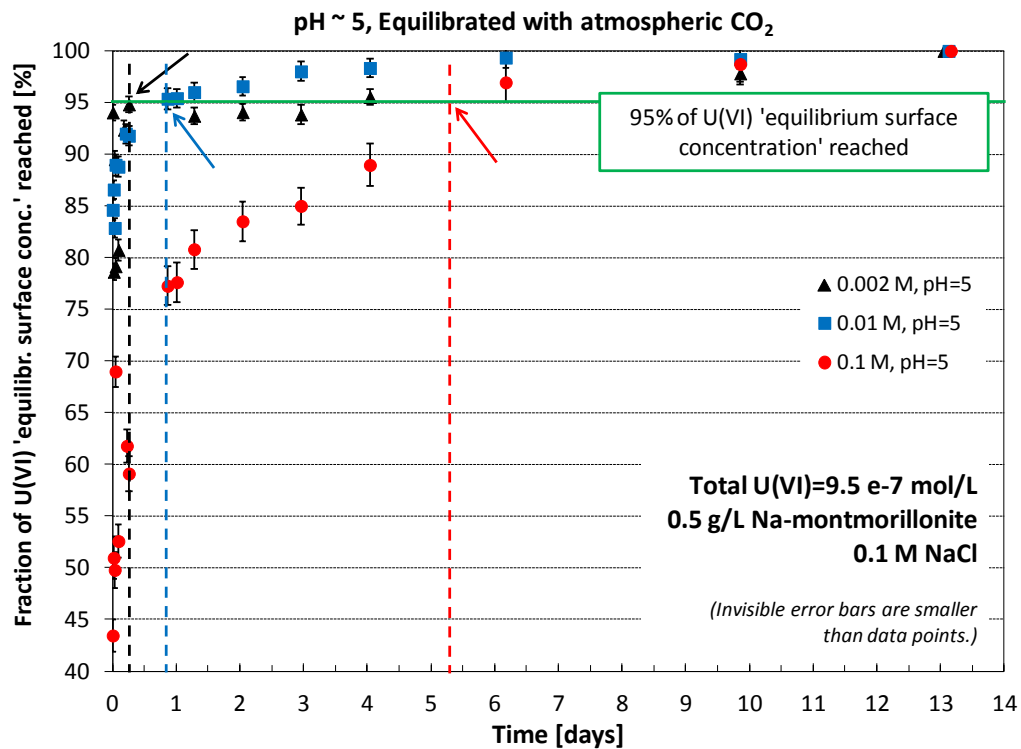
Figure 5.15. Fractional approach to equilibrium for U(VI) sorption at pH 5. The 95%-fraction of U(VI) surface concentrations is reached at each ionic strength when the series of experimental data points crosses the green horizontal line.
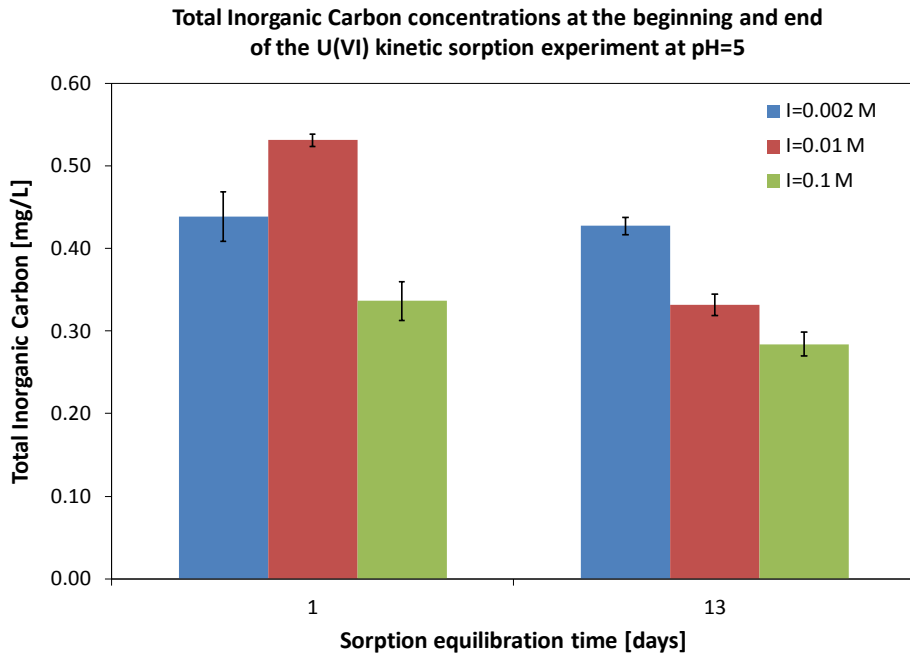
Figure 5.16. Dissolved inorganic carbon concentrations at the beginning and end of the U(VI) kinetic experiments at pH 5 in air.
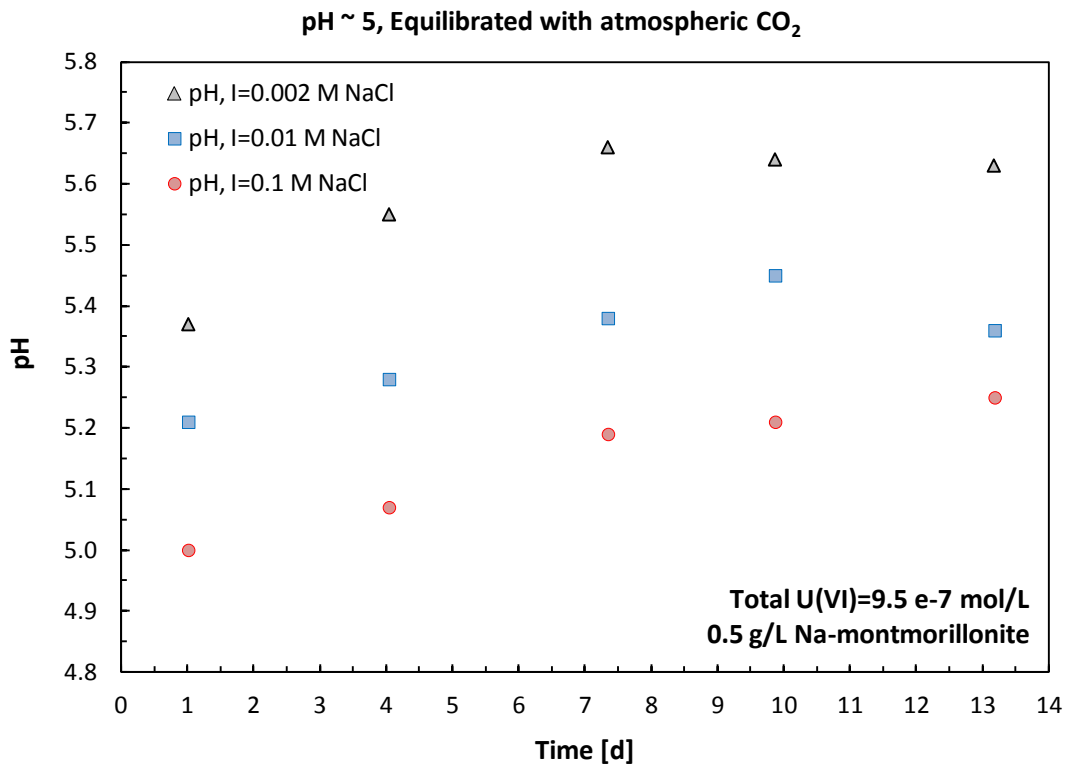
Figure 5.17. pH as a function of time in the U(VI) sorption experiments near pH 5 in air.

5.3.4   Surface Complexation Modeling

Preliminary surface complexation models have been developed to describe the experimental data as a function of chemical composition that are presented above. There are alternative approaches, depending on the type of electrical double layer model that is used as part of the surface complexation model. These results are an important step forward but were considered too preliminary to present at this stage.

5.4   Summary and Conclusions

Experimental studies of U(VI) sorption on montmorillonite show that K_d values are highly dependent on the values of pH and bicarbonate concentration. We also expect that the values will be highly sensitive to the Ca concentration, based on work by Fox et al. (2006). In current models for radionuclide diffusion through bentonite in an engineered barrier, the apparent and effective diffusion coefficients are linked through the K_d value, which is often believed to be a constant value for a particular radionuclide. In the case of U(VI), this is less likely to be true because of the very high sensitivity of the K_d value to pH, and bicarbonate and calcium concentrations. It should be noted that the waste forms, and possibly concrete in the vicinity of an EBS, are likely to create gradients in these chemical variables within the EBS. Because of this, it is important to represent U(VI) partitioning within an EBS with a surface complexation model rather than a constant K_d value.

Furthermore, in many diffusion studies that have been conducted, the chemistry of the diffusing ion (or neutral species) has been extremely simple, e.g., Cl^-, tritium. This is also true for cations, e.g. Cs^+, Sr^{2+}, which primarily bind to montmorillonite at ion exchange sites located in the interlamellar space within the mineral structure. Binding at these sites is substantially affected by compaction. However, binding of U(VI) is dramatically different from these cations. Although UO_2^{2+} can bind to ion exchange sites at low pH and low ionic strength, it should be expected that under field-relevant conditions for an EBS U(VI) will bind to montmorillonite primarily by surface complexation at edge sites. It is unknown how this type of binding will affect U(VI) diffusion when montmorillonite is compacted.

In FY12, uranium(VI) sorption onto purified, Na-montmorillonite was studied in 0.1M NaCl solutions as a function of pH in systems equilibrated with $N_2(g)$, air, or a 98%/2% N_2/CO_2 gas mixture. K_d values for U(VI) sorption onto bentonite equilibrated with air ranged from 13 L/kg at pH 9.0 to 21,500 L/kg at pH 6.5. At pH 4, the K_d value was 191 L/kg. For systems equilibrated with $N_2(g)$, the K_d values were approximately the same as in air in the pH range 4-6, but had much higher values in the range pH 7-9. The reason for the higher pH values was the lack of aqueous U(VI)-carbonate complexes in the pure $N_2(g)$ environment, which are more weakly adsorbed than the $UO_2(OH)_2(aq)$ species. For systems equilibrated with a CO_2 partial pressure of ~1%, K_d values were much lower than in air in the pH range 6-8 because of higher concentrations of the aqueous U(VI)-carbonate complexes.

6.   OVERALL SUMMARY

Bentonite and bentonite-sand mixtures have been found to have favorable properties for use as a backfill/buffer material for nuclear waste repositories. This report focuses on analyses of bentonite as a component of the EBS. Specific analyses presented here highlight progress made in areas of THM coupled processes models, reactive transport models, and reactive transport experiments for bentonite. These research activities address key Features, Events and Processes (FEPs) with rankings from medium to high, as listed in Tables 7 and 8 of *Used Fuel Disposition Campaign Disposal Research and Development Roadmap* (FCR&D-USED-2011-000065 REV0) (Nutt, 2011).

6.1   THM Process Modeling in Bentonite

We are developing and applying coupled THMC models for the analysis of EBS coupled processes in bentonite-backfilled repositories. This activity addresses FEP 2.2.01, Excavation Disturbed Zone (EDZ), for shale by investigating the effects of coupled processes on interactions between shale (clay) disposal formations and the EBS; FEPs 2.1.04.01, Buffer/Backfill; FEPs 2.1.07.02, 03, 04, 09, Mechanical Processes; FEPs 2.1.08.03, 07, 08, Hydrologic Processes; and FEP 2.1.11.04, Thermal Processes, by studying coupled processes in the EBS. In FY11, we developed an advanced modeling capability by implementing the Barcelona Basic Model into the TOUGH-FLAC simulator. In FY12, we have further improved our modeling capability and initiated a modeling validation study using international data sets. Our FY12 accomplishments for this activity include:

- We expanded the Barcelona Basic Model to a dual-structure model for expansive clay, such as bentonite. We have implemented a dual-structure model and are currently testing and verifying this implementation against published numerical modeling and experimental data. The next step will then be to link the dual-structure model with diffuse double layer theory for the coupling between chemistry and mechanics resulting in a coupled THMC model for the analysis of the long-term EBS behavior.

- We have initiated the work on the modeling of the HE-E heater test along with our participation in the DECOVALEX project. The first phase will involve modeling of a previous HE-D heater test for calibration and validation of the rock mass model related to THM processes under heating of the Opalinus clay.

In the remaining months of FY12, we will

- Complete testing and documentation of dual-structure model.

- Perform Mont Terri HE-heater test modeling along with DECOVALEX schedule in FY12:
  - Final Task description to be delivered to research teams in June.
  - Modeling previous Mont Terri rock mass HE-D heater test for calibration of THM rock properties (until October 2012).

- Link dual-structure model with diffuse double layer theory for the development of THMC EBS model.

- Test THMC model against laboratory experiments (e.g. swelling under different salinity).

For FY13, we propose to conduct

- Mont Terri HE-heater test modeling along with DECOVALEX schedule in FY13

- Buffer material study of THM experimental data provided by DECOVALEX to determine and calibrate buffer properties (until October 2013)

- Dual-structure material modeling of FEBEX mock-up test

- Application of new THMC model for generic repository cases

6.2   Modeling Reactive-Diffusive Transport in Bentonite

The focus of this activity has been on developing rigorous and yet practically useful approaches to modeling diffusive process in bentonite. This activity addresses Features, Events and Processes (FEPs), FEPs 2.1.04.01, Buffer/Backfill; and FEPs 2.1.09.52, 53, 54, Chemical Processes—Transport by investigating reactive-diffusive radionuclide transport in bentonite. Our FY12 accomplishments include:

- We have improved the DDL modeling capability based on the Donnan equilibrium or mean electrostatic approach. It allows for calculating a DDL thickness (or volume) using ionic strength.

- We have developed an improved model involving the coupling of the PNP set of equations with a suitable surface complexation model as an attempt to advance our capability in modeling diffusion processes in clay. The corresponding code is calibrated against previously provided benchmarks and an example 2D simulation of the electrical potential field is shown for the case in which charged clay surfaces modify the result. The good agreement we have achieved with available experimental data supports the usefulness of our model. In addition, the present study has served to reconcile the theory of the Poisson–Boltzmann equation with seemingly conflicting experimental evidence of non-zero anion concentrations found in highly compacted clays, by making use of the theory of fractals. If proved suitable, that would have relevant implications in the process of upscaling results from the nano- up to macro-scales, based on the self-similarity of the fractal structure of clays.

In the remaining months of FY12, we will:

- Complete implementation of multicomponent Poisson-Boltzmann equation in new finite element code.

- Test against full range of Van Loon et al (2007) diffusion data for model validation.

For FY13, we propose to

- Complete implementation of multicomponent Poisson-Boltzmann Equation in general purpose reactive transport simulator.

- Use mean electrostatic and Poisson-Boltzmann models to simulate Fernández and Mäder (2011) experiments involving flow and transport through clay

- Use mean electrostatic and Poisson-Boltzmann models to simulate the experiments on uranium sorption and transport conducted in Section 5.

- Introduce calculations of the swelling pressure based on both the Poisson-Boltzmann and mean electrostatic (Donnan) approach.

6.3 Molecular Dynamics Prediction of Nanopore-Scale Diffusion Coefficients

The objective of our MD simulations is to develop the capability (based on first principles) to predict the temperature dependence of water and solute diffusion coefficients (D) in clay interlayer nanopores, considering that EBS is subject to substantial temperature variations. This activity addresses Features, Events and Processes (FEPs), FEPs 2.1.04.01, Buffer/Backfill; and FEPs 2.1.09.52, 53, 54, Chemical Processes—Transport by investigating reactive-diffusive radionuclide transport in bentonite. Our FY12 accomplishments for this activity include:

- We have developed a robust MD simulation methodology that correctly predicts the temperature dependence of sodium diffusion in bulk liquid water. This methodology predicts that sodium diffusion has a lower activation energy (E_A) in the three-layer hydrate of Na-montmorillonite than in bulk liquid water. These results open up a promising avenue for modeling and interpreting experimental results on the activation energy of diffusion of ionic solutes in macroscopic samples of compacted montmorillonite.

In the remaining months of FY12, we will

- Make efforts to obtain more precise E_A values (by extending the duration of our simulations).

- Predict the E_A value of sodium in the two-layer hydrate of Na-montmorillonite (to better understand the influence of compaction).

For FY13, we propose to

- Determine the activation energy of diffusion of Cs^+ in Na-MMT interlayers (by replacing a few Na^+ ions by Cs^+ ions in our simulations) and integrate the work with that described in Section 3.

- Develop a simulation methodology for investigating ion exchange between bulk liquid water and clay interlayers, which would enable us to predict the adsorption of UO_2 complexes in montmorillonite interlayer nanopores and its impact on effective diffusion coefficients. This last task would aid in the interpretation of the uranium diffusion experiments that are being carried out as described in Section 5.

6.4 Experimental Study on Reactive-Diffusive Transport

The major objective of this activity is to develop an improved understanding of radionuclide transport mechanisms and providing data sets for more accurately modeling the transport process in bentonite. This activity addresses Features, Events and Processes (FEPs), FEPs 2.1.04.01, Buffer/Backfill; and FEPs 2.1.09.52, 53, 54, Chemical Processes—Transport by investigating reactive-diffusive radionuclide transport in bentonite. In current models for radionuclide diffusion through bentonite in an engineered barrier, the apparent and effective diffusion coefficients are linked through the K_d value, which is often believed to be a constant value for a particular radionuclide. In the case of U(VI), this is less likely to be true because of the very high sensitivity of the K_d value to pH and bicarbonate and calcium concentrations. Our FY12 accomplishments for this activity include:

- We completed literature survey of diffusion experiments into montmorillonite and bentonites and surface complexation modeling of U(VI) on montmorillonite.

- We developed experiment setup in the laboratory and obtained preliminary results of Uranium(VI) equilibrium and kinetic sorption studies (K_d values) under different test conditions.

Plans for the remainder of FY12 and for FY13 include the diffusion studies of U(VI) into bentonite and montmorillonite at various degrees of compaction and under various aqueous chemical conditions. Further studies of U(VI) sorption onto montmorillonite will also be conducted, especially as a function of Ca concentration.

Specifically, in the remainder of FY12, we will

- Complete analysis of batch kinetic studies of U(VI) sorption on montmorillonite. Conduct additional experiments if needed for interpretation of subsequent diffusion studies.

- Conduct kinetic and equilibrium U(VI) sorption experiments on montmorillonite as a function of calcium concentration

- Conduct one additional equilibrium experiment of U(VI) sorption on montmorillonite at an elevated partial pressure of $CO_2(g)$, e.g. 10% CO_2.

- Complete/refine the surface complexation model for U(VI) sorption on montmorillonite by incorporating all experimental data collected in FY12.

- Design and complete fabrication of multiple diffusion cells for the study of U(VI) diffusion into montmorillonite and bentonite.

- Conduct preliminary study of U(VI) diffusion into montmorillonite for one set of chemical conditions.

- Engage in modeling collaborations with the diffusion modeling work conducted in Sections 3 and 4 to develop a diffusion model for U(VI) that is consistent with our experimental data.

In FY13, we will complete the following tasks listed below. These tasks are important for improving predictive models of diffusion of all actinide radionuclides through bentonite barriers. Such predictive models are an important component of performance assessment models for deep nuclear waste disposal.

- Conduct batch kinetic and equilibrium U(VI) sorption experiments on montmorillonite as a function of temperature. Complete/refine the surface complexation model for U(VI) sorption on montmorillonite by incorporating all experimental data.

- Conduct study of Br^- and Ca^{2+} diffusion into montmorillonite at low compaction and at pH 7 in 0.1M NaCl solutions equilibrated with air.

- Conduct studies of U(VI) diffusion into montmorillonite at low compaction and at low pH (5.0), circumneutral pH (7.0) and high pH (8.5) in 0.1M NaCl solutions equilibrated with air.

- Conduct study of U(VI) diffusion into montmorillonite at low compaction at pH 7 in 0.1M NaCl/1 mm $CaCl_2$ solution equilibrated with air.

- Conduct study of U(VI) diffusion into montmorillonite at intermediate and high compaction at pH 7 in 0.1M NaCl/1 mm $CaCl_2$ solution equilibrated with air.

- Conduct study of Br^- and Ca^{2+} diffusion into <u>bentonite</u> at low compaction and at pH 7 in 0.1M NaCl solutions equilibrated with air.

- Conduct studies of U(VI) diffusion into <u>bentonite</u> at low compaction and at low pH (5.0), circumneutral pH (7.0) and high pH (8.5) in 0.1M NaCl solutions equilibrated with air.

- Employ X-ray spectroscopic and electron-based imaging techniques to evaluate U(VI) diffusion on scales of microns up to one mm.

- Engage in modeling collaborations with the activities described in Section 3 and 4 to develop a diffusion model for U(VI) that is consistent with our experimental data.

7.   References

Alonso E.E., Vaunat, J., Gens A., 1999, Modelling the mechanical behavior of expansive clays. Engineering Geology, 54, p. 173–183.

Appelo, C.A.J. and Wersin, P., 2007, Multicomponent diffusion modeling in clay systems with application to the diffusion of tritium, iodide, and sodium in Opalinus Clay. Environ. Sci. Technol. 41, p. 5002-5007.

Appelo, C.A.J., Vinsot, A., Mettler, S. and Wechner, S., 2008, Obtaining the porewater composition of a clay rock by modeling the in- and out-diffusion of anions and cations from an in-situ experiment. J. Contam. Hydrol. 101, p. 67-76.

Arai, Y., M. McBeath, J.R. Bargar, J. Joye, J.A. Davis, 2006, Uranyl adsorption and surface speciation at the imogolite-water interface: Self-consistent spectroscopic and surface complexation models, Geochimica et Cosmochimica Acta, 70, p. 2492-2509.

Avena, M.J., De Pauli, C.P., 1998, Proton adsorption and electrokinetics of an Argentinean montmorillonite, Journal of Colloid Interface Science 202, p. 195-204.

Bargar, J.R., R. Reitmeyer, J.J Lenhart, J.A. Davis, 2000, Characterization of U(VI)-carbonato ternary complexes on hematite: EXAFS and electrophoretic mobility measurements, Geochimica et Cosmochimica Acta, 64(16), p. 2737-2749.

Bickmore, B.R., K.M. Rosso, K.L. Nagy, R.T. Cygan, C.J. Tadanier, 2003, Ab initio determination of edge surface structures for dioctahedral 2:1 phyllosilicates: Implications for acid-base reactivity, Clays and Clay Minerals 51, p. 359-371.

Birgersson M., Karnland, O., 2009, Ion equilibrium between montmorillonite interlayer space and an external solution - Consequences for diffusional transport, Geochimica et Cosmochimica Acta 73(7), p. 1908-1923.

Bourg, I.C., Sposito, G., 2010, Connecting the molecular scale to the continuum scale for diffusion processes in smectite-rich porous media, Environmental Science and Technology 44, p. 2085-2091.

Bourg, I.C., Bourg, A.C.M., and Sposito, G., 2003, Modeling diffusion and adsorption in compacted bentonite: a critical review, J. Contam. Hydrol. 61, p. 293–302.

Bourg, I.C., Sposito, G., and Bourg, A.C.M., 2006, Tracer diffusion in compacted, water-saturated bentonite, Clays Clay Miner. 54, p. 363–374.

Bourg, I.C., Sposito, G., and Bourg, A.C.M., 2007, Modeling cation diffusion in compacted water-saturated sodium bentonite at low ionic strength. Environ. Sci. Technol. 41, 8118–8122.

Bourg, I.C., Sposito, G., Bourg, A.C.M., 2007, Modeling the acid–base surface chemistry of montmorillonite, Journal of Colloid and Interface Science, 312, p. 297-310.

Bradbury, M. and Baeyens, B., 2000, A generalized sorption model for the concentration dependent uptake of caesium by argillaceous rock, Geochimica et Cosmochimica Acta, 42, p. 141-163.

Bradbury, M. and Baeyens, B., 2002, Sorption of Eu on Na- and Ca-montmorillonites: Experimental investigations and modelling with cation exchange and surface complexation, Geochimica et Cosmochimica Acta, 66, p. 2325-2334.

Bradbury, M. and Baeyens, B., 2005, Modeling the sorption of Mn(II), Co(II), Ni(II), Cd(II), Eu(III), Am(III), Sn(IV), Th(IV), Np(V) and U(VI) on montmorillonite: linear free energy relationships and estimates of surface binding constants for some selected heavy metals and actinides. Geochimica et Cosmochimica Acta, 69, p. 875-892.

Bradbury, M. and Baeyens, B., 2011, Predictive sorption modelling of Ni(II), Co(II), Eu(III), Th(IV) and U(VI) on MX-80 bentonite and Opalinus Clay: A "bottom-up" approach, Applied Clay Science, 52, p. 27-33.

Catalano, J.G. and Brown, G.E., 2005, Uranyl adsorption onto montmorillonite: Evaluation of binding sites and carbonate complexation, Geochimica et Cosmochimica Acta, 69(12), p. 2995-3005.

Chen, T., Smit, B., and Bell, A.T., 2009, Are pressure fluctuation-based equilibrium methods really worse than nonequilibrium methods for calculating viscosities? Journal of Chemical Physics 131, p. 246101.

Chipera, S.J. and Bish, D.L., 2001, Baseline studies of the Clay Minerals Society source clays: Powder X-ray diffraction analysis, Clays and Clay Minerals, 49, p. 398-409.

Costanzo, P.A. and Guggenheim, S., 2001, Baseline studies of the Clay Minerals Society source clays: Preface, Clays and Clay Minerals, 49, p. 371.

Cygan, R.T., Liang, J.-J., Kalinichev, A.G., 2004, Molecular models of hydroxide, oxyhydroxide, and clay phases and the development of a general force field, Journal of Physical Chemistry B 108, p. 1255-1266.

Davis, J.A., Meece, D.M., Kohler, M., and Curtis, G.P., 2004, Approaches to surface complexation modeling of uranium(VI) adsorption on aquifer sediments, Geochimica et Cosmochimica Acta, 68, p. 3621-3641.

Ersahin, S., Gunal, H., Kutlu, T., Yetgin, B., and Coban, S., 2006, Estimating specific surface area and cation exchange capacity in soils using fractal dimension of particle-size distribution, Geoderma 136, p. 588–597.

Espenson, J. H., Chemical kinetics and reaction mechanisms. McGraw-Hill, Inc., New York, 1995.

Fernández, R. and Mäder, U., 2011, Modelling the bentonite column with CrunchFlow and comparison with PhreeqC, including diffuse layer features. NAGRA Report, April 18, 2011.

Ferrage, E., Sakharov, B.A., Michot, L.J., Delville, A., Bauer, A., Lanson, B., Grangeon, S. , Frapper, G., Jiménez-Ruiz, M., and Cuello, G.J., 2011, Hydration properties and interlayer organization of water and ions in synthetic Na-smectite with tetrahedral layer charge. Part 2. Toward a precise coupling between molecular simulations and diffraction data, Journal of Physical Chemistry C 115, p. 1867-1881.

Fox, P.M., Davis, J.A., and Zachara, J.M., 2006, The effect of calcium on aqueous uranium(VI) speciation and adsorption to ferrihydrite and quartz, Geochimica et Cosmochimica Acta, 70, p. 1379-1387.

Garitte, B., and others, HE-E experiment - In situ Heater Test, Presentation given at 1th DECOVALEX 2015 workshop, April 2012, Berkeley.

Gens, A, Alonso, E., 1992, A framework for the behaviour of unsaturated expansive clays. Can. Geotech. J. 29, p. 1013–1032.

Gens, A., Sánchez, M., Sheng, D., 2006, On constitutive modelling of unsaturated soils. Acta Geotechnica, 1, p. 137–147.

Gens, A., Vaunat, J., Garitte, B., and Wileveau, Y., 2007, In situ behaviour of a stiff layered clay subject to thermal loading, observations and interpretation. Geotechnique 57(2), p. 207–228.

Glaus, M.A., Baeyens, B., Bradbury, M.H., Jakob, A., Van Loon, L. , and Yaroshchuk, A., 2007, Diffusion of ^{22}Na and ^{85}Sr in montmorillonite: evidence of interlayer diffusion being the dominant pathway at high compaction, Environmental Science and Technology, 41, p. 478-485.

Gonçalvès, J., Rousseau-Gueutin, P., and Revil, A., 2007, Introducing inter-acting diffuse layers in TLM calculations: A reappraisal of the influence on the swelling pressure and the osmotic efficiency of compacted bentonites, Journal of Colloid Interface Science 316, p. 92-99.

Holmboe, M., Wold, S., and Jonsson, M., 2012, Porosity investigation of compacted bentonite using XRD profile modeling, Journal of Contaminant Hydrology 128, p. 19-32.

Hsi, C.K.D. and Langmuir, D., 1985, Adsorption of uranyl onto ferric oxyhydroxides: Application of the surface complexation site-binding model. Geochimica et Cosmochimica Acta, 49, p. 1931-1941.

Kalinichev, A.G., Kirkpatrick, R.J., and Cygan, R.T., 2000, Molecular modeling of the structure and dynamics of the interlayer and surface species of mixed-metal layered hydroxides: Chloride and water in hydrocalumite (Friedel's salt), American Mineralogist 85, p. 1046-1052.

Kozaki, T., Sato, H., Fujishima, A., Sato, S., and Ohashi, H., 1996, Activation energy for diffusion of cesium in compacted sodium montmorillonite, Journal of Nuclear Science and Technology 33, p. 522-524.

Kozaki, T., Fujishima, A., and Sato, S., 1998, Self-diffusion of sodium ions in compacted sodium montmorillonite, Nuclear Technology 121, p. 63-69.

Kozaki, T., Sato, H., Sato, S., and Ohashi, H., 1999, Diffusion mechanism of cesium ions in compacted montmorillonite, Engineering Geology 54, p. 223-230.

Kozaki, T., Fujishima, A., Saito, N., Sato, S., Ohashi, H., 2005, Effects of dry density and exchangeable cations on the diffusion process of sodium ions in compacted montmorillonite, Engineering Geology 81, p. 246-254.

Kozaki, T., Liu, J., and Sato, S., 2008, Diffusion mechanism of sodium ions in compacted montmorillonite under different NaCl concentration, Physics and Chemistry of the Earth 33, p. 957-961.

Leroy, P. and Revil, A., 2004, A triple-layer model of the surface electrochemical properties of clay minerals, Journal of Colloid Interface Science 270(2), p. 371-380.

Leroy, P., Revil, A., and Coelho, D. 2006, Diffusion of ionic species in bentonite, J. Colloid Interface Sci. 296 (1), p. 248–255.

Leroy P., Revil A., Altmann S., and Tournassat C., 2007, Modeling the composition of a pore water in a clay-rock geological formation (Callovo-Oxfordian, France). Geochimica et Cosmochimica Acta 71(5), p. 1087-1097.

Lichtner P.C., 1998, Modeling reactive flow and transport in natural systems. Proceedings of the Rome Seminar on Environmental Geochemistry, 5-72.

Mandelbrot, B., The fractal geometry of nature, W.H. Freeman and Co., New York, 1999.

McKinley, J.P., Zachara, J.M., Smith, S.C. and Turner, G.D., 1995, The influence of uranyl hydrolysis and multiple site-binding reactions on adsorption of U(VI) to montmorillonite, Clays and Clay Minerals, 43, p. 586-598.

Mermut, A.R. and Cano, A.F., 2001, Baseline studies of the Clay Minerals Society source clays: Layer-charge determination and characteristics of those minerals containing 2:1 layers, Clays and Clay Minerals, 49, p. 393-397.

Nagasaki, S., 2001, Sorption of uranium(VI) on Na-montmorillonite colloids - effect of humic acid and its migration. In: Y. Iwasawa, N. Oyama, H. Kunieda (Eds.), Studies in Surface Science and Catalysis. Elsevier.

Nutt, M. et al., 2011, Used Fuel Disposition Campaign Disposal Research and Development Roadmap (FCR&D-USED-2011-000065 REV0), U.S. DOE Used Fuel Disposition Campaign.

OECD, 2003, Engineering barrier systems and the safety of deep geological repositories (State-of-the-art Report), ISBN 92-64-18498-8.

Plimpton, S., 1995, Fast parallel algorithms for short range molecular dynamics, Journal of Computational Physics 117, 1-19.

Rutqvist J., Ijiri Y. and Yamamoto H., 2011, Implementation of the Barcelona Basic Model into TOUGH-FLAC for simulations of the geomechanical behavior of unsaturated soils. Computers & Geosciences, 37, p. 751–762.

Sánchez, M., Gens, A., Guimarães, L. do N., Olivella, S., 2005, A double structure generalized plasticity model for expansive materials. Int. J. Numer. Anal. Meth. Geomech., 29, p. 751–787.

Schoch, R.B., Han, J., Renaud, P., 2006, Transport phenomena in nanofluidics. Reviews of Modern Physics 80, p. 839-883.

Stone, A. T. and Morgan, J.J., 1990, Kinetics of chemical transformations in the environment. In: W. Stumm (Ed.), Aquatic chemical kinetics: reaction rates of processes in natural waters. John Wiley & Sons, Inc., New York.

Steefel, C.I., 2009, CrunchFlow - Software for modeling multicomponent reactive flow and transport.

Steefel, C.I. and Maher, K., 2009, Fluid-rock interaction: A reactive transport approach. Reviews in Mineralogy and Geochemistry 70, p. 485-532.

Stumm, W., 1992, Chemistry of the Solid Water Interface: Processes at the Mineral Water Particle Water Interface in Natural Systems, John Wiley & Sons, 428 pp.

Tournassat, C., and Appelo, C.A.J., 2011, Modelling approaches for anion-exclusion in compacted Na-bentonite, Geochimica et Cosmochimica Acta 75(13), p. 3698-3710.

Tournassat, C., Ferrage, E., Poinsignon, C., and Charlet, L., 2004, The titration of clay minerals: II. Structure-based model and implications for clay reactivity, Journal of Colloid and Interface Science, 273, p. 234-246.

Van Loon, L.R., Glaus, M.A., Müller, W., Anion exclusion effects in compacted bentonites: Towards a better understanding of anion diffusion, Applied Geochemistry 22(11), 2536-2552, 2007

Viani, B.E., Low, P.F., and Roth, C.B., 1983, Direct measurement of the relation between interlayer force and interlayer distance in the swelling of montmorillonite, Journal of Colloid and Interface Science 96, p. 229–244.

Wersin, P., Curti, E. and Appelo, C.A.J., 2004, Modelling bentonite-water interactions at high solid/liquid ratios: swelling and diffuse double layer effects. Appl. Clay Sci. 26, p. 249-257.

Xu, Y.F., Sun, D., Yao, Y.P., 2004, Surface fractal dimension of bentonite and its application to determination of swelling properties, Chaos, Solitons and Fractals 19, p. 347–356.

Xu, Y.F., 2004, Calculation of unsaturated hydraulic conductivity using a fractal model for the pore-size distribution, Computers and Geotechnics 31, p. 549–557.

Yeh, I.-C., Hummer, G., 2004, System-size dependence of diffusion coefficients and viscosities from molecular dynamics simulations with periodic boundary conditions, Journal of Physical Chemistry B 108, p. 15873-15879.

Clay Stability and Clay – Metal Interactions
(PART III)

1. Introduction and Objective

The Used Fuel Disposition (UFD) Campaign is presently engaged in looking at various generic options for disposal of used fuel. The focus of this experimental work is to characterize and bound Engineered Barrier Systems (EBS) conditions in repositories sited in igneous rocks. Previous research for the Yucca Mountain Project limited repository conditions to less than 100°C and atmospheric conditions. The UFD now has the ability to evaluate multiple EBS materials, waste containers, and rock types at higher heat loads and pressures (including deep boreholes). The set of geologic conditions available to the U.S.A. for crystalline rock repositories include saturated and reduced water conditions, along with higher pressure and temperature regimes. Most of these experimental repository conditions have not been studied in the U.S. for decades and little has been done by the international community at high pressures and temperatures. The experiments performed as part of this work package will focus on the importance of repository chemical and mineralogical conditions at high temperatures. This will allow for both a better understanding of deep borehole environments and provide input to the assessment of the scientific basis for elevating the temperature limits in clay barriers and their evaluation of their performance.

2. Previous Work

Clay minerals – as backfill, buffer materials, or host-rock constituents – are critical to the performance of the EBS. Some of the fundamental factors of clay mineral performance include chemical interactions, radionuclide retention, and physical and mechanical behavior. This section focuses primarily on previous studies of chemical changes in smectite clay at elevated temperatures and pressures. The potential uses of smectites and the smectite-rich rock (i.e., bentonite) in geologic disposal of radioactive-waste have been recognized for decades, and many studies have been devoted to issues of smectite stability under repository conditions. Earlier studies consider smectite illitization as a geothermometer to allow reconstructions of thermal and tectonic history of sedimentary basins and active and fossil geothermal systems.

Altaner and Ylagan (1997) provide a good introduction to the concepts of smectite alteration. Smectite illitization is considered to proceed through mixed-layer illite/smectite (I/S) intermediates as the amount of illite interlayer increases. Central factors to illite conversion are elevated temperatures, high potassium (K) concentration in the reacting solution, and time. Possible reaction mechanisms for smectite illitization include solid-state phase transformation, dissolution and crystallization, and Oswald ripening.

This section summarizes a selection of relevant studies from rather extensive literature on smectite alteration. Previous and ongoing work can be divided into experimental laboratory studies, and studies of natural alteration (including natural analogs). Field experiments are in progress, but are not included here. Several review papers have been published as well.

Experimental Studies of Clay Stability

Wu et al. (1997) partially dehydrated Ca- and Mg-exchanged montmorillonite by heating samples at pressures from the H_2O liquid-vapor saturation boundary to about 10 kbars. Progressive dehydration caused contraciton of the crystal lattice indicating various hydration states from fully to partially hydrated. Similar experiments with Na-exchanged montmorillonite (Huang et al., 1994) also indicated shrinkage at various hydration states at temperatures of up to 500ºC. The 19 Å fully hydrated montmorillonite therefore, is stable up to 200-380 ºC in the

absence of potassium. Dehydration and lattice contraction that occurs in this temperature range is fully or almost fully reversible. However, at higher pressures, the rehydration initially follows a lower-temperature path relative to the thermal path of dehydration.

Tang and Cui (2010) conducted thermal conductivity, water retention, and swelling measurements of two MX80 bentonite samples with different quartz content (15.2 % and 2.8 % quartz). The two samples exhibited significantly different thermal conductivities that seemed to correlate with quartz content. The thermal conductivity of quartz is 8.8 W/(m K) versus 2.5 W/(m·K) for other constituents, so that differences in quartz content may affect the bulk thermal properties. Differences in bulk swelling behavior also correlate with variations in the quartz/montmorillonite ratio.

The experimental work of Ferrage et al. (2011) presents some of the best evidence for the mechanism of S to I/S transformation. They studied the hydrothermal reactivity of K-exchanged SWy-2 low-charge montmorillonite at 250 – 400 °C and 1 kbar, with reaction times of 5 to 120 days. The authors provide experimental evidence for a dissolution-crystallization mechanism following the Ostwald step rule in which metastable smectite transforms into illite through a series of metastable illite-smectite phases.

Ferrage et al. (2011) use various analytical techniques such as X-ray diffraction (XRD), transmission electron microscopy (TEM), and chemical microanalysis to document the illitization process. TEM and chemical analyses show several particle morphologies with different interlayer K content and Al-Si substitution that appears to correspond to the phases detected by XRD. The illitization mechanisms are not a progressive solid-state reaction but rather a result of multiple dissolution-precipitation processes.

Ferrage et al. (2011) concluded that the process of illitization is a complex reaction with multiple phenomena occurring at different temperatures. Although their illitization reaction rates at 350-400 °C did not fit a first- or higher-order kinetic model, they were able to calculate an activation energy of 6.1 kcal/mol. It is unclear what this value actually represents and it seems to be too low for a dissolution and crystallization reaction.

The authors also emphasize that determination of non-expandable layers in K-exchanged I/S clay by ethylene glycol solvation and XRD gave erroneously high concentrations of non-expandable layers. This occurred because some of the dehydrated smectite layers failed to re-expand. Better results were obtained by Ca-exchange and glycolation of the test materials.

Natural Alteration

Pusch and Madsen (1995) investigated illitization of the Ordovician Kinnekulle bentonite due to the intrusion of a diabase dike 300 million years ago. The thermal regime of bentonite alteration was reconstructed from models of cooling rates and thermal conduction for the magma intrusion, with some corroborating analyses of conodonts in adjacent limestone beds. Thermal analysis suggests the main 2 m thick bentonite bed underwent heating to 150°C for ~300 years, followed by 100-130 °C for ~700 years. These authors summarized various studies on the illitization of the Kinnekulle bentonites. There are differences in characterization of the clay phases between the various investigations. However, there is general agreement that I/S mixed-layers (illite content in the range of about 32-65%) dominate, but smectite, kaolinite, illite, and chlorite also are present within the Kinnekulle bentonites. Pusch and Madsen (1995) favor neoformation and developed a transformation rate model based on an assumption that the conversion from smectite

to illite is an Arrhenius-type process, i.e., the rate is solely a function of temperature. They also identified K^+ availability as a rate-limiting factor because they calculated that the K^+ content of *in situ* pore water was insufficient to support the observed degree of illite conversion.

McCarty et al. (2009) studied the illitization of a 2.5-m-thick bentonite bed in upper Cretaceous marine shale in Montana by XRD, chemical analysis, and thermal gravimetric analysis. Modeling of the XRD patterns from air-dried and glycolated oriented specimens shows a mixture of co-existing, randomly interlayered (R0) and regularly interlayered (R1) I/S throughout the bed. The authors assume that the original volcanic ash was altered to smectite with a homogeneous Al-rich composition throughout the bed.

2.0 Experimental Studies of Clay Stability Interacting With Metals

Clay – Steel

Xia et al. (2005) designed experiments to investigate the corrosion of carbon steel in contact with bentonite under anoxic conditions with clay buffer materials. Results indicate that even under anoxic conditions, the carbon steel oxidizes by scavenging oxygen from the water (Reactions 2.1 through 2.3):

$$Fe^o + 2H_2O = Fe(OH)_2 + H_2(g) \tag{2.1}$$

$$3Fe(OH)_2 = Fe_3O_4 + 2H_2O + H_2(g) \tag{2.2}$$

$$3Fe^o + 4H_2O = Fe_3O_4 + 4H_2(g) \tag{2.3}$$
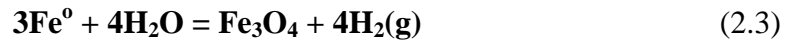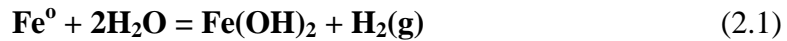
Anaerobic corrosion of the carbon steel occurred in the bentonite. This resulted in H^+ generation leading to further reducing conditions (Reactions 1, 2, 3). The corrosion rate was estimated to be ~0.1 μm/year. The presence of bentonite and corrosion products at the interface of carbon steel and bentonite possibly caused a passivating surface.

The reactions provided by Lantenois et al. (2005) can be summarized for the two pH realms (near neutral and basic) as follows:

pH 6 - Fe^o in the presence of smectite (which was unaltered) is oxidized to form magnetite according to Reaction 4:

$$3Fe^o + (smectite) + 4H_2O = Fe_3O_4 + (smectite) + 4H_2 \tag{2.4}$$
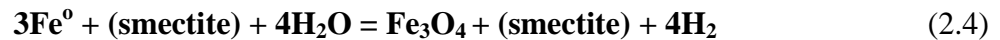
pH > 7- Reaction 2.4 is very different as dioctahedral smectites are involved in the reaction. (destabilization of dioctahedral smectite is common)

$$Fe^o + smectite = 1:1 \text{ Fe-rich phyllosilicate} + \text{Fe oxides} \tag{2.5}$$

Lantenois et al. (2005) have provided a pivotal paper on Fe/clay interactions, especially at pH>7. Both reaction products developed at neutral and basic pH will play a critical role in the use of concrete in repository setting. Their model of smectite destabilization will be very useful in further attempts to model bentonite stability.

Mosser-Ruck et al. (2010) performed experiments to determine the conversion of smectite to Fe-rich clay phases in contact with Fe metal at different temperatures, pH's, and Fe/clay (Fe/C) and liquid/clay (L/C) ratios. All experiments were run under low oxygen fugacity ($<10^{-40}$) and temperatures <300 ℃. With the results of the mineral phase transformations listed below, Mosser-Ruck et al. (2010) were able to propose a conceptual model for the main mineralogical transformations which can be expected in clay formations surrounding high-level nuclear waste repositories. Smectite changes in the presence of Fe^o and low redox conditions via reactions 2.6 through 2.10 (Mosser-Ruck et al., 2010).

Neutral pH (6-7)

150℃, L/C > 5

dioctahedral smectite = 7 Å Fe-rich phase (berthierine, odinite, or cronstedtite) (2.6)

150℃, Fe/C ratios=0.1

dioctahedral smectite = Fe-rich dioctahedral smectite + Fe-rich trioctahedral smectite (2.7)

300℃, L/C > 5. Fe/C ratio =0.1

dioctahedral smectite = Fe-rich saponite = trioctahedral chlorite + feldspar + zeolite (2.8)

Montmorillonite + Iron = Chamosite + Feldspar +Clinoptilolite

$$10(Na,Ca)_{0.33}(Al_{1.67}, Mg_{.33}) Si_4O_{10}(OH)_2 \cdot 2H_2O +5 Fe =$$
$$(Fe,Mg)_5AlSi_3O_{10} OH_8 + (Na,Ca)(Al,Si)_4O_8 + (Na,Ca)_2Al_3Si_2Si_{13}O_{36} \cdot 12H_2O$$

High pH (10-12)

150℃, L/C > 5, Fe/C ratio = 0.1

dioctahedral smectite = Fe dioctahedral smectite (+/-palygorskite) (2.9)

300℃, L/C > 5, Fe/C ratio = 0.1

dioctahedral smectite = Fe-rich vermiculite + mordenite (2.10)
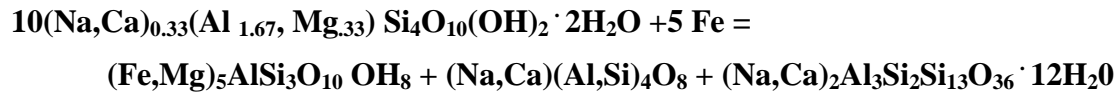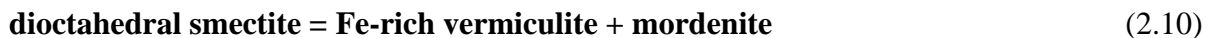
The occurrence of quartz, feldspars, magnetite, and zeolites as reaction by-products in all experiments is consistent with thermodynamic modeling predictions (Cathelineau et al., 2001; Kluska et al., 2002; Montes et al., 2005) and data from other experiments on bentonites. The conversion of montmorillonite to chlorite allows for production of silica, which crystallizes as quartz and/or to other silicates (feldspars, zeolites) depending on the presence and type of cations in solution and silica concentrations.

Clay - Copper

Taniguchi and Kawasaki (2008) described a very careful approach and experimental methods in their work. Immersion tests and slow strain rate tests (SSRT) on pure copper were conducted using synthetic seawater containing Na_2S at low temperatures for a time period of one year. The experimental results indicate a reaction rim on the copper of cuprite in an S-free environment. Once sulfur is added, the dominant corrosion product is chalcocite (Reactions 2.11 and 2.12):

$$2Cu^o + H_2O = Cu_2O + H_2 \tag{2.11}$$

or

$$S^o + 2Cu^o = Cu_2S \tag{2.12}$$
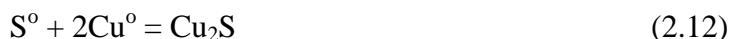
Review Papers

Meunier et al. (1998) compared experimental data sets and put them into the perspective of two general geologic settings: diagenetic and hydrothermal. Data from natural occurrences included geothermal areas such as the Salton Sea (Velde and Lanson, 1993) and burial diagenesis in the East Slovak Basin (Šucha et al., 1993). Several concepts were highlighted, including the understanding that heating experiments with smectite altering to I/S (random and regular interstratification) proceeded according to more than one reaction with increasing time and temperature and the recognition that additional equilibria with low- and high-charge montmorillonite, chlorite, quartz, saponite, beidellite, and other minerals are involved. Smectite-heating experiments are more similar to natural hydrothermal alteration than to diagenetic alteration in terms of duration, rates of heating, and perhaps chemical interactions.

Wersin et al. (2007) summarized information on irreversible changes to bentonite properties above 100°C, based on experiments and natural analogs. They identify critical parameters following repository closure, including ambient rock temperature, waste heat output, initial moisture content of the bentonite, and hydraulic and thermal properties of the rock; all of which may vary with time. There are two general processes of concern for alteration of bentonite properties: precipitation of SiO_2 cement and conversion of smectite to non-swelling illite layers. The authors infer that (1) bentonite experiences no significant changes up to 110-120 °C under wet conditions, (2) SiO_2 precipitation occurs at 130°C, (3) there are more significant changes by 150°C due to increased SiO_2 precipitation and some phase transition to illite, and (4) chlorite may form when clay closely interacts with Fe at elevated temperatures (Lantenois et al., 2005). Under dry conditions, it is possible that bentonite can be stable at temperatures as high as 350°C in some EBS designs.

The literature review by Laine and Karttunen (2010) is mainly a treatment of smectite stability as it is affected by water chemistry. Results of laboratory experiments, field studies, and modeling efforts are summarized. The authors note that few data exist pertaining to natural pore fluids in bentonite deposits, making it difficult to draw connections between pore-fluid composition and long-term stability of bentonite.

Summary of Illitization Studies and Implications to EBS Investigations

Within the UFD campaign, there are options for repository designs with very high heat loads. Meunier et al. (1998) and Wersin et al. (2007) summarize that when smectites are heated in the range of 110-150 °C and above, mineralogic changes may occur that alter the bentonite properties relevant to backfill/buffer performance. Potential changes include silica precipitation

above 130°C, increased silica precipitation/cementation and illite formation above ~150°C, and chlorite formation in the presence of Fe at higher temperatures. Once these phase changes have occurred, the clays will not revert to pure smectite when the backfill/buffer cools. This is due in part to the loss of silica from the clay structure. Imaging evidence seems to support the operation of dissolution and precipitation processes during illitization, although additional solid-state changes cannot be ruled out. Simultaneous nucleation and growth mechanisms proposed by Eberl et al. (2011) require further investigation.

Chemical and structural changes to the clays, in either backfill/buffer or clay-rich host rock, may have significant effects on repository conditions. Reduction of smectite rehydration and expansion capacity due to heating could affect the isolation provided by a buffer. Processes such as cementation by silica and neoformed illite could change the hydraulic properties of clay-rich materials.

The relatively few experiments at above-ambient pressure suggest that high pressure may stabilize fully hydrated smectites at temperatures as high as 385°C in the absence of K. However, once smectites are dehydrated at high pressure and temperature, rehydration with decreasing temperature may be retarded.

The work completed in the FY-11 EBS deliverable has identified knowledge gaps that are now sufficiently clear to embark on new hydrothermal experiments. The defining experimental research at 300°C is that of Mosser-Ruck et al. (2010). However, their experimental conditions did not consider 1) high pressure, 2) buffered redox conditions, 3) different metal types other than iron, 4) clay from mines as will be used for backfill/ buffers. LANL has the capability to provide these experiments with a fully operational high pressure/temperature laboratory (see next section). As part of the UFD Campaign, we developed preliminary experiments in the areas listed below.

2.1   Experimental Setup and Parameters

The intent of the experiments we conducted in FY-11 were twofold: 1) to compare product results with the experimental findings of Mosser-Ruck et al. (2010) and 2) determine post-experiment mineral phases that have properties which may be either beneficial or detrimental to the UFD campaign. We developed four proof-of-principal experimental mixtures to explore EBS chemistry in crystalline rock repositories at elevated repository temperatures and pressures using unprocessed bentonite from Colony, Wyoming (Bentonite Performance Minerals, LLC, a Halliburton Company). All experiments were run at approximately 150 bars and 125° to 300 ^{o}C for 5 weeks. Liquid samples were extracted at 125°, 200°, and 300 ^{o}C to characterize water chemistry trends due to mineral reactions. Each experiment was buffered at the magnetite-iron oxygen fugacity univariant curve using Fe_3O_4 and Fe^o filings. The experimental mixtures were 1) brine – clay, 2) brine – clay – 304 stainless steel (304SS), 3) brine – clay – 316 stainless steel (316SS), and 4) 2) brine – clay – copper (Cu).

The brine chemistry used in the experiments was chosen from the "Disposal Systems Evaluations and Tool Development – Engineered Barrier System (EBS) Evaluation" document (Jové Colón, 2010). Section 2.5.2 of that document covered deep groundwaters in crystalline rock of shield areas with Table 2.5.1 presenting the geochemistry of representative groundwater samples. Stripa sample V2(69-4) was chosen as our "generic" brine because of the rock type (granite), depth (822 m), total dissolved solids (790 ppm), and general water chemistry (Na-Ca-Cl). This brine chemistry is a good representation of a deep seated shield groundwater

composition. We prepared the synthetic brine following the published data and methods. Note that the potassium value in the synthetic brine is higher than Stripa V2 due to titration with KOH to increase pH. The two steel samples (304SS and 316SS) used in the experiments are NIST standards. Copper used in the experiments is pure Cu foil.

The experiments were conducted at LANL's high pressure hydrothermal laboratory. The reaction cells that contain the experimental mixtures were either gold (see Figure 2.1) or titanium bags and were sealed within steel pressure vessels (Figure 2.2). The assembled reaction vessel was then placed within the autoclaves (Figure 2.3) and brought up to pressure and temperature. All experiments followed a similar run duration and set of conditions.

The experiments were held at 150 bar during their duration, and final temperatures obtained were 300°C. Each experiment was first brought to ~125 °C and the liquid phase was sampled at the end of the first and second week. The experiments were then raised to ~210°C and the liquid phase was sampled in the second and at the end of the third week. Finally, the experiments were raised to ~300 °C, with the liquid phase sampled at the end of the fourth week. The temperature was shut down after sampling at ~300 °C and experiments were allowed to quench along the steam curve. A final liquid sample was taken upon cooling and the solid phases were removed from the reaction vessel for characterization

| Figure 2.1 | Figure 2.2 |

Figure 2.1. Gold reaction cells: Top: 120 ml cell, Bottom: 240 ml cell with cap, thrust ring, and head disassembled.

Figure 2.2. Left: HIP (thrust ring seal type) pressure vessel, for 400°C/600 bar furnaces; Right: AE (Bridgeman seal-type) pressure vessel, for 600 °C/1.5 kbar furnaces (vessel is ~24" tall).

Figure 2.3. 400ºC/600 bar rocking autoclave rack (autoclave drums are ~24" tall)

2.2   Analytical Techniques

X-ray diffraction (XRD) analyses of experimental materials conducted at LANL were used to determine mineral compositions of each clay sample. Samples were ground with a 20 wt.% corundum (Al_2O_3) standard. Addition of the corundum standard allowed for quantitative XRD analysis of the bulk rock following the internal standard method described by Chung (1974). XRD measurements were conducted with a Siemens D500 diffractometer using CuKα radiation. Data were collected from 2 to 70º 2θ with 0.02º step-size and count times of 8 to 12 s per step. Quantitative phase analyses were performed with the FullPat program (Chipera and Bish, 2002).

SEM analyses were performed on both pre- and post- experimental materials using a FEI InspectF at the MST-6 facility at LANL. SEM images provided both crystal morphology and paragenetic sequences. EDX analyses gave qualitative chemical data and the ability to quickly identify mineral phases.   Images were captured using an accelerating voltage of 30 kV in backscattered electron mode, and X-ray spectra were collected with a take off angle of 35 degrees.

Reaction liquids were extracted and analyzed to investigate the cation/anion transfers between liquids/solids. Major cations and trace metals were analyzed by inductively coupled plasma optical emission spectrometry (Perkin Elmer Optima 2100 DV ICP-OES) and inductively coupled plasma mass spectrometry (Elan 6100 ICP-MS) utilizing EPA methods 200.7 and 200.8. Ultra-high purity nitric acid (Fisher Trace Metal Grade) was used in sample and calibration preparation prior to sample analysis. Internal standards (Sc, Ge, Bi, and In) were added to both samples and standards to correct for matrix effects which can result in differing sample introduction rates. Some samples were diluted prior to analysis in order to minimize matrix effects as well as allow the analytes of interest to remain within the linear dynamic range of the calibration. Standard Reference Material (SRM) 1643e Trace Elements in Water was used to

check the accuracy of the multi-element calibrations. Typical ICP parameters were: 1300 W forward power, 15 mL/min cooling gas, 0.2 mL/min auxiliary flow; 0.8 mL/min nebulizer flow; and 1.5 mL/min sample uptake. Small volume samples used the following parameters: 1250 W forward power, 15 mL/min cooling gas, 0.2 mL/min auxiliary flow; 0.88 mL/min nebulizer flow; and 15 μL/min sample uptake.

Alkalinity measurements were made following EPA method 310.1 which is a titrimetric analysis with an endpoint of pH = 4.5. Inorganic anion samples were analyzed by ion chromatography (IC) following EPA method 300 on a Dionex DX-600 system. Charge balance (milli equivalence (meq)) was calculated based on concentrations of major and minor cations and anions. The charge Balance Error or (Cation – Anion Balance) was calculated as:

$$((\Sigma\text{Cation meq/L} - \Sigma\text{Anion meq/L}) / (\Sigma\text{Cation meq/L} + \Sigma\text{Anion meq/L}))$$

2.3 Results and Discussion

2.3.1 Pre- Run Characterization Results

Bulk XRD

The minerals identified in the powdered bentonite were primarily montmorillonite with lesser amounts of quartz, muscovite, cristobalite (or opal-CT), and gypsum (Figure 2.4). The granular bentonite sample contained primarily montmorillonite with lesser amounts of quartz, albite, cristobalite (or opal-CT), and clinoptilolite (Figure 2.5). This indicates variability between the starting materials. XRD patterns of the untreated and glycolated smectite fraction revealed that no illite or illite/smectite was present. If illite was a component of the clay, there would be a significant 8.8^o 2θ peak in the glycolated sample of Figure 2.6.
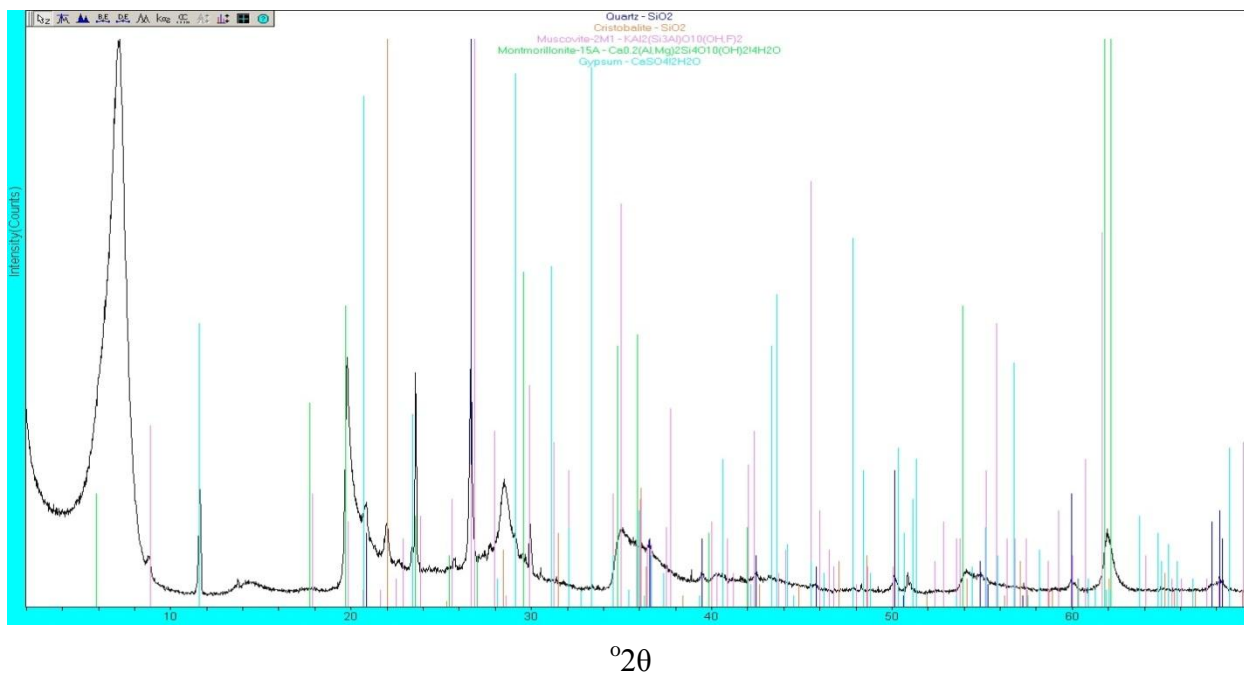
Figure 2.4. XRD pattern of the powdered Wyoming bentonite sample. Note the presence of gypsum.

125

°2θ
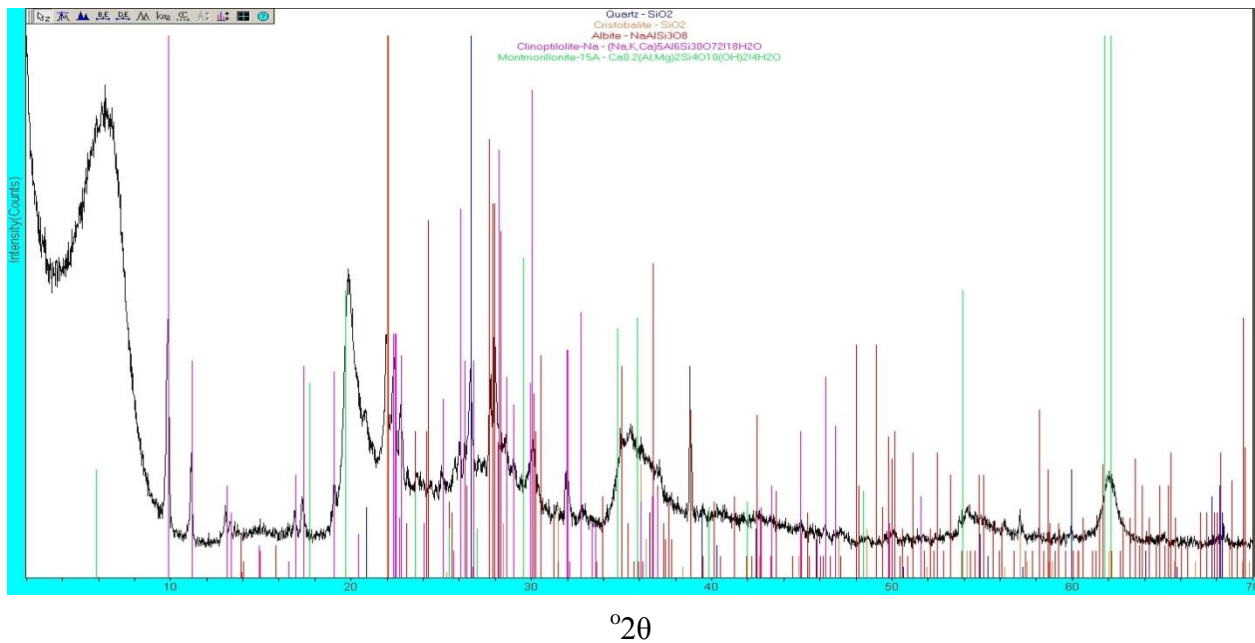
Figure 2.5. XRD pattern of the granular Wyoming bentonite sample. Note the presence of clinoptilolite.
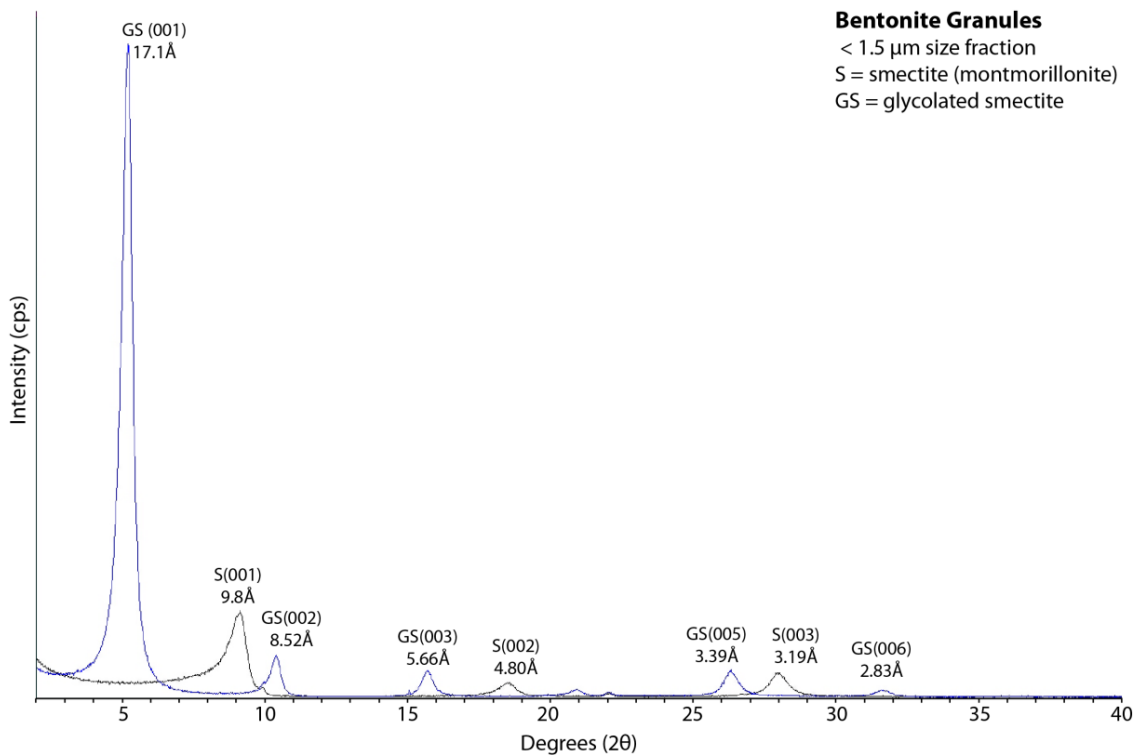
Figure 2.6. XRD pattern of the oriented and glycolated <1.5 μm fraction from the Wyoming bentonite granular sample.

SEM

The unreacted bentonite was also characterized by SEM imaging and EDX. The SEM image of the bentonite is shown in Figure 4a 2.7a and is similar to unreacted smectite of Lantenois et al.

(2005) as depicted in their Figure 3c. The EDX spectra (Figure 4b 2.7b) of our unreacted mine run bentonite in Figure 2.7a shows a montmorillonite composition. Finally, we wanted to ascertain if there is an illite component to the pre-experimental mine run bentonite. As described from the glycolated clay characterization above (Figure 2.6), no illite was identified.

det	HV	spot	WD	mag	mode	3 μm
ETD	30.00 kV	3.0	11.6 mm	40 000 x	SE	crust on 304 SS
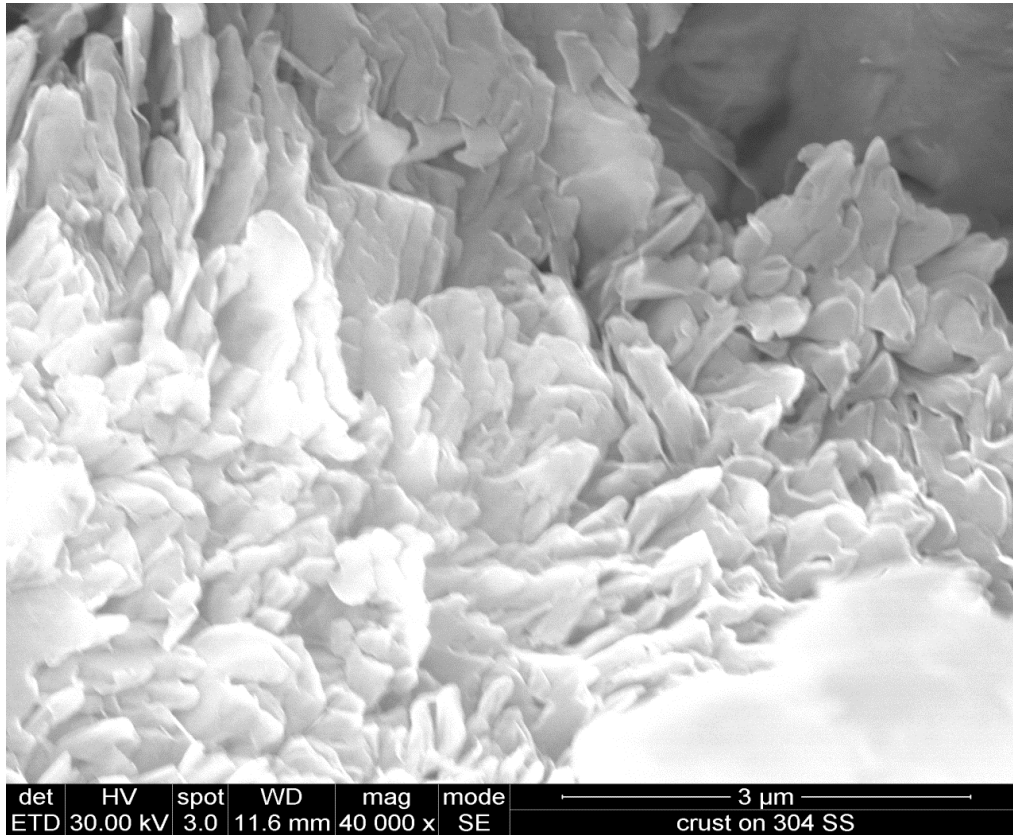
Figure 2.7a. Montmorillonite from mine run samples-not subjected to increased pressure and temperature.
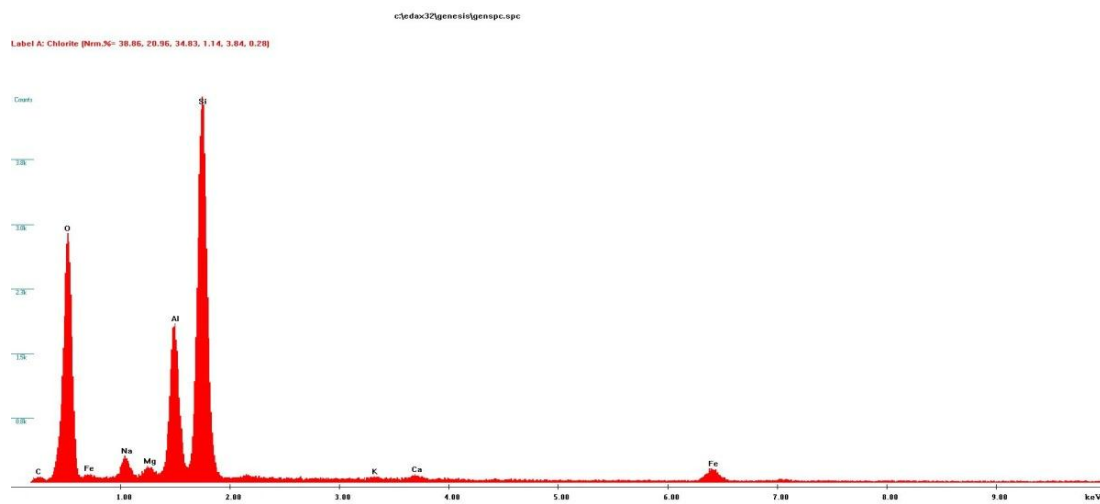
Figure 2.7b. EDX spectra of montmorillonite from mine run samples-not subjected to increased in pressure and temperature.

2.3.2 Post-Run Characterization Results

Samples of the starting solid and liquid materials for the experiments were characterized by various analytical methods after application of increased pressure and temperature. These methods included XRD, optical microscopy, and SEM imaging and EDX. Water brine (synthetic STRIPA brine) was characterized by ICP-MS.

At the time of finalizing this report, two experiments are finalized with reaction products fully characterized. The finalized experiments are 1) brine-clay (EBS-1) and 2) brine-clay-304SS (EBS-2). Experiments still in progress are 3) brine-clay-316SS (EBS-3) and 4) brine-clay-Cu (EBS-4). These two experiments will be finished by the deadline of the report but, the reaction products characterization will not have been completed.

EBS-1 Experiment

The post-run clay from experiment EBS-1 is essentially the same as the pre-experiment clay (Figure 2.8). Mineral abundances from EBS-1 are presented in Table 2.1. Smectite and clinoptilolite occur in significant quantities in both samples with minor amounts (< 5 wt. %) of quartz, cristobalite, muscovite, potassium feldspar and albite. Mineral variations in XRD analyses seen are insignificant in that precision is +/- 5 wt. %. Diffraction patterns of both untreated and glycolated smectite patterns, indicates that no illite or illite/smectite is present (Figure 2.9). If illite was present, there would be an 8.8 ^{o}2θ peak.
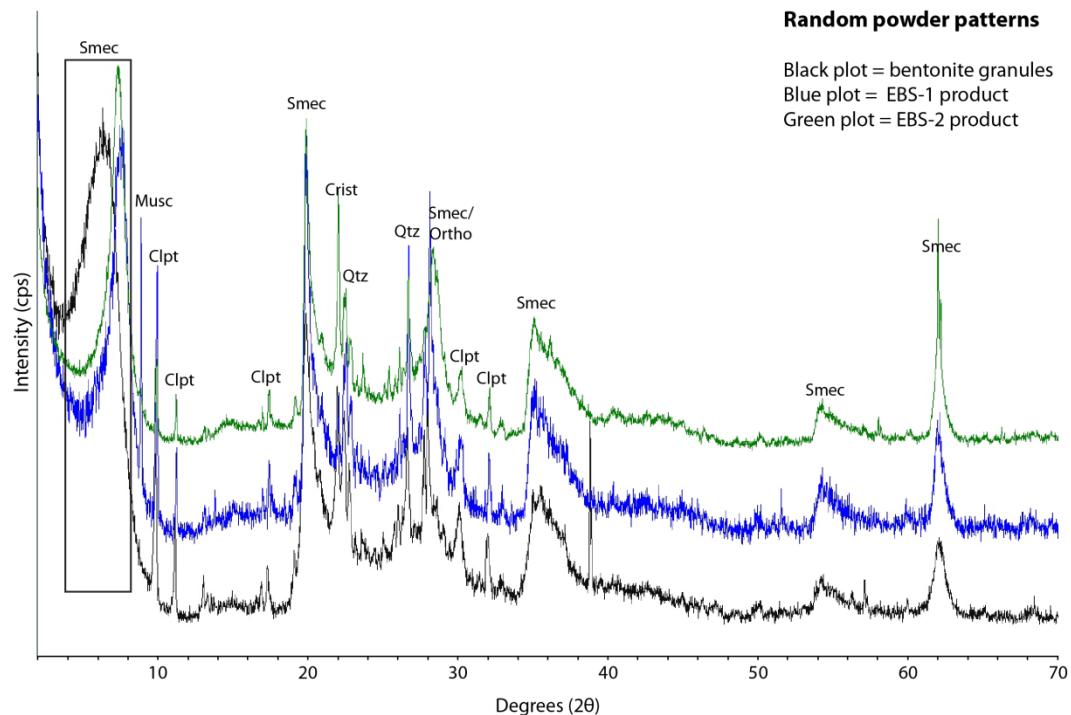
Figure 2.8. Powder XRD spectra of Wyoming mine run clay, post-experiment EBS-1 (clay-brine), post-experiment EBS-2 (clay-brine 304 SS).

Table 2.1. Mineral abundances in experimental clay samples. Note that the pre-experiment clay (Bent-granules) and the post-experiment clay mineral phases are essentially the same. Variations in smectite content are most probably due to variation in clay orientation and sampling.

Mineral	Bent-Granules	EBS-1	EBS-2
Smectite	74	81	69
Quartz	1	1	1
Cristobalite	2	2	2
Clinoptilolite	12	8	10
Mordenite	0	0	2
K-feldspar	3	4	4
Albite	5	2	4
Muscovite	4	2	8
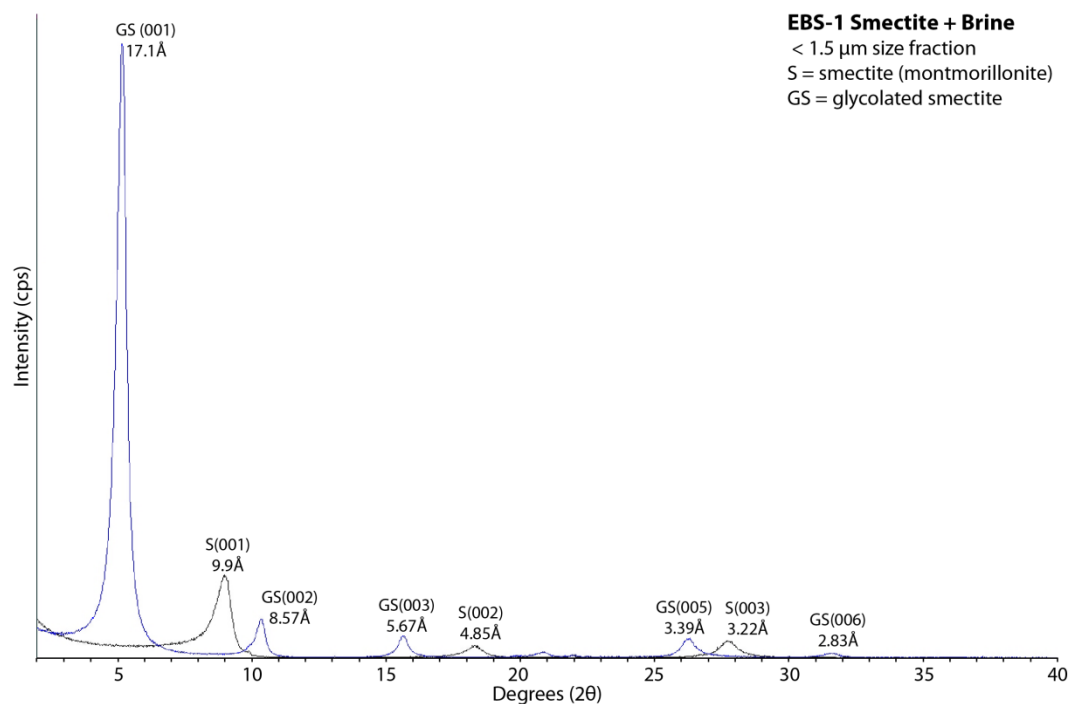
Figure 2.9. Smectite analysis of post EBS-1 experiment

However, some mineral changes (alterations) can be seen with optical microscopy and SEM images. The bentonite samples from Colony, Wyoming are altered non-welded, non-lithified ash flow tuffs. These have a rhyolitic bulk composition. Optically, there are solid phases similar to the opal morphology commonly seen in EBS-1 reaction products, which are rare in the pre-experiment clay. Some of the feldspar phenocrysts appear to be heavily corroded (see Figure 2.10a) and there appears to be a late-stage growth of euhedral clinoptilolite (Figure 2.10c). This alteration of feldspar and growth of zeolite is also confirmed in optical microscopy studies. In the case of minor amounts of material generated optical methods may detect more subtle changes in mineral equilibria than the aforementioned XRD methods.

129
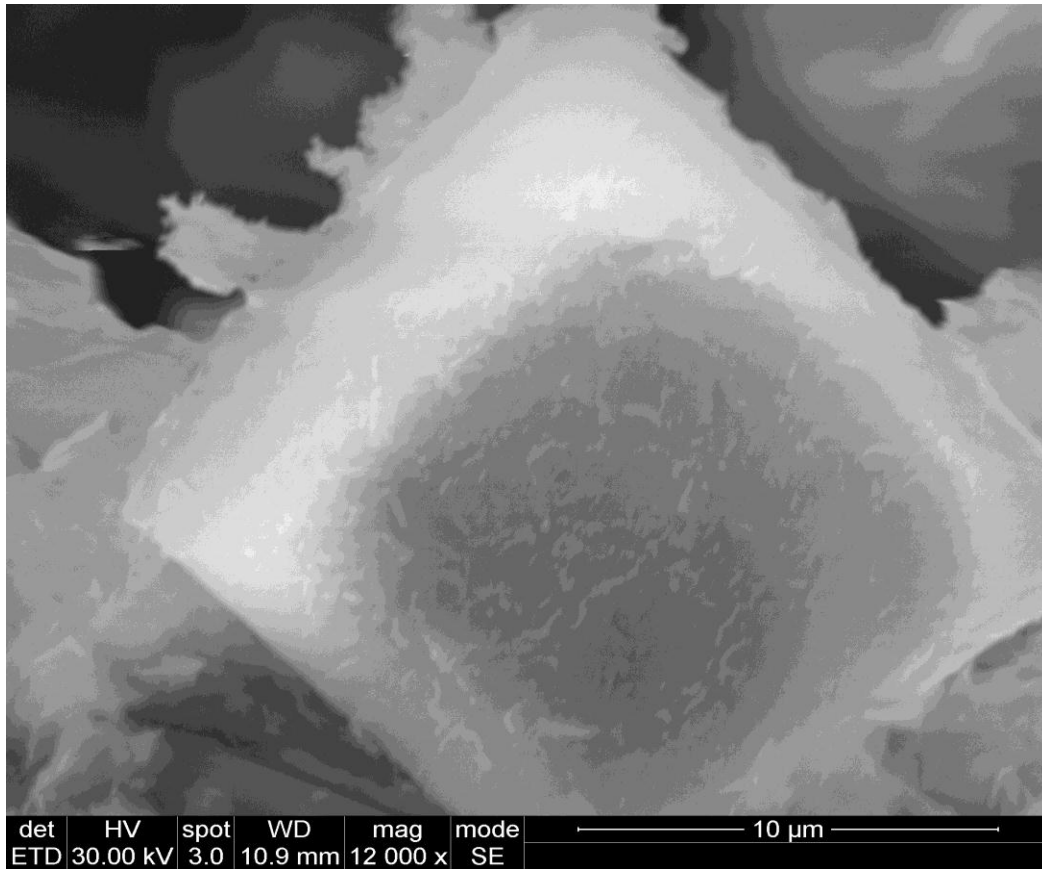
Figure 2.10a. Image of deeply etched (grey region) feldspar EBS-1.
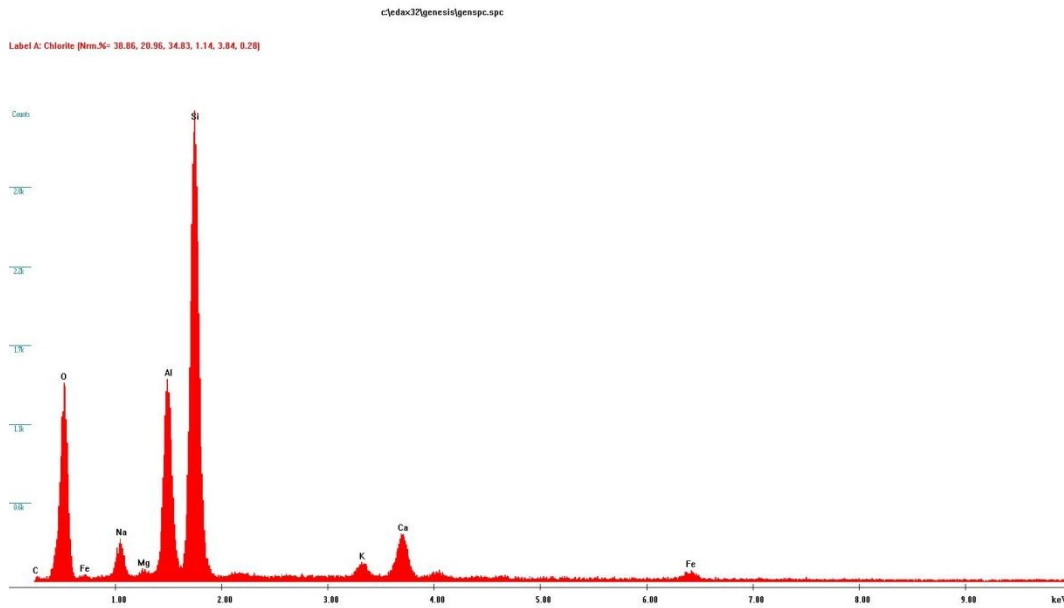
Figure 2.10b. EDX spectra of EBS-1 feldspar.
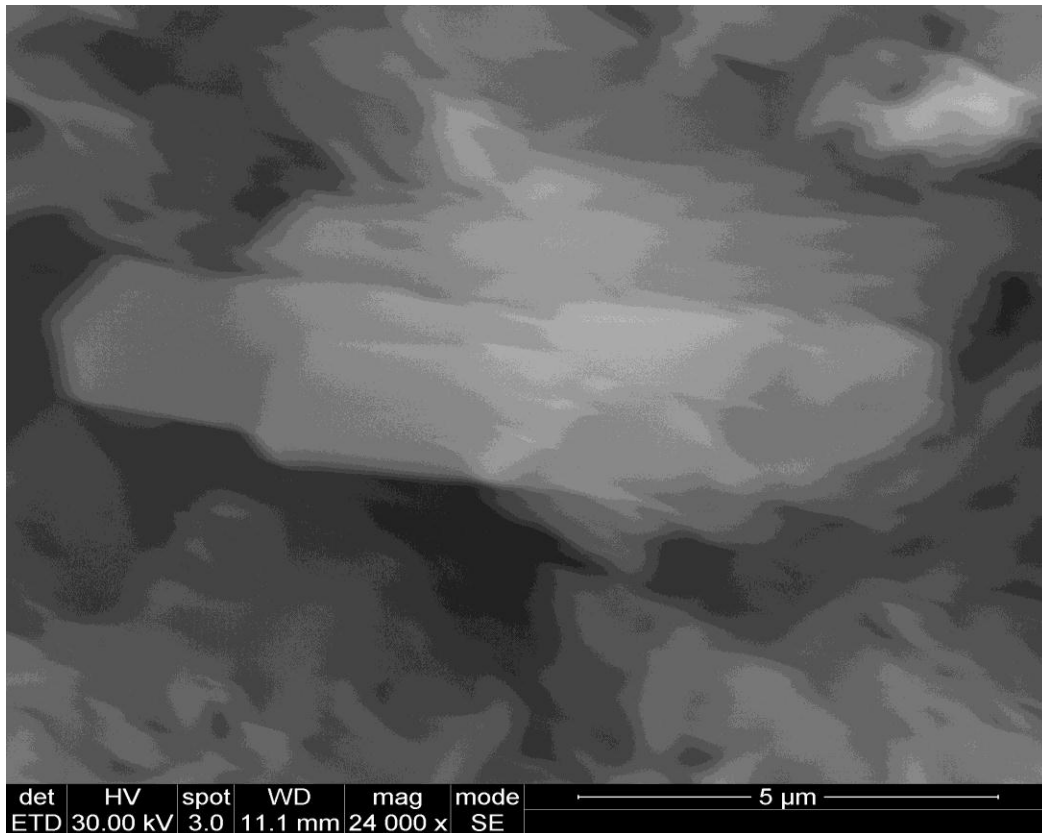
Figure 2.10c. SEM image of euhedral monoclinic clinoptilolite in EBS-1.

The aqueous geochemistry changes produced by this experiment are reflected in Figure 2.11. The full data set is contained in Appendix A of the UFDC report work package FT-12LA080602. Potassium shows a rapid decline in concentration with increasing time, while the correlation with temperature increases is not so obvious. Calcium also declines in concentration relative to the initial brine, however the magnitude is much less than that of potassium. Sodium has a rapid release into the brine from the clay and seems to be time dependent. However, at $300^{o}C$ sodium begins to transfer back to a solid phase, as indicated by the decline of this cation in the solution. Aqueous silica appears to be equally dependent on both time and temperature for its release into solution. Higher concentrations of aqueous silica are observed with increasing reaction temperatures while the aqueous silica concentration drops rapidly during the quenching of the experiments. This change in aqueous silica concentrations is probably due to the dissolution of silica minerals and precipitation of opal-CT.
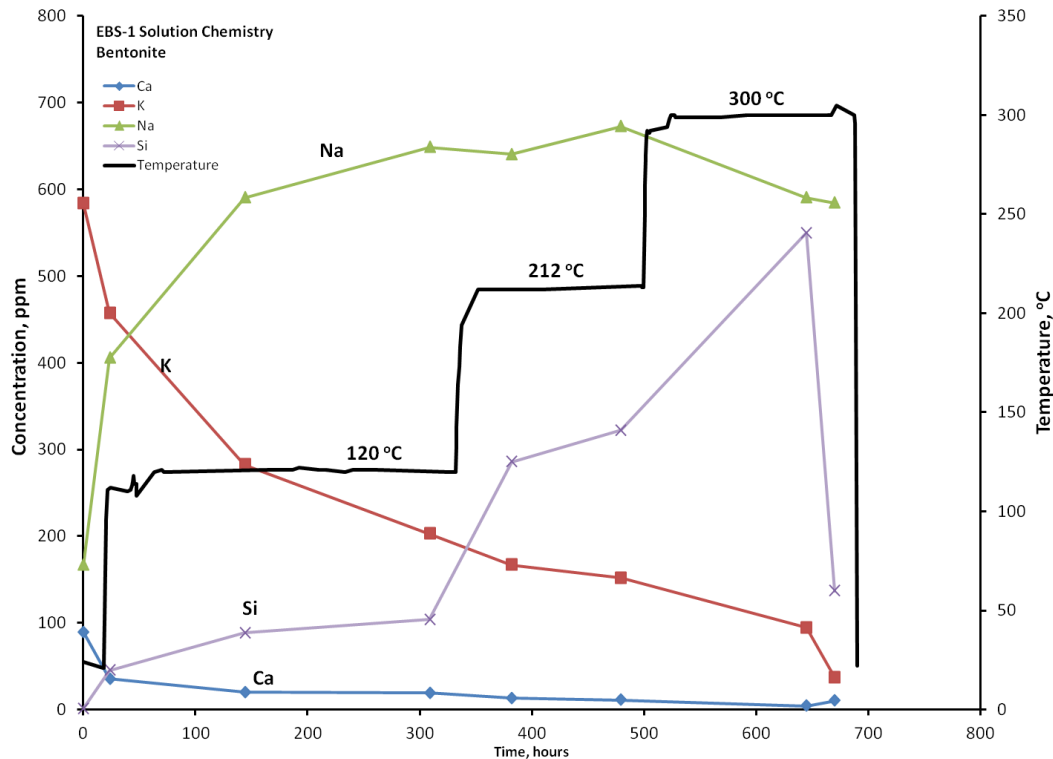
Figure 2.11. EBS-1 aqueous solution chemistry. Note the large decrease in potassium and slight decrease in Ca with time relative to the original brine chemistry (t = 0). There is a substantial increase in both Si and Na concentrations with time. It appears that the Si increase is closely associated with the temperature increases.

One other detail to note during the brine sampling events was the occurrence of H_2S gas in the brine aliquots. SO_4^{2-} reaches a maximum of 352 ppm in solution during the EBS-1 experiment. The gas may have been created by the breakdown of gypsum with increasing temperature, as shown in the reaction below.

$$CaSO_4 \bullet 2H_2O + 10H^+ + 8e^- = Ca^{+2} + H_2S + 6H_2O \tag{13}$$
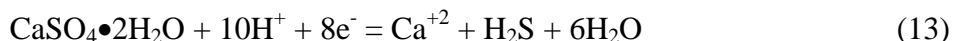
EBS-2 Experiment

The EBS-2 experiment differs from EBS-1 by the addition of 304SS to the bentonite granules. As seen in the powder XRD patterns in Figure 2.8, the post-run clay from experiment EBS-2 look essentially the same as the pre-experiment clay and the post-run clay of experiment EBS-1. Mineral concentrations for experiment EBS-2 are presented in Table 2.1. The mineral phases smectite and clinoptilolite occur in significant amounts in both samples. Minor amounts (< 5 wt. %) of quartz, cristobalite (or opal-CT), muscovite, potassium feldspar and albite also occur in both samples. Diffraction patterns of both untreated and glycolated smectite patterns, indicates that no illite or illite/smectite is present (Figure 2.12). If illite was present, there would be a significant 8.8 ^{o}2θ peak.

132
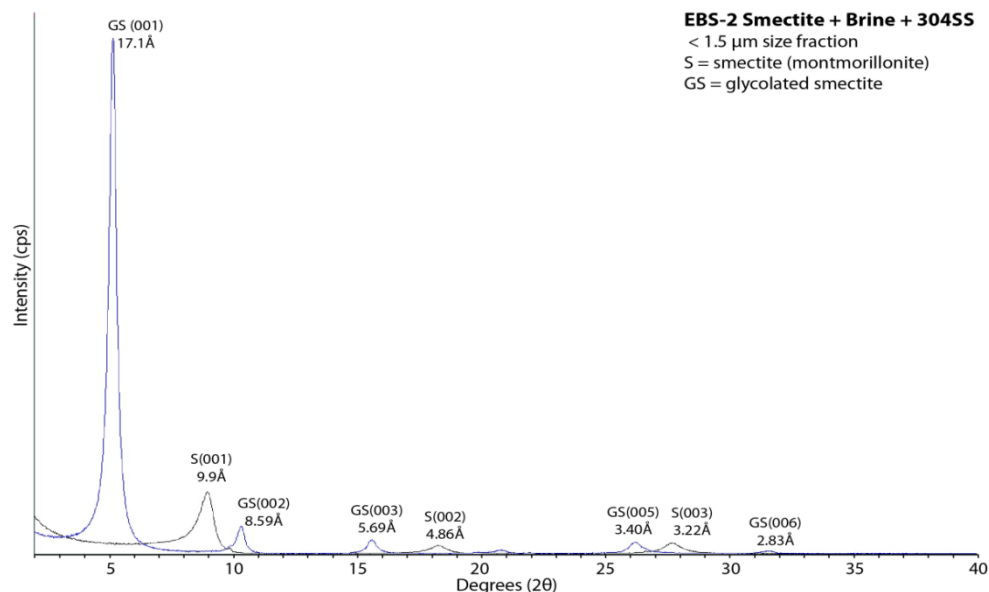
Figure 2.12. Smectite analysis of post EBS-2 experiment.

However, some mineral changes (alterations) can be seen with optical microscopy and SEM images. SEM indicates the presence of opal in the EBS-2 reaction products, which is rare in the starting bentonite. A few of the feldspar phenocrysts fragments appear to be heavily altered in thin-section with what appears to be late stage growth of euhedral clinoptilolite. There also appears to be evidence of late stage low-temperature feldspar growth (Figure 2.13a). The chemistry of the authigenic feldspar (Figure 2.13b) varies from the preexisting ash flow phenocrystic feldspar fragments (Figure 2.10b). SEM images and EDX analyses show that post-experiment montmorillonite has a different morphology (Figure 2.14a) and very slightly different ratio of alkali elements compared to the pre-experiment montmorillonite (Figure 2.14b).

The most significant mineral phase that developed during this experiment is a layer of chlorite on the 304 SS coupon slices. Analysis of the dark coating on the coupons by XRD are shown in Figure 2.15a. The unidentified salt was a precipitation product during quenching of the experiment. This same dark coating was imaged by SEM (Figure 2.15b) and qualitatively analyzed by EDX (Figure 2.15c).
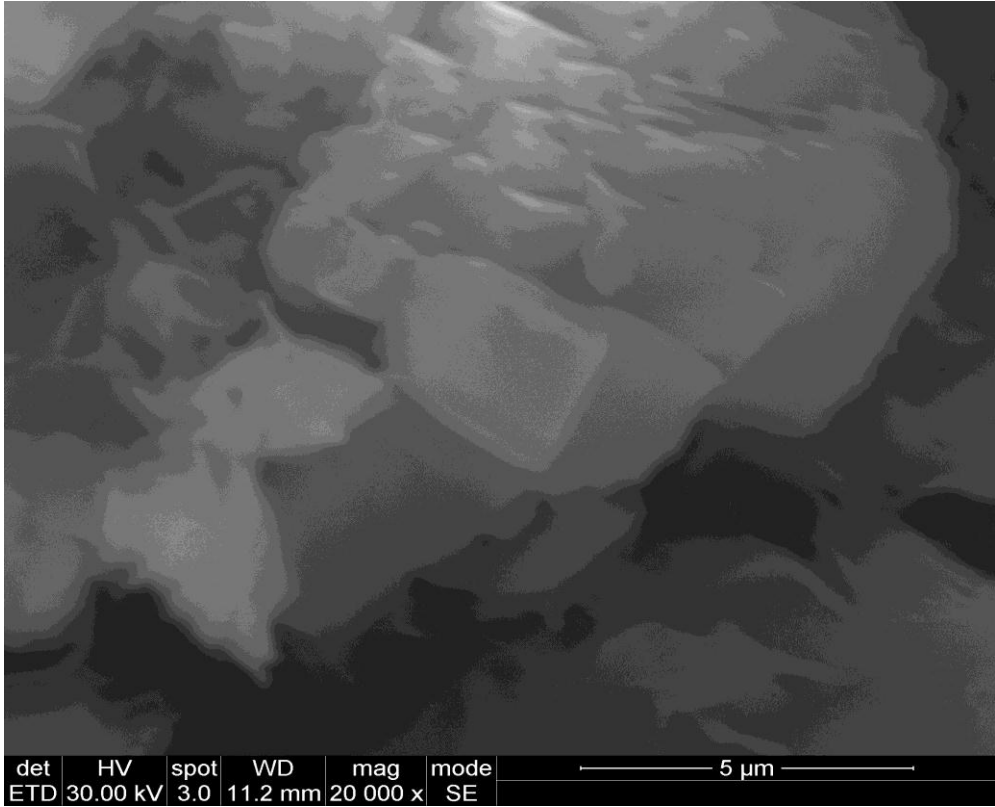
Figure 2.13a. SEM image of newly formed feldspar in EBS-2.
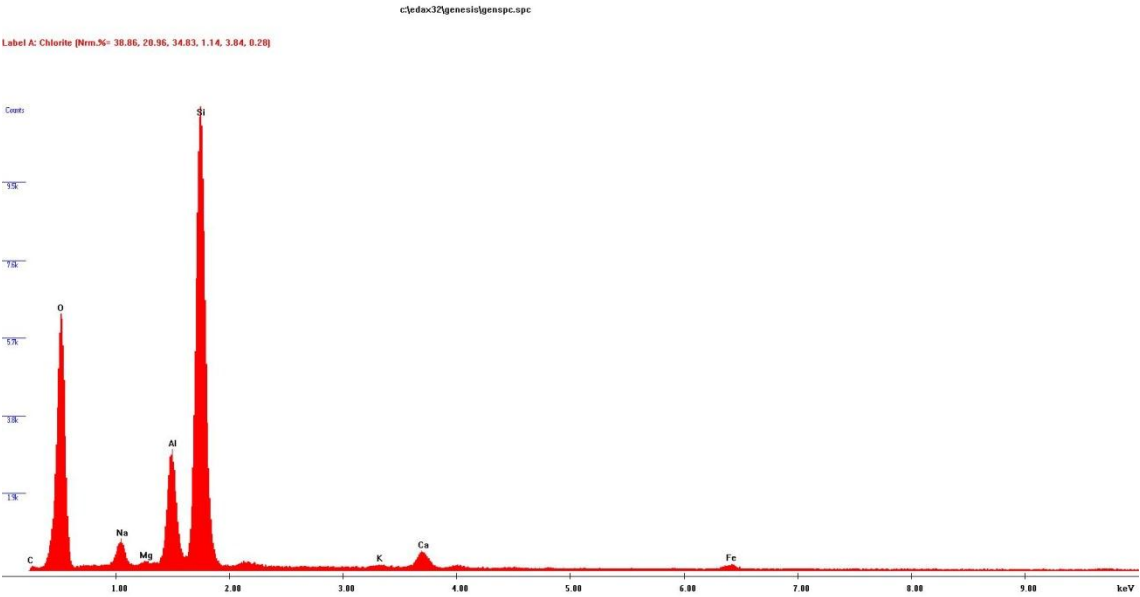
Figure 2.13b. EDX spectra of newly formed feldspar rhombs in EBS-2. Note decrease in K compared to the phenocrystic feldspar of Figure 2.13a.
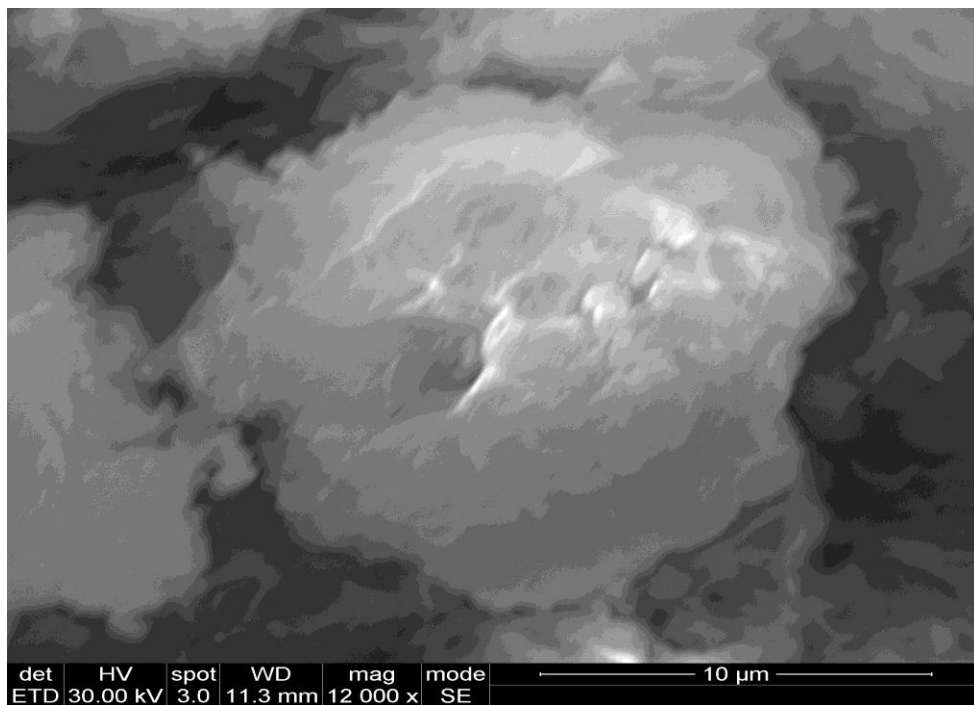
Figure 2.14a. SEM image of montmorillonite from experiment EBS-2 subjected to increased pressure (150 bar) and temperature (300 ºC). Note different morphology compared to the pre-run montmorillonite.
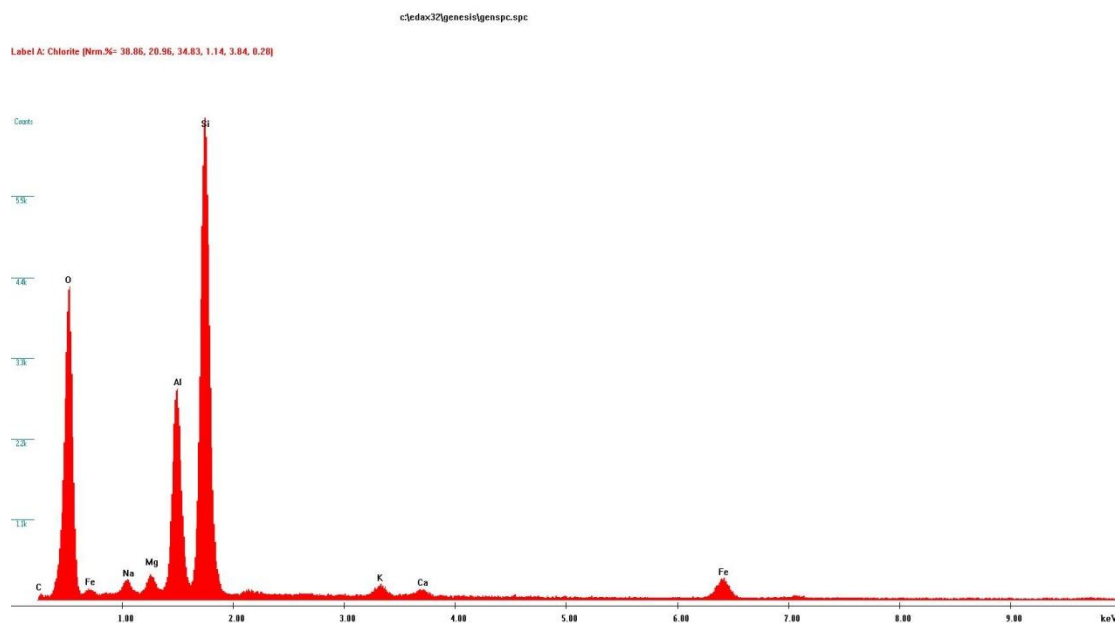
Figure 2.14b. EDX spectra of montmorillonite from experiment EBS-2 subjected to increased pressure (150 bar) and temperature (300 ºC). Note slight increase in Ca and K, decrease in Na compared to Figure 2.10b.
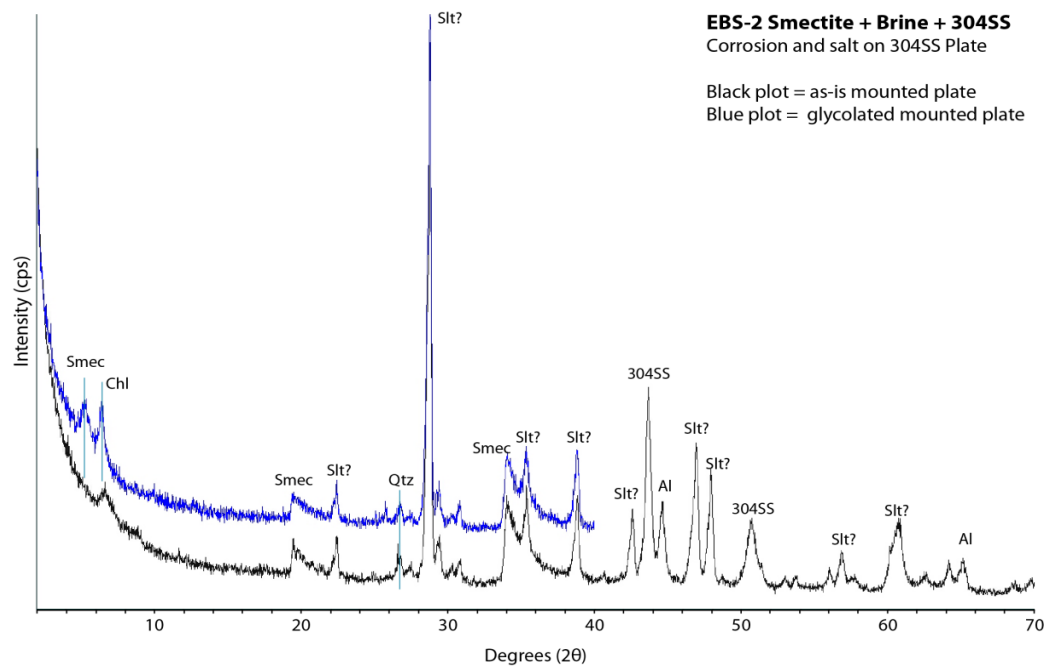
Figure 2.15a. XRD pattern of the chloritized 304 SS coupon. Blue pattern is the glycolated sample showing the expansion of the smectite phase. Note the chlorite peak at 6.2 ^{o}2θ in the blue pattern. Abbreviations used are Smec=smectite, Chl=chlorite, Slt?=salt, Al= aluminium holder, 304SS= Fe from steel
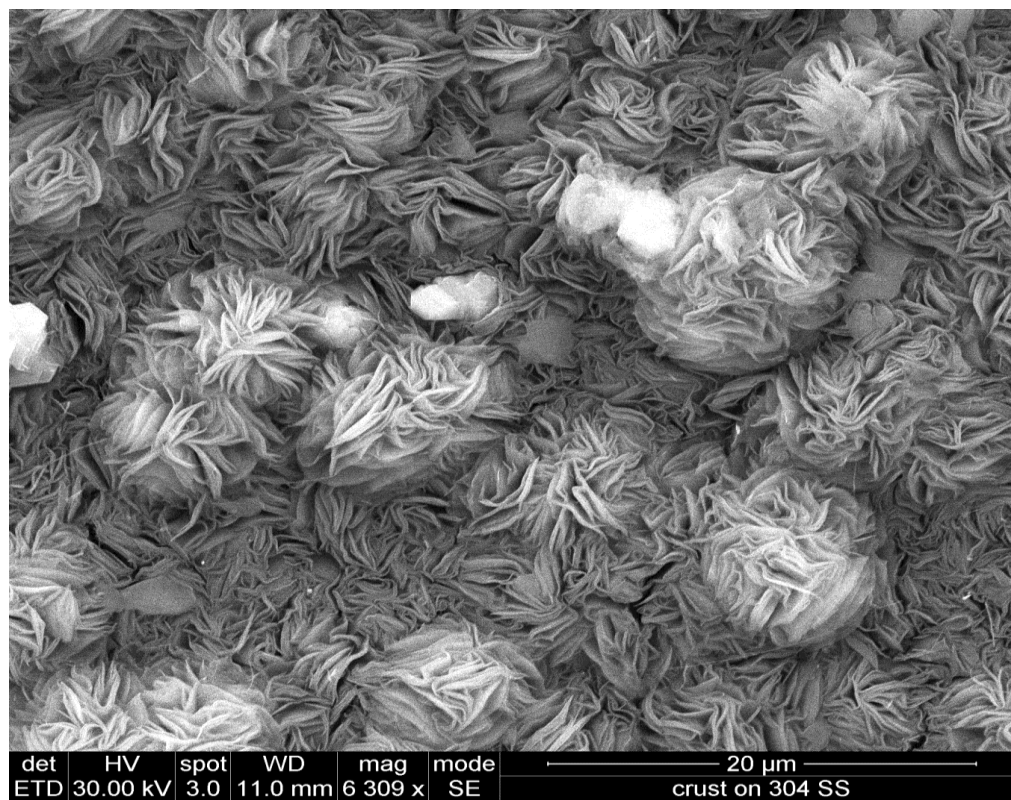
Figure 2.15b. Chlorite layer on 304 SS coupon – EBS-2

136
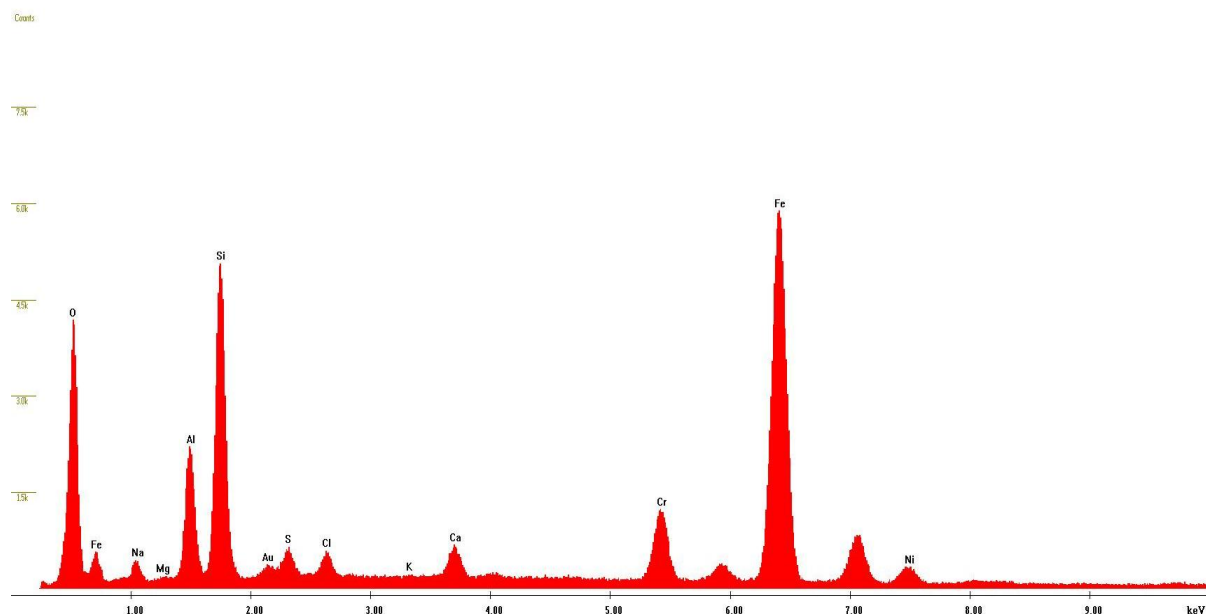
Figure 2.15c. EDX spectra of chlorite layer on 304 SS coupon – EBS-2. The major Fe peak and Cr, Ni minor peaks are most likely due to penetration of electron beam into the 304SS.

Aqueous Geochemistry

The aqueous geochemistry changes produced by this experiment are reflected in Figure 2.16. The solution chemistry evolved in a very similar manner to that of EBS-1. Potassium shows a rapid decline in concentration with increasing time while calcium shows a slight decrease in concentration. Sodium is released into the brine most likely from smectite and seems to be time dependent. However sodium appears to transfer back to a solid phase at 200°C causing a decrease in the brine's sodium concentration. Aqueous silica appears to be equally dependent on both time and temperature for its release into solution. Higher concentrations of aqueous silica are observed with increasing reaction temperatures while its concentration drops rapidly during the quenching of the experiments. This change in aqeous silica concentrations is probably due to the dissolution of silicate minerals and precipitation of opal-CT.

137
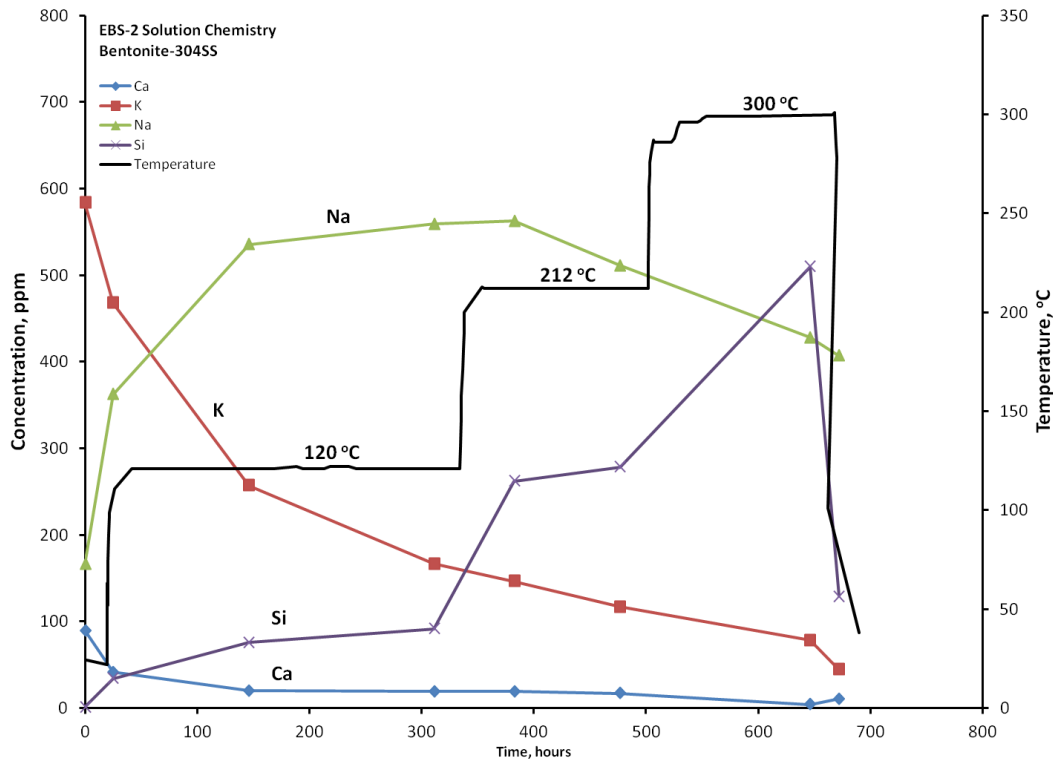
Figure 2.16. Evolution of the EBS-2 aqueous solution chemistry with respect to time and temperature. Changes in solution chemistry are very similar to the observed EBS-1 solution chemistry. The only difference is that the Na concentration peaks earlier and starts to decrease at the 212 °C range. Note the large decrease in K and slight decrease in Ca with time relative to the original brine chemistry (t = 0). There is a substantial increase in both Si and Na concentrations with time. It appears that the Si increase is closely associated with the temperature increases.

The occurrence of H_2S gas was observed in the brine aliquots during sampling. SO_4^{2-} concentration increases to a maximum of 197 ppm in solution during the EBS-2 experiment. It is believed that the gas may have been created by the breakdown of gypsum (Reaction 2.13) with increasing temperature.

The sampled aqueous phase compositions of these experiments were evaluated using activity-activity phase diagrams. These diagrams were generated using the Geochemist Workbench (v.8.0.8) software and associated thermodynamic database at the temperatures and pressures associated with each sampling. The activity coefficients for the activity calculations were assumed to be 1.0 for simplification. These calculations also include preliminary data from EBS-3 and EBS-4 experiments.

Changes to the solution chemistry are fairly consistent between the different EBS experiments. Increasing reaction temperatures is associated with increased silica solubility and decreased aNa^+/aH^+ ratios (Figures 2.17a and b). The decrease in the aNa^+/aH^+ ratio is primarily due to decreasing pH during the experiment even though there is an increase in the aNa^+ from the K^+ for Na^+ exchange in the smectite. The shift in solution chemistry is accompanied by a shift in the mineral stability fields as temperature increases (Figures 2.17a and b). The solution chemistry follows the albite-zeolite (clinoptilolite or mordenite) equilibrium line as the reaction temperatures progress to 300^oC (the 212^oC phase diagram is not presented, however the data is plotted in Figure 2.17a). The lack of significant change in solution chemistry composition with

respect to the albite-zeolite stability fields along with relative short reaction times may explain why there are no major changes in the zeolite and feldspar mineralogy.
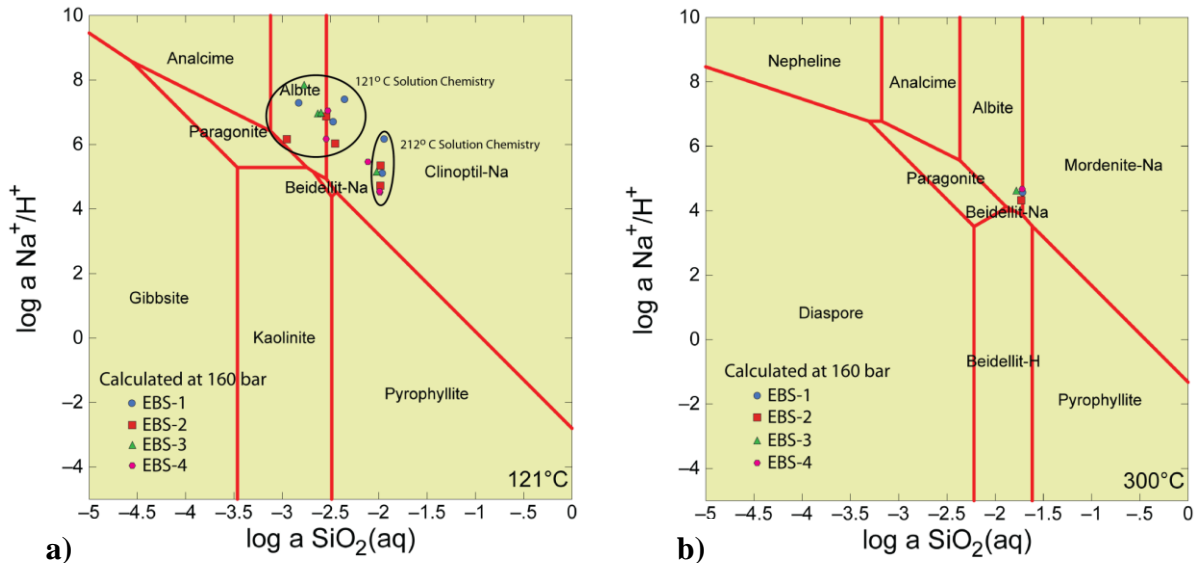
Figure 2.17. a) Log aNa⁺/aH⁺ and Log aSiO₂₍aq₎ data from the 121 and 212 °C EBS (1-4) solution chemistries plotted on a 121°C Na-H₂O-SiO₂ phase diagram. b) 300°C EBS (1-4) solution chemistries plotted on a 300°C Na-H₂O-SiO₂ phase diagram.

The silica activity in the EBS experiments is controlled not only by quartz, but also by cristobalite and opal-CT. This is observed by the continual increase in silica activity across the quartz, cristobalite, and amorphous silica stability fields (Figure 2.18). The silica activity gradually becomes supersaturated with respect to quartz and cristobalite as the temperature increases and eventually becomes supersaturated to all silica phases upon quenching to 22°C. Any one of the silica phases could precipitate at the quenching temperature causing the slight decrease in silica activity.
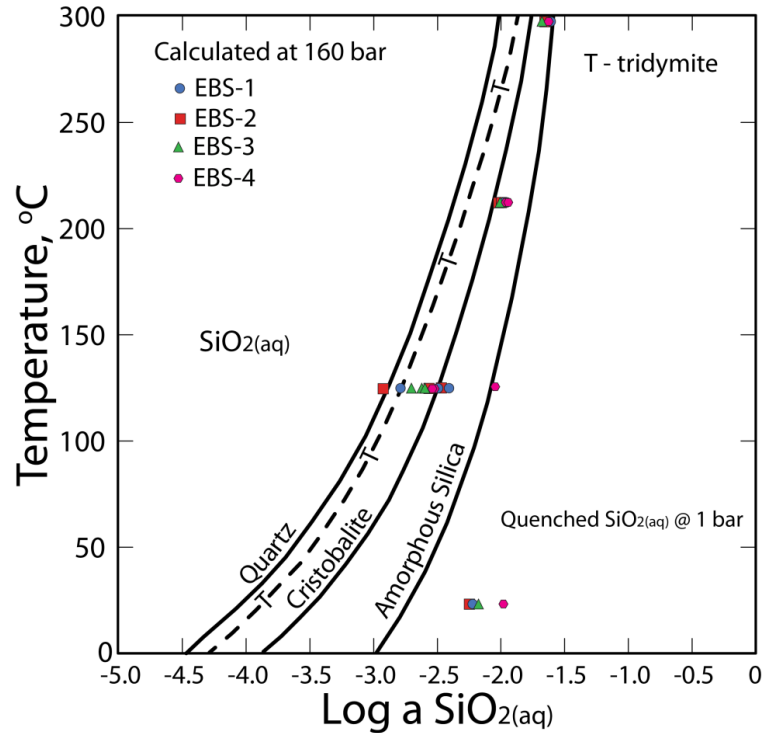
Figure 2.18. Log aSiO$_{2(aq)}$ data from the EBS (1-4) solution chemistries plotted on a Log aSiO$_2$-temperature phase diagram.

These changes in the Na$^+$ (and K$^+$) and aqueous silica activities have substantial implications on the bulk mineralogy of the bentonite barrier system. Studies (Roberson and Lahann, 1981; Smyth, 1982; Bish and Aronson, 1993; Benning et al., 2000) have linked changes in the solution alkalinity along with silica activity with both smectite and zeolite stability. Roberson and Lahann (1981) showed through experimental data that increasing Ca^{2+}, Na$^+$, and Mg^{2+} activities significantly retards the rate of smectite illitization. Therefore, increasing the Na$^+$ and Ca^{2+} activities within the EBS reactions is one possible reason for no illite formation. Aqueous silica activity, controlled by silica minerals (quartz, cristobalite, opal-CT), is one major determining factor in the stability of zeolite minerals in a saturated environment (Benning et al., 2000). Clinoptilolite is not stable with respect to albite or analcime when the silica activity is controlled by quartz. When amorphous silica or opal-CT controls the silica activity then clinoptilolite is not stable with respect to mordenite. The shifting silica activity towards amorphous silica or opal-CT saturation in the EBS experiments would indicate that as temperature increases mordenite is becoming the more stable zeolite phase. Further research is needed to better understand how the silica activity controls the illitization of smectite because this mineral alteration is also significantly influenced by Al^{3+}/Si^{4+} ratios.

2.3.3   Discussion

The understanding of clay degradation and alteration at high temperatures and pressures is critical to the success of repositories with high heat loads. Items such as mineralogical changes from smectite to illite will change the material properties of clay backfill. The sorptive qualities of clay buffers may be compromised, depending on what minerals form at high temperature. Other unknown mineral phases created at high pressures and temperatures may determine the need for other engineered barriers, repository gallery design or restricted heat loads. These are

just a few of the reasons that the experimental program for FY-11 and FY-12 was designed to take advantage of the seminal work of Mosser-Ruck et al. (2010).

The major mineralogical changes identified during the high pressure, temperature experiments are both geologically interesting and significant to EBS component stability and interface chemistry. Four mineralogical reactions are of note in these experiments. The reactions are 1) gypsum breakdown to H_2S gas, 2) aqueous silica liberation resulting in subsequent silica (SiO_2) precipitation, 3) clay retrograde reactions to clinoptilolite during quench, and 4) chlorite layer growth on steel surface. Of these reactions observed, the retrograde zeolite formation and chlorite growth on steel coupons are most significant to EBS research.

As noted in the results section above, during extraction of brine samples from the experiments, it was noted that H_2S gas was a common product. It is speculated that the decomposition of gypsum during heating under reducing conditions has created the gas (Reaction 13). This reaction is expected since the H_2S production occurs above the thermal stability of gypsum (Freyer and Voigt, 2003). The reaction listed may have occurred due to kinetically slower reactions to solids. SO_4^{2-} concentrations increase to maximum values of 352 ppm and 197 ppm in experiments EBS-1 and EBS-2, respectively. This reaction may also be a partial cause of the lower pH of the brine chemistry with time.

Wersin et al. (2007) noted that bentonite breakdown may begin at low temperatures and precipitate SiO_2 at temperatures just over 100 ^{o}C. The brine chemistry of the two experiments indicates that there is significant SiO_2 in solution (> 1000 ppm) at 300°C, which then precipitates upon quenching. The quartz phases observed in thin-section (with botryoidal or spherical form) that formed after cooling from 300°C are first cristobalite and then tridymite. These quartz phases are commonly formed in ash flow composition (rhyolitic) rocks during devitrification and subsequent vapor phase alteration (Caporuscio et al., 2012).

As discussed earlier, Mosser-Ruck et al. (2010) performed high temperature experiments of iron clay reactions at variable pH and liquid/solid ratios. At 300 ^{o}C, their experiments produced:

dioctahedral smectite = Fe-rich saponite =trioctahedral chlorite + feldspar + zeolite .

Our experiment EBS-2 duplicated most of their run conditions with the following exceptions. First, the fluid phase chemistry was slightly different, in that Mosser-Ruck et al. (2010) was NaCl rich and contained no K. Second, their clay was separated and cation exchanged, whereas our clay was straight from a mine and unrefined. Third, our experiment was buffered at the magnetite/iron univarient line. Fourth, our experiment was run at 150 bar, to mimic hydrostatic pressures of a deep geologic repository. Fifth, Mosser-Ruck et al. (2010) used fine iron shaving to enhance reaction rates while our experiment incorporated 304 SS coupon slices. Below is the reaction that occurs in experiment EBS-2:

$$\text{Montmorillonite + Iron = Chamosite + Feldspar + Clinoptilolite}$$

$$10(Na,Ca)_{0.33}(Al_{1.67}, Mg_{.33})\, Si_4O_{10}(OH)_2 \cdot 2H_2O + 5\, Fe = (Fe,Mg)_5AlSi_3O_{10}(OH)_8 +$$

$$(Na,Ca)(Al,Si)_4O_8 + (Na,Ca)_2Al_3Si_2Si_{13}O_{36} \cdot 12H_2O$$
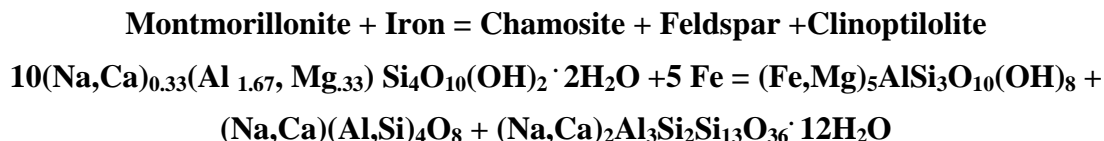
Chamosite is the Fe-end member of chlorite, which at the moment is the assumed phase until compositional data is obtained with electron microprobe analysis. Although Mosser-Ruck et al. (2010) does not list iron in the reactant side of the equation, it is a known component of their experiment. In essence we have produced the same resultant mineral assemblage, even though

the clay and water compositions vary slightly. This indicates the flexible chemistry and mineralogy of low temperature rhyolitic rocks. Since the samples are Si, Al, Ca, Na, K –rich, it allows for easy cation exchange between solid solution feldspars, clays, and zeolites, the primary minerals in this rock composition. The pre-experimental run clays have a minor feldspar component that is slightly different in composition (K-bearing) than post experiment feldspars (K-poor). The liberated K would most likely be incorporated into the smectite. No smectite illitization was observed in these reactions. However, it appears that K-smectite was produced possibly providing a precursor to illitization. Illite formation occurs from Al^{3+} substitution into the tetrahedral site for Si increasing the layer charge. It is unclear if the reaction times were sufficient for the bentonite illitization at 212° and $300\ ^oC$ or the optimal conditions for illite formation were obtained.

In the Mosser-Ruck et al. (2010) equation listed above (equation #8), they describe zeolites as a product. Our study shows the zeolite clinoptilolite both as a reactant and a product. Since clinoptilolite breaks down above 150^oC (Smyth, 1982), it is assumed zeolite breaks down during the high temperature portion of the experiment and then recrystallizes during the quench portion of the experiment. This is supported by the late-stage appearance of small, euhedral clinoptilolite (Figure 2.10c). This is significant in that even if a repository with high heat loads reaches temperatures above 150^oC and precursor zeolites on the clay backfill break down, experiments EBS-1 and EBS-2 indicate that zeolites will form in the backfill when temperatures cool down after the maximum heat pulse.

Mosser-Ruck et al. (2010) found chlorite growth within the clay body, whereas we only observed chlorite growth on the steel surface (Figure 2.15b). The difference is that Mosser-Ruck et al. (2010) dispersed iron shavings into the clay material, while we inserted slices of 304SS into the clay matrix. With the chlorite growing at this interface, the phase took advantage of a readily available iron source. The chlorite growth may have significance in protecting the steel outer casing of a waste canister by acting as a passivating agent. Fe-chlorite may form at the lower temperatures of 180 -250 ^oC depending on the bulk chemistry of the system, whereas Mg-chlorite starts to break down around 768^oC and 3.5 kb (Fawcett and Yoder, 1966; Hutcheon et al., 1980). Fe-chlorites would break down at slightly lower temperatures. This indicates that chlorite is an extremely durable mineral with a large temperature stability range of approximately 500^oC.

2.3.4   Conclusions

Characterization and understanding of EBS component interactions is critical for modeling of high heat load repository environments. Our experimental results so far (brine-clay and brine-clay-304SS) have already provided information on bentonite behavior at the high pressures and temperatures possible for future repositories. For decades, experimental research on EBS components has been limited to temperatures near 100^oC. This was justified because both national and international nuclear repository programs limited repository heat load criteria to be below the boiling point of water. Recently, repository programs have considered higher heat loads to maximize canister packing, minimize the number of canisters and therefore, reduce repository footprints. Mosser-Ruck et al. (2010) initiated EBS component experiments at higher temperatures. The authors provided strong results, however, the clays used (clean, end-member by cation exchange) were not those that would be used as backfill/buffer material (mine run clays). We then ran four proof-of-principle experiments for one month duration each to investigate clay/canister interactions at repository conditions. The EBS materials investigated

are: are 1) brine-clay (EBS-1), 2) brine-clay-304SS (EBS-2), 3) brine-clay-316SS (EBS-3), and 4) brine-clay-Cu (EBS-4). Pressure was controlled at ~150 bar and brine sampling occurred at 120, 210, and 300 ^{o}C.

Characterization of EBS-1 and EBS-2 provided insights into the use of mine run bentonite clay as a backfill/buffer. The original clay was predominantly smectite with no illite or illite/smectite components. We observed no bentonite illitization upon exposure to brine under increased pressure and temperature conditions. Even though K cations were mobile during the experiments and being incorporated into various minerals, illite was not generated. The most plausible explanations include competition for K among aluminosilicates and the fact that Al did not substitute for Si in the tetrahedral site of the smectite structure. Wersin et al. (2007) concluded that SiO_2 is liberated as clays are heated above 150°C and this was documented in our experiments. First, high amounts of Si were liberated into the fluid phase (> 1000 ppm) and then precipitated during the quenching of the experiment. The precipitated silica, even if deposited as opal, transformed to cristobalite and tridymite as cooling progressed. This is significant in that these silica phases are much less soluble than opal. Hence once a repository peaks in temperature and then cools, the precipitated SiO_2 will form stable silica phases. This may potentially seal heating fractures in the clay backfill.

Zeolites, a radionuclide sorbing set of minerals, were a portion (~ 12 wt.%) of the pre-experiment clay sample. After the experimental runs to 300 ^{o}C, post characterization of the clay revealed that only slightly lesser amounts of zeolite exist (8 to 10 wt%). This is very useful information for repository design, since the zeolite identified, clinoptilolite, is unstable above 150 ^{o}C. Hence, the zeolite broke down at high temperatures but recrystallized as the quench event occurred. This was borne out in SEM images that showed clinoptilolite as a very late stage growth mineral. Therefore, this may indicate that even if zeolites break down during the high temperature thermal pulse of a repository, zeolites may form again as the repository inventory cools off and perform as radionuclide sorbing phases. Further investigation is needed to characterize this reaction in detail.

One unexpected result of the experiments was the production of H_2S gas during heating. This was observed both during sampling events (odor) and with brine geochemistry. Mostly likely this was due to the breakdown of gypsum during the experiments. Further experiments are needed to quantify this reaction and observe if this gas has corrosive effects on steel.

The nucleation and production of a chlorite layer on 304SS during the EBS-2 experiment is a result that has not been previously described. Due to its potential to act as a passivation material and prevent corrosion of the steel coupon in the experiment, we will pursue further research on the kinetics and growth rate of chlorite formation on steel. Such an effect may be quite useful to materials degradation prediction, along with providing modeling parameters for the UFD campaign.

Work in an experimental hydrothermal laboratory has also confirmed that experiments can be time consuming and frustrating when experiments fail. At present, all four experiments are finished, but only the two listed above (brine-clay and brine-clay-304SS) will have the run products fully characterized.

Described next are some of the solutions to laboratory problems encountered this year and a very brief outline of anticipated experiments for FY13. First, many experiments were delayed due to old/worn equipment and lack of suitable maintenance. As examples, one rocking autoclave

furnace (30 years old) failed and needs to be rewired or replaced. Exit tubes commonly leaked (5 experiments) after experiment builds and pressure checks but during temperature run up to 100 ^oC and subsequent pressurization. A temperature control unit also failed during an experiment. These types of events delayed experiments for months. The solution to these issues is to have a supply of expendable parts, funds for repairs and a part- to full-time technician to stay ahead of potential mechanical problems. Second, the hydrothermal geochemistry lab is shared among three energy disciplines (UFD repository science, carbon sequestration, geothermal tracer studies). Space and timing to perform experiments is at a premium. To lessen this issue LANL requested (and was allocated) seed money to build six cold seal reactors and furnaces. With that money the furnaces were purchased and design of the reactor vessels was accomplished. Fabrication of the reactor vessels and ancillary parts is underway. Since these vessels and the pressure lines are not stock items but rather hand manufactured, passing the safety envelope (electrical and pressure) will be time consuming. It is projected that the system will be operational in mid FY13. These smaller vessels will allow for much more precise experiments to be accomplished.

2.3.5   FY12 - FY13 experimental program

The objective for the remainder of FY12 is to characterize the results of EBS-3 and EBS-4 and perform further experiments to determine kinetic effects on high temperature phases. Experiment EBS-3 quenched on April 25, 2012 and EBS-4 is expected to quench on May 9, 2012. Since there are now major questions raised about illitization of smectites in our results, we will repeat the EBS reactions at a constant 300º C for 4-5 weeks. This will allow us to investigate the kinetics of both chlorite formation and the ability for smectite to evolve to illite over time.

For FY13 we propose to begin dry clay experiments to investigate clay physical and chemical characteristics in dry systems. Concurrently, we will run the EBS reaction at 1.3 kbar under the same experimental conditions described here. These experiments would more closely duplicate deep borehole repository conditions. These sets of experiments, along with 100°, 200 ºC quenching experiments and characterization should allow us to gather information to unravel the nuances of SiO_2 precipitation and aluminosilicate formation in clay buffer / backfill scenarios. The information will 1) shed light on the ability for SiO_2 to close fractures and or prop open clay structures and 2) give insights on cation transfer and exchange between the aqueous geochemistry and aluminosilcate matrix. If all experiments are successful, we would propose to then add a crystalline host rock component to the experiment to fully duplicate a repository setting.

Other research factors we would like to emphasize in FY13 are to 1) investigate alternate methods for the characterization of the solid phase reaction products, e.g., TEM, Raman spectroscopy, neutron scattering techniques (LANSCE facility), Zeta potential measurements, and various synchrotron techniques. 2) Expand the EBS test plan to investigate how various organic acids and other clay minerals (i.e., palygorskite and sepiolite) will function in an EBS system. These experiments will be completed using smaller Parr reaction vessels because the ability to run several samples at a time, thereby increasing the number of parameters that can be tested. 3) Characterize the interfacial kinetics in the clay-brine and clay-brine-SS systems. In this task, we can also characterize the sorption and desorption of the generated colloids to/from the interfaces (brine-SS interface for example) and how this affects further development of the chlorite layer we have observed.

The proposed lines of study are presented in bullet form below for easy reference.

- Finish 300º C experiment characterizations.
- Repeat EBS reactions at 300º C for 4 -5 weeks to investigate illitization.
- Investigate the chlorite formation kinetics.
- Begin dry/wet clay/sand runs.
- Run the EBS reaction at 1.3 kbar under the same experimental conditions previously tested.
- 100°, 200 ºC quenching experiments and characterization
- Further investigation of SiO_2 precipitation and aluminosilicate formation.
- Incorporate new components (ie, crystalline rock compositions) in the reaction matrix.
- Investigate further methods for the characterization of the solid phase reaction products, e.g., TEM, Raman spectroscopy, neutron scattering techniques (LANSCE facility), Zeta potential measurements, and various synchrotron techniques.
- Expand the EBS test plan to investigate how various organic acids and other clay minerals (i.e., palygorskite and sepiolite) will function in an EBS system. These experiments will be completed using smaller Parr reaction vessels because the ability to run several samples at a time, thereby increasing the number of parameters that can be tested.
- Characterization of the interfacial kinetics in the clay-brine and clay-brine-SS systems. In this task, we can also characterize the sorption and desorption of the generated colloids to/from the interfaces (brine-SS interface for example) and how this affects further development of the chlorite layer we have observed. I am thinking that we can use our direct visualization high P-T system to conduct very informative **dynamic** experiments that will complement the hydrothermal high pressure and temperature experiments.

2.4 References

Altaner, S.P., and Ylagan, R.F., 1997, Comparison of Structural Models of Mixed-Layer Illite-Smectite and Reaction Mechanisms of Smectite Illitization. Clays and Clay Min., Vol. 45, p. 517-533.

Altaner, S.P., Weiss, C.A., Jr., and Kirkpatrick, R.J., 1988, Evidence from ^{29}Si NMR for the structure of mixed-layer illite/smectite clay minerals. Nature, Vol. 331, p. 699-702.

Benning, L.G., Wilkins, R.T., and Barnes, H.L., 2000, Solubility and stability of zeolites in aqueous solution: II. Calcic clinoptilolite and mordenite. American Mineralogist, **85**, 495-508.

Bish, D.L. and Aronson, J.L., 1993, Paleogeothermal and paleohydrologic conditions in silicic tuff from Yucca Mountain, Nevada. Clays and Clay Minerals, **41**, 148-161.

Chipera, S.J. and Bish, D.L. 2002, FULLPAT: a full-pattern quantitative analysis program for X-ray powder diffraction using measured and calculated patterns. J Appl Crystallogr 35:744–749.

Caporuscio, F.A., Gardner, J.N., Schultz-Fellenz, E., Kelley, R., 2012, Fumarolic pipes in the Tshirege member of the Bandelier Tuff, Pajarito Plateau, Jemez Mountains, New Mexico. Bulletin of Volcanology, on line Feb. 28, 2012, DOI 10.1007/s00445-012-0582-4.

Cathelineau, M., Mosser-Ruck, R., and Charpentier, D., 2001, Interactions fluides/argilites en conditions de stockage profond des déchets nucléaires. Intérêt du couplage expérimentation/modélisation dans la compréhension des mécanismes de transformation des argiles et la prédiction a long terme du comportement de la barrière argileuse. Pp. 305_341 in: Actes des Journées Scientifiques ANDRA. EDP Sciences, Nancy, France.

Eberl, D.D., Blum, A.E., and Serravezza, M., 2011, Anatomy of a metabentonite: Nucleation and growth of illite crystals and their coalescence into mixed-layer illite/smectite. Am. Min., Vol. 96, p. 586-593.

Fawcett, J.J., and Yoder, H.S., 1966, Phase Relationships of Chlorites in the System MgO-Al2O3-SiO2-H2O. Am. Min., Vol. 51, p. 353-380.

Ferrage, E., Vidal, O., Mosser-Ruck, R., Cathelineau, M., and Cuadros, J., 2011, A reinvestigation of smectite illitization in experimental hydrothermal conditions: Results from X-ray diffraction and transmission electron microscopy. Am. Min., Vol. 96, p. 207-223.

Freyer, D., and Voigt,W., 2003, Crystallization and Phase Stability of $CaSO_4$ and $CaSO_4$ Based Salts. Monatshefte fur Chem, Vol. 134, p. 693-719.

Huang, W.-L., Bassett, W., and Wu, T., 1994, Dehydration and hydration of montmorillonite at elevated temperatures and pressures monitored using synchrotron radiation. Am. Min., Vol. 79, p. 683-691.

Hutcheon, I., Oldershaw, A., and Ghent,D., 1980, Diagenesis of Cretaceous sandstones of the Kootnay Formation at Elk Valley (southeastern British Columbia) and Mt Allen (southwestern Alberta) Geochem Cosmochem Acta, V. 44, p. 1425-1435

Jové-Colón, C. F., 2010, Disposal Systems Evaluations and Tool Development – Engineered Barrier System (EBS) Evaluation. Sandia National Laboratory, Department of Energy, Fuel Cycle Reasearch and Development, Used Fuel Disposition Campaign Report, 199 pp.

Kluska, J.M., Fritz, B., and Clement, A., 2002, Predictions of the mineralogical transformations in a bentonite barrier surrounding an iron radioactive container. International Meeting, Clays in Natural and Engineered Barriers for Radioactive Waste Confinement, December 9–12, 2002,Reims, France: O-10b-5, pp. 153_154.

Laine, H., and Karttunen, P., 2010, Long-Term Stability of Bentonite: A Literature Review. Posiva Oy Working Report 2010-53 (www.posiva.fi/files/1345/WR_2010-53web.pdf), 132 p.

Lantenois, S., Lanson, B., Muller, F., Bauer, A., Jullian, M., and Plancon, A., 2005, Experimental Study of Smectite Interaction with Metal Fe at low Temperature: 1. Smectite Destabilization. Clay and Clay Min., V53, # 6, pp 597-612.

McCarty, D.K., Sakharov, B.A., and Drits, V.A., 2009, New insights in smectite illitization: A zoned K-bentonite revisited. Am. Min., Vol. 94, p. 1653-1671.

Meunier, A., Velde, B., and Griffault, L., 1998, The Reactivity of Bentonites: a Review.An Application to Clay Barrier Stability for Nuclear Waste Storage. Clay Min., V33, pp 187-196.

Montes, H.G., Fritz, B. Clement, A., and Michau, N., 2005, Modelling of transport and reaction in an engineered barrier for radioactive waste confinement. Appl. Clay Sci. V29, pp 155-171.

Mosser-Ruck, R., Cathelineau, M., Guillaume, D., Charpentier, D., Rousset, D., Barres, O., and Michau, N., 2010, Effects of Temperature, pH, and Iron/Clay and Liquid/Clay Ratios on Experimental Conversion of Dioctahedral Smectite to Berthierine, Chlorite, Vermiculite, or Saponite. Clay and Clay Min., V58, # 2, pp 280-291.

Pusch, R., and Madsen, F.T., 1995, Aspects on the Illitization of the Kinnekulle Bentonites. Clays and Clay Min., Vol. 43, p. 261-270.

Roberson, H.E. and Lahann, R.W.,. 1981, Smectite to illite conversion rates: Effects of solution chemistry. Clays and Clay Minerals, **29**, 129-135.

Smyth, J. R., 1982, Zeolite stability and radioactive waste isolation in n zeolite-bearing volcanic rocks. Jour. Geol. V 90, p. 195-201.

Šucha, V., Kraus, I., Gerthofferova, H., Petes, J., and Serekova, M., 1993, Smectite to illite conversion in bentonites and shales of the East Slovak basin. Clay Minerals, Vol. 28, p. 243-253.

Tang, A.M., and Cui Y.J., 2010, Effects of mineralogy on thermo-hydro-mechanical parameters of MX80 bentonite. Jour. Rock Mech. and Geotech. Engin., Vol. 2, p. 91-96.

Taniguchi, N., and Kawasaki, M., 2008, Influence of sulfide concentration on the corrosion behavior of pure copper in synthetic seawater. Jour. Nuc. Materials, V379, pp 154-161.

Velde B. and Lanson B., 1993, Comparison of I-S transformation and maturity of organic matter at elevated temperature. Clays Clay Min. V41, pp 178 183.

Wersin, P., Johnson, L.H., and McKinley, I.G., 2007, Performance of the Bentonite Barrier at Temperatures beyond 100°C: A Critical Review. Phys. Chem. Earth, V32, pp 780-788.

Whitney, G. and Velde, B., 1993, Changes in particle morphology during illitization: an experimental study. Clays and Clay Min., V41, 209–218.

Wu, T.C., Bassett, W., Huang, W.L., Guggenheim, S., and Koster Van Groos, A.F., 1997, Montmorillonite under High H_2O pressures: Stability of Hydrate Phases, Rehydration Hysteresis, and the Effect of Interlayer Cations. Am. Min., Vol. 82, p. 69-78.

Xia, X. , Idemitsu, K., Arima, T., Inagakia, Y., Ishiderab,T., Kurosawa, S., Iijima, K., and Sato, H., 2005, Corrosion of carbon steel in compacted bentonite and its effect on neptunium diffusion under reducing condition. App. Clay Sci. V28, pp 89-100.

Thermodynamic Database and Model Development: Cement Leaching and Clay Hydration Properties
(Part IV)

1. Thermodynamic Data and Modeling of Cement Leaching and Clay Hydration

1.1 Thermodynamic Modeling Approach to Leaching of C-S-H (Ordinary Portland Cement)

Cementitious materials and associated solids are ubiquitous to EBS design concepts where these are used as backfill/buffer, seals, plugs, and linings in tunnels and disposal galleries. The interaction of cementititous solids with other barrier materials and aqueous fluids in the near-field environment is important to the generation of alkaline solutions that can aggressively react with silica-bearing phases and other EBS materials. Chemically deleterious conditions conducive to cement leaching are an important aspect of the long-term performance of engineer barriers (Pabalan et al., 2009). The extensive review of Pabalan et al. (2009) discusses important characteristics of cement degradation relevant to engineered barriers used in radioactive waste disposal. For example, the performance of cement-based barriers can be affected by chemical and physical degradation processes. Chemical processes generally include cement corrosion, carbonation, and leaching whereas physical degradation mainly comprises mechanical effects such as thermal cracking or shrinkage as a result of drying. An important example is the cement-brine interactions in salt media where loss of Ca during leaching and formation of Mg and sulfate-bearing phases can affect the cement chemo-mechanical properties (Poole et al., 1993; Tumidajski and Chan, 1996; Wakeley et al., 1993). The results of these studies outline the importance of cement-brine interactions and potential effects to sealing performance. Moreover, there is a knowledge gap on the extent of these effects at high temperatures. There has been some recent work on experimental and modeling efforts on cement-brine interactions in the presence of CO_2 at elevated temperatures (Carroll et al., 2011). However, more experimental work is needed to have a better understanding of cement-brine interactions at anticipated repository conditions for high level waste. These limitations have been outlined in the UFD EBS milestone report for FY11 (Jové Colón et al., 2011).

The current focus in this report is the development of a robust chemical equilibrium model to describe cement leaching as a result of interactions with aqueous solutions. Chemical equilibrium models that describe cement solubility and interactions with other fluids use thermodynamic data of aqueous and solid phases as key inputs. Jové Colón et al. (2011) describes the comprehensive expansion of thermodynamic data for cementitious phases along with revisions of existing data and comparisons between data sets. The compilation of thermodynamic data in this report encompassed those developed for the Yucca Mountain Project (YMP) and the CEMDATA07 database. The latter is an extensive compilation of thermodynamic data for cement solids reported by Babushkin et al. (1985), Matschei et al. (2007), Moschner et al. (2008), Blanc et al. (2010a, b), and Lothenbach et al. (2010; 2008; 2006), and Schmidt et al. (2008). Furthermore, the current effort resulted in the compilation of these data sets for the UFD campaign formatted for integration and used with the Cantera code suite for computation of chemical equilibria. The reader is referred to Jové Colón et al. (2011) for more details of this cement database compilation.

The treatment of cement solubility has been to a large extent limited to pure and/or nearly-pure end member compositions. Such approach simplifies the modeling of cement phase solubility taking advantage of the existing thermodynamic data for end-member composition of cementitious phases. However, cement leaching is a complex process given the incongruent

nature of its solubility when interacting with aqueous fluids. Various efforts on the description of incongruent dissolution of cement-based materials have been proposed with a focus on the leaching of calcium silicate hydrate compounds or C-S-H; commonly referred as ordinary Portland cement. For example, Berner (1987, 1988, 1990, 1992) developed a model for cement leaching to predict the chemistry pore solutions for a fairly wide range of C-S-H gel compositions. As explained by Berner (1992), the aim of this approach is to advance a chemical equilibrium model that can be implemented in existing geochemical codes with relative ease exploiting the capability of aqueous speciation and interaction with the cement phase. However, this constraint the model to be defined by a set of cement components that includes specific solubility products for given C-S-H gel compositions. C-S-H leaching data is relatively scarce and limited to a few studies particularly for leachates having pH $\geq$ 11. Still, the existing cement leaching data is sufficient to identify the distinctive dependency in the solubility trends to the Ca/Si ratio in the solid (Berner, 1988, 1992; Fujii and Kondo, 1983; Greenberg and Chang, 1965; Greenberg et al., 1960; Harris et al., 2002).

Thermodynamic modeling approaches have been advanced to simulate leaching for various C-S-H cement compositions (Borjesson et al., 1997; Carey and Lichtner, 2007; Gartner and Jennings, 1987; Kersten, 1996; Kulik and Kersten, 2001; Lichtner and Carey, 2006; Lothenbach et al., 2010; Soler and Mader, 2010; Sugiyama and Fujita, 2006; Thomas and Jennings, 1998). These studies describe simulation methods and approaches to represent the incongruent behavior of C-S-H leaching that fall into two categories: mass action law equations (e.g., Lippmann functions) and Gibbs energy minimization (GEM) methods. The approach of Thomas and Jennings (1998) involves a GEM method accounting for the equilibria between cement solid and aqueous solution. This model uses the Thermo-Calc code and the Redlich-Kister formulation to compute excess Gibbs energies of the cement phase for a given number of sites defined in a two-constituent sublattice. Kulik and Kersten (2001) advanced an ideal solution model where the system can be described by two C-S-H phases in a binary solid solution. This approach was extended by Kulik (2011) to accommodate the structural intricacies of C-S-H gels advanced by Richardson and Groves (1992). Reardon (1990) adopts the Pitzer model for speciation of constituents in the aqueous phase and a C-S-H whose solubility product is dependent on the Ca/Si ratio in the cement phase. Atkinson et al. (1989) used a GEM method along with a non-ideal solid solution model for C-S-H with amorphous silica and $Ca(OH)_2$ as the pure end-members with tobermorite as an intermediate phase with a Ca/Si of 0.8. Borjesson et al. (1997) also advanced non-ideal solid solution model for C-S-H for Ca/Si > 1. Rahman et al. (1999) also put forward a binary non-ideal solid solution model defined by the Margules formulation with solubility product expressions for $Ca(OH)_2$ and CaH_2SiO_4 that are dependent on Ca/Si ratios. Carey and Lichtner (2007) developed a model based on non-ideal mixing between SiO_2 and $Ca(OH)_2$ end-members for C-S-H. The model in Carey and Lichtner (2007) is based on the method described by Glynn and Reardon (Glynn and Reardon, 1990), and Glynn (2000) for the Lippmann representation (Gamsjager et al., 2000; Lippmann, 1980) of a non-ideal solid solution in equilibrium with an aqueous solution. Sugiyama and Fujita (2006) describes a binary non-ideal solid solution model using SiO_2 and $Ca(OH)_2$ as the end-members over a wide range of Ca/Si ratios. In this model, equations for solubility products of the C-S-H mixed composition are a function of Ca/Si ratio similar to the models of Reardon (1990) and Rahman et al. (1999b). Soler (2007) provides a summary of the thermodynamic approaches to describe the solubility of C-S-H. All these modeling approaches to C-S-H leaching produce adequate representations of the existing experimental data.

The approach taken here follows that of Sugiyama and Fujita (2006) adopting the use of amorphous SiO_2 and $Ca(OH)_2$ as the two end-member phases in a binary non-ideal solid solution and is explained in more in the next section.

1.1.1   Thermodynamic Modeling Using the Cantera Code Suite

Cantera is a general purpose open-source object-oriented constitutive modeling toolkit to simulate problems related to chemical thermodynamics, kinetics, and transport processes (Moffat and Jové Colón, 2009). Cantera can perform similar types of equilibrium speciation calculations as those obtained from computer codes using mass action law formulations (e.g., EQ3/6) in aqueous systems and also simulate interactions between solution, solid, and gas phases. The GEM approach is used by Cantera to compute chemical equilibrium between the considered phases having a distinct set of properties and constituents (Karpov et al., 1997; Kulik et al., 1998; Smith and Missen, 1982). That is, instead of invoking prescribed input mass action law reactions, Cantera is based on the specification of chemical potentials for all species in all phases, which in turn is based on the description of a complete total Gibbs free energy function or the total Helmholtz free energy function. The method requires a basis set for the specification of standard entropies and enthalpies. This is currently done for all elements (but the electron) assuming the JANAF tables and the Chemkin standard, where the enthalpies of the elements are assumed to be taken as zero in their stable reference states at 1 bar and 25°C. Chemical equilibrium is obtained by minimizing the total Gibbs energy of the system through optimization of component abundances using the Villars-Cruise-Smith (VCS) approach, described in detail by Smith and Missen (1982). This method, as implemented in Cantera, has been extended to evaluate non-ideal systems making it suitable for the evaluation of many chemical equilibrium problems problems.

Cantera being object-oriented (C++) provides for a versatile and yet robust environment for the use and application of class objects to various types of thermodynamic problems adding the much needed flexibility in code development to evaluate specific processes. Cantera also accepts various types of thermodynamic data inputs including those consistent with the buildup of the EQ3/6 thermodynamic databases including parameters for the Helgeson-Kirkham-Flowers (HKF) equation of state (EoS) (Shock and Helgeson, 1988) used in calculations of thermodynamic properties of aqueous species at elevated pressures and temperatures. It also includes EoS expressions and parameters for the thermodynamic and volumetric properties of liquid and gas phases. For example, the International Association for the Properties of Water and Steam (IAPWS) Equation-of-State (EoS) formulation for H_2O by Wagner and Pruβ (2002) is included in Cantera to compute the thermodynamic and volumetric properties of H_2O as a function of temperature and pressure.

The approach taken here follows that of Sugiyama and Fujita (2006) adopting the use of amorphous SiO_2 and $Ca(OH)_2$ as the two end-member phases in a binary non-ideal solid solution to represent C-S-H solubility over of a wide range of Ca/Si ratios. Sugiyama and Fujita (2006) argue that given the disordered structural nature of C-S-H gels, its thermodynamic stability can be described by SiO_2 and $Ca(OH)_2$ as the two primordial phases. This approach has some advantages:

1. The use of two simple end-member solids (amorphous SiO_2 and $Ca(OH)_2$) to define the C-S-H solid solution. Using simple solids allows for an easier implementation and thus evaluation of the non-ideal solid solution model without the complication of an intermediate phase;

2. The thermodynamic properties of these two solids are well known including temperatures and pressures above 25°C. This also avoids potential inconsistencies when using thermodynamic properties of cement phases having intermediate compositions;

3. It allows for comparisons of results with other modeling schemes using SiO_2 and $Ca(OH)_2$ as end-member solids.

This modeling scheme has been implemented in the Cantera code suite using the thermodynamic properties of amorphous SiO_2 and $Ca(OH)_2$ given in the database compilation for the YMP (Wolery and Jové Colón, 2007). Standard entropy (S°) and molar volume of $Ca(OH)_2$ were obtained from Robie et al. (1979). The thermodynamics of the aqueous phase are handled by a Cantera class for Pitzer calculations. The source of Pitzer parameters were obtained from the YMP thermodynamic database compilation (Mariner, 2007). The Pitzer model is commonly used in the computation of activity coefficients of concentrated electrolyte species in solution but it's also applicable to dilute solutions such as those obtained from C-S-H leaching calculations.

The model was implemented in the form of C++ code that explicitly accounts for the thermodynamic properties of the C-S-H solid solution (including end-members) and the interacting solution. The non-ideal solid solution formulation in Cantera is defined within a Margules class where the excess enthalpy and entropy terms are specified as:

$$H^{EX} = X_{SiO_{2(am)}} X_{Ca(OH)_2} (W_{H1} + W_{H2} X_{Ca(OH)_2}) \qquad (1.1)$$

$$S^{EX} = X_{SiO_{2(am)}} X_{Ca(OH)_2} (W_{S1} + W_{S2} X_{Ca(OH)_2}) \qquad (1.2)$$

$$G^{EX} = H^{EX} - TS^{EX} \qquad (1.3)$$

H^{EX} is the excess enthalpy, S^{EX} corresponds to the excess entropy, and $X_{SiO_{2(am)}}$ and $X_{Ca(OH)_2}$ are the mole fractions of amorphous silica and portlandite, respectively, in the C-S-H mixture. W_{H1} and W_{H2} are the Margules terms for the excess enthalpy terms. Similarly, W_{S1} and W_{S2} define the Margules terms for the excess entropy terms. G^{EX} denotes to the excess Gibbs energy computed in Cantera from the H^{EX} and S^{EX} excess terms at a temperature T in degrees Kelvin. The parameters W_{H1}, W_{H2}, W_{S1}, and W_{S2} are fitted to the leaching experimental data using the DAKOTA optimization toolkit (Adams et al., 2012) through regression of the experimental leaching data. The regression is performed by minimization of the least squares difference between predicted and observed Ca and $SiO_{2(aq)}$ concentrations in solution as a function of the Ca/Si ratio in the C-S-H solid. The model domain is divided in two regions according to the Ca/Si ratio in the C-S-H mixture: Ca/Si ≤ 0.8 and Ca/Si ≥ 0.8. Partitioning of the C-S-H solid solution domains as a function of Ca/Si ratio to simulate C-S-H leaching has been recognized by others (Berner, 1987, 1988; Fujii and Kondo, 1981; Rahman et al., 1999a, b; Sugiyama and Fujita, 2006). Berner (1988) identified three regions for the solubility behavior of C-S-H as a function of Ca/Si ratio where each region is modeled as a non-ideal binary mixture where SiO_2 and $Ca(OH)_2$ are the end-members but having CaH_2SiO_4 as an intermediate component (Ca/Si = 1). In the model of Sugiyama and Fujita (2006), the non-ideal binary solid solution is defined for two regions (Ca/Si ≤ 0.8 and Ca/Si ≥ 0.8) using SiO_2 and $Ca(OH)_2$ as the end members where the Ca/Si ratio of 0.8 closely corresponds to that of tobermorite. The modeling approach of Sugiyama and Fujita (2006) is adopted in the current work but using the Margules formulation

and GEM to compute C-S-H solubility. The aqueous silica species considered in the simulations are $SiO_{2(aq)}$ and $HSiO_3^-$ with thermodynamic data taken from the YMP database (Wolery and Jové Colón, 2007). SiO_3^{--} was not considered given that it's not a predominant aqueous silica species at the peak pH of the simulations (pH~12) and the lack of well-constrained thermodynamic data. The formation of polynuclear silica aqueous species is expected at highly alkaline pH conditions. However, there is still limited knowledge on the accurate characterization of these polynuclear species and their stability constants as a function of pH. Table 1.1 list the thermodynamic properties of the considered solids and Margules mixing parameters for the C-S-H phase.

1.1.2 Discussion and Results

The Cantera simulations were conducted in a "titration" mode starting with the C-S-H equilibration on the basis of $SiO_{2(am)}$ and $Ca(OH)_2$ end-members at a Ca/Si $\approx$ 0 and then adding $Ca(OH)_2$ until reaching a Ca/Si ~ 0.8. Likewise, another "titration" was conducted for Ca/Si $\geq$ 0.8 domain by adding $Ca(OH)_2$ and minor amounts of $SiO_{2(aq)}$ up to a Ca/Si ratio of 2.2. The regression analysis to retrieve the C-S-H Margules parameters using DAKOTA was conducted along this range Ca/Si ratio values. Similarly, Cantera code runs were conducted starting with a Ca/Si ratio of 0.8 to a value of ~2.2 for the Ca/Si $\geq$ 0.8 domain. Figures 1.1 through 1.3 depict the solubility trends for the solution concentrations of Ca, $SiO_{2(aq)}$, and pH as a function of the Ca/Si ratio in the solid. The resulting simulation trends are in very good agreement with the solubility data reported in the literature for the considered large range of Ca/Si ratios in the C-S-H phase.

Sugiyama and Fujita (2006) described their simulated trends as continuous between the domains defined by Ca/Si ratios of less and larger than 0.8. The current study does indicate a *break* in simulated trends for Ca, $SiO_{2(aq)}$, and pH between the two domains which is expected from the regression analysis and retrieval of Margules parameters conducted separately for these two domains. This approach is consistent with the presence of an intermediate phase with Ca/Si = 0.8 as described by Sugiyama and Fujita (2006). The largest trend break between the two domains is that for $SiO_{2(aq)}$. Although various sets of C-S-H solubility data appear to be somewhat "continuous" for a wide range of Ca/Si ratios (i.e., 0 < Ca/Si $\geq$ 0.8), the solubility behavior at the Ca/Si $\geq$ 0.8 range is considered to be distinct given the influence of SiO_2 at pH < 11 corresponding to the Ca/Si $\leq$ 0.8 domain and the marked effect of the $Ca(OH)_2$ component at pH > 11 for Ca/Si $\geq$ 0.8. The Ca/Si $\leq$ 0.8 domain coincides with the composition of low pH cements that are richer in SiO_2 or poor in $Ca(OH)_2$ generating leachates of pH < 11 (Dole and Mattus, 2007). It should be noted that there is an inherent scatter in the C-S-H solubility data sets but the overall trends can still be defined when comparing various data sets.

The results of this equilibrium thermodynamic model implementation for C-S-H leaching indicate a very good agreement with synthetic data for a wide range of Ca/Si ratios. Although there are several model implementations in the literature that to a large extent adequately represent C-S-H solubility data, the current model is relatively simple and based on the use of end-member solids with well-constrained thermodynamic data. The application of a non-ideal Margules formalism accurately predicts the main trends observed for C-S-H leaching for Ca, $SiO_{2(aq)}$, and pH as a function of the Ca/Si ratio in the C-S-H solid. The implementation of such a model in an agile and yet unified object-oriented Cantera toolkit for constitutive modeling provides a robust template for the computation of chemical equilibria using classical

thermodynamic methods. Such flexibility is needed in the rigorous evaluation of process models associated with generic repository concepts.

Table 1.1. Thermodynamic properties of cement end-member phases and Margules parameters for C-S-H

Phase	$H°_{298}$ (J/mol)	$S°_{298}$ (J/K mol)	W_{H1} (J/mol)	W_{H2} (J/mol)	W_{S1} (J/K mol)	W_{S2} (J/K mol)	Remarks
$SiO_{2(am)}$	-897752.51	59.998	-	-	-	-	end-member Wolery and Jové Colón (2007)
$Ca(OH)_2$	-986100.0	83.387	-	-	-	-	end-member Wolery and Jové Colón (2007)
C-S-H < 0.8	-	-	-3.15E+04	-4.00E+04	-	-	"low" pH range - SiO_2 domain (this study)
C-S-H > 0.8	-	-	-1.0E+05	9.0E+4	-1.0E+02	1.75E+02	Alkaline pH range - $Ca(OH)_2$ domain (this study)
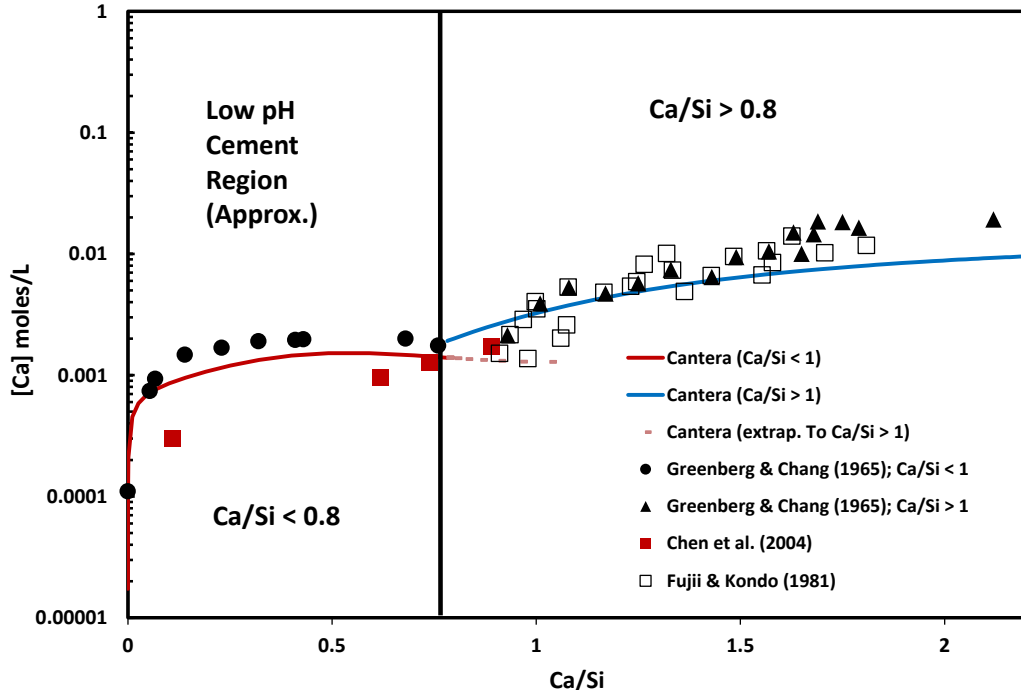
Figure 1.1. Cantera equilibrium simulation of Ca in the aqueous phase for C-S-H solubility as a function of Ca/Si in the solid. The simulations are conducted for the two compositional domains: Ca/Si ≤ 0.8 and Ca/Si ≥ 0.8. Extrapolation of the Ca/Si ≤ 0.8 simulation into Ca/Si ≥ 0.8 domain is shown for comparison.
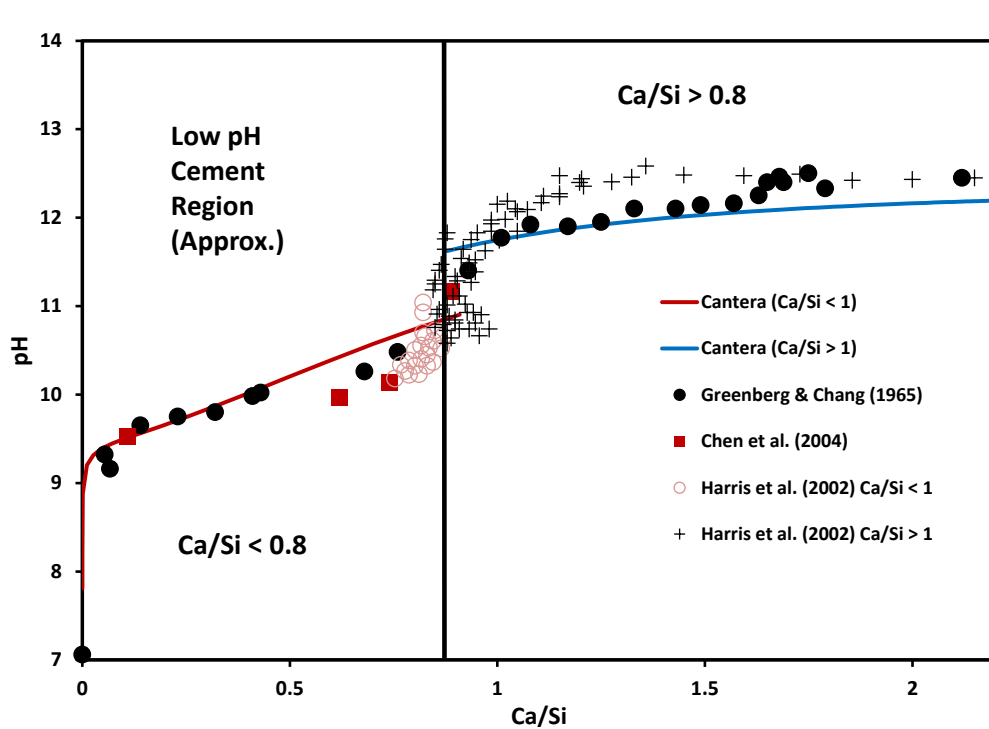
Figure 1.2. Cantera simulation result for pH as a function of Ca/Si in C-S-H. The agreement between data and predicted pH is very good considering the scatter in pH measurements.
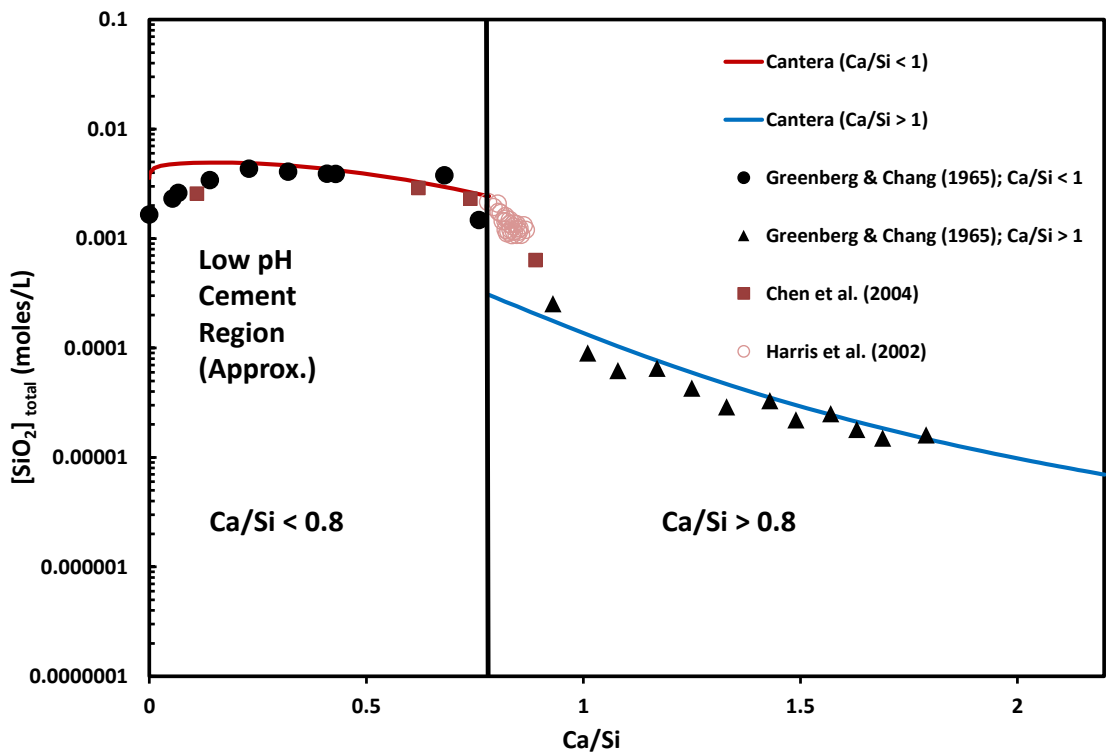
Figure 1.3. Cantera equilibrium simulation result of SiO$_{2(aq)}$ for C-S-H solubility as a function of Ca/Si in the solid.

1.2 Thermodynamic Database Development, with Emphasis on Complex Clay Minerals

1.2.1 Introduction

Thermodynamic data are essential for understanding and evaluating geochemical processes, as by speciation-solubility calculations, reaction-path modeling, or reactive transport simulation. Such data are required to evaluate both equilibrium states and the kinetic approach to equilibrium (via the affinity term in most commonly used rate laws). The development of thermodynamic databases for these purposes has a long history in geochemistry (e.g., Garrels and Christ, 1965; Helgeson et al., 1969; Helgeson et al., 1978, Johnson et al., 1992; Robie and Hemingway, 1995), paralleled by related and applicable work in the larger scientific community (e.g., Wagman et al., 1982, 1989; Cox et al., 1989; Barin and Platzki, 1995; Binneweis and Milke, 1999). The Yucca Mountain Project developed two qualified thermodynamic databases to model geochemical processes, including ones involving repository components such as spent fuel. The first of the two (Wolery and Jové Colón, 2007) was for systems containing dilute aqueous solutions only, the other (Mariner, 2007) for systems involving concentrated aqueous solutions and incorporating a model for such based on Pitzer's (1991) equations . A 25°C-only database with similarities to the latter was also developed for WIPP (cf. Xiong, 2005).

The YMP dilute systems database is widely used in the geochemistry community for a variety of applications involving rock/water interactions. It builds on the work of Prof. Helgeson and his students (see Wolery and Jové Colón 2007 for many applicable references), and covers a significant range of temperature (25-300°C). The last version covers 86 chemical elements, 1219

aqueous species, 1156 minerals and other solids species, and 128 gas species. Many data for actinide species were adopted from the Nuclear Energy Agency (NEA) series of volumes on radionuclide element thermodynamics (see references given in Wolery and Jové Colón, 2007), and the appropriate temperature extrapolations were applied. The YMP concentrated systems database covers a smaller chemical system (40 chemical elements, 237 aqueous species, 470 minerals and other solids, and 11 gas species). It includes temperature dependence, which for many species extends to 200°C, but for others extends to 250°C, to 110°C, or is restricted to 25°C. It is based on many sources (see Mariner, 2007), but draws in particular from the work of Pabalan and Pitzer (1987) and Greenberg and Møller (1989). The YMP databases have some regulatory cachet as qualified products of what was an NQA-1 program.

The purpose of the present task is to improve these databases for use on the Used Fuel Disposition Campaign (UFDC), doing so in an orderly and transparent way that will support qualification in support of the future underground high level nuclear waste disposal. The intent is that the UFDC work will utilize the same conventions and methodologies for treating thermodynamic data, unless substantive reasons drive a change. The Yucca Mountain Project was based on disposal in volcanic tuff, in a thick vadose zone in which oxidizing conditions were expected to prevail. A 50 year period of tunnel ventilation was planned to limit maximum temperature. Concentrated solutions were not originally expected at Yucca Mountain. Later concerns about dust deliquescence and evaporative concentration led to the development of the YMP concentrated solutions thermodynamic database (see Wolery and Jové Colón, 2007). The Yucca Mountain design scenario was unique among those considered in repository research. Planned repositories in other countries have envisioned disposal below the water table (generally under reducing conditions) in clay, salt, granite or other hard rock, usually incorporating relatively low maximum temperature in the designs. The UFDC is investigating potential disposal in mined repositories in these three rock types, plus a deep borehole option (which implies some kind of "hard" or "crystalline" rock as the host rock). However, the UFDC may consider higher maximum temperatures than are presently being considered elsewhere.

Although the Yucca Mountain Project thermodynamic databases incorporated many data of value to generic geochemistry applications, in some areas the development was limited owing to the specific rock type, the expected oxidizing conditions, and limited maximum temperatures associated with the repository design. Consequently, these databases need additional development to adequately address the different design scenarios currently being studied by the UFDC. There is a need to address a wider range of minerals and aqueous species due to different rock types and expected reducing conditions. Finally, in any effort using thermodynamic data, there is the ever present factor of flaws being discovered in existing data, and the potential impact of newly reported or refined data. Errors (and the suspicion of errors) often come to light in the application of the data. Activities impacting thermodynamic data are occurring in geochemistry and related fields on a continuing basis.

National and international standards organizations largely left the field some time ago in regard to thermodynamic data pertinent to geochemistry applications. The last major work by NIST (then NBS) was the volume published by Wagman et al. (1982), followed by an errata to the same (Wagman et al., 1989). CODATA published its last key thermodynamics report (Cox et al., 1989) in the same time period. The NEA thermodynamic data volumes (starting with Grenthe et al., 1992, and continuing to the present day) seem to represent the closest thing to a sanctioned body of work that is still active. However, the NEA has focused mainly on radionuclide

elements, which is helpful but not complete for geochemistry applications in radioactive waste disposal.

The present report details progress in a current effort to develop thermodynamic data and models for complex clay minerals, with some attention on related sheet silicates (principally illites, celadonites, and chlorites), building on and updating data and models that were developed for the YMP database, using linear free energy and similar estimation methods discussed in detail by Wolery and Jové Colón (2007). The previous effort on clays was limited due to the low importance of these minerals in the Yucca Mountain repository design (the host rock contained little clay, particularly in the near-field environment, and there was no planned use of engineered clay). The major shortcoming of the previous work from a UFDC perspective is that it followed some previous development (Tardy and Garrels, 1974; Wolery, 1978) in which the hydration state of smectite clays is treated implicitly. The effects of hydration/dehydration on properties such as molar volumes (and the consequent development of swelling pressure in a confined system) are ignored. There are some other deficiencies having to do with assumptions used in extrapolating the model properties (particularly cation exchange) to elevated temperature.

This report presents updated and new baseline data for the sheet silicates of interest. In particular, data are presented for dehydrated smectites and some hydrated equivalents. Apart from the hydrated smectites, the data presented cover Gibbs energies and enthalpies of formation, entropies, and molar volumes (all for a 298.15K and 1 bar pressure) and Maier-Kelley heat capacity coefficients. For the hydrated smectites, data are presented for all of these quantities except Gibbs energies and enthalpies of formation. Those quantities will be addressed in future work by evaluating models and data for smectite hydration/dehydration ,and the data and models will be further tested by addressing data for ion exchange involving interlayer cations (a phenomenon that is deeply tied to hydration/dehydration). The hydrated smectite data that are developed here will be used in that analysis. The methods used in the work presented here are those that have been used previously (Wolery and Jové Colón, 2007), except that the baseline regressions for Gibbs energies have been revised using a slightly different set of "silicated" oxide components and that for hydrated smectites, the hydration state is now explicitly treated (the actual maximum hydration state is somewhat contentious and a subject of planned future work.)

This report is an updated version of a previous report (*Thermodynamic Database Development, with Emphasis on Complex Clay Minerals*, Level 4 Milestone (M4): M41UF033201, July 29, 2011). That report discussed the clay mineral issues from a UFDC perspective, recognized that some of the YMP-generated thermodynamic data for implicitly hydrated smectites were more properly assigned to corresponding dehydrated compositions, and laid out elements to a path forward. The estimated thermodynamic data presented in the present report are new. Some additional information pertinent to the understanding of clay minerals is also new.

1.2.2 Clay Minerals: Background

Clay minerals play various roles in the geologic disposal of nuclear waste, potentially being present as both host rock minerals and EBS components. [for an overview of clays from the perspective of the UFD Natural Systems activity, see Chapter 4 of *Natural System Evaluation and Tool Development – FY11 Progress Report*: Wang et al., 2011]. Clay minerals are nearly ubiquitous at some level in nearly all rock types, ranging from minor alteration components in igneous rocks to major components in sedimentary rocks, notably shales and claystones. Clays

may be used as components (often with modification) in an engineered repository, usually in an attempt to limit the access of water to waste containers and/or waste forms. Clays may form (or transform, potentially to other clay or non-clay minerals) in a repository, in response to water circulation, associated chemical transport, and the thermal field that decaying waste may generate.

Clay minerals are sheet silicates that have a very wide range of chemical compositions and which exhibit complex behavior. Some clay and clay-like minerals, such as kaolinite ($Al_2Si_2O_5(OH)_4$) and pyrophyllite ($Al_2Si_4O_{10}(OH)2_)$ have a narrow range of chemical composition and relatively simple crystallographic structure. The more complex clays, including the illites, smectites, and vermiculites, vary considerably in chemical composition and are somewhat more complex structurally (in part due to the variable chemical composition). Complex clays (and in most instances, simple clays as well) have crystal sizes that are < 2 μm. Imaging generally requires methods like Scanning Electron Microscopy (Figure 1.4 shows an SEM image of smectite showing a common "wet cornflakes" appearance). Complex clay mineral crystals of 10 μm size would be considered "large"). Such small crystals correlate with high specific surface area. The small size also makes it difficult to separate natural samples from mixtures containing small grains of other minerals. Furthermore, chemical interactions may take place in different parts of a clay crystal, and at different rates. The interpretation of experimental measurement of the thermodynamic properties of complex clays is difficult because the number of variables that can affect results is generally too high to permit full control.
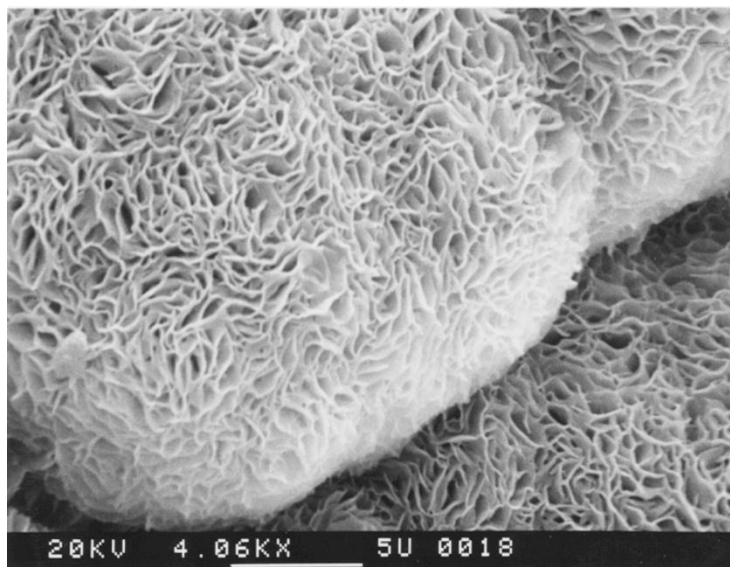
Figure 1.4. SEM image of smectite from Yucca Mountain Nevada (taken by Steve Chipera, Los Alamos National Laboratory).

Smectites are probably the most complex clays, as well as one of the most important types geologically. Smectites are a layered class of clay minerals that are comprised of repeating, parallel nanoscale sheets. Each framework sheet is composed of an octahedral layer of molecules

that is sandwiched between two tetrahedral layers (forming a "t-o-t" structure; see Figure 1.5). Each tetrahedron is arranged so that a point joins the octahedral layer and a base is exposed on the outside of the t-o-t structure. The center of a tetrahedron in the t-layer is typically occupied by Si^{4+}, but Al^{3+} can substitute, leading to a net negative charge in the layer. Similar, the center of an octahedron in the o-layer is typically occupied by Al^{3+}, Mg^{2+}, Fe^{2+}, Fe^{3+}, and Li^+, and usually also by some vacancies. The o-layer can also develop electrical charge. Oxygen is located at the vertices of the tetrahedra and octahedra and some oxygens are shared by adjoining t- and o-layers. Minor hydrogen is tied to some oxygens.

In smectites, t-o-t sheets are separated by a layer (the *interlayer*) that contains mono- and divalent cations (e.g., Na^+, Ca^{2+}) and water. In a fully hydrated smectite, the interlayer is thought to contain two or more layers of water molecules. The exact state of maximum hydration is somewhat contentious. Ransom and Helgeson (1993) estimated it from basal spacing data to be 4.5 moles H_2O per "$O_{10}(OH)_2$" in the common molar formula of smectite (corresponding to ½ unit cell), where the "$(OH)_2$" is considered as containing *structural* water. Others tend to put it higher. For example, Liu and Lin (2005) evaluated different experimental data using the Ransom and Helgeson model framework and concluded that maximum hydration corresponded to 7.14 moles H_2O per "$O_{10}(OH)_2$" The maximum hydration number in these models is somewhat of a fictive construct, as the calculated hydration number for a smectite in equilibrium with liquid water (thermodynamic activity of water near unity) is generally something less. Ransom and Helgeson (1994b) calculate that homoionic (one exchangeable cation) smectites in contact with liquid water have actual hydration numbers that depend on the cation, and which depend strongly on the cation charge (divalent cations have hydration numbers close to the maximum, monovalents have notably smaller ones). Cations in the interlayer are easily exchanged with aqueous solution and smectites in nature are not homoionic. Interlayer water can be removed by heating and other means, to the point that the interlayer becomes essentially dry.

nH₂O, **exchangeable cations**

○ Oxygens ⊚ Hydroxyls ● Aluminum, iron, magnesium
● and o Silicon, occasionally aluminum
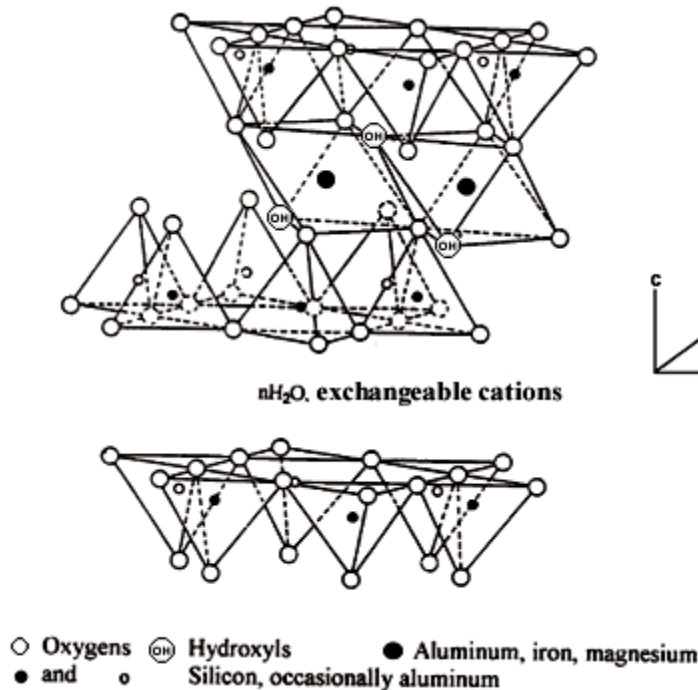
Figure 1.5. The crystal structure of smectite, showing a t-o-t framework layer at the top, with an interlayer shown below, with the t-layer of another t-o-t framework layer shown at the bottom. Figure reproduced from Valenzuela Diaz and de Souza Santos (2001) under the terms of a Creative Commons Attribution License.

Smectites are generally divided into the following types:

- Beidellites, which are aluminous. The o-layer is mainly filled with Al^{3+} and vacancies in nearly 2:1 ration (little or no net electrical charge, and electrical charge is developed in the t-layer by substitution of Al^{3+} or Si^{4+}. The composition of an idealized sodium beidellite is $Na_{0.33}Al_2Al_{0.33}Si_{3.67}O_{10}(OH)_2$.
- Nontronites, which are ferric iron rich: Like beidellites, but with Fe^{3+} replacing Al^{3+} in the o-layer. The composition of an idealized sodium nontronite is $Na_{0.33}Fe_2Al_{0.33}Si_{3.67}O_{10}(OH)_2$.
- Saponites, which are magnesium rich: Like beidellites, but with Mg^{2+} replacing Al^{3+} in the o-layer. The composition of an idealized sodium saponite is $Na_{0.33}Mg_3Al_{0.33}Si_{3.67}O_{10}(OH)_2$.
- Montmorillonites: Unlike the above types, electrical charge in the framework is developed in the o-layer, typically by the substitution of some Mg^{2+} for Al^{3+}, while the t-layer remains largely uncharged. The composition of an idealized sodium montmorillonite is $Na_{0.33}Mg_{0.33}Al_{1.67}Si_4O_{10}(OH)_2$.
- Hectorites (rare), which are lithium rich: Like montmorillonites, but with Mg^{2+} and Li^+ in the o-layer.

Ion exchange in smectites (and vermiculites, which are like smectites but have higher framework charge and higher cation exchange capacity) is rapid. However, ion exchange (and other sorptive processes) may occur not only in the interlayer, but also on the crystal edges and on the basal planes at the top and bottom of the crystal. One would like to distinguish the effects at these different loci. However, it is difficult to do so, and often the gross effect is represented by a lumped exchange constant or a distribution coefficient (K_d). Furthermore, while interactions in the interlayer and the outer clay crystal surface are relatively rapid (seconds to minutes), other reactions such as exchange of cations in the framework layer (o-layer or t-layer) and dissolution and growth of the framework layer itself probably occur much more slowly under most shallow crustal conditions owing to the need to break (or make) covalent bonds.

Illites can be thought of as similar to the smectites as they also have t-o-t framework layers. However, the "interlayers" have little or no water, and somewhat characteristically contain potassium ions, which tend not to easily exchange with aqueous solution. The ion exchange capacity is therefore relatively low. In general, due to common geologic occurrence in deep sedimentary basins and in geothermal systems, illites are often thought of as clays that form at higher temperatures than the smectites. However, dehydrated smectites are stable to very high temperatures as shown by dehydration experiments and experimental synthesis (to 1500°C in one study reported by Tamura et al., 2000). Other clay-like minerals such as pyrophyllite ($Al_2Si_4O_{10}(OH)_2$) and talc ($Mg_3Si_4O_{10}(OH)_2$) contain t-o-t frameworks that are electrically neutral overall and in each type of sublayer (thus no additional cations are required). These may be considered structural analogs, to a point, of smectites and illites.

One feature about the clays and related sheet silicates is that interlayer water (which is significant only in smectites and vermiculites, which have higher framework charge) appears to require a framework charge that falls in a certain range. On the zero-charge end are pyrophyllite and talc. These lack significant interlayer water (and interlayer cations). On the unit-charge end are the micas muscovite ($KAl_2AlSi_3O_{10}(OH)_2$) and paragonite ($NaAl_2AlSi_3O_{10}(OH)_2$). These also have effectively dry interlayers. In between, closer to the low end, are the smectites, with a

charge number of about 0.33 (e.g., Na-beidellite, $Na_{0.33}Al_2Al_{0.33}Si_{3.67}O_{10}(OH)_2$). These do have interlayer water. Also containing interlayer water are the vermiculites, with a charge number of about 0.66 (e.g., Na-Vermiculite, $Na_{0.66}Al_2Al_{0.66}Si_{3.66}O_{10}(OH)_2$).

Interlayer cations are believed to be located mostly at specific sites that are related to the positions of hexagonal rings of tetrahedra in the t-layers. For any of the above sheet silicate types, there is one ring pair (one ring above the interlayer, another below) per $O_{10}(OH)_2$ (cf. Deer et al., 1962, chapters on muscovite and pyrophyllite). In muscovite and paragonite, these interlayer cation sites are completely filled. Presumably there is insufficient room for interlayer water, or the geometric layout of interlayer cations and negatively charged oxygens from the facing side of the t-layers is unfavorable for the addition of water molecules. The interlayer cations likely act as pillars to separate the framework layers on each side. However, they may act to hold them tightly in place as well. In pyrophyllite and talc, the interlayer cation sites are all empty, and the absence of water is presumably due to lack of cations to attract the negatively charged oxygens of water molecules and/or insufficient space (in the absence of interlayer cations acting as pillars to support the interlayer). For the case of only monovalent interlayer cations, about one in three interlayer cation sites are filled in smectites, about two in three in vermiculites. For the case of only divalent interlayer cations, these conditions change to one in six and one in three. Presumably such interlayer cations occupancies offer favorable combinations of attraction of water to the cations, sufficient space, and possibly also favorable configurations in regard to interactions between the hydrogen atoms of water and the interlayer-facing oxygen atoms of the t-layers. This is an area where a better understanding might be obtained, for example from molecular dynamics calculations.

1.2.3   Clay Minerals: Thermodynamic Data

Thermodynamic data and models for the complex clays (including the all-important smectites and illites) have always been problematic to geochemists. Typical experimental approaches such as solubility and calorimetry have been of limited value owing to the reactive nature of these phases and the difficulty in adequately characterizing them. Thus, models are generally used to estimate the relevant thermodynamic data from corresponding data for related phases, generally including simple clays, clay-like minerals, and other sheet silicates including various micas and chlorites.

One of the best known of these is the model of Tardy and Garrels (1974), which derives data for the Gibbs energies of "silicated" oxide components from the known Gibbs energies of the related sheet silicates (kaolinite, micas, chlorites). The Gibbs energies of these "silicated" oxides are generally different from those of the corresponding real oxides, and the difference is referred to as the free energy of silication. A correlation with cation electronegativities developed by Tardy and Garrels (1974) suggests that the free energies of silication of SiO_2 and Fe_2O_3 should be nearly zero and provides one means of extending the set of treatable oxides (whether the free energy of silication should be zero or not). Estimated values for other thermodynamic properties (entropies, heat capacities, and molar volumes) can be estimated by a variety of similar "additive" or quasi-additive schemes (cf. Helgeson et al., 1978; Ransom and Helgeson, 1994b), though methods for obtaining entropies and heat capacities usually use the properties of real oxides. These additional properties are needed to extrapolate the Gibbs energy with respect to temperature (entropy, heat capacity) and pressure (volume).

Tardy and Garrels (1974) developed a similar set of data for oxide components s corresponding to exchangeable cations (e.g., $Na_2O_{(ex)}$). These data are derived from ion exchange constant data. The assumption is made (see Tardy and Garrels, 1974) that the free energy of $K_2O_{(ex)}$ is the same as that for silicated K_2O. Although Tardy and Garrels (1974) offer a justification for this, it is not entirely compelling. The development of data for these exchangeable oxide components allows the method to be applied to clays with exchangeable interlayer cations, which are likely to behave distinctly from the corresponding non-exchangeable interlayer cations such as K_2O in muscovite (or so Tardy and Garrels thought). Tardy and Garrels argued that using a second set of oxide components for interlayer cations was justified because a different set of values could be obtained from the data at hand. Using the data for exchangeable components to calculate Gibbs energies for end-member components forces a simple mixing model to be consistent with the original ion exchange data.

However, when Tardy and Garrels developed their model, they did not explicitly account for the water in the interlayer. Therefore, results from their procedure for an idealized Na-beidellite of formula $Na_{0.33}Al_2Al_{0.33}Si_{3.67}O_{10}(OH)_2$ would imply the interlayer water through the usage of the exchangeable oxide $Na_2O_{(ex)}$. However, this sort of treatment is not suficient if the loss or gain of interlayer water is sufficient to affect other clay properties of interest (e.g., swelling pressure) or change the local mass balance, for example by diluting or concentrating contacting aqueous solution.

As noted previously, Ransom and Helgeson (1993) calculated that a fully hydrated smectite would have about 4.5 H_2O of interlayer water per $O_{10}(OH)_2$ in the chemical formula, equivalent to about 2 water layers in the interlayer. Liu and Lin (2005) using the framework of the Ransom and Helgeson model to interpret a different set of hydration/dehydation data (Fu et al., 1990). They calculated 7.14 H_2O of interlayer water per formula unit for a fully hydrated smectite.

Another factor is that if one were to extrapolate the stabilities of the exchangeable oxide components to higher temperature and pressure, one should be using corresponding entropy, heat capacity, and molar volume functions also derived from exchange data. In fact, exchange data at elevated temperatures and pressures are difficult to come by. We have conducted a literature search for such data and will be using it in future analysis. We may also in the future conduct related experimental work.

In the Ransom and Helgeson hydration/dehydration model, the actual maximum hydration number (corresponding to unit water activity) in these models is generally less than the model maximum (notably so for monovalent interlayer cations, somewhat so for divalents). The model approach is to consider hydration/dehydration in the context of a regular solution mixing model, in which the end members are a dehydrated or anhydrous form ("as") and a maximally hydrated form ("hs"), for which the hydration number may be somewhat arbitrary. When the models are fit to data for relative humidity (equivalent to activity of liquid water) as a function of the mole fraction for of the fully hydrated component (x_{hs}), two parameters are obtained: log K for the reaction hs = as + nH_2O, where n is the maximal hydration number, and W_s, which is the Margules parameter (non-ideality parameter) for the regular solution model. The actual equations are somewhat complex and will not be presented here. At this time, we will merely note some key results.

When evaluated for unit water activity (see Ransom and Helgeson, 1993b), smectite compositions have actual hydration numbers less than the model maximum value (more so for

monovalent interlayer ions than divalents). Thus, part of the hydrous end of the model may not be expressed under real conditions. These models suggest that when hydrating a fully dehydrated smectite, the Gibbs energy of the first-added H_2O has one value, the second someting different, and so forth, with the Gibbs energy of later-added H_2O approaching that of pure liquid water. Thus, to accurately model hydration/dehydration, the interlayer H_2O component cannot be treated in a linear fashion. However, properties other than the Gibbs energy and enthalpy can be estimated for hydrated smectites using linear and quasi-linear methods (cf. Ransom and Helgeson, 1994b).

An interlayer cation is the same physical species, whether it is formally treated using an "exchangeable" oxide component with implicit water or a silicated oxide component with explicit water. When a sodium smectite dissolves, the reaction can be written as producing either aqueous Na^+ ion from $Na_2O_{(ex)}$ (using the implicitly hydrated smectite formula) or aqueous Na^+ plus liquid H_2O (using the explicit smectite hydration number pertinent to the case for unit water activity). The results of the two model approaches must be consistent. This provides a way of reconciling the models for implicitly and explicitly hydrated smectites. A better test, however, would be to compare results for cation exchange reactions using implicitly and explicitly hydrated components, as this avoids the assumption (originally proposed by Tardy and Garrels, 1974) that the Gibbs energies for "exchangeable" and "silicated" K_2O components are equal.

Using schemes like the Tardy and Garrels (1974) estimation method, one can calculate the properties of a clay mineral or other sheet silicate by stoichiometrically summing the values for the relevant oxides. For greater accuracy, such estimations may be made by using component oxide substitutions starting with a closely related phase for which real data exist, such as pyrophyllite ($Al_2Si_4O_{10}(OH)_2$). [The late Robert M. Garrels used to say, "Pyrophyllite is the mother of montmorillonite" to make this point.] Another factor may be to explicitly account for mixing effects, using the basic estimation methods to define the properties of end-members, and assuming (usually) ideal mixing in the site-mixing sense to define the properties of phases of intermediate composition.

The last YMP dilute systems thermodynamic database (data0.ymp.R5) contains data derived by such means for some clay compositions shown below in Table 1.2. A detailed description of the methods and derivation of the corresponding thermodynamic data is given in the Analysis/Model Report ANL-WIS-GS-000003 Rev. 1 (Wolery and Jové Colón, 2007). Basically, this development follows Wolery (1978), who applied the Tardy-Garrels method but using updated values for the Gibbs energy data used to regress the values for the silicate oxides and also, in the case of subsequent calculation of equilibrium constants, updated values for the Gibbs energies of the relevant aqueous species. The later YMP work applied another level of updating. Data were obtained for five idealized beidellites, five idealized montmorillonites, five idealized saponites, five idealized nontronites, three complex smectites, an illite, and three idealized celadonites. Some data were also obtained by the same process for some chlorite and chlorite-related sheet silicates.

The previous estimation exercise has been revised and extended in a number of ways. The most significant is that explicitly dehydrated and hydrated smectite compositions are now treated, in addition to the implicitly hydrated smectite compositions addressed previously. For explicitly hydrated smectite compositions, various plausible maximum values of the interlayer hydration number were used. Calculations for estimating Gibbs energies and molar volumes are now done using a modified, consistent set of silicated oxide components. This set of silicated oxide

components was also used to generate a set of alternative values for molar enthalpies, although these values were only used as a check on adopted values calculated from the Gibbs energies and molar enthalpies of the target minerals. The adopted enthalpy values satisfy the consistency relationship $\Delta G°_f = \Delta H°_f - \Delta S°_f$, where $\Delta S°_f$ is calculated from the entropy of the target mineral and the entropies of the elements in their reference forms. Enthalpies were not included in the previous exercise (Wolery and Jové Colón, 2007). The remaining thermodynamic properties were calculated using the same methods used in that exercise. All calculations presented or discussed below were carried out in the spreadsheet Clays_TJW_2_Rev1.xlsx.

The new calculations follow the previous ones (e.g., Wolery and Jové Colón, 2007) in using obsolete calorie units. This is partly for continuity, and partly to avoid introducing potential numerical inconsistencies at intermediate steps. The final results can be converted to joule units if desired, noting that 1 calorie = 4.184 joules.

Table 1.2 shows the compositional matrix used in the present work for estimating Gibbs energies. A previously employed $Mg(OH)_2$ component was dropped in favor of just using MgO and H_2O (structural water). The single Al_2O_3 component used in the Yucca Mountain work was replaced by octahedral and tetrahedral forms used in the earlier work by Wolery (1978). As noted previously, the same set of components was also used to estimate molar volumes and to make alternative estimates of molar enthalpies.

In the above derivations, the actual amount of water in the exchange layer of a smectite (beidellite, montmorillonite, saponite, nontronite, or "smectite") was not explicitly taken into account (this water does not include the water that is structurally bound in the $(OH)_2$ part of the formula). . In deriving the data for the Na-beidellite, for example, the exchangeable sodium was represented by the $Na_2O_{(ex)}$ component. The associated water can be thought of as being dealt with implicitly, as noted previously. Interestingly, using the silicated Na_2O component instead would yield data for the dehydrated equivalent of this hydrated clay, which is something that we intend to do in future development. We note that data for exchangeable oxide components was based only on 25°C data, and that the temperature dependence of the properties of the exchangeable components was assumed to be the same as those of the corresponding non-exchangeable components. This reduces the reliability of the estimated data at elevated temperature (in particular, the stabilities of affected clays with respect to other minerals becomes more uncertain). Also, because the water in the exchange layer is treated implicitly, dehydration cannot be properly accounted for.

Tables 1.3 and 1.4 show the results of the Gibbs energy regression, using known data for the sheet silicate minerals shown. Mathematically, the problem is a linear regression. The objective is to fit oxide component properties to known data for a set of minerals. Excel's regression tool is used for this purpose. Tables 1.5 through 1.7 are analogous to Tables 1.1 through 1.3 and show the corresponding results for molar volumes. Analogous results for alternate values for enthalpies obtained using the same composition matrix as for Gibbs energies are not included in this report, but can be found in the spreadsheet for all the new estimates presented or discussed in this report (Clays_TJW_2_Rev1.xlsx). Table 1.8 shows values for interlayer water properties from Ransom and Helgeson (1994b). Here data are missing for the Gibbs energy and enthalpy, as those must be evaluated from models that are not linear in the interlayer water component, as noted previously. Dealing with that will be the focus of future work, as noted previously. However, it is noted that the spreadsheet facilitates calculations with any such data one might wish to experiment with.

Table 1.9 shows the reference reactions that were used to estimate the Gibbs energies (and molar volumes) of chlorites and related minerals, an illite, and some celadonites (which are related to illite). The corresponding Gibbs energy and molar volume estimates are given in Table 1.10, along with corresponding estimates for enthalpy, entropy, and Maier-Kelly heat capacity coefficients. A slightly different set of reference reactions was to make estimates for entropies and heat capacity coefficients. A key difference is the use of a single Al_2O_3 component. For heat capacity coefficients, the oxide component values correspond to the actual oxides. This is also true in the case of entropies, although the actual computation is non-linear, but has linear parts (Helgeson et al., 1978, eq 75, p. 51: $S° = \Delta S_s°*(\Delta V_s° + V°)/(2*\Delta V_s°) - 2(cal/mol-K)*(\#$ of ferrous Fe's per mole)). Here $\Delta S_s°$ is computed from a reference reaction involving actual oxide components, and could itself be taken as an estimate of $S°$, albeit a less accurate one. $\Delta V_s°$ is an analogous result for volumes. $V°$ is the molar volume, which in many cases must also be an estimate.

Table 1.11 shows the reference reactions that were used to estimate the Gibbs energies (and molar volumes) of 23 dehydrated smectite compositions. The corresponding Gibbs energy and molar volume estimates are given in Table 1.12, along with corresponding estimates for enthalpy, entropy, and Maier-Kelly heat capacity coefficients. Again, slightly different set of reference reactions was used to make estimates for entropies and heat capacity coefficients. Tables 1.13, 1.14, and 1.15 present estimated thermodynamic properties (without values for Gibbs energies and enthalpies, due to the reasons noted previously) for the corresponding hydrated smectites with hydration numbers of 4.5, 5, and 7, respectively. These data will be used in evaluating hydration/dehydration models to complete a model treating smectite hydration.

Table 1.16 shows revised Gibbs energy estimates only, for the corresponding implicitly hydrated smectite compositions. Previous estimates of the remaining thermodynamic properties (e.g., Wolery, 1978; Wolery and Jové Colón, 2007) were not based on cation exchange data, and, as noted previously, would have been more properly applied to fully dehydrated smectite.

Table 1.17 shows a compilation of values for the entropies of the elements in their reference forms and identifies the values adopted for the present study. This list includes only data for elements that are needed for work on clay minerals and related sheet silicates, for the present work and the foreseeable future. For the most part, the adopted values are taken from the NEA thermodynamic data series (e.g., Grenthe et al., 1992 and succeeding volumes). NEA generally adopts CODATA (Cox et al., 1989) data, as much as possible. No source examined appears to cover all of the chemical elements.

The data calculated here provides the basis for ongoing work to evaluate models for explicitly hydrated smectites, and should be sufficient for that purpose. However, it is noted that revisions may be made to these results due to future revisions in the thermodynamic data used as input. For example, we are now considering such revisions in regard to the Gibbs energies of kaolinite and pyrophyllite. The spreadsheet (Clays_TJW_2_Rev1.xlsx) is easily revisable should such input data be revised. Also, the spreadsheet is supportive of easy calculation of the properties of any of the explicitly hydrated smectites if results are desired for hydration numbers other than those now used in it.

Table 1.2. Composition matrix for regressing Gibbs energies of silicated oxides from the known Gibbs energies of some sheet silicate minerals. The same composition matrix was used to estimate alternate values of enthalpies, which are not presented in this report. In the regressions, the data for Antigorite were scaled by a factor of 1/12 to avoid a much higher effective weighting for this mineral, which has a very large molecular formula. Quartz and Hematite are included in the regression, even though they are not sheet silicates. A justification for this is given by Wolery (1978), and Wolery and Jové Colón (2007).

Name	Formula	K2O	Na2O	CaO	MgO	Fe2O3	FeO	Al2O3(oct)	Al2O3(tetr)	SiO2	H2O
14A-Clinochlore	Mg5AlAlSi3O10(OH)8	0	0	0	5	0	0	0.5	0.5	3	4
7A-Clinochlore	Mg5AlAlSi3O10(OH)8	0	0	0	5	0	0	0.5	0.5	3	4
Annite	KFe3AlSi3O10(OH)2	0.5	0	0	0	0	3	0	0.5	3	1
Antigorite	Mg48Si34O85(OH)62	0	0	0	4	0	0	0	0	2.83333	2.58333
Chrysotile	Mg3Si2O5(OH)4	0	0	0	3	0	0	0	0	2	2
Hematite	Fe2O3	0	0	0	0	1	0	0	0	0	0
Kaolinite	Al2Si2O5(OH)4	0	0	0	0	0	0	1	0	2	2
Margarite	CaAl2Al2Si2O10(OH)2	0	0	1	0	0	0	1	1	2	1
Muscovite	KAl2AlSi3O10(OH)2	0.5	0	0	0	0	0	1	0.5	3	1
Paragonite	NaAl2AlSi3O10(OH)2	0	0.5	0	0	0	0	1	0.5	3	1
Phlogopite	KMg3AlSi3O10(OH)2	0.5	0	0	3	0	0	0	0.5	3	1
Pyrophyllite	Al2Si4O10(OH)2	0	0	0	0	0	0	1	0	4	1
Quartz	SiO2	0	0	0	0	0	0	0	0	1	0
Talc	Mg3Si4O10(OH)2	0	0	0	3	0	0	0	0	4	1

Table 1.3. Fitting error in the Gibbs energy regression for silicate minerals.

Name	Formula	ΔG_f^o cal/mol	Calculated ΔG_f^o cal/mol	Error cal/mol	% Error
14A-Clinochlore	Mg5AlAlSi3O10(OH)8	-1961703	-1959402.0	2301.0	-0.1173
7A-Clinochlore	Mg5AlAlSi3O10(OH)8	-1957101	-1959402.0	-2301.0	0.1176
Annite	KFe3AlSi3O10(OH)2	-1147156	-1147156.0	0.0	0.0000
Antigorite	Mg48Si34O85(OH)62	-1317335	-1317238.9	96.1	-0.0073
Chrysotile	Mg3Si2O5(OH)4	-964871	-965879.6	-1008.6	0.1045
Hematite	Fe2O3	-178155	-178155.0	0.0	0.0000
Kaolinite	Al2Si2O5(OH)4	-905614	-904725.5	888.5	-0.0981
Margarite	CaAl2Al2Si2O10(OH)2	-1394150	-1394150.0	0.0	0.0000
Muscovite	KAl2AlSi3O10(OH)2	-1336301	-1335667.0	634.0	-0.0474
Paragonite	NaAl2AlSi3O10(OH)2	-1326012	-1326012.0	0.0	0.0000
Phlogopite	KMg3AlSi3O10(OH)2	-1396187	-1396821.0	-634.0	0.0454
Pyrophyllite	Al2Si4O10(OH)2	-1255997	-1257519.5	-1522.5	0.1212
Quartz	SiO2	-204656	-204656.0	0.0	0.0000
Talc	Mg3Si4O10(OH)2	-1320188	-1318673.5	1514.5	-0.1147

Table 1.4. Gibbs energies of silicated oxides, obtained from the Gibbs energy regression.

Oxide	Silicated ΔG_f^o cal/mol	Unsilicated ΔG_f^o cal/mol	Silication ΔG_f^o cal/mol
K2O	-187699.1	-77056.0	-110643.1
Na2O	-168389.1	-89883.0	-78506.1
CaO	-168034.6	-144366.0	-23668.6
MgO	-147843.8	-136086.0	-11757.8
Fe2O3	-178155.0	-178155.0	0.0
FeO	-64622.2	-60097.0	-4525.2
Al2O3(oct)	-382377.4	-374824.0	-7553.4
Al2O3(tet)	-377907.9	-374824.0	-3083.9
SiO2	-204656.0	-204656.0	0.0
H2O	-56518.0	-----	-----

Table 1.5. Composition matrix for regressing molar volumes of silicated oxides from the known volumes of some sheet silicate minerals. This composition matrix is similar to that used to regress Gibbs energies (Table 1.2). However, a larger number of minerals are included in the present case, reflecting a greater availability of mineral volume data. Again, the data for Antigorite were scaled by a factor of 1/12 to avoid a much higher effective weighting for this mineral, which has a very large molecular formula. Quartz and Hematite are again included in the regression, even though they are not sheet silicates.

Name	Formula	K2O	Na2O	CaO	MgO	Fe2O3	FeO	Al2O3(oct)	Al2O3(tetr)	SiO2	H2O
14A-Amesite	Mg4Al2Al2Si2O10(OH)8	0	0	0	4	0	0	1	1	2	4
14A-Clinochlore	Mg5AlAlSi3O10(OH)8	0	0	0	5	0	0	0.5	0.5	3	4
14A-Daphnite	Fe5AlAlSi3O10(OH)8	0	0	0	0	0	5	0.5	0.5	3	4
7A-Amesite	Mg2AlAlSiO5(OH)4	0	0	0	2	0	0	0.5	0.5	1	2
7A-Chamosite	Fe2AlAlSiO5(OH)4	0	0	0	0	0	2	0.5	0.5	1	2
7A-Clinochlore	Mg5AlAlSi3O10(OH)8	0	0	0	5	0	0	0.5	0.5	3	4
7A-Cronstedtite	Fe2FeFeSiO5(OH)4	0	0	0	0	1	2	0	0	1	2
7A-Daphnite	Fe5AlAlSi3O10(OH)8	0	0	0	0	0	5	0.5	0.5	3	4
Annite	KFe3AlSi3O10(OH)2	0.5	0	0	0	0	3	0	0.5	3	1
Antigorite	Mg48Si34O85(OH)62	0	0	0	4	0	0	0	0	2.83333	2.58333
Celadonite	KMgAlSi4O10(OH)2	0.5	0	0	1	0	0	0.5	0	4	1
Chrysotile	Mg3Si2O5(OH)4	0	0	0	3	0	0	0	0	2	2
Greenalite	Fe3Si2O5(OH)4	0	0	0	0	0	3	0	0	2	2
Hematite	Fe2O3	0	0	0	0	1	0	0	0	0	0
Kaolinite	Al2Si2O5(OH)4	0	0	0	0	0	0	1	0	2	2
Margarite	CaAl2Al2Si2O10(OH)2	0	0	1	0	0	0	1	1	2	1
Minnesotaite	Fe3Si4O10(OH)2	0	0	0	0	0	3	0	0	4	1
Muscovite	KAl2AlSi3O10(OH)2	0.5	0	0	0	0	0	1	0.5	3	1
Paragonite	NaAl2AlSi3O10(OH)2	0	0.5	0	0	0	0	1	0.5	3	1
Phlogopite	KMg3AlSi3O10(OH)2	0.5	0	0	3	0	0	0	0.5	3	1
Pyrophyllite	Al2Si4O10(OH)2	0	0	0	0	0	0	1	0	4	1
Quartz	SiO2	0	0	0	0	0	0	0	0	1	0
Sepiolite	Mg4Si6O15(OH)2:6H2O	0	0	0	4	0	0	0	0	6	7
Talc	Mg3Si4O10(OH)2	0	0	0	3	0	0	0	0	4	1

Table 1.6. Fitting error in the molar volume regression for silicate minerals.

Name	Formula	V° cm³/mol	Calculated V° cm³/mol	Error cm³/mol	% Error
14A-Amesite	Mg4Al2Al2Si2O10(OH)8	205.400	202.053	-3.347	-1.6297
14A-Clinochlore	Mg5AlAlSi3O10(OH)8	207.110	209.857	2.747	1.3265
14A-Daphnite	Fe5AlAlSi3O10(OH)8	213.420	218.761	5.341	2.5025
7A-Amesite	Mg2AlAlSiO5(OH)4	103.000	101.026	-1.974	-1.9162
7A-Chamosite	Fe2AlAlSiO5(OH)4	106.200	104.588	-1.612	-1.5181
7A-Clinochlore	Mg5AlAlSi3O10(OH)8	211.500	209.857	-1.643	-0.7767
7A-Cronstedtite	Fe2FeFeSiO5(OH)4	110.900	110.076	-0.824	-0.7432
7A-Daphnite	Fe5AlAlSi3O10(OH)8	221.200	218.761	-2.439	-1.1027
Annite	KFe3AlSi3O10(OH)2	154.320	156.643	2.323	1.5050
Antigorite	Mg48Si34O85(OH)62	145.761	147.523	1.762	1.2089
Celadonite	KMgAlSi4O10(OH)2	157.100	150.826	-6.274	-3.9937
Chrysotile	Mg3Si2O5(OH)4	108.500	108.831	0.331	0.3051
Greenalite	Fe3Si2O5(OH)4	115.000	114.173	-0.827	-0.7190
Hematite	Fe2O3	30.274	31.098	0.824	2.7227
Kaolinite	Al2Si2O5(OH)4	99.520	100.552	1.032	1.0367
Margarite	CaAl2Al2Si2O10(OH)2	129.400	129.400	0.000	0.0000
Minnesotaite	Fe3Si4O10(OH)2	147.860	143.153	-4.707	-3.1837
Muscovite	KAl2AlSi3O10(OH)2	140.710	143.021	2.311	1.6425
Paragonite	NaAl2AlSi3O10(OH)2	132.530	132.530	0.000	0.0000
Phlogopite	KMg3AlSi3O10(OH)2	149.660	151.300	1.640	1.0961
Pyrophyllite	Al2Si4O10(OH)2	126.600	129.531	2.931	2.3153
Quartz	SiO2	22.688	22.182	-0.506	-2.2316
Sepiolite	Mg4Si6O15(OH)2:6H2O	285.600	285.711	0.111	0.0388
Talc	Mg3Si4O10(OH)2	136.250	137.810	1.560	1.1453

Table 1.7. Molar volumes of silicated oxides, obtained from the molar volumes regression.

Oxide	Silicated V° cm³/mol	Unsilicated V° cm³/mol	Silication ΔV° cm³/mol
K2O	45.543	40.380	5.163
Na2O	24.561	25.000	-0.439
CaO	18.432	16.764	1.668
MgO	11.233	24.630	-13.397
Fe2O3	31.098	11.248	19.850
FeO	13.014	30.274	-17.260
Al2O3(oct)	25.420	12.000	13.420
Al2O3(tet)	25.800	25.575	0.225
SiO2	22.182	22.688	-0.506
H2O	15.384	-----	-----

Table 1.8. Thermodynamic properties of interlayer water in smectite (Ransom and Helgeson, 1994b, Table 2, p. 4541.

$\Delta G_f°$ kcal/mol	$\Delta H_f°$ kcal/mol	S° cal/mol-K	Cp° cal/mol-K	a cal/mol-K	b x 10³ cal/mol-K²	c x 10⁻⁵ cal-K/mol	V° cm³/mol
-----	-----	13.15	11.46	9.044	12.34	-0.979	17.22

Table 1.9. Reference reactions for estimating Gibbs energies, molar volumes, and alternative enthalpy values for chlorites and related minerals, an illite, and some celadonites. The reference reactions used to estimate entropies and heat capacity coefficients are similar but slightly different (in particular, there is no distinction between octahedral and tetrahedral Al_2O_3).

Name	Formula	Reference Reaction
7A-Ripidolite	Mg3Fe2AlAlSi3O10(OH)8	7A-Ripidolite = 7A-Clinochlore + 2FeO - 2MgO
14A-Ripidolite	Mg3Fe2AlAlSi3O10(OH)8	14A-Ripidolite = 14A-Clinochlore + 2FeO - 2MgO
7A-Daphnite	Fe5AlAlSi3O10(OH)8	7A-Daphnite = 7A-Clinochlore + 5FeO - 5MgO
14A-Daphnite	Fe5AlAlSi3O10(OH)8	14A-Daphnite = 14A-Clinochlore + 5FeO - 5MgO
7A-Amesite	Mg2AlAlSiO5(OH)4	7A-Amesite = 7A-Clinochlore - 3MgO - 2SiO2 - 2H2O
14A-Amesite	Mg4Al2Al2Si2O10(OH)8	14A-Amesite = 14A-Clinochlore - MgO + 0.5Al2O3(oct) + 0.5Al2O3(tetr) - SiO2
7A-Chamosite	Fe2AlAlSiO5(OH)4	7A-Chamosite = 7A-Clinochlore- 5MgO + 2FeO - 2SiO2 - 2H2O
7A-Cronstedtite	Fe2FeFeSiO5(OH)4	7A-Cronstedtite = 7A-Clinochlore - 5MgO + 2FeO +Fe2O3 - 0.5Al2O3(oct) -0.5Al2O3(tetr) - 2SiO2 - 2H2O
Greenalite	Fe3Si2O5(OH)4	Greenalite = Chrysotile + 3FeO - 3MgO
Minnesotaite	Fe3Si4O10(OH)2	Minnesotaite = Talc + 3FeO - 3MgO
Illite	K0.6Mg0.25Al2.3Si3.5O10(OH)2	Illite = Pyrophyllite + 0.3K2O + 0.25MgO - 0.1Al2O3(oct) + 0.25Al2O3(tetr) - 0.5SiO2
Celadonite	KMgAlSi4O10(OH)2	Celadonite = Pyrophyllite + 0.5K2O + MgO - 0.5Al2O3(oct)
Ferroceladonite	KFeFeSi4O10(OH)2	Ferroceladonite = Pyrophyllite + 0.5K2O + 0.5Fe2O3 + FeO - Al2O3(oct)
Ferroaluminoceladonite	KFeAlSi4O10(OH)2	Ferroaluminoceladonite = Pyrophyllite + 0.5K2O + FeO - 0.5Al2O3(oct)

Table 1.10. Estimated thermodynamic data for chlorites and related minerals, an illite, and some celadonites. Data in purple cells are taken from Helgeson et al. (1978).

Name	Formula	$\Delta G_f°$ cal/mol	$\Delta H_f°$ cal/mol	S° cal/mol-K	V° cm³/mol	a cal/mol-K	b x 10³ cal/mol-K²	c x 10⁻⁵ cal-K/mol
7A-Ripidolite	Mg3Fe2AlAlSi3O10(OH)8	-1792651.4	-1942787.4	126.147	215.380	166.700	51.280	39.420
14A-Ripidolite	Mg3Fe2AlAlSi3O10(OH)8	-1797253.4	-1946119.2	130.407	209.634	170.380	42.760	36.010
7A-Daphnite	Fe5AlAlSi3O10(OH)8	-1540992.6	-1686174.0	138.900	221.200	172.530	52.280	37.230
14A-Daphnite	Fe5AlAlSi3O10(OH)8	-1545594.6	-1689702.7	142.500	213.420	176.210	43.760	33.820
7A-Amesite	Mg2AlAlSiO5(OH)4	-991221.4	-1070157.5	52.000	103.000	81.030	24.738	20.230
14A-Amesite	Mg4Al2Al2Si2O10(OH)8	-1989345.9	-2145757.1	108.900	205.400	172.590	34.980	41.670
7A-Chamosite	Fe2AlAlSiO5(OH)4	-824778.1	-899159.5	64.700	106.200	84.910	25.400	18.770
7A-Cronstedtite	Fe2FeFeSiO5(OH)4	-622790.4	-694402.7	73.500	110.900	84.790	41.840	12.476
Greenalite	Fe3Si2O5(OH)4	-715206.0	-786483.0	72.600	115.000	81.650	32.600	15.390
Minnesotaite	Fe3Si4O10(OH)2	-1070523.0	-1153847.4	83.500	147.860	88.310	42.610	11.150
Illite	K0.6Mg0.25Al2.3Si3.5O10(OH)2	-1303178.9	-1394137.6	62.871	135.888	86.044	38.567	17.823
Celadonite	KMgAlSi4O10(OH)2	-1306501.6	-1395512.0	74.900	157.100	80.250	25.300	18.540
Ferroceladonite	KFeFeSi4O10(OH)2	-1121168.7	-1208082.5	80.400	152.514	85.062	52.089	11.867
Ferroaluminoceladonite	KFeAlSi4O10(OH)2	-1223280.0	-1311623.9	75.847	149.675	87.062	44.199	14.282

Table 1.11. Reference reactions for estimating Gibbs energies, molar volumes, and alternative enthalpy values for 23 dehydrated smectite compositions. The reference reactions used to estimate entropies and heat capacity coefficients are similar but slightly different (in particular, there is no distinction between octahedral and tetrahedral Al$_2$O$_3$).

H-Beidellite	H0.33Al2.33Si3.67O10(OH)2	H-Beidellite = Pyrophyllite + 0.165H2O + 0.165Al2O3(tetr) - 0.33SiO2
Na-Beidellite	Na0.33Al2.33Si3.67O10(OH)2	Na-Beidellite = Pyrophyllite + 0.165Na2O + 0.165Al2O3(tetr) - 0.33SiO2
K-Beidellite	K0.33Al2.33Si3.67O10(OH)2	K-Beidellite = Pyrophyllite + 0.165K2O + 0.165Al2O3(tetr) - 0.33SiO2
Ca-Beidellite	Ca0.165Al2.33Si3.67O10(OH)2	Ca-Beidellite = Pyrophyllite + 0.165CaO + 0.165Al2O3(tetr) - 0.33SiO2
Mg-Beidellite	Mg0.165Al2.33Si3.67O10(OH)2	Mg-Beidellite = Pyrophyllite + 0.165MgO + 0.165Al2O3(tetr) - 0.33SiO2
H-Saponite	H0.33Mg3Al0.33Si3.67O10(OH)2	H-Saponite = Talc + 0.165H2O + 0.165Al2O3(tetr) - 0.33SiO2
Na-Saponite	Na0.33Mg3Al0.33Si3.67O10(OH)2	Na-Saponite = Talc + 0.165Na2O + 0.165Al2O3(tetr) - 0.33SiO2
K-Saponite	K0.33Mg3Al0.33Si3.67O10(OH)2	K-Saponite = Talc + 0.165K2O + 0.165Al2O3(tetr) - 0.33SiO2
Ca-Saponite	Ca0.165Mg3Al0.33Si3.67O10(OH)2	Ca-Saponite = Talc + 0.165CaO + 0.165Al2O3(tetr) - 0.33SiO2
Mg-Saponite	Mg0.165Mg3Al0.33Si3.67O10(OH)2	Mg-Saponite = Talc + 0.165MgO + 0.165Al2O3(tetr) - 0.33SiO2
H-Nontronite	H0.33Fe2Al0.33Si3.67O10(OH)2	H-Nontronite = Pyrophyllite + 0.165H2O + Fe2O3 - Al2O3(oct) + 0.165Al2O3(tetr) - 0.33SiO2
Na-Nontronite	Na0.33Fe2Al0.33Si3.67O10(OH)2	Na-Nontronite = Pyrophyllite + 0.165Na2O + Fe2O3 - Al2O3(oct) + 0.165Al2O3(tetr) - 0.33SiO2
K-Nontronite	K0.33Fe2Al0.33Si3.67O10(OH)2	K-Nontronite = Pyrophyllite + 0.165K2O + Fe2O3 - Al2O3(oct) + 0.165Al2O3(tetr) - 0.33SiO2
Ca-Nontronite	Ca0.165Fe2Al0.33Si3.67O10(OH)2	Ca-Nontronite = Pyrophyllite + 0.165CaO + Fe2O3 - Al2O3(oct) + 0.165Al2O3(tetr) - 0.33SiO2
Mg-Nontronite	Mg0.165Fe2Al0.33Si3.67O10(OH)2	Mg-Nontronite = Pyrophyllite + 0.165MgO + Fe2O3 - Al2O3(oct) + 0.165Al2O3(tetr) - 0.33SiO2
H-Montmorillonite	H0.33Mg0.33Al1.67Si4O10(OH)2	H-Montmorillonite = Pyrophyllite + 0.165H2O + 0.33MgO - 0.165Al2O3(oct)
Na-Montmorillonite	Na0.33Mg0.33Al1.67Si4O10(OH)2	Na-Montmorillonite = Pyrophyllite + 0.165Na2O + 0.33MgO - 0.165Al2O3(oct)
K-Montmorillonite	K0.33Mg0.33Al1.67Si4O10(OH)2	K-Montmorillonite = Pyrophyllite + 0.165K2O + 0.33MgO - 0.165Al2O3(oct)
Ca-Montmorillonite	Ca0.165Mg0.33Al1.67Si4O10(OH)2	Ca-Montmorillonite = Pyrophyllite + 0.165CaO + 0.33MgO - 0.165Al2O3(oct)
Mg-Montmorillonite	Mg0.495Al1.67Si4O10(OH)2	Mg-Montmorillonite = Pyrophyllite + 0.495MgO - 0.165Al2O3(oct)
Low Fe-Mg Smectite	see below	Low Fe-Mg Smectite = Pyrophyllite + 0.075Na2O + 0.1K2O + 0.02CaO + 0.9MgO + 0.08Fe2O3 + 0.29FeO - 0.5Al2O3(oct) + 0.125Al2O3(tetr) - 0.25SiO2
Fe-Mg Smectite	see below	High Fe-Mg Smectite = Pyrophyllite + 0.05Na2O + 0.1K2O + 0.025CaO + 1.15MgO + 0.1Fe2O3 + 0.5FeO - 0.625Al2O3(oct) + 0.125Al2O3(tetr) - 0.5SiO2
Reykjanes Smectite	see below	Reykjanes Smectite = Pyrophyllite + 0.165Na2O + 0.015K2O + 0.66CaO + 1.29MgO + 0.175Fe2O3 + 0.33FeO + 0.01MnO - 0.86Al2O3(oct) + 0.415Al2O3(tetr) - 0.83SiO2

Low Fe-Mg Smectite = Na0.15K0.2Ca0.02(Mg0.9Fe(+++)0.16Fe(++)0.29Al)(Al0.25Si3.75)O10(OH)2

Fe-Mg Smectite = Na0.1K0.2Ca0.025(Mg1.15Fe(+++)0.2Fe(++)0.5Al0.75)(Al0.5Si3.5)O10(OH)2

Reykjanes Smectite = Na0.33K0.03Ca0.66(Mg1.29Fe(+++)0.35Fe(++)0.33Mn0.01Al0.28)(Al0.83Si3.17)O10(OH)2

Table 1.12. Estimated thermodynamic data for 23 dehydrated smectite compositions.

Name	Formula	$\Delta G_f°$ cal/mol	$\Delta H_f°$ cal/mol	S° cal/mol-K	V° cm³/mol	a cal/mol-K	b x 10³ cal/mol-K²	c x 10⁻⁵ cal-K/mol
H-Beidellite	H0.33Al2Al0.33Si3.67O10(OH)2	-1260140.8	-1351137.7	57.636	126.075	81.438	38.333	17.774
Na-Beidellite	Na0.33Al2Al0.33Si3.67O10(OH)2	-1278599.5	-1368880.0	58.931	127.590	83.277	37.780	18.251
K-Beidellite	K0.33Al2Al0.33Si3.67O10(OH)2	-1281785.7	-1372093.1	59.896	131.052	83.319	38.401	17.919
Ca-Beidellite	Ca0.165Al2Al0.33Si3.67O10(OH)2	-1278541.0	-1368495.6	57.618	126.578	82.191	37.152	18.031
Mg-Beidellite	Mg0.165Al2Al0.33Si3.67O10(OH)2	-1275209.6	-1365228.7	57.050	125.391	81.945	37.260	18.018
H-Saponite	H0.33Mg3Al0.33Si3.67O10(OH)2	-1324331.8	-1409762.5	62.777	135.725	84.486	40.729	13.832
Na-Saponite	Na0.33Mg3Al0.33Si3.67O10(OH)2	-1342790.5	-1427505.2	64.071	137.240	86.325	40.176	14.309
K-Saponite	K0.33Mg3Al0.33Si3.67O10(OH)2	-1345976.7	-1430717.5	65.039	140.702	86.367	40.797	13.977
Ca-Saponite	Ca0.165Mg3Al0.33Si3.67O10(OH)2	-1342732.0	-1427120.5	62.760	136.228	85.239	39.548	14.089
Mg-Saponite	Mg0.165Mg3Al0.33Si3.67O10(OH)2	-1339400.6	-1423853.8	62.190	135.041	84.993	39.656	14.076
H-Nontronite	H0.33Fe2Al0.33Si3.67O10(OH)2	-1055918.4	-1140192.3	66.657	131.753	77.438	54.113	12.944
Na-Nontronite	Na0.33Fe2Al0.33Si3.67O10(OH)2	-1074377.1	-1157936.8	67.945	133.267	79.277	53.560	13.421
K-Nontronite	K0.33Fe2Al0.33Si3.67O10(OH)2	-1077563.2	-1161143.7	68.931	136.730	79.319	54.181	13.089
Ca-Nontronite	Ca0.165Fe2Al0.33Si3.67O10(OH)2	-1074318.6	-1157550.6	66.638	132.256	78.191	52.932	13.201
Mg-Nontronite	Mg0.165Fe2Al0.33Si3.67O10(OH)2	-1070987.1	-1154285.8	66.063	131.068	77.945	53.040	13.188
H-Montmorillonite	H0.33Mg0.33Al1.67Si4O10(OH)2	-1251018.7	-1340729.7	58.968	128.651	79.429	40.683	16.388
Na-Montmorillonite	Na0.33Mg0.33Al1.67Si4O10(OH)2	-1269477.4	-1358472.2	60.263	130.165	81.267	40.130	16.865
K-Montmorillonite	K0.33Mg0.33Al1.67Si4O10(OH)2	-1272663.5	-1361685.0	61.229	133.627	81.310	40.750	16.533
Ca-Montmorillonite	Ca0.165Mg0.33Al1.67Si4O10(OH)2	-1269418.9	-1358087.6	58.951	129.154	80.181	39.501	16.645
Mg-Montmorillonite	Mg0.495Al1.67Si4O10(OH)2	-1266087.4	-1354820.7	58.382	127.966	79.935	39.610	16.632
Low Fe-Mg Smectite	see below	-1261694.8	-1351295.0	65.313	134.706	84.327	41.014	15.634
High Fe-Mg Smectite	see below	-1213458.8	-1303302.8	66.390	131.625	86.685	40.089	15.493
Reykjanes Smectite	see below	-1299800.6	-1390109.9	69.942	138.295	90.231	39.005	15.618

Low Fe-Mg Smectite = Na0.15K0.2Ca0.02(Mg0.9Fe(+++)0.16Fe(++)0.29Al)(Al0.25Si3.75)O10(OH)2

Fe-Mg Smectite = Na0.1K0.2Ca0.025(Mg1.15Fe(+++)0.2Fe(++)0.5Al0.75)(Al0.5Si3.5)O10(OH)2

Reykjanes Smectite = Na0.33K0.03Ca0.66(Mg1.29Fe(+++)0.35Fe(++)0.33Mn0.01Al0.28)(Al0.83Si3.17)O10(OH)2

Table 1.13. Estimated thermodynamic data for 23 smectite compositions with interlayer hydration number of 4.5. The data in Table 1.5 for interlayer water properties are used along with the data for the corresponding dehydrated compositions from Table 1.9. See footnote for more information on Gibbs energies and enthalpies.

Name	Formula	$\Delta G_f°$ cal/mol[a]	$\Delta H_f°$ cal/mol[a]	S° cal/mol-K	V° cm^3/mol	a cal/mol-K	b x 10^3 cal/mol-K^2	c x 10^{-5} cal-K/mol
H-Beidellite	H0.33Al2Al0.33Si3.67O10(OH)2			116.811	203.565	122.136	93.863	13.368
Na-Beidellite	Na0.33Al2Al0.33Si3.67O10(OH)2			118.106	205.080	123.975	93.310	13.845
K-Beidellite	K0.33Al2Al0.33Si3.67O10(OH)2			119.071	208.542	124.017	93.931	13.513
Ca-Beidellite	Ca0.165Al2Al0.33Si3.67O10(OH)2			116.793	204.068	122.889	92.682	13.626
Mg-Beidellite	Mg0.165Al2Al0.33Si3.67O10(OH)2			116.225	202.881	122.643	92.790	13.612
H-Saponite	H0.33Mg3Al0.33Si3.67O10(OH)2			121.952	213.215	125.184	96.259	9.426
Na-Saponite	Na0.33Mg3Al0.33Si3.67O10(OH)2			123.246	214.730	127.023	95.706	9.903
K-Saponite	K0.33Mg3Al0.33Si3.67O10(OH)2			124.214	218.192	127.065	96.327	9.571
Ca-Saponite	Ca0.165Mg3Al0.33Si3.67O10(OH)2			121.935	213.718	125.937	95.078	9.684
Mg-Saponite	Mg0.165Mg3Al0.33Si3.67O10(OH)2			121.365	212.531	125.691	95.186	9.670
H-Nontronite	H0.33Fe2Al0.33Si3.67O10(OH)2			125.832	209.243	118.136	109.643	8.538
Na-Nontronite	Na0.33Fe2Al0.33Si3.67O10(OH)2			127.120	210.757	119.975	109.090	9.015
K-Nontronite	K0.33Fe2Al0.33Si3.67O10(OH)2			128.106	214.220	120.017	109.711	8.683
Ca-Nontronite	Ca0.165Fe2Al0.33Si3.67O10(OH)2			125.813	209.746	118.889	108.462	8.796
Mg-Nontronite	Mg0.165Fe2Al0.33Si3.67O10(OH)2			125.238	208.558	118.643	108.570	8.782
H-Montmorillonite	H0.33Mg0.33Al1.67Si4O10(OH)2			118.143	206.141	120.127	96.213	11.982
Na-Montmorillonite	Na0.33Mg0.33Al1.67Si4O10(OH)2			119.438	207.655	121.965	95.660	12.459
K-Montmorillonite	K0.33Mg0.33Al1.67Si4O10(OH)2			120.404	211.117	122.008	96.280	12.127
Ca-Montmorillonite	Ca0.165Mg0.33Al1.67Si4O10(OH)2			118.126	206.644	120.879	95.031	12.240
Mg-Montmorillonite	Mg0.495Al1.67Si4O10(OH)2			117.557	205.456	120.633	95.140	12.226
Low Fe-Mg Smectite	see below			124.488	212.196	125.025	96.544	11.228
High Fe-Mg Smectite	see below			125.565	209.115	127.383	95.619	11.088
Reykjanes Smectite	see below			129.117	215.785	130.929	94.535	11.213

Low Fe-Mg Smectite = Na0.15K0.2Ca0.02(Mg0.9Fe(+++)0.16Fe(++)0.29Al)(Al0.25Si3.75)O10(OH)2

Fe-Mg Smectite = Na0.1K0.2Ca0.025(Mg1.15Fe(+++)0.2Fe(++)0.5Al0.75)(Al0.5Si3.5)O10(OH)2

Reykjanes Smectite = Na0.33K0.03Ca0.66(Mg1.29Fe(+++)0.35Fe(++)0.33Mn0.01Al0.28)(Al0.83Si3.17)O10(OH)2

[a] Gibbs energies and enthalpies are not given here as these would depend on specific hydration models and cannot be estimated from linear or quasi-linear methods analogous to those that were used here for the remaining properties

Table 1.14. Estimated thermodynamic data for 23 smectite compositions with interlayer hydration number of 5. The data in Table 1.5 for interlayer water properties are used along with the data for the corresponding dehydrated compositions from Table 1.9.

Name	Formula	$\Delta G_f°$ cal/mol[a]	$\Delta H_f°$ cal/mol[a]	S° cal/mol-K	V° cm³/mol	a cal/mol-K	b x 10³ cal/mol-K²	c x 10⁻⁵ cal-K/mol
H-Beidellite	H0.33Al2Al0.33Si3.67O10(OH)2			123.386	212.175	126.658	100.033	12.879
Na-Beidellite	Na0.33Al2Al0.33Si3.67O10(OH)2			124.681	213.690	128.497	99.480	13.356
K-Beidellite	K0.33Al2Al0.33Si3.67O10(OH)2			125.646	217.152	128.539	100.101	13.024
Ca-Beidellite	Ca0.165Al2Al0.33Si3.67O10(OH)2			123.368	212.678	127.411	98.852	13.136
Mg-Beidellite	Mg0.165Al2Al0.33Si3.67O10(OH)2			122.800	211.491	127.165	98.960	13.123
H-Saponite	H0.33Mg3Al0.33Si3.67O10(OH)2			128.527	221.825	129.706	102.429	8.937
Na-Saponite	Na0.33Mg3Al0.33Si3.67O10(OH)2			129.821	223.340	131.545	101.876	9.414
K-Saponite	K0.33Mg3Al0.33Si3.67O10(OH)2			130.789	226.802	131.587	102.497	9.082
Ca-Saponite	Ca0.165Mg3Al0.33Si3.67O10(OH)2			128.510	222.328	130.459	101.248	9.194
Mg-Saponite	Mg0.165Mg3Al0.33Si3.67O10(OH)2			127.940	221.141	130.213	101.356	9.181
H-Nontronite	H0.33Fe2Al0.33Si3.67O10(OH)2			132.407	217.853	122.658	115.813	8.049
Na-Nontronite	Na0.33Fe2Al0.33Si3.67O10(OH)2			133.695	219.367	124.497	115.260	8.526
K-Nontronite	K0.33Fe2Al0.33Si3.67O10(OH)2			134.681	222.830	124.539	115.881	8.194
Ca-Nontronite	Ca0.165Fe2Al0.33Si3.67O10(OH)2			132.388	218.356	123.411	114.632	8.306
Mg-Nontronite	Mg0.165Fe2Al0.33Si3.67O10(OH)2			131.813	217.168	123.165	114.740	8.293
H-Montmorillonite	H0.33Mg0.33Al1.67Si4O10(OH)2			124.718	214.751	124.649	102.383	11.493
Na-Montmorillonite	Na0.33Mg0.33Al1.67Si4O10(OH)2			126.013	216.265	126.487	101.830	11.970
K-Montmorillonite	K0.33Mg0.33Al1.67Si4O10(OH)2			126.979	219.727	126.530	102.450	11.638
Ca-Montmorillonite	Ca0.165Mg0.33Al1.67Si4O10(OH)2			124.701	215.254	125.401	101.201	11.750
Mg-Montmorillonite	Mg0.495Al1.67Si4O10(OH)2			124.132	214.066	125.155	101.310	11.737
Low Fe-Mg Smectite	see below			131.063	220.806	129.547	102.714	10.739
High Fe-Mg Smectite	see below			132.140	217.725	131.905	101.789	10.598
Reykjanes Smectite	see below			135.692	224.395	135.451	100.705	10.723

Low Fe-Mg Smectite = Na0.15K0.2Ca0.02(Mg0.9Fe(+++)0.16Fe(++)0.29Al)(Al0.25Si3.75)O10(OH)2

Fe-Mg Smectite = Na0.1K0.2Ca0.025(Mg1.15Fe(+++)0.2Fe(++)0.5Al0.75)(Al0.5Si3.5)O10(OH)2

Reykjanes Smectite = Na0.33K0.03Ca0.66(Mg1.29Fe(+++)0.35Fe(++)0.33Mn0.01Al0.28)(Al0.83Si3.17)O10(OH)2

[a] Gibbs energies and enthalpies are not given here as these would depend on specific hydration models and cannot be estimated from linear or quasi-linear methods analogous to those that were used here for the remaining properties

Table 1.15. Estimated thermodynamic data for 23 smectite compositions with interlayer hydration number of 7. The data in Table 1.5 for interlayer water properties are used along with the data for the corresponding dehydrated compositions from Table 1.9.

Name	Formula	$\Delta G_f°$ cal/mol[a]	$\Delta H_f°$ cal/mol[a]	S° cal/mol-K	V° cm³/mol	a cal/mol-K	b x 10³ cal/mol-K²	c x 10⁻⁵ cal-K/mol
H-Beidellite	H0.33Al2Al0.33Si3.67O10(OH)2			149.686	246.615	144.746	124.713	10.921
Na-Beidellite	Na0.33Al2Al0.33Si3.67O10(OH)2			150.981	248.130	146.585	124.160	11.398
K-Beidellite	K0.33Al2Al0.33Si3.67O10(OH)2			151.946	251.592	146.627	124.781	11.066
Ca-Beidellite	Ca0.165Al2Al0.33Si3.67O10(OH)2			149.668	247.118	145.499	123.532	11.178
Mg-Beidellite	Mg0.165Al2Al0.33Si3.67O10(OH)2			149.100	245.931	145.253	123.640	11.165
H-Saponite	H0.33Mg3Al0.33Si3.67O10(OH)2			154.827	256.265	147.794	127.109	6.979
Na-Saponite	Na0.33Mg3Al0.33Si3.67O10(OH)2			156.121	257.780	149.633	126.556	7.456
K-Saponite	K0.33Mg3Al0.33Si3.67O10(OH)2			157.089	261.242	149.675	127.177	7.124
Ca-Saponite	Ca0.165Mg3Al0.33Si3.67O10(OH)2			154.810	256.768	148.547	125.928	7.236
Mg-Saponite	Mg0.165Mg3Al0.33Si3.67O10(OH)2			154.240	255.581	148.301	126.036	7.223
H-Nontronite	H0.33Fe2Al0.33Si3.67O10(OH)2			158.707	252.293	140.746	140.493	6.091
Na-Nontronite	Na0.33Fe2Al0.33Si3.67O10(OH)2			159.995	253.807	142.585	139.940	6.568
K-Nontronite	K0.33Fe2Al0.33Si3.67O10(OH)2			160.981	257.270	142.627	140.561	6.236
Ca-Nontronite	Ca0.165Fe2Al0.33Si3.67O10(OH)2			158.688	252.796	141.499	139.312	6.348
Mg-Nontronite	Mg0.165Fe2Al0.33Si3.67O10(OH)2			158.113	251.608	141.253	139.420	6.335
H-Montmorillonite	H0.33Mg0.33Al1.67Si4O10(OH)2			151.018	249.191	142.737	127.063	9.535
Na-Montmorillonite	Na0.33Mg0.33Al1.67Si4O10(OH)2			152.313	250.705	144.575	126.510	10.012
K-Montmorillonite	K0.33Mg0.33Al1.67Si4O10(OH)2			153.279	254.167	144.618	127.130	9.680
Ca-Montmorillonite	Ca0.165Mg0.33Al1.67Si4O10(OH)2			151.001	249.694	143.489	125.881	9.792
Mg-Montmorillonite	Mg0.495Al1.67Si4O10(OH)2			150.432	248.506	143.243	125.990	9.779
Low Fe-Mg Smectite	see below			157.363	255.246	147.635	127.394	8.781
High Fe-Mg Smectite	see below			158.440	252.165	149.993	126.469	8.640
Reykjanes Smectite	see below			161.992	258.835	153.539	125.385	8.765

Low Fe-Mg Smectite = Na0.15K0.2Ca0.02(Mg0.9Fe(+++)0.16Fe(++)0.29Al)(Al0.25Si3.75)O10(OH)2

Fe-Mg Smectite = Na0.1K0.2Ca0.025(Mg1.15Fe(+++)0.2Fe(++)0.5Al0.75)(Al0.5Si3.5)O10(OH)2

Reykjanes Smectite = Na0.33K0.03Ca0.66(Mg1.29Fe(+++)0.35Fe(++)0.33Mn0.01Al0.28)(Al0.83Si3.17)O10(OH)2

[a] Gibbs energies and enthalpies are not given here as these would depend on specific hydration models and cannot be estimated from linear or quasi-linear methods analogous to those that were used here for the remaining properties

181

Table 1.16. Estimated thermodynamic data for 23 smectite compositions with implicit hydration (corresponding to unit water activity). At the present time, only Gibbs energy data are available.

Name	Formula	$\Delta G_f°$ cal/mol	$\Delta H_f°$ cal/mol	S° cal/mol-K	V° cm³/mol	a cal/mol-K	b x 10³ cal/mol-K²	c x 10⁻⁵ cal-K/mol
H-Beidellite	H0.33Al2Al0.33Si3.67O10(OH)2	-1269753.6						
Na-Beidellite	Na0.33Al2Al0.33Si3.67O10(OH)2	-1279700.1						
K-Beidellite	K0.33Al2Al0.33Si3.67O10(OH)2	-1281785.7						
Ca-Beidellite	Ca0.165Al2Al0.33Si3.67O10(OH)2	-1280921.1						
Mg-Beidellite	Mg0.165Al2Al0.33Si3.67O10(OH)2	-1277076.6						
H-Saponite	H0.33Mg3Al0.33Si3.67O10(OH)2	-1324619.1						
Na-Saponite	Na0.33Mg3Al0.33Si3.67O10(OH)2	-1343891.1						
K-Saponite	K0.33Mg3Al0.33Si3.67O10(OH)2	-1345976.7						
Ca-Saponite	Ca0.165Mg3Al0.33Si3.67O10(OH)2	-1345112.1						
Mg-Saponite	Mg0.165Mg3Al0.33Si3.67O10(OH)2	-1341267.6						
H-Nontronite	H0.33Fe2Al0.33Si3.67O10(OH)2	-1056205.6						
Na-Nontronite	Na0.33Fe2Al0.33Si3.67O10(OH)2	-1075477.6						
K-Nontronite	K0.33Fe2Al0.33Si3.67O10(OH)2	-1077563.2						
Ca-Nontronite	Ca0.165Fe2Al0.33Si3.67O10(OH)2	-1076698.6						
Mg-Nontronite	Mg0.165Fe2Al0.33Si3.67O10(OH)2	-1072854.1						
H-Montmorillonite	H0.33Mg0.33Al1.67Si4O10(OH)2	-1255040.0						
Na-Montmorillonite	Na0.33Mg0.33Al1.67Si4O10(OH)2	-1274312.0						
K-Montmorillonite	K0.33Mg0.33Al1.67Si4O10(OH)2	-1276397.6						
Ca-Montmorillonite	Ca0.165Mg0.33Al1.67Si4O10(OH)2	-1275533.0						
Mg-Montmorillonite	Mg0.495Al1.67Si4O10(OH)2	-1271688.5						
Low Fe-Mg Smectite	see below	-1272667.3						
High Fe-Mg Smectite	see below	-1227165.4						
Reykjanes Smectite	see below	-1325017.9						

Low Fe-Mg Smectite = Na0.15K0.2Ca0.02(Mg0.9Fe(+++)0.16Fe(++)0.29Al)(Al0.25Si3.75)O10(OH)2

Fe-Mg Smectite = Na0.1K0.2Ca0.025(Mg1.15Fe(+++)0.2Fe(++)0.5Al0.75)(Al0.5Si3.5)O10(OH)2

Reykjanes Smectite = Na0.33K0.03Ca0.66(Mg1.29Fe(+++)0.35Fe(++)0.33Mn0.01Al0.28)(Al0.83Si3.17)O10(OH)2

Table 1.17. Entropies of the elements in their reference forms, compiled from various sources. The list here addresses only elements of interest in relation to clay minerals. Colors correspond to sources. Values adopted here are given on the right hand side.

Elemental Reference Entropies (S°)

	NBS 1982	CODATA 1989	NEA 1992-	Barin 1995		Used Here	Used Here
Element	J/mol-K	J/mol-K	J/mol-K	J/mol-K	Element	J/mol-K	cal/mol-K
Al	28.33	28.30	28.300	28.275	Al	28.300	6.764
Ba	62.8	-----	62.420	62.417	Ba	62.420	14.919
Ca	41.42	41.59	41.590	41.422	Ca	41.590	9.940
Cs	85.23	85.23	85.230	85.147	Cs	85.230	20.370
F	101.39	101.3955	101.3955	101.3975	F	101.3955	24.234
Fe	27.28	-----		27.280	Fe	27.280	6.520
H	65.342	65.340	65.340	65.340	H	65.340	15.617
K	64.18	64.68	64.680	64.670	K	64.680	15.459
Li	29.12	29.12	29.120	29.080	Li	29.120	6.960
Mg	32.68	32.67	32.670	32.677	Mg	32.670	7.808
Mn	32.01	-----		32.008	Mn	32.008	7.650
Na	51.21	51.30	51.300	51.455	Na	51.300	12.261
O	102.569	102.576	102.576	102.5735	O	102.576	24.516
Ra	71	-----		-----	Ra	71	16.969
Rb	76.78	76.78	76.780	76.780	Rb	76.780	18.351
Si	18.83	18.81	18.810	18.820	Si	18.810	4.496
Sr	52.3	-----	55.700	55.690	Sr	55.700	13.313

For future work, we intend to obtain and analyze additional data to construct more accurate estimates of the thermodynamic properties of complex clays, with a focus on hydration/dehydration and ion exchange. We intend to carry forward the implicitly hydrated model as at least a point of comparison. However, the main goal of present and future work is to develop a corresponding model that explicitly treats the interlayer water and covers states of variable hydration and which reasonably explains a wide variety of types of physical measurements, including thermogravimetry and XRD studies of dehydration, ion exchange measurements, solubilities, and swelling pressures. We also intend to work in such insight as is possible from molecular dynamics studies (e.g., Cygan et al., 2004). The goal here would be do develop data for end-member compositions such as $Na_{0.33}Al_2Al_{0.33}Si_{3.67}O_{10}(OH)_2$.n H_2O, where n is likely to have a maximum value between 4.5 and 7, and to appropriately describe the thermodynamics of mixing.

Ransom and Helgeson (1993, 1994ab, 1995) developed an approach to deal with variable hydration. It has some excellent features. However, it does not extend to a complete treatment of smectite thermodynamics in that it does not develop estimates of Gibbs energies for the various end member compositions that are discussed. Rather, it only addresses Gibbs energies of dehydration between fully hydrated and dehydrated end-members of otherwise fixed composition. It doesn't cover the full range of clay mineral compositions that is desired. Also, it leaves open some questions as to how to handle hydration/dehydration when that depends on the interlayer cation content, which can be quite variable. In their 1995 paper, they make an attempt at modeling the case of mixed Na and Ca in the interlayer, but this aspect was insufficiently developed and tested. Nevertheless, their model does show a path forward to extending the Tardy-Garrels type model thus far developed.

Tardy and Duplay (1992) go farther than Ransom and Helgeson (papers cited above) in that they address both interlayer water and the full thermodynamic stability of end-member clay compositions. Their approach provides a counterpoint to both aspects of the model we are working to develop, and various parts of their model may simply be incorporated into ours. Some papers by Viellard (1994ab, 2000) are also of interest in this regard (his 2000 paper addresses interlayer water). Vidal and Dubacq (2009) have recently proposed a model for interlayer water and full stability that is also of great interest. Work that remains to be done is to compare and evaluate these models, as they have different ranges of focus and often have implications beyond what is addressed directly. Section 2.3.3 describes the implementation of a clay hydration using a Gibbs energy minimization method based on that by Vieillard et al. (2011). There are, for example, implications of these models to high temperature ion exchange and swelling pressure behavior that are not fully developed or explored. This is a reflection of the complexity of the topic area. There appears to have been only rather limited penetration of such models into geochemical modeling and reactive transport simulation. In fact, there seem to be few computational tools available to readily assess the consequences of these models. Section 2.3.3.1 describes the implementation of a thermodynamic model in the Cantera constitutive model toolkit using a Margules solid solution formulation to evaluate clay hydration phenomena.

In summary, this remains a work in process. We will improve the existing data/models for complex clays by:

- Explicitly accounting for water in the exchange layers of smectites and vermiculites
- Accounting for a broader spectrum of physical measurements (e.g., basal spacing studies of clay dehydration, swelling pressure data, ion exchange data over a wide range of temperature)
- Including insights from molecular dynamics (MD) modeling regarding dehydration (in part via informal collaboration with R. Cygan's MD modeling group at SNL).
- Developing computational tools to evaluate existing and new models.

1.3   Thermodynamic Modeling of Clay Hydration

Clay hydration/ dehydration plays a key role in EBS performance due to the swelling properties of these materials and also being the main barrier component with a high degree of exposure to thermal, mechanical, hydrological (i.e., THM) phenomena in nuclear waste repository environments. The swelling behavior of bentonite clay and water transport through this barrier material has been identified by various repository research programs as key aspects of the barrier performance (Karnland, 1997; Karnland et al., 2007; Kim et al., 2011). The importance of clay expansive properties to barrier performance in repository environments can be outlined on the basis of (Kim et al., 2011):

- The generation of swelling pressure to induce sealing and self-healing in clay, therefore causing a decrease in permeability

- Inhibit canister sinking and microbial activity

Clay expansive properties can be undesirable to buffer/backfill emplacement leading to cracking when exposed to various levels of relative humidity (RH) (Dueck et al., 2008). Upon emplacement, clay swelling behavior and therefore sealing properties at EBS interfaces can be greatly affected by high levels of saturation and elevated temperatures (Akesson et al., 2009; Dueck et al., 2008; Karnland et al., 2008). However, it is expected that the clay buffer/backfill material will remain relatively unsaturated during most of the repository performance period, even with the various levels of episodic resaturation. Many experimental studies of clay barrier materials have been conducted at various scales. For example, the FEBEX experiment has produced long-term data representative of a full-scale *in situ* heating test (Fernandez and Villar, 2010; Gens et al., 2009; Samper et al., 2008; Sanchez et al., 2010, 2012; Villar et al., 2007). Other studies have been focused on smaller scale experiments to study clay swelling behavior with respect to potential conditions in repository and sedimentary basin environments (Dueck et al., 2008; Karnland, 1997; Karnland et al., 2007; Liu and Lin, 2005; Ransom and Helgeson, 1995). All these studies emphasize the need for the accurate understanding of clay expansive properties coupled with fluid interactions as anticipated in long-term conditions in subsurface environments such as disposal galleries in nuclear waste repositories. Knowledge of clay thermodynamic properties is critical to the evaluation and prediction of stability relations when assessing their interaction with fluids. Hydration/dehydration phenomena can significantly affect the stability of the clay phase. Moreover, the few experimental data sets for clay hydration are limited to a few compositions and low temperatures. This calls for the need of developing models to evaluate clay hydration/dehydration exploiting the use of chemical equilibrium and thermodynamic relations

along with the existing data to make predictions about clay stability and phase equilibria (Ransom and Helgeson, 1994a, b, 1995; Vidal and Dubacq, 2009; Vieillard et al., 2011).

1.3.1 Modeling Approach and Discussion

Estimation methods for the thermodynamic properties of clays have been developed capturing the compositional complexities of sheet silicates and this topic is discussed in very much detail in Section 1.2. Ransom and Helgeson (1994a, 1995) developed a solid solution mixing model to describe the hydration/dehydration of smectite clay solely based on the H_2O content within the interlayer region. That is, no other sheet components in the smectite phase are exchanged in the hydration/dehydration process making it suitable for studying partially saturated clay (Vieillard et al., 2011). The approach of Ransom and Helgeson (1994a, 1995) is then based on a regular solid solution mixing between hydrated and dehydrated end-member components allowing for the application of thermodynamic formalisms to describe chemical equilibria at various levels of clay hydration. Their model can be expressed by the following reaction for Na-smectite dehydration:

$$Na - smectite \; _{(hyd.,n_{H_2O,max}H_2O)} = Na - smectite \; _{(dehyd.)} + n_{H_2O,max}H_2O \qquad (1.4)$$
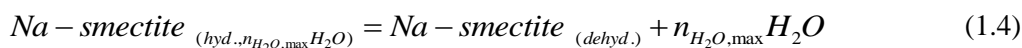
where $Na - smectite \; (hyd.,n_{H_2O,max}H_2O)$ and $Na - smectite \; (dehyd.)$ delineate the fully hydrated and dehydrated Na-smectite, respectively. $n_{H_2O,max}$ stands for the maximum number of moles of H_2O in the clay structure. The mass action law expression for reaction 1.4 is given by:

$$K = \frac{a_{Na-smectite \; (dehyd.)}a_{H_2O}^{n_{H_2O,max}}}{a_{Na-smectite \; (hyd.,n_{H_2O,max}H_2O)}} \qquad (1.5)$$

where the $a_{Na-smectite \; (dehyd.)}$ and $a_{Na-smectite \; (hyd.,n_{H_2O,max}H_2O)}$ are the activities of the dehydrated and hydrated Na-smectite phase, respectively. a_{H_2O} denotes the activity of H_2O in the aqueous phase. The treatment of a_{H_2O} by Ransom and Helgeson (1994a) is to directly equate this parameter to the RH given by the clay swelling experimental data. Such equivalent designation of RH with a_{H_2O} is consistent with the liquid standard state reference for H_2O.

Other clay hydration models have been advanced recently (Vidal and Dubacq, 2009; Vieillard et al., 2011), however, their modeling basis is still consistent with the fundamental treatment of Ransom and Helgeson (1994a). Vidal and Dubacq (2009) developed a model centered on the description of the gradual stepwise evolution of clay dehydration using a non-ideal solid solution mixing model between a mica phase and smectite clay at various hydration levels (0.7, 2, 4, and 7 moles H_2O per $O_{10}(OH)_2$ in the interlayer region). In this model, the hydration levels correspond to the number of water layers in the clay interlayer domain. The model is parameterized in accord with estimations of thermodynamic properties of anhydrous and hydrous clays and hydration/dehydration experimental data from the literature. Vieillard et al. (2011) advanced a model also based on that by Ransom and Helgeson (1994a, 1995) consistent with hydration/dehydration data using the Margules formalism to represent a non-ideal solid solution between the anhydrous and hydrous smectite clay end-members. Their approach also accounts for the treatment of all thermodynamic entities (G°, H°, S°) in the evaluation of the excess Gibbs energy of mixing. Their model is also validated against experimental data on hydration/dehydration of hetero- and homo-ionic smectites at different temperatures. All these models, even with their differences, provide a reasonable representation of

the existing experimental data of smectite hydration/dehydration and related thermodynamic properties.

The model developed in the current study closely follows the approach of Vieillard et al. (2011) using the Margules formalism to represent a non-ideal solid solution between hydrated and dehydrated smectite clay end-members given by Equations 1.6 through 1.7 to compute chemical equilibrium between smectite and H_2O phase as a function of RH:

$$H^{EX} = X_{smect.\,hyd.} X_{smect.\,dehyd.} (W_{H1} + W_{H2} X_{smect.\,dehyd.}) \tag{1.6}$$

$$S^{EX} = X_{smect.\,hyd.} X_{smect.\,dehyd.} (W_{S1} + W_{S2} X_{smect.\,dehyd.}) \tag{1.7}$$

$$G^{EX} = H^{EX} - TS^{EX} \tag{1.8}$$

The model is implemented using the Cantera code suite for computation of chemical equilibria and a description is given in Section 1.1, and Moffat and Jové Colón (2009). The model was implemented in the form of C++ code that explicitly accounts for the thermodynamic properties of the clay solid solution (including end-members) and the gas state of H_2O when computing chemical equilibria as a function of RH. Therefore, the properties of all phases are properly captured in the computation of Gibbs energies by the GEM method in Cantera. The treatment of the H_2O phase in this work is different from that in Ransom and Helgeson (1994a, 1995), Vidal and Dubacq (2009), and Vieillard et al. (2011). Here the smectite solids interact with the stable phase of H_2O in the gas phase at the partial pressures and temperature that corresponds to the RH conditions in the experiments and delineated by the data. This treatment is important as to ensure thermodynamic consistency with the stable H_2O phase corresponding to the experimental methods when defining the theoretical equilibrium relations of this process.

The thermodynamic properties ($H°$ and $S°$) of the Na-smectite at 25°C is that of dehydrated Na beidellite obtained from the thermodynamic estimations for clay described in Section 1.2. Since the current model is developed to be closely consistent with that of Vieillard et al. (2011) so the properties of the hydrated clay end-member were retrieved to be partially consistent with those of their work. $H°$ and $S°$ for hydrated end-member were retrieved by using the enthalpy ($\Delta H°_{hyd}$) and entropy of hydration ($\Delta S°_{hyd}$) given in Vieillard et al. (2011) and those for dehydrated Na beidellite described in this report. The computation of the number of moles of H_2O per $O_{10}(OH)_2$ (clay half-cell) or $n_{H_2O,il}$ in the clay interlayer is given by:

$$n_{H_2O,il} = X_{Na-beid,hyd} n_{H_2O,max} \tag{1.9}$$

where $X_{Na-beid,hyd}$ denotes the mole fraction of hydrated Na beidellite component. The value of $n_{H_2O,max}$, as described in Section 1.2 is still a matter of debate. Vidal and Dubacq (2009) adopts a value of 7 whereas Ransom and Helgeson (1994a) estimated a value of 4.5 (see Section 1.2.2 for more details). The value of 5.5 adopted by Vieillard et al. (2011) was based on the attainment of adequate fits to the adsorption/desorption data for the considered clay compositions. For consistency with Vieillard et al. (2011), the adopted value of $n_{H_2O,max}$ in this study is taken as 5.5. The thermodynamic and physical properties of H_2O are computed using the IAPWS EoS formulation by Wagner and Pruβ (2002) implemented in Cantera. The computation of RH is

performed by specifying the partial pressure ($P_{H_2O,gas}$) and mass of H_2O (treated as a pure phase) in linear increments until saturation (i.e., RH $\approx$ 1) is reached. RH is calculated at 25°C from the ratio of H_2O gas density ($\rho_{H_2O,gas}$) to that of this phase at saturation ($\rho_{H_2O,gas,sat}$). This is equivalent to the ratio of H_2O partial pressure ($P_{H_2O,gas}$) multiplied by the fugacity coefficient (χ_{H_2O}) to that of H_2O partial pressure at saturation ($P_{H_2O,sat}^\circ$):

$$RH = a_{H_2O} = \frac{f_{H_2O}}{P_{H_2O,sat}} = \frac{\chi_{H_2O} P_{H_2O}}{P_{H_2O,sat}^\circ} = \frac{\rho_{H_2O,gas}}{\rho_{H_2O,gas,sat}} \tag{1.10}$$

where $\rho_{H_2O,gas}$ is computed from the IAPWS EoS in Cantera at each increment in pressure for each equilibrium step in the calculation. The regression analysis to retrieve the Margules parameters was conducted using the DAKOTA (Adams et al., 2012) optimization package along with iterative analyses to evaluate and adjust the Margules terms and S° of the hydrated smectite end-member. The adjustment of the S° parameter the hydrated smectite end-member was needed to refine the data fitting through the entire RH range. However, these adjustments were relatively minimal relative to the expected values for the Na smectite hydrated end-member ($n_{H_2O,max}$ = 5.5) used in this study. It should be noted that the enthalpy value remain unchanged for all isotherm fitted curves. The optimization procedure consisted of minimization of least squared differences between model prediction and reported isotherm data in the form of an objective function using a nongradient-based local optimization routine in the DAKOTA SCOLIB library (Adams et al., 2012). The experimental data of Cases et al. (1992) and Berend et al. (1995) as reported by Vieillard et al. (2011) and model fits therein were used in the isotherm fitting procedure.

The experimental data given by Cases et al. (1992) and Berend et al. (1995) was corrected by Vieillard et al. (2011) for H_2O surface coverage as a function of RH. Ransom and Helgeson (1994a, 1995) describe the hysteretic behavior of H_2O adsorption and desorption isotherms as nonrepresentative of an equilibrium state for these processes. This is because the derivatives of their thermodynamic properties are by definition exact differentials. However, the two isotherms can be used as reversal bounding limits to "bracket" the retrieval of equilibrium values for the Margules parameters. The Margules parameter values given by Vieillard provided good initial points to the fitting strategy yielding the shape of the isotherm curves but shifted from the actual data. Figure 1.6 shows the Cantera results for the adsorption, desorption, and theoretical equilibrium curves. Overall, the modeling results are in excellent agreement with the sigmoidal fits obtained by Vieillard et al. (2011). Table 1.18 provides the thermodynamic data for the Na smectite end-members (hydrated and dehydrated) and the resulting Margules parameters used in this study. As in Vieillard et al. (2011), the fit to the adsorption data of Berend et al. (1995) is better than that for the desorption data. Fitting of the desorption data at low RH values was not possible due to limitations of the Margules two-term formulation to retrieve fitting parameters that could represent $n_{H_2O,il}$ through the whole RH range. The theoretical equilibrium curve bounded between the adsorption/desorption curves was fitted to correspond with that given by Vieillard et al. (2011). Overall, there is very good agreement between the model curves of Vieillard et al. (2011) and the ones developed in this study. The model presented here is for Na-smectite but further work is planned to expand it to other clay compositions with divalent cations such as Ca and Mg.

188

Estimations of the thermodynamic properties of the clay interlayer H_2O are also planned for comparisons with other studies.

The current model implementation to describe clay hydration and that of cement leaching in an object-oriented Cantera constitutive toolkit provides excellent examples of model development in a flexible, agile, and rigorous platform to compute fluid-solid chemical equilibria. The model implementation allows for evaluation of clay hydration with the thermodynamic rigor necessary to advance predictions on the stability relations of these phases as a function of pressure, temperature, and composition. Such approach in the advancement of model constructs is envisioned for future integration with other models allowing for the comprehensive evaluation of EBS process phenomena under a wide range of repository conditions.
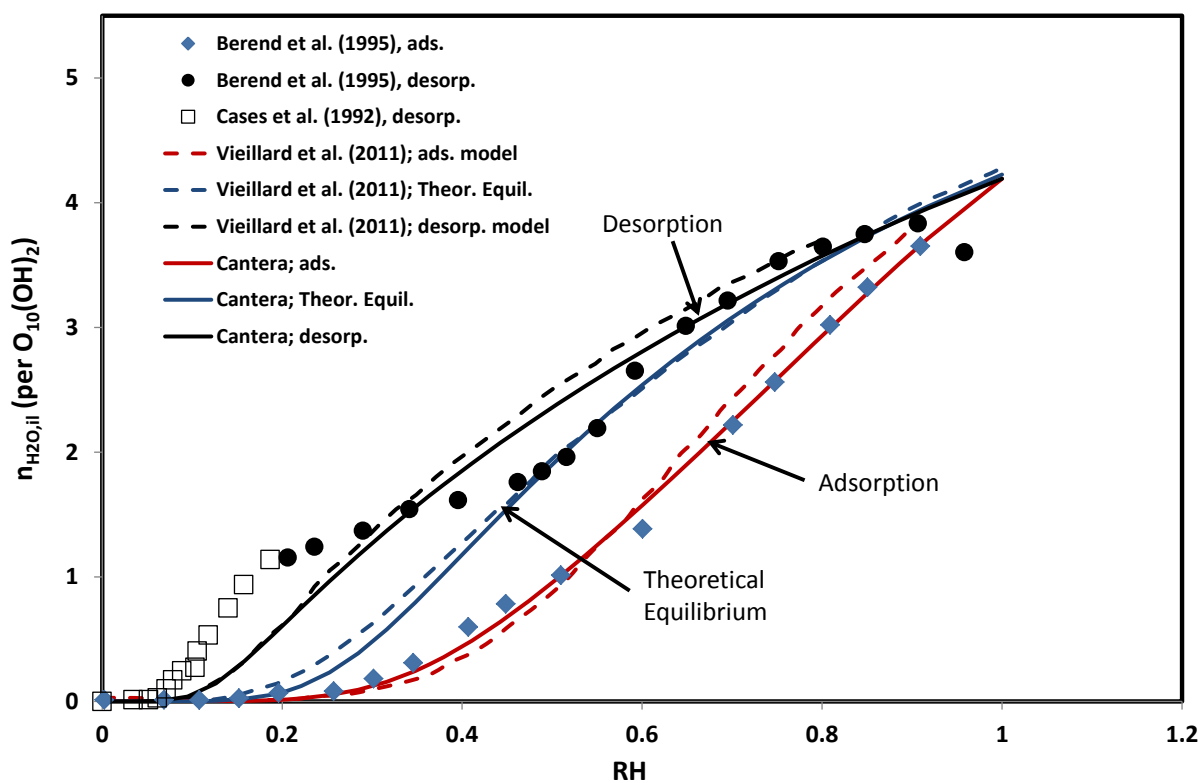
Figure 1.6. Plot of the of the number of moles of H_2O (per $O_{10}(OH)_2$) $\left(n_{H_2O,il}\right)$ in the clay interlayer versus RH for adsorption/desorption experimental and computed isotherms using Cantera. Notice the excellent agreement between the computed and model isotherms of Vieillard et al. (2011) for adsorption, desorption, and theoretical equilibrium (see text).

189

Table 1.18. Thermodynamic properties of clay end-members and Margules parameters for clay solid solution

Phase	$H°_{298}$ (J/mol)	$S°_{298}$ (J/K mol)	W_{H1} (J/mol)	W_{H2} (J/mol)	W_{S1} (J/K mol)	W_{S2} (J/K mol)	Remarks
Na-smectite (hyd.)	-7319302.92	567.54	-	-	-	-	Na-smectite hydrated end-member. Values retrieved assuming $n_{H_2O,max} = 5.5$
Na-smectite (dehyd.)	-5727393.92	246.57	-	-	-	-	Na-smectite dehydrated end-member (Table 2.12).
Na-smectite (Solid Sol.) adsorption	-	579.0[a]	8.0E+03	-3.50E+04	37.5	-125.0	[a] $S°_{298}$ was modified for Na-smectite (hyd.) for the isotherm fitting
Na-smectite (Solid Sol.) desorption	-	593.0[b]	1.0E+02	-8.00E+03	40.0	-40.0	[b] $S°_{298}$ was modified for Na-smectite (hyd.) for the isotherm fitting
Na-smectite (Solid Sol.) Theoretical Equilibrium	-	585.5[c]	9.5E+03	-6.5E+03	50.0	-20.0	[c] $S°_{298}$ was modified for Na-smectite (hyd.) for the isotherm fitting

1.4 *Remainder of FY12 and FY13 Work on Clay Hydration Modeling*

For the rest of the FY12 the following work is planned:

- Expansion and further testing of the clay hydration model to more clay compositions: Ca, Mg, and Sr.

- Utilize and test end-member thermodynamic properties developed in this work for hydrated clay end-members having various maximum numbers of H_2Os.

- Further testing of the C-S-H cement leaching model and cement phase solubilities

For FY13:

- Continue assessment of thermodynamic data for clays and cementitious materials at elevated temperatures (in conjunction with LLNL).

- Thermodynamic description of clay interactions and phase relations at high temperatures and pressures (with LANL experimental work on barrier material interactions).

- Explore the use of GEM models for sorption and ion exchange for potential implementation with the Cantera code.

- Establish collaboration with the CI experimental (cement-clay interaction) program at Mont Terri, Switzerland. The current phase of this program is focused on material characterization but there will also be a modeling activity on cement-clay interactions.

1.5　References

Adams, B. M., Dalbey, K. R., Eldred, M. S., Swiler, L. P., Bohnhoff, W. J., Eddy, J. P., Vigil, D. M., Hough, P. D., and Lefantzi, S., 2012, DAKOTA, A Multilevel Parallel Object-Oriented Framework for Design Optimization, Parameter Estimation, Uncertainty Quantification, and Sensitivity Analysis: Version 5.2+ User's Manual (SAND2010-2183): Sandia National Laboratories, SAND2010-2183.

Akesson, M., Jacinto, A. C., Gatabin, C., Sanchez, M., and Ledesma, A., 2009, Bentonite THM behaviour at high temperatures: experimental and numerical analysis: Geotechnique, v. 59, no. 4, p. 307-318.

Atkinson, A., Hearne, J. A., and Knights, C. F., 1989, Aqueous Chemistry and Thermodynamic Modeling of CaO-SiO$_2$-H$_2$O Gels: Journal of the Chemical Society-Dalton Transactions, no. 12, p. 2371-2379.

Babushkin, V. I., Matveyev, G. M., and Mchedlov-Petrossyan, O. P., 1985, Thermodynamics of silicates, Berlin, Germany, Springer-Verlag.

Barin, I. and Platzki, G. 1995. *Thermochemical Data of Pure Substances.* 3rd Edition. Two volumes. New York, New York: VCH Publishers.

Berend, I., Cases, J. M., Francois, M., Uriot, J. P., Michot, L., Masion, A., and Thomas, F., 1995, Mechanism of Adsorption and Desorption of Water-Vapor by Homoionic Montmorillonites .2. The Li$^+$, Na$^+$, K$^+$, Rb$^+$ and Cs$^+$ - Exchanged Forms: Clays and Clay Minerals, v. 43, no. 3, p. 324-336.

Berner, U. R., Modeling porewater chemistry in hydrated Portland cement, *in* Proceedings Scientific Basis for Nuclear Waste Management X Symposium Boston, Massachusetts, 1987, Volume 84, Material Research Society, p. 319-330.

-, 1988, Modelling the Incongruent Dissolution of Hydrated Cement Minerals: Radiochimica Acta, v. 44/45, p. 387-393.

-, 1990, A Thermodynamic description of the evolution of pore water chemistry and uranium speciation during the degradation of cement, PSI-Bericht 62: Wurenlingen und Villigen, Switzerland, Paul Scherrer Institute.

-, 1992, Evolution of Pore Water Chemistry During Degradation of Cement in a Radioactive Waste Repository Environment: Waste Management, v. 12, p. 201-219.

Blanc, P., Bourbon, X., Lassin, A., and Gaucher, E. C., 2010a, Chemical model for cement-based materials: Temperature dependence of thermodynamic functions for nanocrystalline and crystalline C-S-H phases: Cement and Concrete Research, v. 40, no. 6, p. 851-866.

-, 2010b, Chemical model for cement-based materials: Thermodynamic data assessment for phases other than C-S-H: Cement and Concrete Research, v. 40, no. 9, p. 1360-1374.

Binnewies, M. and Milke, E. 1999. *Thermochemical Data of Elements and Compounds.* New York, New York: Wiley-VCH.

Borjesson, S., Emren, A., and Ekberg, C., 1997, A thermodynamic model for the calcium silicate hydrate gel, modelled as a non-ideal binary solid solution: Cement and Concrete Research, v. 27, no. 11, p. 1649-1657.

Carey, J. W., and Lichtner, P. C., 2007, Calcium silicate hydrate (C-S-H) solid solution model applied to cement degradation using the continuum reactive transport model FLOTRAN, *in* Mobasher, B., and Skalny, J., eds., Transport Properties and Concrete Quality: Materials Science of Concrete, John Wiley & Sons, Inc., p. 73-106.

Carroll, S. A., McNab, W. W., and Torres, S. C., 2011, Experimental Study of Cement - Sandstone/Shale - Brine - CO_2 Interactions: Geochemical Transactions, v. 12.

Cases, J. M., Berend, I., Besson, G., Francois, M., Uriot, J. P., Thomas, F., and Poirier, J. E., 1992, Mechanism of Adsorption and Desorption of Water-Vapor by Homoionic Montmorillonite .1. The Sodium-Exchanged Form: Langmuir, v. 8, no. 11, p. 2730-2739.

Cox, J.D.; Wagman, D.D.; and Medvedev, V.A., eds. 1989. *CODATA Key Values for Thermodynamics*. CODATA Series on Thermodynamic Values. New York, New York: Hemisphere Publishing Company.

Cygan, R. T., Liang, J.-J., and Kalinichev, A. G., 2004, Molecular models of hydroxide, oxyhydroxide, and clay phases and the development of a general force field: Journal of Physical Chemistry B, v. 108, no. 4, p. 1255-1266.

Deer, W.A., Howie, R.A., and Zusman, J. 1962. *Rock-Forming Minerals. Vol. 3, Sheet Silicates*. Longmans, London. 270 p.

DOE, 1988, Consultation Draft - Site Characterization Plan Deaf Smith County, Texas; Volumes 7, Volume 7, Office of Civilian Radioactive Waste Management Salt Repository Project Office U.S. Department of Energy, p. 208-249.

Dole, L. R., and Mattus, C. H., Low pH concrete for use in the US High-Level Waste repository: Part I Overview., *in* Proceedings 3rd Workshop on R&D on Low-pH cement for a Geological Repository, Paris, France, June 13 -14 2007.

Dueck, A., Borgesson, L., Goudarzi, R., Lonnqvist, M., and Akesson, M., 2008, Humidity-induced water absorption and swelling of highly compacted bentonite in the project KBS-3H: Physics and Chemistry of the Earth, v. 33, p. S499-S503.

Fernandez, A. M., and Villar, M. V., 2010, Geochemical behaviour of a bentonite barrier in the laboratory after up to 8 years of heating and hydration: Applied Geochemistry, v. 25, no. 6, p. 809-824.

Fu, M.H., Zhang, Z.Z. and Low, P.F. 1990. "Changes in the properties of a montmorillonite-water system during the adsorption and desorption of water: hysteresis." *Clays and Clay Minerals*, 38, 485-492.

Fujii, K., and Kondo, W., 1981, Heterogeneous Equilibrium of Calcium Silicate Hydrate in Water at 30°C: Journal of the Chemical Society-Dalton Transactions, no. 2, p. 645-651.

Fujii, K., and Kondo, W., 1983, Estimation of thermochemical data for calcium silicate hydrate (C-S-H): Journal of the American Ceramic Society, v. 66, no. 12, p. C220-C221.

Garrels, R.M., and Christ, C.L. 1965 *Solutions, Minerals, and Equilibria*. Boston, Massachusetts: Jones and Bartlett Publishers

Gamsjager, H., Konigsberger, E., and Preis, W., 2000, Lippmann diagrams: Theory and application to carbonate systems: Aquatic Geochemistry, v. 6, no. 2, p. 119-132.

Gartner, E. M., and Jennings, H. M., 1987, Thermodynamics of Calcium Silicate Hydrates and Their Solutions: Journal of the American Ceramic Society, v. 70, no. 10, p. 743-749.

Geneste, P., Raynal, M., Atabek, R., Dardaine, M., and Oliver, J., 1990, Characterization of a French Clay Barrier and Outline of the Experimental Program: Engineering Geology, v. 28, no. 3-4, p. 443-454.

Gens, A., Sanchez, M., Guimaraes, L. D., Alonso, E. E., Lloret, A., Olivella, S., Villar, M. V., and Huertas, F., 2009, A full-scale in situ heating test for high-level nuclear waste disposal: observations, analysis and interpretation: Geotechnique, v. 59, no. 4, p. 377-399.

Glynn, P., 2000, Solid-solution solubilities and thermodynamics: Sulfates, carbonates and halides: Sulfate Minerals - Crystallography, Geochemistry and Environmental Significance, v. 40, p. 481-511.

Glynn, P. D., and Reardon, E. J., 1990, Solid-Solution Aqueous-Solution Equilibria - Thermodynamic Theory and Representation: American Journal of Science, v. 290, no. 2, p. 164-201.

Greenberg, S. A., and Chang, T. N., 1965, Investigation of the Colloidal Hydrated Calcium Silicates. II. Solubility Relationships in the Calcium Oxide-Silica-Water System at $25^{o}X$: Journal of Physical Chemistry, v. 69, no. 1, p. 182-188.

Greenberg, S. A., Chang, T. N., and Anderson, E., 1960, Inestigation of Colloidal Hydrated Calcium Silicates: I. Solubility Products: Journal of Physical Chemistry, v. 64, no. 9, p. 1151-1157.

Greenberg, J.P. and Moller, N. 1989. "The Prediction of Mineral Solubilities in Natural Waters: A Chemical Equilibrium Model for the $Na-K-Ca-Cl-SO_4-H_2O$ System to High Concentration from 0 to 250°C." Geochimica et Cosmochimica Acta 53, 2503–2518.

Grenthe, I., Fuger, J., Konings, R.J.M., Lemire, R.J., Muller, A.B., Nguyen-Trung, C., and Wanner, H. 1992. *Chemical Thermodynamics of Uranium. Volume 1 of Chemical Thermodynamics.* Wanner, H. and Forest, I., eds. Amsterdam, The Netherlands: North-Holland Publishing Company.

Harris, A. W., Manning, M. C., Tearle, W. M., and Tweed, C. J., 2002, Testing of models of the dissolution of cements - leaching of synthetic CSH gels: Cement and Concrete Research, v. 32, no. 5, p. 731-746.

Helgeson, H.C. 1969. "Thermodynamics of Hydrothermal Systems at Elevated Temperatures and Pressures." American Journal of Science, 267(6), 729-804.

Helgeson, H.C.; Delany, J.M.; Nesbitt, H.W.; and Bird, D.K. 1978. "Summary and Critique of the Thermodynamic Properties of Rock Forming Minerals." American Journal of Science, *278-A*. New Haven, Connecticut: Yale University, Kline Geology Laboratory.

Jobmann, M., and Buntebarth, G., 2009, Influence of graphite and quartz addition on the thermo-physical properties of bentonite for sealing heat-generating radioactive waste: Applied Clay Science, v. 44, no. 3-4, p. 206-210.

Johnson, J.W.; Oelkers, E.H.; and Helgeson, H.C. 1992. "SUPCRT92: A Software Package for Calculating the Standard Molal Thermodynamic Properties of Minerals, Gases, Aqueous

Species, and Reactions from 1 to 5000 Bar and 0 to 1000°C." Computers & Geosciences, *18,* (7), 899-947. New York, New York: Pergamon Press.

Jové Colón, C. F., Caporuscio, F. A., Levy, S. S., Blink, J. A., Greenberg, H. R., Halsey, W. G., Fratoni, M., Sutton, M., Wolery, T. J., Rutqvist, J., Liu, H. H., Birkholzer, J., Steefel, C. I., and Galindez, J., 2011, Disposal Systems Evaluations and Tool Development - Engineered Barrier System (EBS) Evaluation, p. 1-192.

Jové Colón, C. F., Caporuscio, F. A., Levy, S. S., Xu, H., Blink, J. A., Halsey, W. G., Buscheck, T., Sutton, M., Serrano de Caro, M. A., Wolery, T. J., Liu, H. H., Birkholzer, J., Steefel, C. I., Rutqvist, J., Tsang, C.-F., and Sonnenthal, E., 2010, Disposal Systems Evaluations and Tool Development - Engineered Barrier System (EBS) Evaluation p. 1-200.

Karnland, O., 1997, Bentonite swelling pressure in strong NaCl solutions - Correlation between model calculations and experimentally determined data: Swedish Nuclear Fuel and Waste Management Co.

Karnland, O., Nilsson, U., Weber, H., and Wersin, P., 2008, Sealing ability of Wyoming bentonite pellets foreseen as buffer material - Laboratory results: Physics and Chemistry of the Earth, v. 33, p. S472-S475.

Karnland, O., Olsson, S., Nilsson, U., and Sellin, P., 2007, Experimentally determined swelling pressures and geochemical interactions of compacted Wyoming bentonite with highly alkaline solutions: Physics and Chemistry of the Earth, v. 32, no. 1-7, p. 275-286.

Karpov, I. K., Chudnenko, K. V., and Kulik, D. A., 1997, Modeling chemical mass transfer in geochemical processes: Thermodynamic relations, conditions of equilibria, and numerical algorithms: American Journal of Science, v. 297, no. 8, p. 767-806.

Kersten, M., 1996, Aqueous solubility diagrams for cementitious waste stabilization systems .1. The C-S-H solid solution system: Environmental Science & Technology, v. 30, no. 7, p. 2286-2293.

Kim, J. S., Kwon, S. K., Sanchez, M., and Cho, G. C., 2011, Geological Storage of High Level Nuclear Waste: KSCE Journal of Civil Engineering, v. 15, no. 4, p. 721-737.

Kulik, D. A., 2011, Improving the structural consistency of C-S-H solid solution thermodynamic models: Cement and Concrete Research, v. 41, no. 5, p. 477-495.

Kulik, D. A., and Kersten, M., 2001, Aqueous solubility diagrams for cementitious waste stabilization systems: II, end-member stoichiometries of ideal calcium silicate hydrate solid solutions: Journal of the American Ceramic Society, v. 84, no. 12, p. 3017-3026.

Kulik, D. A., Sinitsyn, V. A., and Karpov, I. K., 1998, Prediction of solid-aqueous equilibria in cementitious systems using Gibbs energy minimization: II. Dual thermodynamic approach to estimation of the non-ideality and end-member parameters: Scientific Basis for Nuclear Waste Management XXI, v. 506, p. 983-990.

Landolt, D., Davenport, A., Payer, J., and Shoesmith, D., 2009, A Review of Materials and Corrosion Issues Regarding Canisters for Disposal of Spent Fuel and High-level Waste in Opalinus Clay, Technical Report 09-02: Wettingen, Switzerland, National Cooperative for the Disposal of Radioactive Waste (NAGRA), 73 pp.

Lichtner, P. C., and Carey, J. W., 2006, Incorporating solid solutions in reactive transport equations using a kinetic discrete-composition approach: Geochimica Et Cosmochimica Acta, v. 70, no. 6, p. 1356-1378.

Lippmann, F., 1980, Phase Diagrams Depicting Aqueous Solubility of Binary Mineral Systems: N. Jb. Miner. Abh., v. 139, no. 1, p. 1-25.

Liu, C. W., and Lin, W. S., 2005, A smectite dehydration model in a shallow sedimentary basin: Model development: Clays and Clay Minerals, v. 53, no. 1, p. 55-70.

Lothenbach, B., Damidot, D., Matschei, T., and Marchand, J., 2010, Thermodynamic modelling: state of knowledge and challenges: Advances in Cement Research, v. 22, no. 4, p. 211-223.

Lothenbach, B., Matschei, T., Moschner, G., and Glasser, F. P., 2008, Thermodynamic modelling of the effect of temperature on the hydration and porosity of Portland cement: Cement and Concrete Research, v. 38, no. 1, p. 1-18.

Lothenbach, B., and Winnefeld, F., 2006, Thermodynamic modelling of the hydration of Portland cement: Cement and Concrete Research, v. 36, no. 2, p. 209-226.

Mariner, P. E., 2007, In-Drift Precipitates/Salts Model (ANL-EBS-MD-000045 REV 03). Las Vegas, Nevada, Sandia National Laboratories; OCRWM Lead Laboratory for Repository Systems, .

Matschei, T., Lothenbach, B., and Glasser, F. P., 2007, Thermodynamic properties of Portland cement hydrates in the system $CaO-Al_2O_3-SiO_2-CaSO_4-CaCO_3-H_2O$: Cement and Concrete Research, v. 37, no. 10, p. 1379-1410.

Moffat, H. K., and Jové Colón, C. F., 2009, Implementation of Equilibrium Aqueous Speciation and Solubility (EQ3 type) Calculations into Cantera for Electrolyte Solutions: Sandia National Laboratories, SAND2009-3115.

Moschner, G., Lothenbach, B., Rose, J., Ulrich, A., Figi, R., and Kretzschmar, R., 2008, Solubility of Fe-ettringite ($Ca_6[Fe(OH)_6]_2(SO4)_3*26H_2O$): Geochimica et Cosmochimica Acta, v. 72, no. 1, p. 1-18.

Pabalan, R. T., Glasser, F. P., Pickett, D. A., Walter, G. R., Biswas, S., Juckett, M. R., Sabido, L. M., and Myers, J. L., 2009, Review of Literature and Assessment of Factors Relevant to Performance of Grouted Systems for Radioactive Waste Disposal (CNWRA 2009-001): Report prepared for the U.S. Nuclear Regulatory Commission by the Center for Nuclear Waste Regulatory Analyses, San Antonio, Texas; 359 pp.

Pabalan, R.T. and Pitzer, K.S. 1987. "Thermodynamics of Concentrated Electrolyte Mixtures and the Prediction of Mineral Solubilities to High Temperatures for Mixtures in the System Na-K-Mg-Cl-SO$_4$-OH-H$_2$O." Geochimica et Cosmochimica Acta, 51(9), 2429-2443

Parker, V.B. and Khodakovskii, I.L. 1995. "Thermodynamic Properties of the Aqueous Ions (2+ and 3+) of Iron and the Key Compounds of Iron." Journal of Physical and Chemical Reference Data, *24,* (5), 1699-1745. Washington, D.C.: American Chemical Society.

Pitzer, K.S. 1991. "Ion Interaction Approach: Theory and Data Correlation."Chapter 3 of Activity Coefficients in Electrolyte Solutions. 2nd Edition. Pitzer, K.S.,ed. Boca Raton, Florida: CRC Press.

Poole, T. S., Wakeley, L. D., and Young, C. L., 1993, individual and Combined Effects of Chloride, Sulfate, and Magnesium Ions on Hydrated Portland-Cement Paste: Sandia National Laboratories.

Pusch, R., Drawrite, A. B., Yong, R. N., and Nakano, M., 2010, Stiffening of smectite buffer clay by hydrothermal effects: Engineering Geology, v. 116, no. 1-2, p. 21-31.

Rahman, M. M., Nagasaki, S., and Tanaka, S., 1999a, A model for dissolution of CaO-SiO_2-H_2O gel at Ca/Si < 1 by considering disordered structure: Scientific Basis for Nuclear Waste Management XXII, v. 556, p. 1237-1244.

-, 1999b, A model for dissolution of CaO-SiO_2-H_2O gel at Ca/Si > 1: Cement and Concrete Research, v. 29, no. 7, p. 1091-1097.

Ransom, B. and Helgeson, H.C. 1993. "Compositional End Members and Thermodynamic Components of Illite and Dioctahedral Aluminous Smectite Solid Solutions." Clays and Clay Minerals 41(5), 537-550.

Ransom, B., and Helgeson, H. C., 1994a, A Chemical and Thermodynamic Model of Aluminous Dioctahedral-2/1 Layer Clay-Minerals in Diagenetic Processes - Regular Solution Representation of Interlayer Dehydration in Smectite: American Journal of Science, v. 294, no. 4, p. 449-484.

-, 1994b, Estimation of the Standard Molal Heat Capacities, Entropies, and Volumes of 2/1-Clay-Minerals: Geochimica et Cosmochimica Acta, v. 58, no. 21, p. 4537-4547.

-, 1995, A Chemical and Thermodynamic Model of Dioctahedral 2-1 Layer Clay-Minerals in Diagenetic Processes - Dehydration of Dioctahedral Aluminous Smectite as a Function of Temperature and Depth in Sedimentary Basins: American Journal of Science, v. 295, no. 3, p. 245-281.

Reardon, E. J., 1990, An Ion Interaction-Model for the Determination of Chemical-Equilibria in Cement Water-Systems: Cement and Concrete Research, v. 20, no. 2, p. 175-192.

Richardson, I. G., and Groves, G. W., 1992, Models for the Composition and Structure of Calcium Silicate Hydrate (C-S-H) Gel in Hardened Tricalcium Silicate Pastes: Cement and Concrete Research, v. 22, no. 6, p. 1001-1010.

Robie, R. A., Hemingway, B. S., and Fisher, J. R., 1979, Thermodynamic properties of minerals and related substances at 298.15K and 1 bar (10^5 pascals) pressure and at higher temperatures, Washington, U.S. Govt. Print. Off., Geological Survey bulletin 1452, iii, 456 p. p.:

Robie, R.A., and Hemingway, B.S. 1995. *Thermodynamic Properties of Minerals and Related Substances at 298.15 K and 1 Bar (10^5 Pascals) Pressure and at Higher Temperatures.* Bulletin 2131. Reston, Virginia: U.S. Geological Survey.

Samper, J., Zheng, L., Montenegro, L., Fernandez, A. M., and Rivas, P., 2008, Coupled thermo-hydro-chemical models of compacted bentonite after FEBEX in situ test: Applied Geochemistry, v. 23, no. 5, p. 1186-1201.

Sanchez, M., Gens, A., and Olivella, S., 2010, Effect of thermo-coupled processes on the behaviour of a clay barrier submitted to heating and hydration: Anais Da Academia Brasileira De Ciencias, v. 82, no. 1, p. 153-168.

-, 2012, THM analysis of a large-scale heating test incorporating material fabric changes: International Journal for Numerical and Analytical Methods in Geomechanics, v. 36, no. 4, p. 391-421.

Schmidt, T., Lothenbach, B., Romer, M., Scrivener, K., Rentsch, D., and Figi, R., 2008, A thermodynamic and experimental study of the conditions of thaumasite formation: Cement and Concrete Research, v. 38, no. 3, p. 337-349.

Shock, E. L., and Helgeson, H. C., 1988, Calculation of the Thermodynamic and Transport-Properties of Aqueous Species at High-Pressures and Temperatures - Correlation Algorithms for Ionic Species and Equation of State Predictions to 5 kb and 1000°C: Geochimica et Cosmochimica Acta, v. 52, no. 8, p. 2009-2036.

Smith, W. R., and Missen, R. W., 1982, Chemical reaction equilibrium analysis: theory and algorithms, New York, Wiley, 364 p.:

Soler, J. M., 2007, Thermodynamic Description of the Solubility of C-S-H Gels in Hydrated Portland Cement - Literature Review.

Soler, J. M., and Mader, U. K., 2010, Cement-rock interaction: Infiltration of a high-pH solution into a fractured granite core: Geologica Acta, v. 8, no. 3, p. 221-233.

Sugiyama, D., and Fujita, T., 2006, A thermodynamic model of dissolution and precipitation of calcium silicate hydrates: Cement and Concrete Research, v. 36, no. 2, p. 227-237.

Tamura, K., Yamada, H., and Nakazawa, H. 2000. "Stepwise Hydration of High-Quality Synthetic Smectite with Various Cations." Clays and Clay Minerals 48, 400-404.

Tardy, Y., and Garrels, R.M. 1974. "A Method of Estimating the Gibbs Energies of Formation of Layer Silicates." Geochimica et Cosmochimica Acta 38(7), 1101-1116.

Tardy, Y., and Duplay, J. 1992. "A Method of Estimating the Gibbs Free Energies of Formation of Hydrated and Dehydrated Clay Minerals." Geochimica et Cosmochimica Acta 56(16), 3007-3029

Thomas, J. J., and Jennings, H. M., 1998, Free-energy-based model of chemical equilibria in the CaO-SiO_2-H_2O system: Journal of the American Ceramic Society, v. 81, no. 3, p. 606-612.

Tumidajski, P. J., and Chan, G. W., 1996, Durability of high performance concrete in magnesium brine: Cement and Concrete Research, v. 26, no. 4, p. 557-565.

Valenzuela Díaz, F.R., and de Souza Santos, P. 2001. "Studies on the Acid Activation of Brazilian Smectite Clays." Química Nova 24(3), 345-353.

Vidal, O., and Dubacq, B., 2009, Thermodynamic modelling of clay dehydration, stability and compositional evolution with temperature, pressure and H_2O activity: Geochimica et Cosmochimica Acta, v. 73, no. 21, p. 6544-6564.

Vieillard, P. 1994a. "Prediction of Enthalpy of Formation Based on Refined Crystal Structures of Multisite Compounds: Part 1. Theories and Examples." Geochimica et Cosmochimica Acta 58(19), 4049-4063.

Vieillard, P. 1994b. "Prediction of Enthalpy of Formation Based on Refined Crystal Structures of Multisite Compounds: Part 2. Application to Minerals Belonging to the System Li_2O-Na_2O-

K_2O-BeO-MgO-CaO-MnO-FeO-Fe_2O_3-Al_2O_3-SiO_2-H_2O. Results and Discussion." *Geochimica et Cosmochimica Acta,* 58(19), 4065-4107.

Vieillard, P. 2000. "A New Method for the Prediction of Gibbs Free Energies of Formation of Hydrated Clay Minerals Based on the Electronegativity Scale." Clay and Clay Minerals, 48(4), 459-473.

Vieillard, P., Blanc, P., Fialips, C. I., Gailhanou, H., and Gaboreau, S., 2011, Hydration thermodynamics of the SWy-1 montmorillonite saturated with alkali and alkaline-earth cations: A predictive model: Geochimica et Cosmochimica Acta, v. 75, no. 19, p. 5664-5685.

Villar, M. V., Fernandez, A. M., Gomez, R., Barrenechea, J. F., Luque, F. J., Martin, P. L., and Barcala, J. M., 2007, State of a bentonite barrier after 8 years of heating and hydration in the laboratory: Scientific Basis for Nuclear Waste Management XXX, v. 985, p. 593-598

Wagman, D.D.; Evans, W.H.; Parker, V.B.; Schumm, R.H.; Halow, I.; Bailey, S.M.; Churney, K.L.; and Nuttall, R.L. 1982. "The NBS Tables of Chemical Thermodynamic Properties, Selected Values for Inorganic and C_1 and C_2 Organic Substances in SI Units." Journal of Physical and Chemical Reference Data, *11,* (Supplement No. 2), 2-276 - 2-282. Washington, D.C.: American Chemical Society.

Wagman, D.D.; Evans, W.H.; Parker, V.B.; Schumm, R.H.; Halow, I.; Bailey, S.M.; Churney, K.L.; and Nuttall, R.L. 1989. "Erratum: The NBS Tables of Chemical Thermodynamic Properties, Selected Values for Inorganic and C_1 and C_2 Organic Substances in SI Units." Journal of Physical and Chemical Reference Data, *18,* (4), 2-276 - 2-282, 1807-1812. Washington, D.C.: American Chemical Society.

Wagner, W., and Pruβ, A., 2002, The IAPWS formulation 1995 for the thermodynamic properties of ordinary water substance for general and scientific use: Journal of Physical and Chemical Reference Data, v. 31, no. 2, p. 387-535.

Wakeley, L. D., Poole, T. S., Ernzen, J. J., and Neeley, B. D., 1993, Salt Saturated Mass Concrete Under Chemical Attack, *in* Zia, P., ed., High Performance Concrete in Severe Environments, Volume SP-140: Detroit, MI, American Concrete Institute.

Wang, Y., Simpson, M., Painter, S., Liu, H.-H., and Kersting, A.B. 2011. *Natural System Evaluation and Tool Development – FY11 Progress Report*: Fuel Cycle Research and Development. Document FCRD-USED-2011-000223 (originated from Sandia National Laboratories).

Wersin, P., Johnson, L. H., and McKinley, I. G., 2007, Performance of the bentonite barrier at temperatures beyond 100°C: A critical review: Physics and Chemistry of the Earth, v. 32, no. 8-14, p. 780-788.

Wolery, T.J. 1978. Some Chemical Aspects of Hydrothermal Processes at Mid-Oceanic Ridges - A Theoretical Study. I. Basalt-Sea Water Reaction and Chemical Cycling Between the Oceanic Crust and the Oceans. II. Calculation of Chemical Equilibrium Between Aqueous Solutions and Minerals. Ph.D. dissertation. Evanston, Illinois: Northwestern University.

Wolery, T. J., and Jové Colón, C. F., 2007, Qualification of Thermodynamic Data for Geochemical Modeling of Mineral–Water Interactions in Dilute Systems (ANL-WIS-GS-000003 REV 01):

Las Vegas, Nevada, Sandia National Laboratories; OCRWM Lead Laboratory for Repository Systems, p. 412 pp.

Xiong, Y.-L. 2005. "Release of FMT-050405.CHEMDAT."E-mail to J.F. Kanney and J.J. Long, April 5, 2005. Carlsbad, NM: Sandia National Laboratories. ERMS 539304.

Molecular Dynamic (MD) Study of Clay Hydration
(Part V)

1. Clay Mineral Properties and Swelling Behavior through Molecular Simulation

1.1 Overview

Clay is considered to be a ubiquitous barrier material in repository disposal galleries given its swelling and adsorptive properties that are critical to the long-term storage of nuclear waste. However, the physico-chemical properties of clay phases are difficult to characterize relative to other silicate materials. Part IV of this report describes the compositional and structural complexities of clay-based materials making their characterization and analysis a problematic task that commonly ends up yielding ambiguous results. However, advanced computational chemistry methods, particularly advanced molecular dynamic (MD) simulation approaches, have furnished the much needed theoretical tool to resolve the characterization of clay minerals at the atomic scale. MD simulations provide accurate and robust predictive models of clay mineral structure as well as swelling phenomena supplying key information that would be very difficult to obtain using experimental approaches.

The goal of this task is to understand trends in clay mineral swelling behavior using MD simulation. Bulk properties such as the structural basal d-spacing and molecular properties such as interlayer structure are determined as a function of interlayer cation hydration and relative humidity.

1.1.1 Modeling Methods

The model systems represent endmembers in smectite minerals and in cation species. Both clay mineral models have a layer charge of -0.75 e/unit cell contained exclusively in the octahedral (montmorillonite) or tetrahedral (beidellite) sheets. The general chemical formula for sodium montmorillonite can be expressed by $Na_{0.75}[Mg_{0.75}Al_{3.25}]Si_4O_{10}(OH)_2 \cdot nH_2O$, and the chemical formula for beidellite can be expressed as $Na_{0.75}Al_4(Si_{7.25}Al_{0.75})O_{20}(OH)_4 \cdot nH_2O$. Representative snapshots of the clay mineral models and their corresponding unit cell formulae are shown in Figure 1.1.

The simulation supercell consisted of 5 clay layers, each containing 40 unit cells, with water contents ranging from dry clay to approximately 0.45 g H_2O per g clay. The total number of atoms contained in these simulations varied from 8200 atoms to 17,650 atoms. Negative layer charge was created by randomly substituting Mg for Al in the octahedral sheet (montmorillonite) or Al for Si in the tetrahedral sheet (beidellite). A Monte Carlo algorithm was created for this project to produce these disordered configurations, with Al avoidance according to Loewenstein's Rule (Loewenstein et al., 1954). This combination of clay mineral layers and charge substitution scheme has not been attempted in any previous simulation study of clay mineral swelling.

Force field parameters include van der Waals and electrostatic atomic interactions and were taken from the Clayff force field (Cygan et al., 2004). Clayff is an established energy force field successfully used in a wide range of mineral and environmental applications involving the accurate modeling of structure, thermodynamics, spectroscopy, physical properties, adsorption, and transport behavior of minerals and other environmental phases. For this study, clay swelling behavior was observed through the use of orthogonal supercells and constant-pressure MD simulations at temperatures of 298 K, 375 K, and 425 K. Data from the final 3 ns of simulation were averaged to obtain thermodynamic and structural properties.

In addition to variable water content, the MD simulations included variable interlayer cations: Na^+, Cs^+, Mg^{2+}, and Ca^{2+}. Theses cations were selected to provide a range of cation hydration energies representative of the alkali and alkaline earth groups. Only pure endmember interlayer compositions were examined while mixed interlayer cations and natural interlayer compositions will be simulated in a subsequent task.

All of the work presented in this report was completed using Sandia's institutional capacity supercomputer. The large systems sizes used in this study, which are necessary to avoid system size effects, required approximately 31,000 CPU hours to complete. Both the MD code LAMMPS (Plimpton, 1995) and the force field (ClayFF) used in this work were developed at Sandia.

Montmorillonite

$Na_{0.75}(Al_{3.25}Mg_{0.75})Si_8O_{20}(OH)_4 \cdot nH_2O$

Beidellite

$Na_{0.75}Al_4(Si_{7.25}Al_{0.75})O_{20}(OH)_4 \cdot nH_2O$
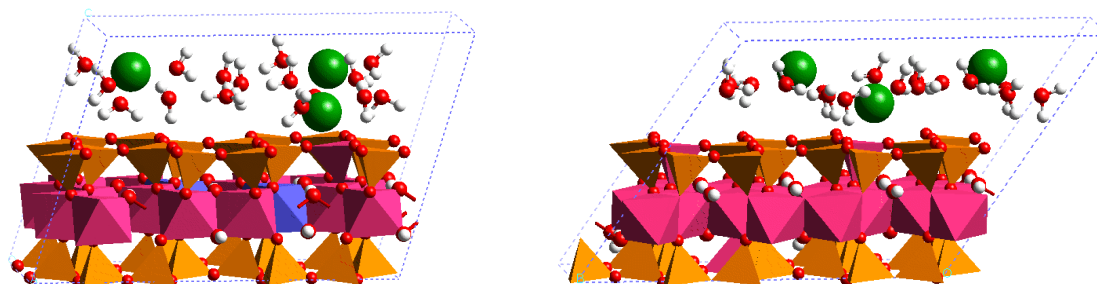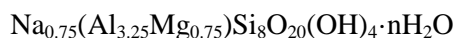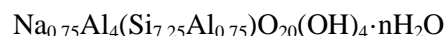
Figure 1.1. Models of expanded unit cells of endmember clay minerals considered in the MD simulations.

1.1.2   Results and Discussion

Atomic trajectories obtained from the large-scale MD simulations provide an opportunity to evaluate structural, thermodynamic, and transport properties of the various hydration states of the smectite clay phases. To date, we have completed an analysis of montmorillonite models with Na^+, Cs^+, Mg^{2+}, and Ca^{2+} interlayer cations as a function of water content and two temperatures (298 K and 425 K). Figure 1.2 provides an orthographic view of the simulation supercell for Na-montmorillonite taken from the equilibrated trajectory. The model clearly shows the octahedral Mg sites that create the negative charge on the clay layer. The interlayer water representative of a two-layer hydrate exhibits a preferred orientation of water molecules with hydrogen atoms directed toward the clay interface and most oxygens coordinating to the interlayer Na^+. Further structural details in terms of atomic density profiles are presented in a later section of this report.
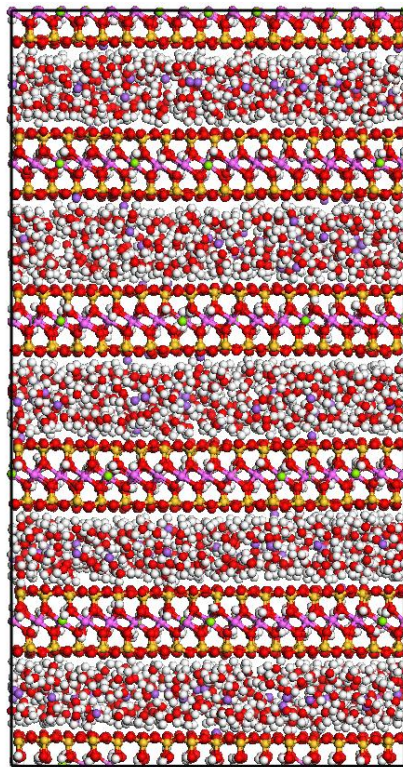
Figure 1.2. A snapshot (*xz* plane) of the orthogonal Na-montmorillonite simulation supercell containing 450 water molecules in each of the five clay interlayers. Octahedral Mg sites are shown as green atoms; interlayer Na$^+$ are shown as purple spheres. Approximate dimensions in the *x*, *y*, and *z* dimensions are 41 Å, 45 Å, and 81 Å.

MD simulations of twenty-one hydration states for each smectite model were completed, providing cell parameters for the variable dimensions of the supercell. Mean basal *d*-spacings (analogous to X-ray diffraction determinations) were calculated from the cell parameters to allow analysis of the swelling phenomenon as a function of water content. The basal (001) spacing associated with the *c*-axis is typically used to describe the expansion of layered materials. Figure 1.3 includes a comparison of the swelling response for each of the interlayer cations for up to approximately 0.45 g H$_2$O per g clay. Uncertainties in the *d*-spacing values from the simulations are less than the symbol size in the swelling plots. Smectite clay phases like montmorillonite and beidellite, having relatively small layer charge, are easily expanded to significant interlayer volumes (and *d*-spacings) by water. The four swelling curves at 298 K show an expansion with initial water addition that leads to a stabilized one-layer hydrate at about 0.12 g H$_2$O per g clay. Additional water expands the clay layers further apart by overcoming the layer-layer electrostatic energy while stabilizing the system through the formation of a hydrogen bonded water network and the hydration of interlayer cations. This process continues and stabilizes the two-layer hydrate up to about 0.3 g H$_2$O per g clay. Further addition of water expands the clay interlayer but no fine structure associated with a stable three layer hydrate structure is observed by the MD simulations.

Cs-montmorillonite appears to exhibit the greatest expansion compared to the other interlayer cations, but using a mass-basis for the water content amplifies the swelling behavior for a large atomic mass associated with Cs (cf. Figure 1.4). Nonetheless, Figure 1.3 shows a small but discernible (~0.5 Å) difference among the swelling curves for the one-layer hydrates and somewhat less variation for two-layer hydrates (excluding the skewed Cs results). We use the recent study of

Na-saponite clay by Ferrage et al. (2010) to correlate the mass ratio of hydrated clays with the relative humidity (RH) (Figure 1.3b). A 25% RH is expected at approximately the transition between one and two-layer hydrates, while 60% RH is associated with mass water values above the two-layer hydrate stability, but is interpreted by Ferrage et al. (2010) to produce pore water rather than a further expanded clay phase. Our MD simulations do not suggest the stability of a three layer hydrate and are consistent with this interpretation.
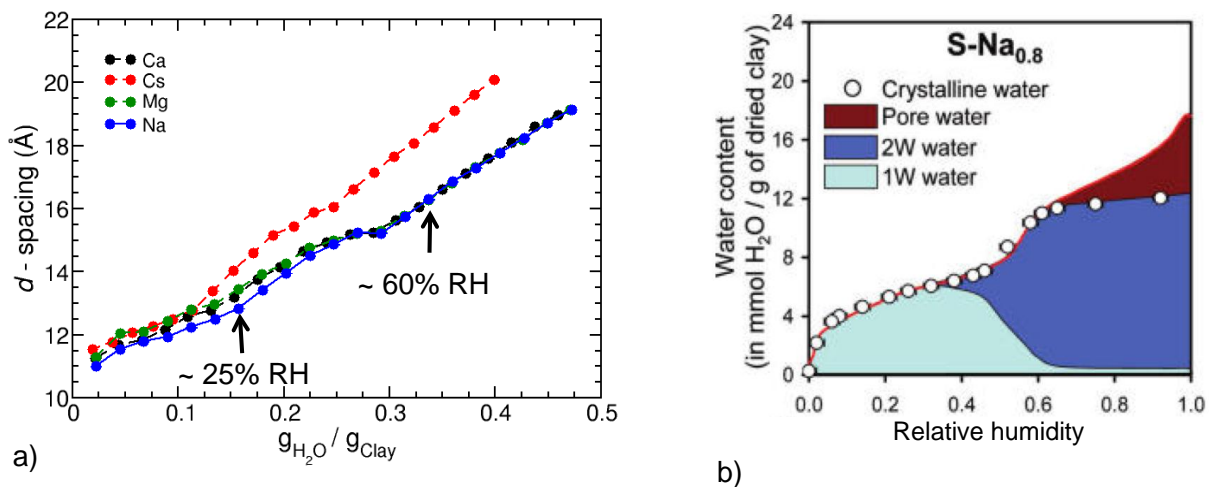
Figure 1.3. a) Swelling curves for Na$^+$, Ca^{2+}, Mg^{2+}, and Cs$^+$ montmorillonite at T = 298 K as a function of mass of water per mass of clay. These curves were generated from MD simulations, and reported with RH values taken from the experimental data of Ferrage et al. (2010). b) The experimental data from Ferrage et al. (2010) illustrating the water content as a function of RH for Na-saponite.

Figure 1.4 presents the same swelling curves as Figure 1.3a but based on a molar comparison for the water content. As with our interpretation of the mass-based swelling curves, the major differences are associated with the one-layer hydrate region. Within the uncertainty in the simulated d-spacing values, the swelling curves for the two-layer hydrates are similar except for those associated with Cs-montmorillonite. Expansion of Cs-montmorillonite leads to a less-defined two-layer hydrate stability above eight waters per clay unit cell, and at higher water content the Cs-montmorillonite exhibits larger d-spacing by almost 1 Å.
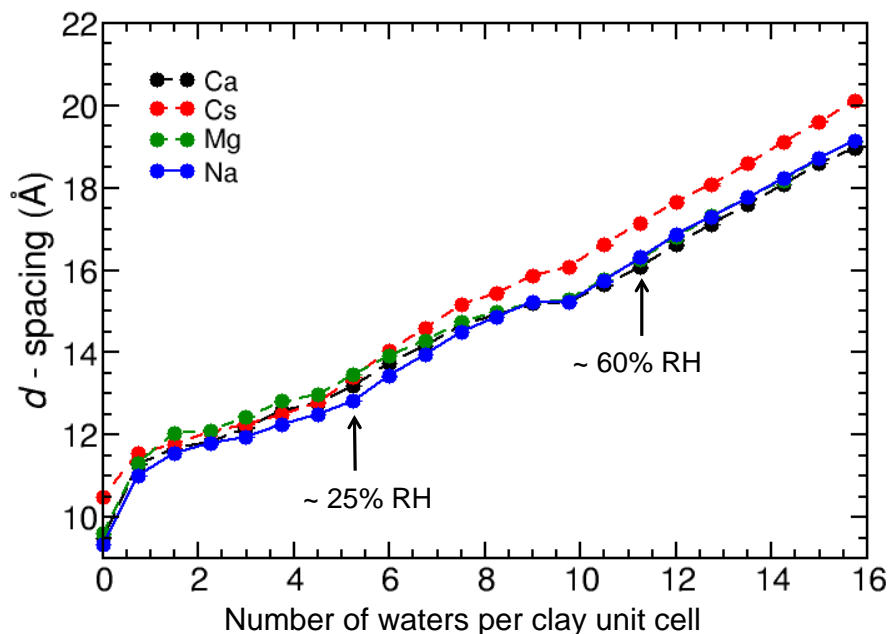
Figure 1.4. Swelling curves for montmorillonite with interlayer cations Ca^{2+}, Cs^{+}, Mg^{2+}, and Na^{+} at T = 298 K. The interlayer d-spacing is shown as a function of number of waters per clay unit cell. As with Figure 1.3, RH values were taken from the experimental work of Ferrage et al. (2010) are mapped to the simulation data.

Figure 1.5 compares the temperature dependence of the swelling curves for the four interlayer cations at 298 K and 425 K. The results show a significant difference in clay expansion for a given water content for each interlayer cation. For one-layer hydrates, the equilibrated d-spacing values at the two temperatures are typically within 0.5 Å of each other. The d-spacing difference for Cs-montmorillonite at the two temperatures increases to almost 1 Å for a two-layer hydrate and to more than 1.7 Å at very high water contents where this phase may not be stable. Temperature effects in the hydration of the Na-, Ca-, and Mg-montmorillonites are less than 0.4 Å in the two-layer hydrate region, and increase at higher water contents. We universally observe the expansion of the clay interlayer with temperature while the layer framework of the clay phase exhibits insignificant volume change. Subsets of the temperature dependence are presented in Figure 1.6 for a more direct comparison of the 425 K swelling curves for each of the four interlayer cations, and separately for Na-montmorillonite. These simulations provide unique structural data for clay mineral swelling that has not been previously obtained through experiment.
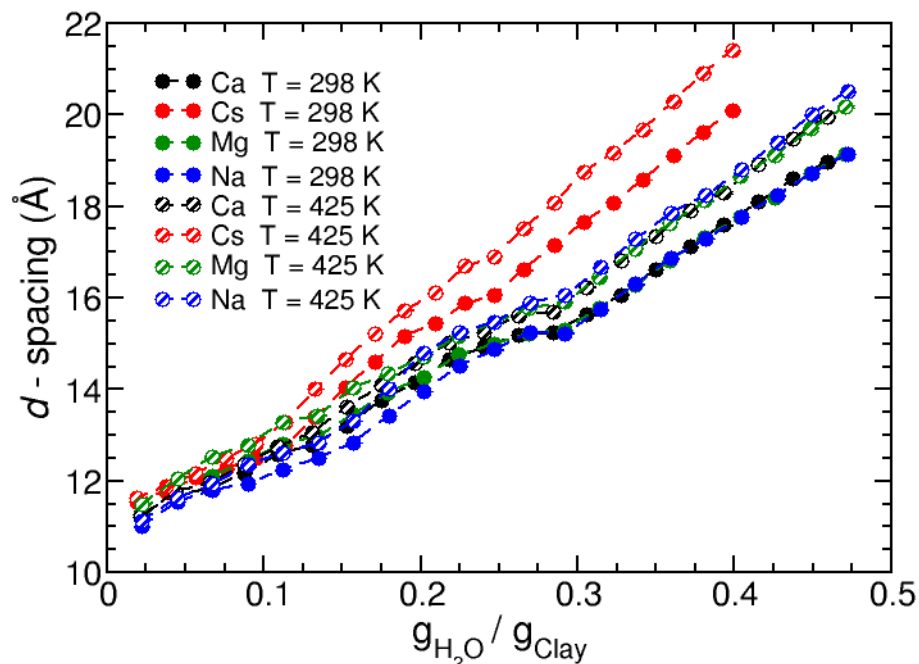
Figure 1.5. Swelling curves for montmorillonite with interlayer ions Ca^{2+}, Mg^{2+}, Cs^{+}, and Na^{+} at two different temperatures, T = 298 K and T = 425 K. Data at T = 298 K are shown with solid symbols while the data for T = 425 K are shown with cross-hatched symbols.

a)

b)
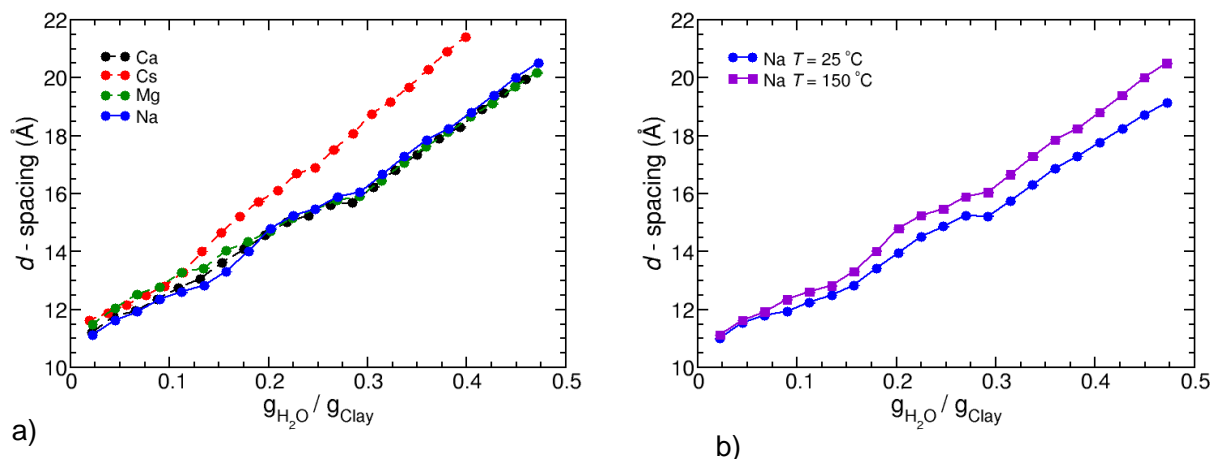
Figure 1.6. a) Swelling curves for montmorillonite with interlayer cations Ca^{2+}, Mg^{2+}, Cs^{+}, and Na^{+} at T = 425 K. b) Swelling curves for Na-montmorillonite for T = 298 K and T = 425 K. The temperature effect on the Na-montmorillonite curves is representative of the other cation systems.

Atomic density profiles for the interlayer species of the one-layer and two-layer hydrates derived from the equilibrated 298 K MD simulations are presented together in Figure 1.7. Several features of water and ion structure are observed regardless of interlayer cation or water content. The interlayer region is bound by atoms in the clay layers, represented in Figure 1.7 as the clay hydroxyl oxygen atoms. Water molecules forming hydrogen bonds to the clay siloxane surface are indicated by the water hydrogen and oxygen peaks closest to the clay surface. Cation peaks near the adsorbed water peaks indicate that those cations are directly adsorbed to the clay siloxane surface. At the low water content corresponding to the one-layer hydrate (top graphs in Figure 1.7), it is difficult to assign interlayer ions as inner- or outer-sphere surface complexes because there is not enough

207

interlayer water to form outer-sphere complexes. At the high water content corresponding to the two-layer hydrate (bottom graphs in Figure 1.7), water molecules form two discrete layers. Interlayer cations in outer-sphere surface complexes are indicated by a prominent peak at the midplane (Mg^{2+}, Ca^{2+}, Na^+). Cations in inner-sphere surface complexes are indicated by smaller peaks near the clay siloxane surface (Mg^{2+}, Ca^{2+}, Cs^+).
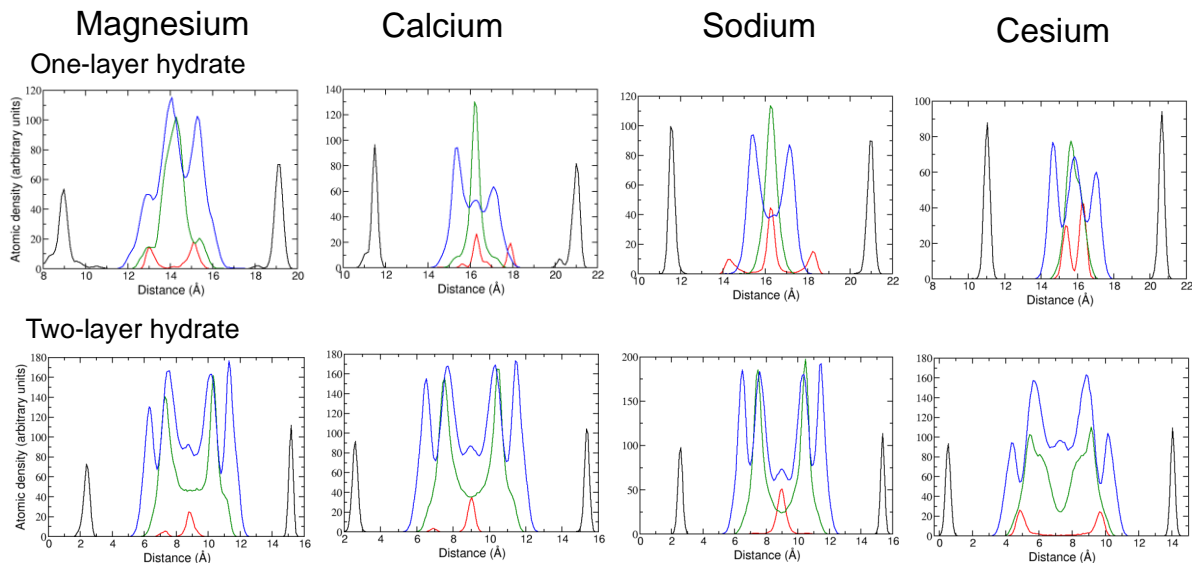
Figure 1.7. 1D atomic density profiles along the *c*-axis for one and two-layer hydrates of montmorillonite with Mg^{2+}, Ca^{2+}, Na^+, and Cs^+ interlayer cations. The clay hydroxyl oxygens are shown in black, the water oxygens are shown in green, the water hydrogens are shown in blue, and the cations are shown in red.

Density profiles for each interlayer cation are compared with representative simulation snapshots to provide a greater level of atomistic detail to the swelling phenomenon. In the one-layer hydrate, Na^+ ions are located both at the midplane and at the surface (Figure 1.8). All adsorbed Na^+ ions are centered directly above hexagonal siloxane rings, as indicated in the inset. As more water is added and the two-layer hydrate forms, nearly all Na^+ ions are located at the midplane in outer-sphere complexes (Figure 1.9). This result clearly indicates that interlayer Na^+ ions are energetically favored in the fully hydrated outer-sphere complex compared to the inner-sphere complex with both water oxygen atoms and clay surface oxygen atoms coordinating to Na^+ ions.

Figure 1.8. a) One-dimensional atomic density profiles along the *c*-axis for Na-montmorillonite for a one-layer hydrate at $T = 298$ K. Atom designations are the same as in Figure 1.7. b) A simulation snapshot of the interlayer representing the structural detail in a). Adsorbed Na^+ ions at 14.2 Å and 18.2 Å are centered directly above hexagonal siloxane rings (shown in the figure inset).

208

Figure 1.9. a) One-dimensional atomic density profiles along the *c*-axis for Na-montmorillonite for a two-layer hydrate at *T* = 298 K. Atom designations are the same as in Figure 1-7. b) A simulation snapshot of the interlayer representing the structural detail in a).

The interlayer structure of Cs^+ in the one-layer hydrate (Figure 1.10) is nearly identical to Na^+, with all Cs^+ ions centered above siloxane rings. The slightly larger *d*-spacing for the one-layer hydrate of Cs-montmorillonite compared to Na-montmorillonite is likely due to the larger ionic radius of Cs^+. However, the interlayer structures of the two-layer hydrates are very different, which is the likely explanation for the increased *d*-spacing of approximately 1 Å for Cs-montmorillonite as compared to Na -montmorillonite (Figure 1.3). Even at higher water contents, interlayer Cs^+ ions remain adsorbed to the siloxane surface as inner-sphere complexes with only partial hydration (Figure 1.11). The two layers of Cs^+ ions result in a slight expansion of the interlayer region compared to the other model systems, which are dominated by cations at the midplane in outer-sphere surface complexes.

Figure 1.10. a) One-dimensional atomic density profiles along the *c*-axis for Cs-montmorillonite for a one-layer hydrate at *T* = 298 K. Atom designations are the same as in Figure 1.7. b) A snapshot of the interlayer representing the structural detail in a). Adsorbed Cs^+ ions at 15.3 Å and 16.2 Å are centered directly above hexagonal siloxane rings (shown in the figure inset).

209

a)   b)

Figure 1.11. a) One-dimensional atomic density profiles along the *c*-axis for Cs-montmorillonite for a two-layer hydrate at *T* = 298 K. Atom designations are the same as in Figure 1.7. b) A snapshot of the interlayer representing the structural detail in a).

The disposition of both alkaline earth cations (Mg^{2+} and Ca^{2+}) in the two-layer hydrate of montmorillonite is quite similar. Atomic density profiles across the interlayer are comparable for both Mg^{2+} (Figure 1.12) and Ca^{2+} (Figure 1.13) and are characterized by a dominant midplane cation peak in which the outer-sphere complex is most stable. A second peak representing inner-sphere adsorbed cations on the siloxane surface is observed but at a significantly reduced intensity compared to the outer-sphere cation. This behavior is consistent with the relatively large hydration energies associated with cations having divalent charge and small ionic size, especially by Mg^{2+} as represented here. Such cations prefer to be fully coordinated to water molecules in the central region of the two-layer hydrate interlayer. Oxygen peaks for interlayer water molecules are symmetrical about the central cation; water hydrogens are evident by four symmetrical peaks with the water molecule typically disposed in a vertical orientation with the dipole vector within the interlayer plane. However, direct water adsorption to the siloxane surface can occur as in the Ca^{2+} example (Figure 1.13) where not all water molecules associate with the interlayer cation (as evidenced in the shoulder of the oxygen profile); Ca^{2+} has a smaller hydration energy than Mg^{2+}. In this case, the adsorbed water molecules align themselves with their hydrogens and dipoles directed toward the negative siloxane surface. In addition, because of stoichiometry, montmorillonites with divalent interlayer cations have fewer interlayer cations and therefore more water molecules available to interact with the clay surface.

a)   b)
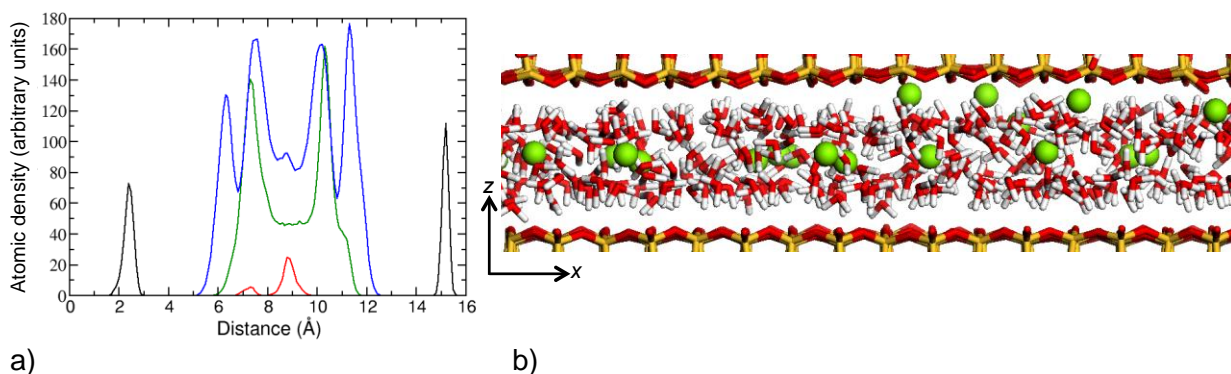
Figure 1.12. a) One-dimensional atomic density profiles along the *c* axis for Mg-montmorillonite for a two-layer hydrate at *T* = 298 K. Atom designations are the same as in Figure 1.7. b) A snapshot of the interlayer representing the structural detail in a).
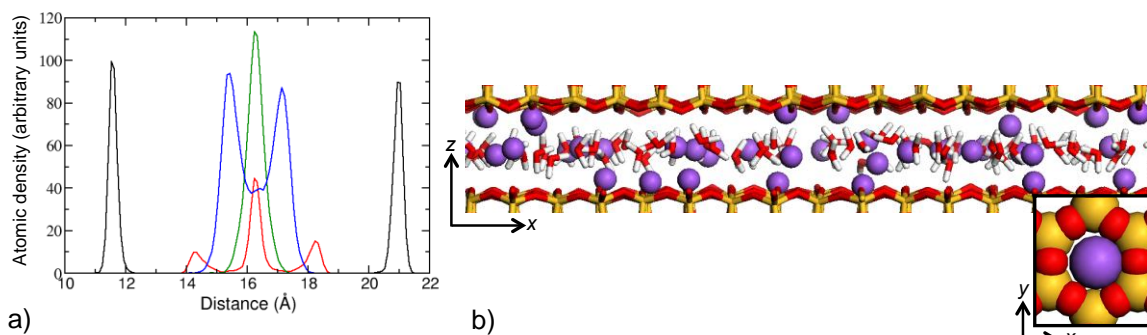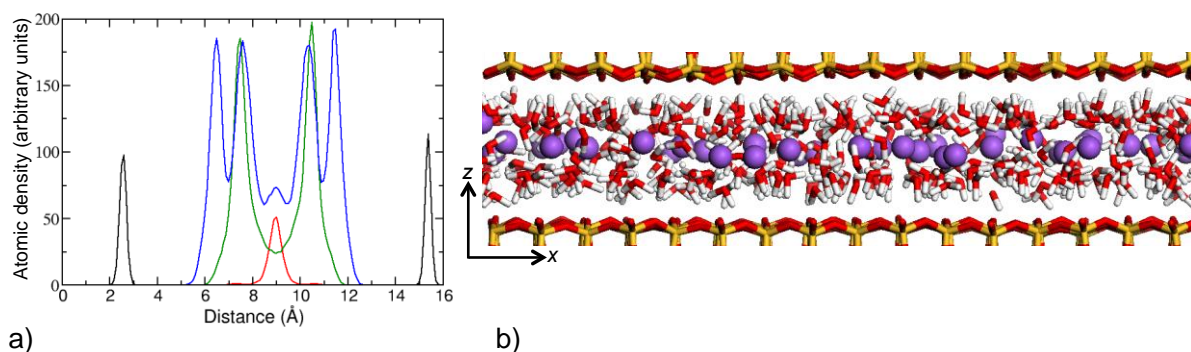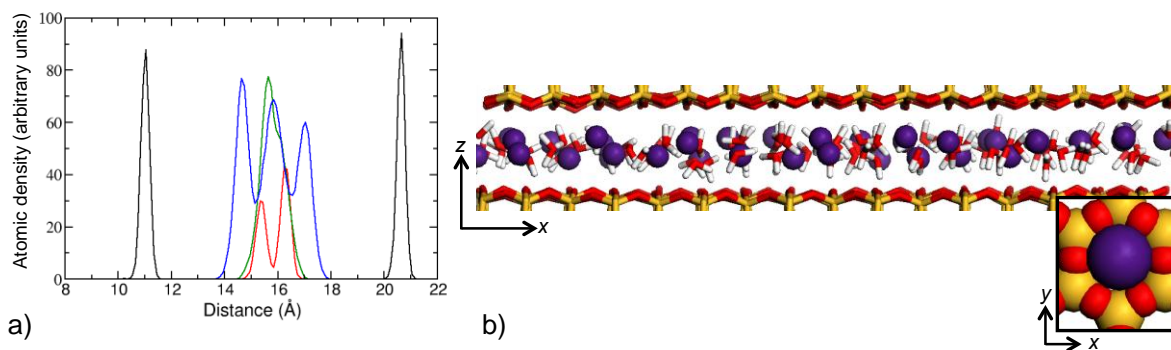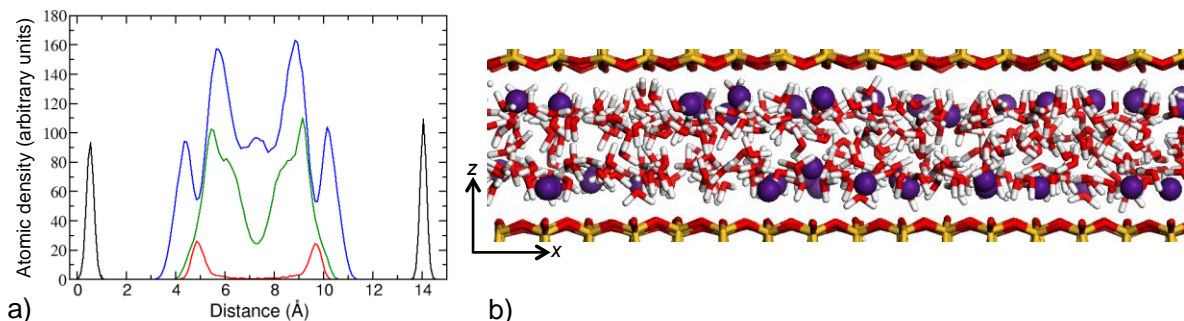
210
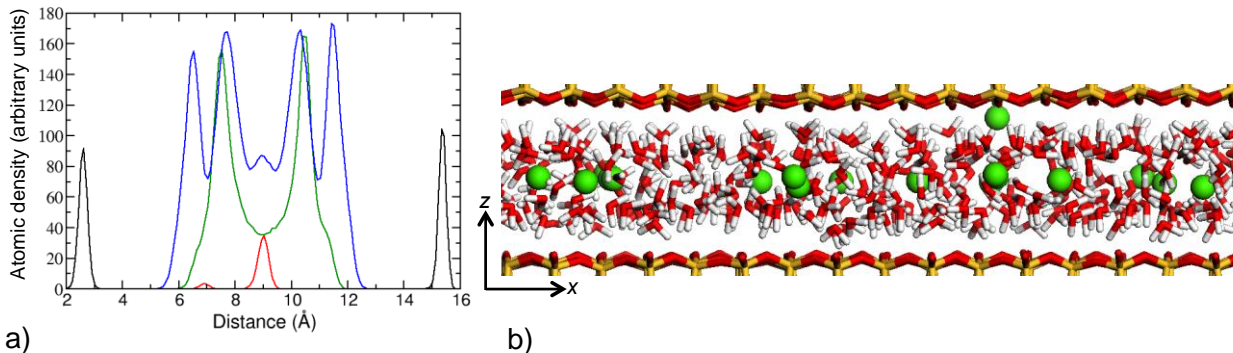
Figure 1.13. a) One-dimensional atomic density profiles along the *c* axis for Ca-montmorillonite for a two-layer hydrate at *T* = 298 K. Atom designations are the same as in Figure 1.7. b) A snapshot of the interlayer representing the structural detail in a).

1.1.3   Summary and Planned Work for FY12 and FY13

Analysis of atomic trajectories from our MD simulations clearly shows the molecular controls associated with the swelling of smectite phases as a function of interlayer cation, hydration state, and temperature. Detailed structural evaluation demonstrates the significance of the relative hydration energy of the interlayer cation and whether the cation is able to directly interact with the clay surface. Additionally, the ionic size of the interlayer cation relative to the hexagonal ring structure of the siloxane surface controls inner-sphere adsorption mechanisms and the degree of interlayer swelling with hydration. Further insights into these mechanisms will require comparison of these results with our MD simulations of beidellite where the layer charge of the clay resides in the near-surface tetrahedral sheet. Collectively, our molecular simulations provide unique and significant insights into the fundamental processes that control structure, adsorption, swelling, and other properties of clay minerals that, due to their nanocrystalline and complex nature, are not amenable to experimental characterization or instrumental analysis.

1.1.3.1   Planned Work for FY13

Planned work for the remainder of FY12 will be focused on:

- Complete MD simulations of clay hydration, including both montmorillonite and beidellite systems at three temperatures (27 °C, 100 °C, and 150 °C). A detailed structural analysis will explain differences in swelling behavior with temperature and interlayer cation. This analysis will include the following: 1D atomic density profiles (cation surface complexes, water orientation); 2D atomic density profiles (water and cation orientation on the basal plane); radial distribution functions (cation coordination numbers); thermodynamics (hydration enthalpies). A manuscript of this work will be submitted to a scientific journal.

- Plan and complete GCMC simulations to determine the relationship between clay water content and RH.

Planned work for FY13 will be focused on:

- Additional MD simulations of clay hydration, including the effects of variable layer charge (magnitude and location) for comparison with published experimental data (Ferrage et al., 2010).

- Additional MD simulations of clay hydration, including the effect of pressure on swelling behavior.

- MD simulations to evaluate the mechanical properties of hydrated clays.

- MD simulations to evaluate the thermal conductivity of hydrated clays and clay interfaces (e.g., clay-graphite and clay-sand) relevant to the GDSM.

2. References

Cygan, R. T., Liang, J.-J., and Kalinichev, A. G., 2004, Molecular models of hydroxide, oxyhydroxide, and clay phases and the development of a general force field: Journal of Physical Chemistry B, v. 108, no. 4, p. 1255-1266.

Ferrage, E., Lanson, B., Michot, L. J., and Robert, J. L., 2010, Hydration Properties and Interlayer Organization of Water and Ions in Synthetic Na-Smectite with Tetrahedral Layer Charge. Part 1. Results from X-ray Diffraction Profile Modeling: Journal of Physical Chemistry C, v. 114, no. 10, p. 4515-4526.

Loewenstein, W., 1954, The Distribution of Aluminum in the Tetrahedra of Silicates and Aluminates: American Mineralogist, v. 39, no. 1-2, p. 92-96.

Plimpton, S., 1995, Fast Parallel Algorithms for Short-Range Molecular Dynamics: J Comp Phys, v. 117, p. 1-19.

Coupled Thermal-Mechanical (TM) and Thermo-hydrological (TH) Modeling in Salt

(Part VI)

1. Coupled Thermal-Mechanical (TM) Modeling in Salt

1.1 Introduction

The impact of different physic-chemical processes (e.g., Thermal (T), Hydrologic (H), Mechanical (M), and chemical (C) or THMC) and the coupled interactions between these must be evaluated to assess the performance of a waste storage facility situated in subsurface geologic media. A thorough examination of repository performance, typically in a Performance Assessment (PA) evaluation, requires the use of process models that accurately capture key phenomena relevant to a nuclear waste repository design concept. Different repository settings (or host rock media) will experience a combination of these processes in a more unique fashion. For example, the WIPP facility in southeastern New Mexico is used to store waste that does not produce significant heat therefore the influence of thermal effects has been considered less important than other processes. Repository design concepts that are currently under investigation consider waste packages with high heat loads. Therefore, it is very important to describe thermally-driven processes making THMC coupled phenomena a research priority in their model representation.

The modeling work described in this part of the report incorporates coupled TM processes with the additional treatment of TH to describe moisture transport. It includes the influence of heat generated by a single waste package and the transfer of heat by conduction to the crushed salt backfilling the excavated region and the host salt. The thermal influence is important in salt as it has a significant impact on the rate at which the host rock creeps inward. This work extends the work described in the Repository Science THMC Coupled Process Investigations (FY11) report (Chapter 5 in Hardin et al., 2011) by examining the influence of larger initial porosity and moisture content in the crushed salt backfill. The numerical models used in these simulations could be easily modified to study waste forms with different heat characteristics as well as additional waste containers making this approach amenable to the study of generic EBS concepts for salt. Other geologic features such as clay seams and anhydrite layers could also be included in future cases.

1.2 Coupled TM Modeling

Thermal-mechanical analyses described in this chapter were carried out using the Sierra family of modeling codes developed at Sandia National Laboratories. Sierra/Arpeggio, an interface controller, effectively couples the thermal code Sierra/Aria (Notz et al, 2007) and the mechanics code Sierra/Adagio (Spencer et al., 2011) by controlling the transfer of data between the codes and the solution time stepping in the TM simulation.

Sierra/Aria is a Galerkin finite element based code capable of treating coupled thermal-hydraulic single and two-phase flow in porous media. Sierra/Adagio is a Galerkin-based finite element mechanical code which solves the equations of linear momentum for quasi-static conditions. Sierra/Adagio interfaces with the LAME library of constitutive models (Scherzinger and Hammerand, 2007) which includes a constitutive model suitable for modeling crushed and intact salt behavior.

Sierra/Arpeggio handles the transfer of the temperature field computed in Sierra/Aria to the Sierra/Adagio code. Following the Sierra/Adagio solution the mesh displacements are passed to back to Sierra/Aria for updating the computational grid. The deformations computed by Sierra/Adagio can be used in Sierra/Aria to compute an updated porosity field. The thermal conductivity of the crushed salt is updated based on this porosity and used in the next time step for

the thermal solution. In the more general THM case the pore pressure is also passed from Sierra/Aria to Sierra/Adagio since the constitutive models use effective stresses. The mass and energy conservation equations in Sierra/Aria have been formulated to account for the mesh deformations provided by the Sierra/Adagio solution. These code-to-code transfers are illustrated in Figure 1.1.
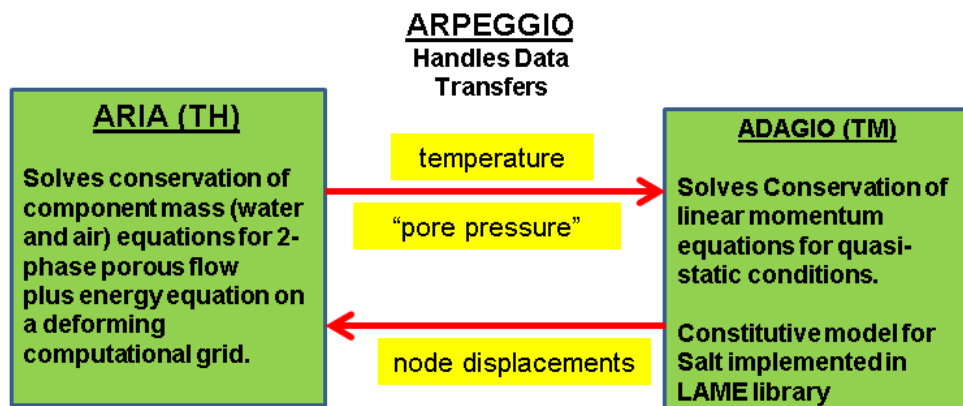
Figure 1.2. Sierra THM code data transfers.

1.3 Geometry/Finite Element Discretization

For these TM analyses, an interior portion of a generic salt repository was modeled with a 2.7 m (9 ft) long, 0.61 m (2 ft) diameter waste canister (WP in Figure 1.2) in a 6.4 m (21 ft) long, 3.35 m (11 ft) wide, 3.05 m (10 ft) tall alcove. It was assumed that the alcove connects at right angle to a 3.05 m (10 ft) tall, 3.35 m (11 ft) wide access drift (AD in Figure 1.2) and it is 12.2 m (40 ft) from the center of the waste canister to a neighboring waste canister. The alcove and access drift were assumed to be filled with 33% porosity run-of-mine salt and surrounded by a 2 m excavation damage zone (EDZ). The EDZ region was included for representing a region of enhanced permeability when hydrogeologic effects are included in future studies. The remainder of the modeled region consists of intact salt. Symmetry conditions for displacement and conduction were used for the four vertical sides of the model so that the modeled domain represented an alcove within the interior of the repository.
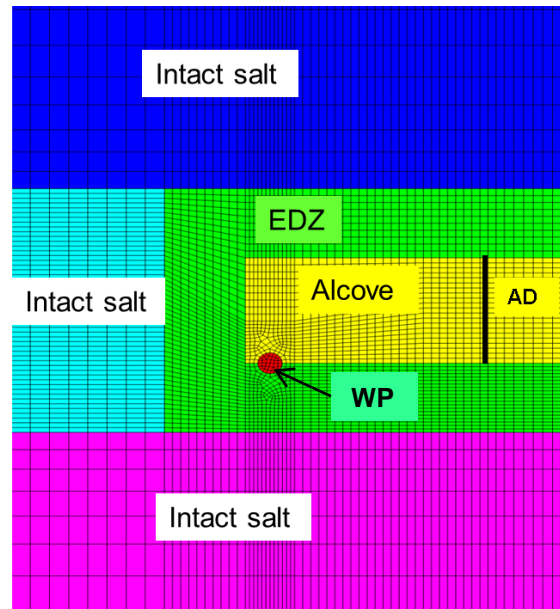
Figure 1.2. Generalized geometry of the salt disposal room adopted in the current model. AD stands for access drift and WP denotes waste package (see text).

The finite element grid was constructed using 3D hexagonal elements. A view of the three dimensional finite element mesh used in both the thermal and mechanical models is shown below in Figure 1.3. The grid was extended 30.5m (100 ft) above and below the alcove so that the alcove response would not be greatly affected by the boundary conditions during the 10 year simulation period. This time period is sufficient for the crushed salt backfill porosity to be reduced from an initial value of 33% to less than 5% except in the dry backfill case.
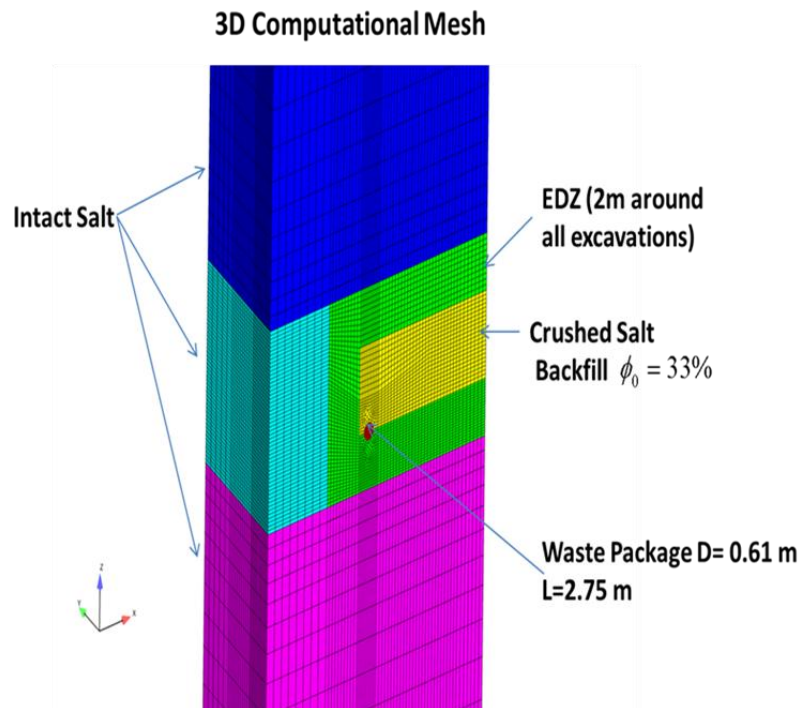
Figure 1.3. View of 3D finite element mesh with model domain dimensions.

217

1.4   Salt Parameters for THM Modeling

Development of Thermal-hydrologic-mechanical (THM) model for a generic salt repository requires properties of relevant parameters for the media of interest. The media include the intact salt host rock, the Excavated Disturbed Zone (EDZ) and the crushed salt backfill material. To support the modeling effort properties of intact (rock) salt, crushed salt, and EDZ have been collected from the scientific literature. Data sources include the WIPP site, the Gorleben salt dome, the Asse salt mine, and various laboratory tests. The literature search is not exhaustive, and thus the properties will be further updated and when additional data are available. As these materials will be subject to elevated temperatures, additional data will be required to capture material behavior at higher temperatures.

1.5   Thermal-Hydrologic Properties

1.5.1   Permeability, porosity, and density

Literature-derived permeability data for intact (rock) salt, crushed salt and EDZ are given in Tables 1.1 through 1.3. Crushed salt permeability depends on the degree of compaction. EDZ permeability could be subject to healing and could also be affected by creep closure. A detailed representation of such processes is not shown in this section. Bechthold et al. (2004) also give laboratory measured permeability and porosity data from German and Canadian reconsolidated crushed salt samples of backfill material. Figure 2.59 of Bechthold et al. (2004) presents a plot of mean permeability (k) vs. mean porosity for the measured data. Equation (1) is a fit ($R^2 = 0.9776$) to the measured points:

$$k = 7.0 \times 10^{-17} \, e^{43.94\phi} \tag{1.1}$$

where, ϕ is porosity and k denotes permeability in m^2.

Porosity data compiled from the literature for intact (rock) salt, crushed salt and EDZ are given in Table 1.4. As with permeability, crushed salt porosity depends on the degree of compaction. Density data for intact (rock) salt and crushed salt are given in Table 1.5. Similar to permeability and porosity, crushed salt density depends on the degree of compaction. EDZ density is assumed to be the same as that of intact salt.

Table 1.1. Permeability values for salt.

Value (m^2)	Description	Source
1×10^{-20} to 1×10^{-17}	Rock salt: decreasing with increasing hydrostatic pressure from 5MPa to 20MPa	Langer and Wallner (1998)
3.2×10^{-23}	Rock salt – WIPP (mean)	Helton et al. (1998)
1×10^{-12}	Crushed salt - uncompacted	Olivella et al. (2011)
1×10^{-21} to 1×10^{-18}	Crushed salt	Clayton et al. (2011, Table 3.1-10)
1×10^{-18} to 1×10^{-15}	EDZ – (German sources)	Bechthold et al. (2004, Section 4)
1×10^{-17}	EDZ – WIPP	Helton et al. (1998)

Table 1.2. Permeability values for coarse-grained crushed salt as a function of porosity. Source: Bechthold et al. (1999, Table 3.9a)

Porosity	Average gas permeability (kkrg) (m^2)	Comment
0.278	1.67 x 10^{-12}	Initial condition
0.275	1.59 x 10^{-12}	After hydrostatic compaction
0.216	1.42 x 10^{-12}	After hydrostatic compaction
0.204	1.27 x 10^{-12}	After hydrostatic compaction
0.174	7.89 x 10^{-13}	After hydrostatic compaction
0.139	8.62 x 10^{-13}	After hydrostatic compaction
0.106	7.77 x 10^{-14}	After hydrostatic compaction

Table 1.3. Permeability values for fine-grained crushed salt as a function of porosity. Source: Bechthold et al. (1999, Table 3.9b)

Porosity	Average gas permeability (kkrg) (m^2)	Density (kg/m^3)	Temperature (°C)
0.1	5.36 x 10^{-14}	1975	Ambient
0.071	1.43 x 10^{-14}	2040	Ambient
0.068	6.19 x 10^{-15}	2046	Ambient
0.053	2.20 x 10^{-15}	2078	Ambient
0.044	1.18 x 10^{-15}	2099	Ambient
0.030	9.75 x 10^{-17}	2129	Ambient
0.026	7.48 x 10^{-17}	2138	Ambient
0.015	2.56 x 10^{-18}	2162	Ambient
0.012	1.08 x 10^{-21}	2168	107.0

Table 1.4. Porosity values for salt.

Porosity Value	Description	Source
0.01	Rock salt – WIPP (mode)	Clayton (2010)
0.3	Crushed salt - initial	Olivella et al. (2011)
0.015	EDZ – (German sources)	Bechthold et al. (2004, Section 4)
0.0129	EDZ – WIPP (mode)	Helton et al. (1998)

Table 1.5. Rock density values for salt.

Value, kg/m^3	Description	Source
2163	Rock salt - grain	Carmichael (1984, Table 2)
1946.7	Crushed salt – dynamically compacted to fractional density of 0 .9	Callahan and Hansen (2002)
Porosity range (ϕ): 0 – 0.35	Crushed salt (Asse): $\rho cs = \rho s (1-\phi)$ $\rho s = 2187$	Bechthold et al. (2004, Equation 2.11)

1.5.2   Thermal and Saturation Properties of Salt

Thermal conductivity data from the literature for intact (rock) salt and crushed salt are given in Table 1.6. For crushed salt thermal conductivity depends on porosity (i.e. degree of compaction) and temperature. Intact salt and crushed salt thermal conductivities also depend on degree of saturation. Table 1.6 provides thermal conductivity of crushed salt as a function of liquid saturation. Figure 1.4 shows calculated thermal conductivity of dry crushed salt as a function of porosity and temperature given by the formulation of Olivella et al. (2011). Calculations were based on gas

thermal conductivity of 0.1 W/mK. The figure shows temperature has a significant effect on the thermal conductivity of intact salt and compacted crushed salt, while its effect is much reduced for loose crushed salt. EDZ thermal conductivity is assumed to be the same as that of intact salt. Specific heat data for intact (rock) salt and crushed salt are given in Table 1.7. For crushed salt and EDZ, thermal conductivity is assumed to be the same as that of intact salt. The coefficient of linear thermal expansion for intact (rock) and crushed salt are given in Table 1.8. These are assumed to be the same for intact rock salt, crushed salt, and EDZ. Some data exist to describe the extent of the EDZ and values for its thickness based on studies at the WIPP (USA) and Asse (Germany) sites are given in Table 1.9.

Initial brine saturation and pressure data from the literature are given in Table 1.10. The intact salt is considered to be at full saturation conditions, while crushed salt is assumed to be partially saturated. In the WIPP project, simulations are first carried out for a short period of time representing disposal operations. This portion of the run is called the initialization period and lasts for 5 years, corresponding to the time a typical waste panel is expected to be open during disposal operations. EDZ initial brine saturation starts out with 1.0. However, adjacent excavated regions start out with 0.0 brine saturation, and thus brine drains towards the excavated regions during the first five years of the simulation. The main WIPP simulation starts after the first 5 years at which time the EDZ brine saturation is much lower than the initial 1.0. This saturation value depends on sampled values such as permeability but an average could be calculated. The moisture content of salt samples from the site characterization study at the Deaf Smith site, Texas (US DOE, 1988, Table 2-33) showed total moisture loss from specimen in the range $0.07 - 5.53$ % by weight. Bechthold et al. (2004, Table 2.10) give residual water content in backfill samples of 0.03-0.05 wt%.

The water or moisture retention of crushed salt can be represented by several models to generate characteristic curves for this medium. The WIPP project used a modified version of the Brooks-Corey model as the primary model for two-phase flow in the repository, surrounding the Salado formation and EDZ (Helton et al., Section 4). For marker beds either the Brooks-Corey model or the van Genuchten-Parker model was used. Olivella et al. (2011) used the van Genuchten model to characterize water retention in crushed salt. Parameter values for these models for intact salt, crushed salt and EDZ are given in Tables 1.11 through 1.13. Most of the parameters are applicable to any of the models. In the Brooks-Corey model capillary pressure is defined by:

$$Pc = p_t(k)/S_{e2}^{1/\lambda} \qquad\qquad (1.2)$$

where $p_t(k)$ equals a k^η which stands for the capillary threshold pressure (in Pa) as a function of intrinsic permeability (k). Other related parameters are defined as follows:

$S_{e2} = (S_l - S_{lr})/ (1-S_{gr} - S_{lr})$

S_l = liquid saturation

S_{lr} = residual liquid saturation

S_{gr} = residual gas saturation

λ = pore distribution parameter, also known as *m*

The values of λ, a, η, S_{lr}, S_{gr} are given in Tables 1.11 and 1.12.

Table 1.6 Rock density values for salt.

Value, $W\ m^{-1}\ K^{-1}$	Salt	Source
5.44 (330K); 4.53 (350K); 3.88 (400K); 3.02 (500K); 2.47 (600K)	Rock salt – varies with temperature	Langer and Wallner (1998)
6.1 (0 °C); 5.02 (50 °C); 4.19 (100 °C); 3.57 (150 °C); 3.11 (200 °C); 2.78(250 °C)	Rock salt – varies with temperature	Pudewills and Droste (2003)
5.4 (27 C), 4.2 (100C), 3.65 (150 C) and 3.2 (200 C)	Rock salt (Heated test room at WIPP) – varies with temperature $K_{rs}=5.4(300/T)^{1.14}$; T in K	Munson et al. (1990)
0.48 (0 °C); 0.52 (50 °C); 0.57 (100 °C); 0.62 (150 °C); 0.67 (200 °C); 0.72(250 °C)	Crushed salt (initial porosity 35%)	Pudewills and Droste (2003)
5.734	Rock salt at ambient conditions	Olivella et al. (2011)
Porosity range (ϕ): 0-001-0.40	Crushed salt $K_{cs}(\phi) = -270\phi^4+370\phi^3-136\phi^2+1.5\phi +5$ $K_{cs}(\phi,T) = K_{cs}(\phi)[300/T_k]^{1.14}$ Where, T_k is temperature in Kelvin.	Bechthold et al. (2004, Figure 2.37)
A1=-1.83e-2, A2=2.86e-5, A3=-1.51e-8 Temperature range: 20 – 200°C Porosity range (ϕ): 0 – 0.35	Rock salt thermal conductivity: $K_{solid} = 5.734 + A1T + A2T^2 + A3T^3$ Crushed salt (Asse) - thermal conductivity as a function of porosity and liquid saturation: $K_{dry} = K_{solid}^{(1-\phi)}K_{gas}^{\phi}$ $K_{wet} = K_{solid}^{(1-\phi)}K_{liq}^{\phi}$ $K_{cs} = K_{dry}^{(1-Sl)}K_{wet}^{Sl}$	Bechthold et al.(1999, Section 4.3.2) and Olivella et al. (2011) Olivella et al. (2011)
4.04*	Crushed salt – dry	Olivella et al. (2011)
4.19*	Crushed salt - wet	Olivella et al. (2011)

*Calculated using porosity of crushed salt of 0.3, solid thermal conductivity of 5.734 W/mK , liquid thermal conductivity of 0.6 W/mK and gas thermal conductivity of 0.1 W/mK
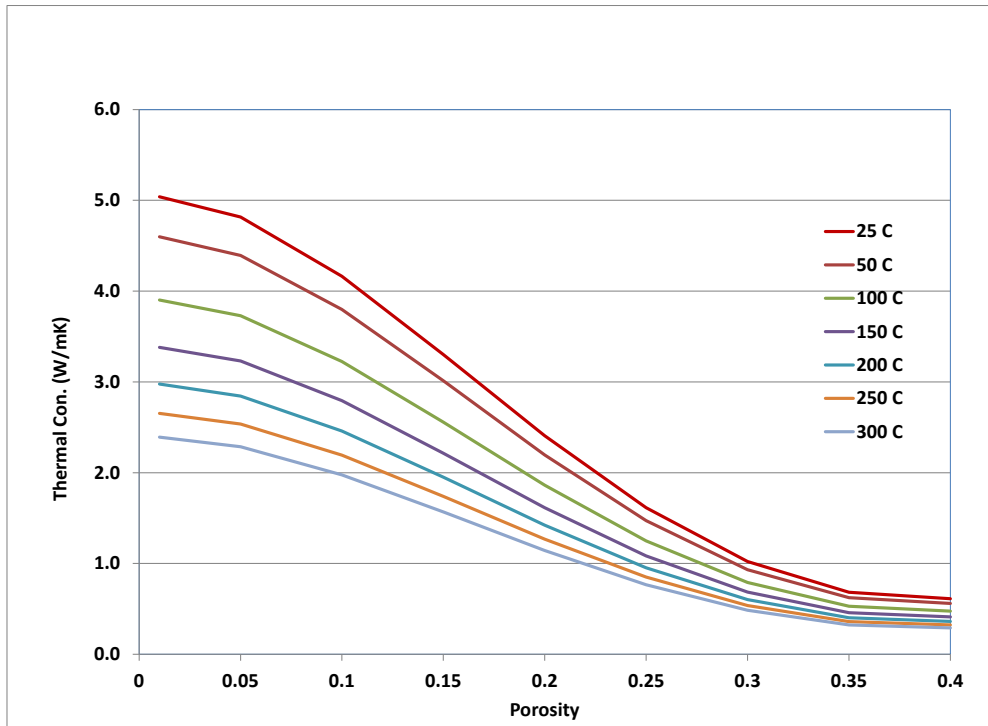
Figure 1.4 Thermal conductivity of dry crushed salt as function of porosity and temperature (Olivella et al., 2011)

Table 1.7 Specific heat values for salt.

Value	Description	Source
$\rho c_p = 1.9E{+}06$ J/m³K	Rock salt volumetric heat capacity. To obtain heat capacity, divide by density.	Pudewills and Droste (2003)
$\rho c_p = 1.8705E{+}06 + 387.72T$ J/m³°C	Rock salt volumetric heat capacity (Asse) with temperature in °C.	Bechthold et al. (2004, Section 7.1.3)
$\rho c_p = 1.37E{+}06$ J/m³K	Volumetric heat capacity for crushed salt (porosity 0.35). To obtain heat capacity, divide by density.	Pudewills and Droste (2003)
Porosity range (φ): 0 – 0.35, Temperature range: 20 – 200 °C	Crushed salt (Asse): Cpcs = Cps Cps = 855+0.177φ (J/Kg K)	Bechthold et al. (1999, Table 3.7)

Table 1.8 Coefficient of linear thermal expansion values for salt

Value (°C)	Description	Source
4.2×10^{-5}	Rock salt	Rothfuchs et al., 1998
4.2×10^{-5}	Rock salt and crushed salt	Pudewills and Droste (2003)

Table 1.9 Excavated Disturbed Zone (EDZ) thickness values for salt

Value, m	EDZ Locality	Source
0.5 – 1.5	Asse site, Germany	Bechthold et al. (2004, Section 4.6)
2	WIPP, New Mexico, USA	Holcomb and Hardy (2001)

Table 1.10. Initial brine saturation and pressure values for salt

Value	Description	Pressure, MPa	Source
0.1-0.4	Crushed salt (sample used for laboratory experiments)	lithostatic	Olivella et al. (2011, Table 1, Figures 5 and 8)
0.015-0.1	Alcove and dry out regions (crushed salt and EDZ)	0.1-lithostatic	Clayton et al. (2011)
1.0	Intact salt	lithostatic	Clayton et al. (2011)

Table 1.11. Retention curve parameter values for rock salt

Value	Parameter	Source
0.7	λ	Helton et al. (1998)
0.3	Residual liquid saturation	Helton et al. (1998)
0.2	Residual gas saturation	Helton et al. (1998)
0.56	a	Helton et al. (1998)
-0.346	η	Helton et al. (1998)

Table 1.12. Retention curve parameter values for EDZ

Value	Parameter	Source
0.7	λ	Helton et al. (1998)
0.0	Residual liquid saturation	Helton et al. (1998)
0.0	Residual gas saturation	Helton et al. (1998)
0.0	a	Helton et al. (1998)
0.0	η	Helton et al. (1998)

Table 1.13. Van Genuchten parameter values for crushed salt

Value	Parameter	Source
0.012 MPa	air entry pressure	Olivella et al. (2011)
0.6	λ	Olivella et al. (2011)
0.2	Residual liquid saturation	Helton et al. (1998)
0.2	Residual gas saturation	Helton et al. (1998)

1.5.3   Mechanical Properties

Mechanical properties and associated parameters for intact salt, crushed salt, and EDZ have been compiled from various sources as given in the tabulations below. A detailed description of a constitutive model for the deformation of crushed salt is given by Callahan (1999) and Callahan and Hansen (2002) which is used in this study. However, it should be noted that other constitutive models to describe creep and compaction of intact and crushed salt, respectively, have been advanced by Rothfuchs et al. (1998), Langer and Wallner (1998), Olivella and Gens (2002), Pudewills and Droste (2003), Liang et al. (2007). As the materials will be subjected to decay heat, there is a need for mechanical data at elevated temperatures. Poisson's ratio values from the literature are given in Table 1.14. Young's modulus values including those as a function of confining pressure are listed in Tables 1.15 and 1.16, respectively.

Table 1.14 Poisson's ratio values for salt

Value	Salt Phase	Source
0.25	Rock salt	Rothfuchs et al., 1998
0.3	Rock salt	Langer and Wallner (1998)
0.27	Rock salt	Pudewills and Droste (2003)
0.35-0.43	Rock salt - WIPP	Hansen et al. (2003)
0.17-0.26	Rock-salt WIPP	Hansen et al., 1984
0.25	Crushed salt	Pudewills and Droste (2003)
0.31	Rock salt	Liang et al., 2007
0.2,0.27	Anhydrite	Liang et al., 2007
0.16,0.3	Rock salt w/anhydrite	Liang et al., 2007

Table 1.15. Young's modulus values for salt

Value, MPa	Salt Phase	Source
2.4×10^4	Rock salt	Rothfuchs et al., 1998
$(2.96\text{-}3.65) \times 10^4$	Rock salt – SE New Mexico	Hansen et al., 1984
2.5×10^4	Rock salt	Langer and Wallner, 1998
2.4×10^4	Rock salt	Pudewills and Droste (2003)
4.4,5.9	Rock salt	Liang et al., 2007
20.9,22.6	Anhydrite	Liang et al., 2007
7.6,5.3	Rock salt w/anhydrite	Liang et al., 2007
2.0×10^4	Crushed salt	Rothfuchs et al., 1998
1×10^4	Crushed salt (initial porosity 35%)	Pudewills and Droste (2003)

Table 1.16. Young's Modulus for salt at various confining pressures (Liang et al., 2007)

Confining Pressure (MPa)	Young's modulus- rock salt MPa	Young's modulus- anhydrite MPa	Young's modulus- mixed MPa
0	$(4.40\text{-}5.9) \times 10^3$	$(2.09\text{-}2.26) \times 10^4$	$(5.3\text{-}7.6) \times 10^3$
5	2.04×10^4	6.18×10^4	1.03×10^4
10	2.08×10^4	1.73×10^4	1.96×10^4
15	2.52×10^4	3.27×10^4	2.41×10^4

1.6 Thermal Model Description

For the thermal analysis, a convective boundary condition was applied to the top and bottom of the model to simulate the heat transfer into the host rock above and below the repository. To assess this choice of boundary conditions a simulation was performed with no-heat flow conditions on the top and bottom surfaces. No significant difference in the alcove closure rate was observed between these calculations for the 10 year period. All the materials are assumed to be initially at 300K (about 25°C). A thermal load of 2 kW was applied uniformly throughout the waste canister at time zero. The thermal load follows the decay curve shown in Figure 1.5. After 10 years the heat load has only been reduced to approximately 76% of the initial value. Simulations periods much greater than 10 years would be required to return to ambient thermal conditions.
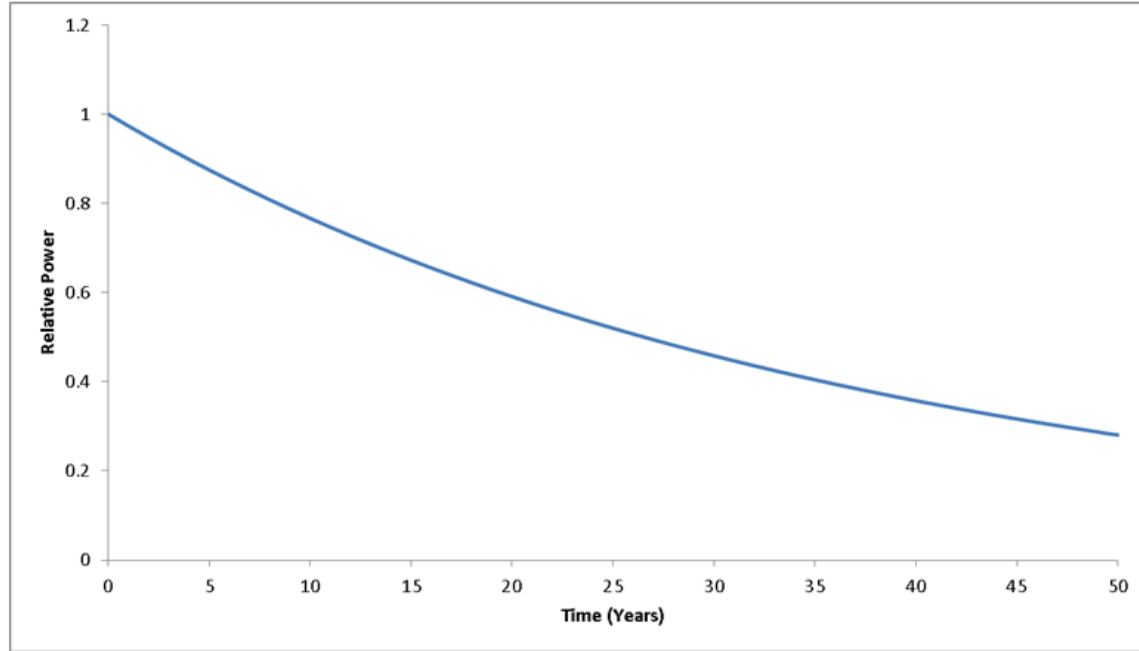
Figure 1.5. Decay curve used in the thermal analyses.

Constitutive Model for Thermal Conductivity

The temperature dependent thermal conductivity of intact salt used in the analysis is given by equation (1.3):

$$\lambda_{salt}(T) = \lambda_{300}\left(\frac{300}{T}\right)^{\gamma}$$

(1.3)

where:

λ_{300} = material constant, 5.4 [W/m K]

γ = material constant, 1.14

T = temperature [K].

The thermal conductivity of the crushed salt used in the analysis is based on the results of the BAMBUS II study (Bechthold et al. 2004) where the thermal conductivity of crushed salt was determined from field experiments on drifts backfilled with crushed salt. From this study, a fourth-order polynomial was fit to the field data to describe crushed-salt thermal conductivity as a function of porosity (ϕ):

$$k_{cs}(\phi) = -270\,\phi^4 + 370\,\phi^3 - 136\,\phi^2 + 1.5\,\phi + 5$$

(1.4)

This representation is valid for porosities between zero and forty percent. When the porosity is zero, Equation (1.4) produces a thermal conductivity of 5.0 W/m K. Therefore, Equation (1.4) is modified by a factor (f) to correspond with the salt, such that the thermal conductivity of 5.4 W/m K is reproduced at zero porosity. Equation (1.4) is rewritten as:

225

$$k_{cs}(\phi) = \left(-270\,\phi^4 + 370\,\phi^3 - 136\,\phi^2 + 1.5\,\phi + 5\right) \cdot f \tag{1.5}$$

where f is simply (5.4/5.0 or 1.08). For this study, the initial porosity of the crushed salt is assumed to be 33%. The temperature-dependent nature of the crushed-salt thermal conductivity is assumed to be the same as for intact salt. Therefore, the crushed-salt thermal conductivity is given by:

$$\lambda_{c-salt}(T) = k_{cs}(\phi)\left(\frac{300}{T}\right)^{\gamma} \tag{1.6}$$

This model for thermal conductivity of crushed salt has been incorporated in Sierra/Aria through a user module. The density of the crushed salt was calculated as a linear function of porosity. A summary of the thermal material properties assumed for the waste, intact and EDZ salt and crushed salt are shown in Table 1.17.

Table 1 1.17. Thermal properties for the waste and salt

Material	Thermal Conductivity (W/m K)	Specific Heat (J/kg K)	Density (kg/m^3)
Waste	1.0	840	2,220
Intact and EDZ Salt	Equation (1.6)	931	2,160 ($=\rho_0$)
Crushed Salt	Equation (1.6)	931	$\rho_0(1-\phi)$

1.7 Thermo-Mechanical Model Description

For the mechanical analysis, the boundary conditions were set so that lateral displacements were specified to be zero along the vertical boundaries. No vertical displacement boundary conditions were specified on the bottom surface. The applied mechanical loads acting on the model consisted of an overburden pressure applied to the top of the model to reflect an alcove depth of approximately 600 m. The intact and EDZ salt regions were initialized with lithostatic stresses corresponding to depth, while the waste canister and crushed salt began with no stress. The lithostatic stresses at the level of the alcove were approximately 14.8 MPa. All salt regions were modeled using the crushed salt constitutive model (Callahan 1999) described below. By setting the initial density equal to the intact density the crushed salt model replicates the Multimechanism Deformation model of Munson et al. (1989) for intact salt. The linear thermal expansion coefficient for crushed and host salt material was taken to be 4.5×10^{-5} K^{-1}.

Constitutive Model for Salt

The constitutive model outlined in this section was developed by Callahan (1999) for examining the performance of crushed salt as a component in the shaft and panel seals at the Waste Isolation Pilot Plant (WIPP) near Carlsbad NM. The model has been implemented in the LAME constitutive model library (Scherzinger and Hammerand, 2007) used by the Sierra/Mechanics codes at Sandia National Laboratories.

It is assumed herein that tensile stresses and strain rates are positive. All stress variables in this section should be interpreted as effective stresses. In the crushed salt constitutive model, the total

226

strain rate is additively decomposed into elastic strain rate ($\dot{\varepsilon}^e_{ij}$) and inelastic (creep) strain rate $\left(\dot{\varepsilon}^c_{ij}\right)$ contributions:

$$\dot{\varepsilon}_{ij} = \dot{\varepsilon}^e_{ij} + \dot{\varepsilon}^c_{ij} \tag{1.7}$$

The elastic strain rate may be decomposed into deviatoric ($\dot{e}^e_{ij}$) and volumetric ($\dot{\varepsilon}^e_{kk}$) contributions

$$\dot{\varepsilon}^e_{ij} = \dot{e}^e_{ij} + \frac{1}{3}\dot{\varepsilon}^e_{kk}\delta_{ij} \tag{1.8}$$

In this model the Cauchy stress rate ($\dot{\sigma}_{ij}$) is related to the elastic strain rate by the isotropic hypo-elastic relation:

$$\dot{\sigma}_{ij} = 2G\dot{e}^e_{ij} + K\dot{\varepsilon}^e_{kk}\delta_{ij} = 2G\left(\dot{e}_{ij} - \dot{e}^c_{ij}\right) + K\left(\dot{\varepsilon}_{kk} - \dot{\varepsilon}^c_{kk}\right)\delta_{ij} \tag{1.9}$$

where G and K are the shear and bulk moduli respectively. Following the work of Sjaardema and Krieg (1987) these moduli are assumed to be non-linear functions of the material density (ρ). No temperature dependency is included in the functional form of the elastic moduli. The functional forms for these elastic moduli are:

$$\begin{aligned} G &= G_0 e^{G_1\rho} \\ K &= K_0 e^{K_1\rho} \end{aligned} \tag{1.10}$$

where G_0, G_1, K_0, and K_1 are constants determined from laboratory testing.

The total creep strain rate ($\dot{\varepsilon}^c_{ij}$) contains contributions from two time-dependent inelastic mechanisms – dislocation creep ($\dot{\varepsilon}^d_{ij}$) and grain boundary diffusional pressure solution ($\dot{\varepsilon}^w_{ij}$).

$$\dot{\varepsilon}^c_{ij} = \dot{\varepsilon}^d_{ij} + \dot{\varepsilon}^w_{ij} \tag{1.11}$$

$$\dot{\varepsilon}^d_{ij} = \left[\dot{\varepsilon}^d_{eq}\left(\sigma^f_{eq}\right)\right]\frac{\partial\sigma_{eq}}{\partial\sigma_{ij}} \tag{1.12}$$

$$\dot{\varepsilon}^w_{ij} = \left[\dot{\varepsilon}^w_{eq}\left(\sigma^f_{eq}\right)\right]\frac{\partial\sigma_{eq}}{\partial\sigma_{ij}} \tag{1.13}$$

When a deviatoric stress is applied to a crystalline material (e.g. salt) it causes dislocations in the lattice to move resulting in inelastic macroscopic deformations. The second creep mechanism, grain boundary diffusional pressure solution, results from the migration of salt through the liquid phase and is developed from grain to grain contacts resulting in dissolution at the contact and precipitation in adjacent pores. The driving force for pressure solution is the gradient of the chemical potential induced by differences in contact stresses.

The terms in brackets in Equations (1.12) and (1.13) are the kinetic equations for dislocation creep $\left(\dot{\varepsilon}^d_{eq}\right)$ and grain boundary diffusional pressure solution ($\dot{\varepsilon}^w_{eq}$). The notation used in Equations (1.12)

and (1.13) indicates these equivalent creep strain rates are scalar functions of the equivalent stress measure (σ_{eq}^f), defined below in Equation (1.14).

The creep flow potential used in the model is defined using a different equivalent stress measure (σ_{eq}). This non-associative formulation was introduced to control dilatancy which occurs as a result of including the mean stress term in the model. The partial derivatives $\dfrac{\partial \sigma_{eq}}{\partial \sigma_{ij}}$ appearing in Equations (1.12) and (1.13) are the components of the gradient of the creep flow potential. The two equivalent stress measures are given by:

$$\sigma_{eq}^f = \left[\eta_0 \Omega_f^{\eta_1} \sigma_m^2 + \left(\frac{2-D}{D} \right)^{\frac{2n_f}{n_f+1}} \left(\sigma_1 - \sigma_3 \right)^2 \right]^{\frac{1}{2}} \tag{1.14}$$

$$\sigma_{eq} = \left[\kappa_0 \Omega^{\kappa_1} \sigma_m^2 + \left(\frac{2-D}{D} \right)^{\frac{2n}{n+1}} \left(\sigma_1 - \sigma_3 \right)^2 \right]^{\frac{1}{2}} \tag{1.15}$$

where,

$$\Omega_f = \left[\frac{(1-D)n_f}{\left[1-(1-D)^{1/n_f} \right]^{n_f}} \right]^{\frac{2}{n_f+1}} \tag{1.16}$$

$$\Omega = \left[\frac{(1-D_v)n}{\left[1-(1-D_v)^{1/n} \right]^{n}} \right]^{\frac{2}{n+1}} \tag{1.17}$$

and

$$D_v = \begin{cases} D_t & D \le D_t \\ D & D > D_t \end{cases} \tag{1.18}$$

where:

$D=$ fractional density $= \dfrac{\rho}{\rho_{int}}$

$\rho =$ current density

$\rho_{int} =$ intact salt density

$\sigma_m =$ mean stress $= \dfrac{1}{3}\sigma_{kk}$

$\sigma_1 =$ maximum principal stress

$\sigma_3 =$ minimum principal stress

$\eta_0, \eta_1, \kappa_0, \kappa_1, n_f, n, D_t =$ material parameters.

As the crushed salt approaches full consolidation $(D \to 1)$ Ω_f and Ω both approach zero and the mean stress influence on the creep strain rate is eliminated. This is consistent with observed deformation isochoric (constant volume) deformation characteristics of intact salt. When the salt is fully consolidated, $D = 1$, Equations (1.14) and (1.15) reduce to:

$$\sigma_{eq}^f = \sigma_{eq} = \sigma_1 - \sigma_3 \tag{1.19}$$

The quantity $\sigma_1 - \sigma_3$ is equal to the Tresca equivalent stress (σ_{eq}^T):

$$\sigma_1 - \sigma_3 = \sigma_{eq}^T = 2\cos\psi \sqrt{J_2} \tag{1.20}$$

where ψ is the Lode angle and J_2 is the second invariant of the deviatoric stress tensor defined by Equations (1.19) and (1.20), respectively. The Lode angle is dependent on both the second (J_2) and third invariant (J_3) of the deviatoric stress tensor:

$$\psi = \frac{1}{3}\sin^{-1}\left[\frac{-3\sqrt{3}J_3}{2J_2^{3/2}}\right] \qquad -\frac{\pi}{6} \leq \psi \leq \frac{\pi}{6} \tag{1.21}$$

$$J_2 = \frac{1}{2}s_{ij}s_{ji} \tag{1.22}$$

$$J_3 = \frac{1}{3}s_{ij}s_{jk}s_{ki} \tag{1.23}$$

The gradient of the flow potential may be written:

$$\frac{\partial \sigma_{eq}}{\partial \sigma_{ij}} = \frac{\partial \sigma_{eq}}{\partial \sigma_m}\frac{\partial \sigma_m}{\partial \sigma_{ij}} + \frac{\partial \sigma_{eq}}{\partial J_2}\frac{\partial J_2}{\partial \sigma_{ij}} + \frac{\partial \sigma_{eq}}{\partial J_3}\frac{\partial J_3}{\partial \sigma_{ij}} \tag{1.24}$$

The partial derivatives of the three stress invariants (σ_m, J_2, and J_3) with respect to the Cauchy stresses are given by:

$$\frac{\partial \sigma_m}{\partial \sigma_{ij}} = \frac{\delta_{ij}}{3} \tag{1.25}$$

$$\frac{\partial J_2}{\partial \sigma_{ij}} = s_{ij} \tag{1.26}$$

$$\frac{\partial J_3}{\partial \sigma_{ij}} = t_{ij} = s_{ik} s_{kj} - \frac{2}{3} J_2 \delta_{ij} \tag{1.27}$$

The partial derivatives of the equivalent stress with respect to the stress invariants are given by:

$$\frac{\partial \sigma_{eq}}{\partial \sigma_m} = \frac{\kappa_0 \Omega^{\kappa_1} \sigma_m}{\sigma_{eq}} \tag{1.28}$$

$$\frac{\partial \sigma_{eq}}{\partial J_2} = \frac{2}{\sigma_{eq}} \left(\frac{2-D}{D} \right)^{\frac{2n}{n+1}} \frac{\cos \psi \cos 2\psi}{\cos 3\psi} \tag{1.29}$$

$$\frac{\partial \sigma_{eq}}{\partial J_3} = \frac{\partial \sigma_{eq}}{\partial \psi} \frac{\partial \psi}{\partial J_3} \tag{1.30}$$

where,

$$\frac{\partial \sigma_{eq}}{\partial \psi} = -\frac{4}{\sigma_{eq}} \left(\frac{2-D}{D} \right)^{\frac{2n}{n+1}} \cos \psi \sin \psi J_2 \tag{1.31}$$

$$\frac{\partial \psi}{\partial J_3} = -\frac{\sqrt{3}}{2 J_2^{3/2} \cos 3\psi} \tag{1.32}$$

Making these substitutions in Equation (1.11) gives the following result:

$$\dot{\varepsilon}_{ij}^c = \frac{\dot{\varepsilon}_{eq}^d + \dot{\varepsilon}_{eq}^w}{\sigma_{eq}} \left\{ \frac{\kappa_0 \Omega^{k_1} \sigma_m}{3} \delta_{ij} + \left(\frac{2-D}{D} \right)^{\frac{2n}{n+1}} 2\sqrt{J_2} \cos \psi \left(\left[\frac{\cos 2\psi}{\cos 3\psi} \right] \frac{s_{ij}}{\sqrt{J_2}} + \left[\frac{\sqrt{3} \sin \psi}{J_2 \cos 3\psi} \right] t_{ij} \right) \right\} \tag{1.33}$$

At stress states where $\psi = \pm \frac{\pi}{6}$ the gradient is not uniquely defined. This is due to the presence of corners in the flow potential; therefore, special consideration must be given to the gradient computation at these locations. To complete the description of the creep strain rate, the kinetic equations (i.e. equivalent creep strain rate equations) for dislocation ($\dot{\varepsilon}_{eq}^d$) and grain boundary diffusional pressure solution ($\dot{\varepsilon}_{eq}^w$) need to be defined.

The dislocation creep model, known as the Multimechanism Deformation model (MD model) developed by Munson and Dawson (1979) and extended by Munson et al. (1989), provides the dislocation creep component of the crushed salt model. Recall that as the crushed salt approaches

230

the density of intact salt the two stress measures are identical; therefore, the crushed salt model transitions in a logical manner to the MD model as the fractional density approaches a value of one.

The kinetic equation for dislocation creep in the MD model is given by Equation (1.34) where F is a function which accounts for transient creep effects and $\dot{\varepsilon}_s$ is the steady state dislocation creep strain rate:

$$\dot{\varepsilon}_{eq}^d = F\dot{\varepsilon}_s \tag{1.34}$$

The transient function F has three branches: a work hardening branch ($F > 1$), an equilibrium branch ($F = 1$), and a recovery branch ($F < 1$):

$$F = \begin{cases} \exp\left[\Delta\left(1-\dfrac{\zeta}{\varepsilon_t^f}\right)^2\right] & \zeta < \varepsilon_t^f & \text{Transient Branch} \\[3mm] 1 & \zeta = \varepsilon_t^f & \text{Equilibrium Branch} \\[3mm] \exp\left[-\delta\left(1-\dfrac{\zeta}{\varepsilon_t^f}\right)^2\right] & \zeta > \varepsilon_t^f & \text{Recovery Branch} \end{cases} \tag{1.35}$$

The choice of the particular branch depends on the transient strain limit (ε_t^f) and the internal variable (ζ). The transient strain limit is defined by Equation (1.36) where K_0, c, and m are material parameters, T is the absolute temperature, and μ is the shear modulus of intact salt:

$$\varepsilon_t^f = K_0 e^{cT}\left(\frac{\sigma_{eq}^f}{\mu}\right)^m \tag{1.36}$$

The internal variable ζ, used in the calculation of the transient function F, is obtained by integration of the evolution equation:

$$\dot{\zeta} = (F-1)\dot{\varepsilon}_s \tag{1.37}$$

Δ and δ, appearing in Equation (1.35), are the work hardening and recovery parameters and are given by Equations (1.38) and (1.39), respectively. In these equations α, β, α_r, and β_r are material parameters. In the crushed salt model the recovery parameter δ is taken to be constant (i.e. $\delta = \alpha_r$) because of insufficient data:

$$\Delta = \alpha + \beta \log\left(\frac{\sigma_{eq}^f}{\mu}\right) \tag{1.38}$$

$$\delta = \alpha_r + \beta_r \log\left(\frac{\sigma_{eq}^f}{\mu}\right) \tag{1.39}$$

In the MD model, three steady state dislocation mechanisms are considered: dislocation climb $\left(\dot{\varepsilon}_{s_1}\right)$, an unidentified but experimentally observed mechanism ($\dot{\varepsilon}_{s_2}$), and dislocation slip ($\dot{\varepsilon}_{s_3}$).

231

Because these mechanisms are assumed to act in parallel, their contribution to the steady state dislocation creep strain rate is simply the sum of the three:

$$\dot{\varepsilon}_s = \sum_{i=1}^{3} \dot{\varepsilon}_{s_i} \tag{1.40}$$

$$\dot{\varepsilon}_{s_1} = A_1 \left(\frac{\sigma_{eq}^f}{\mu} \right)^{n_1} \exp\left(-\frac{Q_1}{RT} \right) \tag{1.41}$$

$$\dot{\varepsilon}_{s_2} = A_2 \left(\frac{\sigma_{eq}^f}{\mu} \right)^{n_2} \exp\left(-\frac{Q_2}{RT} \right) \tag{1.42}$$

$$\dot{\varepsilon}_{s_3} = \left(B_1 e^{-Q_1/RT} + B_2 e^{-Q_2/RT} \right) \sinh\left[q \left(\frac{\sigma_{eq}^f - \sigma_0}{\mu} \right) \right] H\left(\sigma_{eq}^f - \sigma_0 \right) \tag{1.43}$$

where,

A_1, A_2, B_1, B_2 are structure factors

Q_1, Q_2 are activation energies

R is the universal gas constant

T is the absolute temperature (K)

q is the activation volume

σ_0 is the stress limit above which dislocation slip become active

H is the Heaviside function = 1 when $\sigma_{eq}^f - \sigma_0 > 0$ otherwise = 0.

The first mechanism (dislocation climb) dominates at low equivalent stress (σ_{eq}^f) and high temperature. The second mechanism (unidentified or unnamed) dominates at low stress and temperature. The third mechanism (dislocation slip) is predominately active at high stress for all temperatures.

The kinetic equation for grain boundary diffusional pressure solution, used in the WIPP crushed salt model, is a modified version of the Spiers and Brzesowsky (1993) model for wet crushed salt:

$$\dot{\varepsilon}_{eq}^w = \frac{r_1 w^a}{d^p} e^{-\bar{\varepsilon}_v} \left(\frac{e^{r_3 \bar{\varepsilon}_v}}{\left| e^{\bar{\varepsilon}_v} - 1 \right|^{r_4}} \right) \frac{e^{-\frac{Q_s}{RT}}}{T} \Gamma \sigma_{eq}^f \tag{1.44}$$

where:

r_1, r_3, r_4, Q_s, a, p are material constants

T is temperature (K)

R is the universal gas constant

d is grain size

w is Moisture fraction by weight

$\bar{\varepsilon}_v$ is the true or natural volumetric strain

Γ is the geometry function

232

Note that if the crushed salt is dry ($w = 0$), the grain boundary diffusional pressure solution contribution to the total strain rate vanishes (i.e. $\dot{\varepsilon}_{eq}^w = 0$) and grain size has no influence in the model.

In Equation (1.43), the term $e^{\bar{\varepsilon}_v} - 1$ appears in the denominator. An initial volumetric strain ε_{v*}, corresponding to the volumetric strain accumulated in going from a fractional density $D_0 = 0.64$ to the fractional density at the time the crushed salt is placed is included in the formulations to avoid division by zero when the volume strain at the start of the simulation is zero.

The geometry function Γ used in Equation (1.44) has two functional forms given by Equation (1.45); the choice of which one to use depends on the magnitude of the engineering volumetric strain e_v. For compressive volumetric strains less than 15% a constant value of one is used:

$$\Gamma = \begin{cases} 1 & \text{small strain } (e_v > -0.15) \\[2ex] \left[\dfrac{e^{\bar{\varepsilon}_v} + \phi_0 - 1}{\phi_0 e^{\bar{\varepsilon}_v}} \right]^{n_s} & \text{large strain } (e_v < -0.15) \end{cases} \tag{1.45}$$

where n_5 is a material constant.

As the crushed salt density approaches the density of intact salt the value of Γ approaches zero; therefore, $\dot{\varepsilon}_{eq}^w = 0$ when the salt is fully consolidated. Table 1.18 lists the parameter values used in these simulations. The waste was assumed to respond elastically using the properties of steel shown in Table 1.19.

Table 1.18. Mechanical Properties used for salt

Symbol	Crushed Salt	Intact and EDZ Salt	Units
G_0	1.06×10^4	1.24×10^{10}	Pa
G_1	0.00653	0.0	m^3/kg
K_0	1.76×10^4	2.07×10^{10}	Pa
K_1	0.00653	0.0	m^3/kg
ρ_*	Problem Dependent: 1447 for initial porosity = 33%	2160.	kg/m^3
ρ_{int}	2160.	2160.	kg/m^3
μ	1.24×10^{10}	1.24×10^{10}	Pa
A_1	8.386×10^{22}	8.386×10^{22}	1/s
Q_1/R	12580	12580	K
n_1	5.5	5.5	-
B_1	6.086×10^6	6.086×10^6	1/s
A_2	9.672×10^{12}	9.672×10^{12}	1/s
Q_2/R	5032	5032	K

Table 1.18 (Cont.) Mechanical Properties used for salt

Symbol	Crushed Salt	Intact and EDZ Salt	Units
n_2	5.0	5.0	-
B_2	3.034 x 10^{-2}	3.034 x 10^{-2}	1/s
σ_0	20.57 x 10^6	20.57 x 10^6	Pa
q	5335.	5335.	-
m	3.0	3.0	-
K_0	6.275 x 10^5	6.275 x 10^5	-
c	9.198 x 10^{-3}	9.198 x 10^{-3}	1/K
α	-17.37	-17.37	-
β	-7.738	-7.738	-
δ	0.58	0.58	-
κ_0	10.119	10.119	-
κ_1	1.005	1.005	-
n	1.331	1.331	-
D_t	0.896	0.896	-
η_0	0.1029	0.1029	-
η_1	3.9387	3.9387	-
n_f	3.5122	3.5122	-
a	0.3147	0.3147	-
p	1.6332	1.6332	-
n_s	0.5576	0.5576	-
Q_s/R	1077.46	1077.46	K
r_1	1.041 x 10^{-12}	1.041 x 10^{-12}	m^p·K/(Pa·s)
r_3	15.1281	15.1281	-
r_4	0.1678	0.1678	-
w	Problem Dependent 0, 0.01% , 0.1%, 1%	0.0	-
d	Problem Dependent 0.001, 0.005	0.001	m

Table 1.19. Mechanical properties used for the waste.

Material	Young's Modulus (Pa)	Poisson's Ratio	Thermal Expansion (K^{-1})
Heater	2.0E+11	0.3	2.0E-6

1.8 Coupled Mechanical and Thermal Analysis Results

The finite element discretization shown in Figure 1.3 was used in the coupled thermo-mechanical calculations. The same finite element mesh was used in the thermal and mechanical models though this is not a requirement of the Sierra codes; interpolation from different grids is allowed. The thermal-mechanical simulations performed in this study examine the closure of the backfilled regions and how the closure rate is affected by water content. The salt backfill is compacted due to the inward creep of the host rock. Initially the rate of compaction of the backfilled region depends on the stresses produced in the host rock by the mining of the access drifts and alcoves. Thermal effects become increasingly important as the heat from the waste package is conducted out into the backfill and host rock. Ultimately the salt backfill begins to provide resistance to closure as its porosity is reduced.

In all cases, the water content in the backfill is assumed to be constant throughout the simulation. If moisture movement were included (e.g. THM model) regions of dry-out near the heater would be expected as well as wetter regions due to moisture transport and water vapor condensation in cooler areas of the backfilled alcove and access drifts.

1.8.1 Mechanical Modeling Results

Average Backfill Porosity

The salt backfill porosity can be used to provide information about how long it will take for the waste to be encapsulated due to the creep of the host rock. The permeability of the crushed salt backfill decreases as the porosity decreases. Figure 1.6 illustrates the average backfill porosity as a function of time when the water content of the waste is varied from dry (w=0) to w = 1%. For the dry case the average porosity has been reduced from 33% to around 14.5% after 10 years. Recall that if the backfill is dry the dislocation creep portion of the model is active but the pressure solution mechanism is not active. A comparison of the dry case with cases where moisture is present illustrates the influence of the pressure solution creep mechanism. A significant reduction in backfill porosity is predicted by the presence of water in the crushed salt. The backpressure exerted by the backfill on the inward creeping host rock is less when the backfill has higher moisture content.

The non-zero water content cases are very similar to each other up to approximately 4 years but at later times the consolidation (porosity reduction) is greater for increasing water content. After 10 years the average porosity has been reduced to less than 3% in these cases. Also shown in Figure 1.6 is the effect of the increasing the grain size ($d = $ gs) from 1 mm to 5 mm (dashed curve). The larger grain size increases the time to reach a given porosity for the same water content.

An isothermal simulation was performed so the thermal effect on the creep closure can be understood. This is illustrated in Figure 1.7 by the difference between the case with thermal effect and the isothermal case. The average closure rate for the isothermal simulation (water content of 1%, grain size 1 mm) is generally similar to the non-isothermal dry case (water content of 0%, grain size 1 mm) for the 10 year simulation period. At 10 years, the average backfill porosity for the isothermal case is 13.6% while the non-isothermal case for the same water content and grain size conditions is a much lower 1%.

A plane strain simulation was performed to examine backfill consolidation rates using two and three-dimensional numerical models. While computationally much faster the plane strain model effectively ignores the host rock pillars located between the parallel alcoves as well as the finite

length of the waste package. The plane strain model shows the backfill porosity has been reduced to less than 1% after about 2 years; a significantly faster consolidation rate than that seen in the three-dimensional model simulations. It is obvious that a three-dimensional numerical representation is necessary for the alcove and access drifts geometries assumed in these simulations.
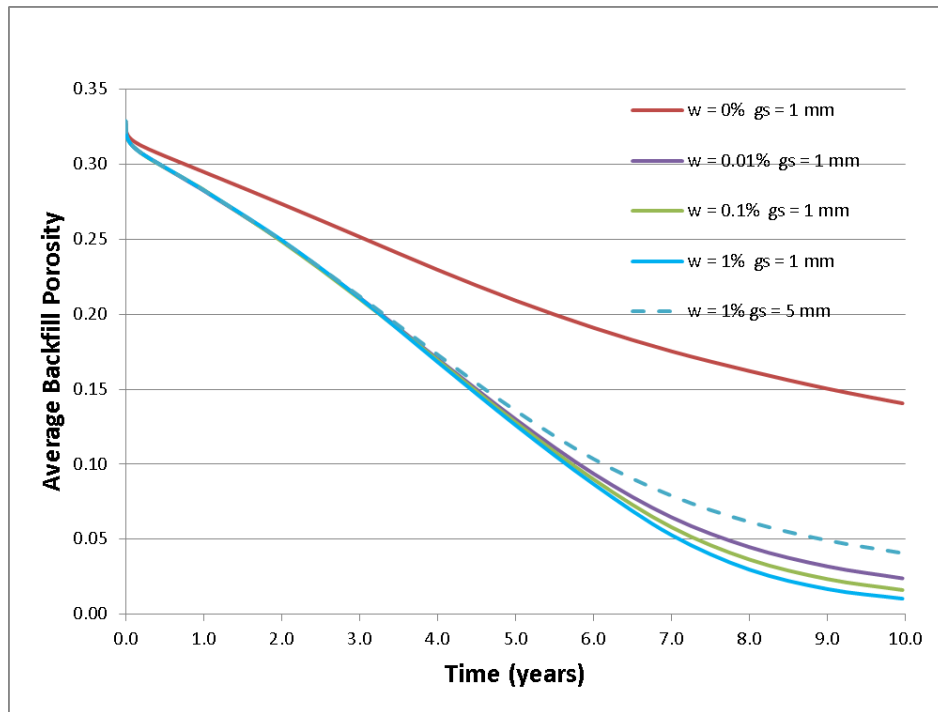

Figure 1.6. Influence of water content and grain size on the average backfill porosity
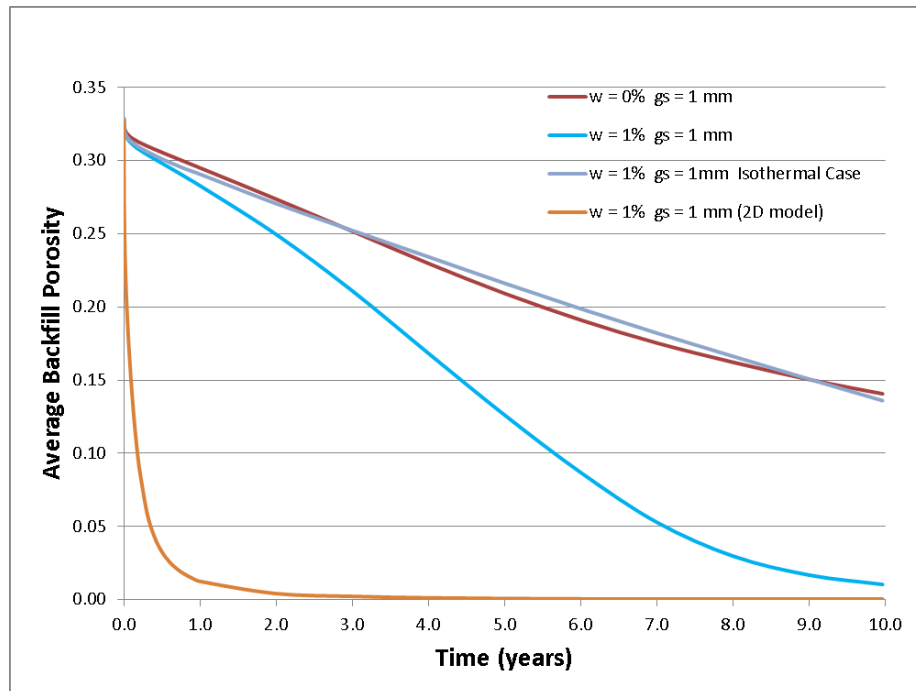

Figure 1.7. Influence of thermal effects and 2D-3D model geometry on the average backfill porosity

236

Vertical Closure of Excavated Alcove and Access Drift

Figure 1.8 illustrates the locations where the vertical closure histories, shown in Figure 1.9, have been recorded. These results are for the case where the water content is 1% and the grain size is 1 mm. The early time (t<<1year) rapid closure is the result of primary creep effects in the host salt. The rate of closure decreases at later times due to the consolidation of the backfill as it approaches the density of intact salt (2160 kg/m^3). The volume strain at which the crushed salt backfill reaches 1% porosity is:

$$\varepsilon_v = \ln\frac{1-\phi_{ini}}{1-\phi} = \ln\frac{1-0.33}{1-0.01} = -0.39$$

where ϕ_{ini} is the initial porosity (33%). The vertical strain $\left(\varepsilon_{zz}\right)$ based on vertical closure of 0.6 m is equal to:

$$\varepsilon_{zz} = \ln\frac{h}{h_{ini}} = \ln\left(\frac{3.05-0.6}{3.05}\right) = -0.22$$

where h, h_{ini} are the current and initial heights of the excavated access and alcove regions. These simple calculations indicate there is a contribution to the consolidation of the backfill salt provided by the inward creep of the host salt pillars in the lateral directions (x and y):

$$\varepsilon_v = -0.39 = \varepsilon_{xx} + \varepsilon_{yy} + \varepsilon_{zz} = \varepsilon_{xx} + \varepsilon_{yy} - 0.22$$
$$\varepsilon_{xx} + \varepsilon_{yy} = -0.39 - (-0.22) = -0.17$$

In the plane strain case the only non-zero lateral component is ε_{xx} since $\varepsilon_{yy} = 0$ for the coordinate directions selected in these simulations (the y-direction is parallel to the access drift). In the plane strain case the volumetric strain is dominated by the vertical strain component and the vertical closure (not shown) was 0.9 m; therefore, the vertical strain was -0.35. The lateral strain contribution ε_{xx} was approximately -0.05 in the plane strain case.
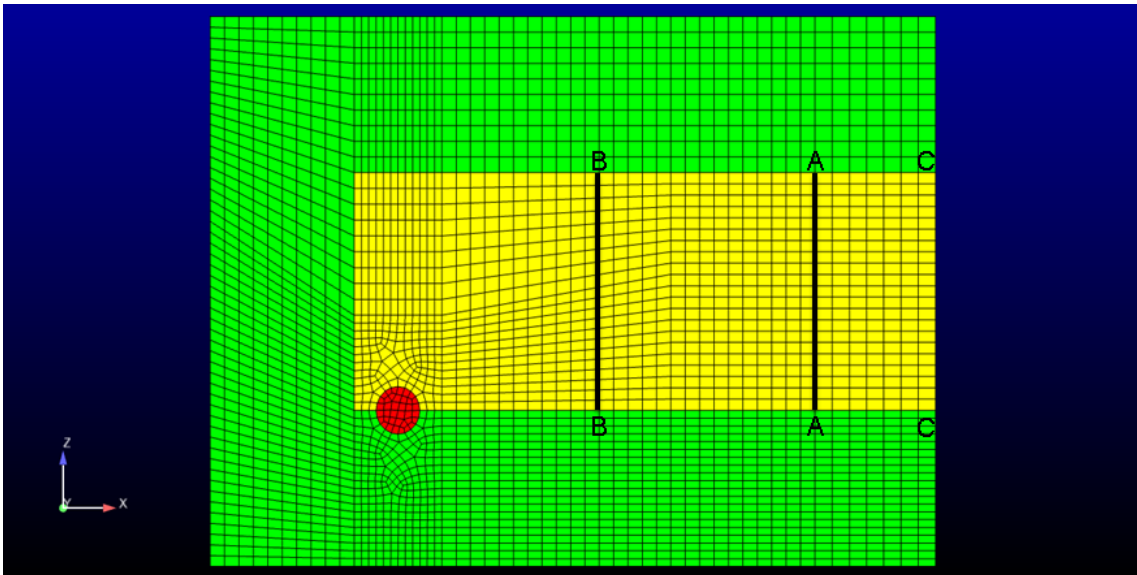
Figure 1.8. Vertical closure history locations. A – A location of alcove junction with access drift, B – B is the midpoint of alcove, and C- C is the center of access drift.
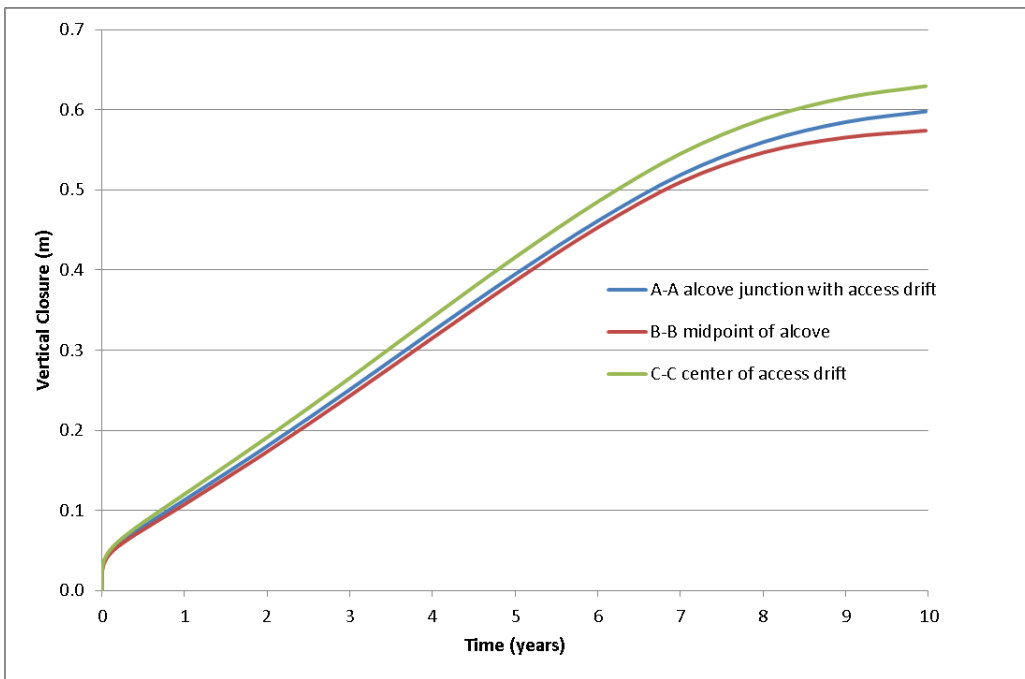

Figure 1.9. Vertical closure histories for the 3D case with water content = 1% and grain size=0.001m

Thermal Model Results

Figure 1.10 illustrates the locations in the alcove where temperatures have been examined. These five points are all located on the symmetry plane through the middle of the alcove. Point E corresponds to the center of the waste package while points B and D are located at the intersection

239

of the access drift and the alcove. Figure 1.11 shows the temperature histories at these five locations for the cases where the water content was 1% and the grain size was 1 mm. The waste package temperature (Point E) reaches a maximum value of 365 K (92°C) around 2 years then deceases a few degrees to 362 K (89°C) at 10 years while all the other locations are still experiencing rising temperatures at 10 years.
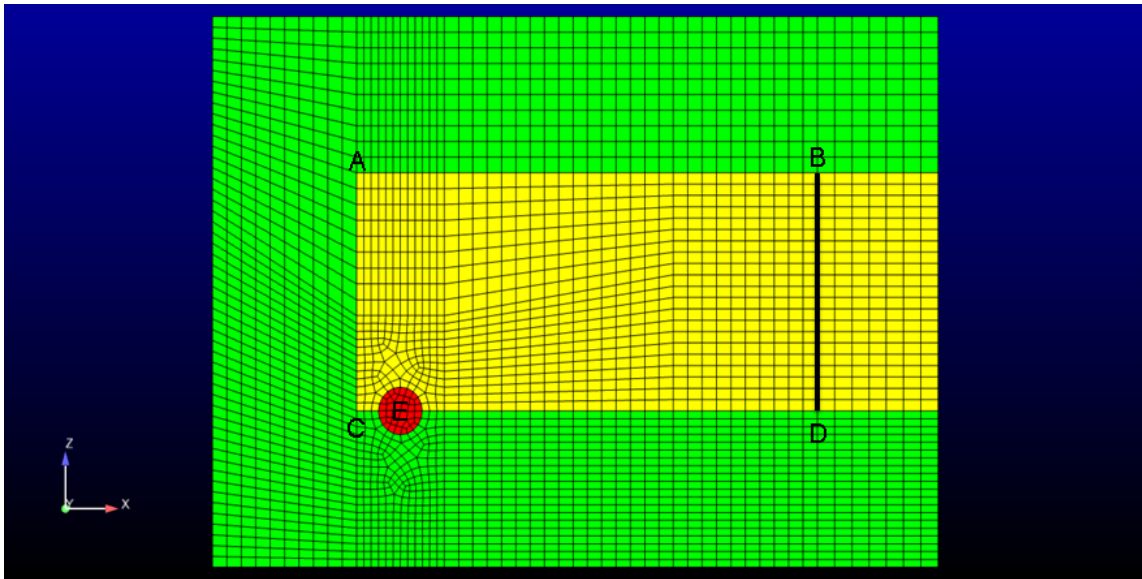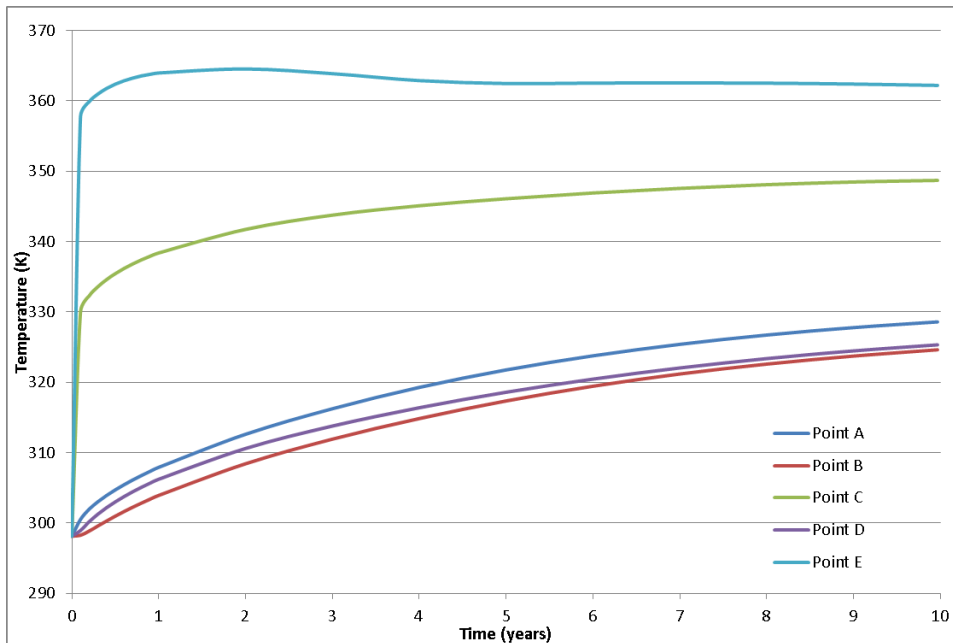

Figure 1.10. Temperature history locations

Figure 1.11. Temperatures at five locations (water content = 1%, grain size= 1 mm)

240

Summary of Thermal-Mechanical Modeling

A series of coupled thermo-mechanical (TM) calculations of a generic salt repository have been completed using the Sandia National Laboratories (SNL) Sierra codes. These results extend earlier TM modeling (Hardin et al., 2011) where the crushed salt backfill was assumed to be dry and placed at an initial porosity of 20%. Results from these TM analyses, where the impact of moisture content was examined, provide estimates of the time for the crushed salt backfill to compact to levels approaching intact salt density. Future calculations will take advantage of the hydrogeologic capability of Sierra/Aria to include fully coupled thermal, hydrological and/or chemical calculations. The inclusion of hydraulic models (e.g. single or multi-phase flow) is important because the mechanical behavior is directly influenced by the pore-fluid pressures. The low permeability of the host salt could result in significant pore-fluid pressures being generated.

1.9 Moisture Transport

Moisture movement in crushed porous salt backfill is an important aspect of vapor phase water transport as a result of heat generation from the waste package. Previous sections on the mechanical modeling of salt outlines the importance of moisture on crushed salt consolidation. In this section we consider the thermal-hydrological (TH) problem un-coupled from the geomechanics. Though the ultimate goal is to study the coupled flow and geomechanics, this uncoupled example helps to facilitate understanding the moisture movement due to decay heat separately from the effects due to mechanics. It should also be noted that chemical interactions between the H_2O phase and salt are ignored when it comes to two-phase flow and stabilization of brine in the crushed salt pores.

The model geometry was discussed in a previous section. We consider the moisture transport due to a 2 kW waste canister with a half-life of approximately 28 years, using the multiphase flow module in the SNL Sierra/Aria simulator (Martinez et. al., 2011). Thermophysical and transport properties in the various materials are listed in Table 1.20. Owing to the very low permeability in the intact salt, over the time scale for the present simulation, it acts like an impermeable boundary for the flow problem, but is needed for modeling the conduction of heat above and below the repository. The van Genuchten capillary pressure function given by:

$$p_c = p_{c0}\left(s^{-\frac{1}{\lambda}} - 1\right)^{\frac{1}{\beta}} \quad \lambda = 1 - 1/\beta, \quad \beta > 1$$
$$s = \left(S_l - S_{lr}\right)\Big/\left(\left(1 - S_{gr}\right) - S_{lr}\right)$$

$$(1.45)$$

was used in the EDZ and crushed salt, with a structure parameter $\beta = 1.7$, entry pressure parameter $Pc_0 = 5$ kPa and zero residual saturations, in the capillary pressure function only. This is done in order to avoid unrealistic behavior of the van Genuchten function at low liquid saturations. Initially the entry pressure parameter in the crushed salt may be lower than the EDZ, however as discussed in the geomechanics section, the backfill region is expected to reconsolidate in a few years time. Cubic relative permeability functions given by,

$$k_{rl} = s^3$$
$$k_{rg} = \left(1 - s\right)^3$$

$$(1.46)$$

were specified for all materials, with residual saturations as listed in Table 1.20.

The initial temperature is 25°C. The top and bottom of the domain are held at the initial temperature. The lateral sides are symmetry boundaries, insulated from heat and mass flow. The initial saturation in the crushed salt backfill is assumed to be 4%. The EDZ is arbitrarily assumed to be at 50% saturation, assuming the waste emplacement takes place some time after the repository is mined, and has had time to dewater between excavation and waste emplacement.

Figure 1.12 shows the distribution of temperature and Figure 1.13 the corresponding liquid saturation distribution at various times. Figure 1.14 shows the distribution of vapor mass fraction at 1 and 30 years. At 1 year the waste package attains a temperature of about 125°C and Figure 1.13 shows the formation of a dry out zone on the lower half of the waste canister, caused by the evaporation of moisture in the lower permeability EDZ region. There is a large difference in behavior above and below the waste canister. Figure 1.15 depicts the time history of temperature, liquid saturation and vapor mass fraction at the center (temperature only), top and bottom of the waste canister. In the crushed salt above the canister the evaporated moisture at the waste canister is readily transported through the high permeability, high porosity backfilled region with small pressure gradient, where it can re-condense in cooler regions of the backfill. Figures 1.14 and 1.15 show high concentrations of water vapor in the backfill region compared to the EDZ below the canister. In contrast, below the canister a higher pressure gradient is needed to transport the evaporated moisture in the lower permeability, (substantially) lower porosity EDZ material. Moreover, the evaporated moisture is trapped by the very low permeability of the intact rock salt, 2 m below the canister, resulting in accumulation of moisture in the EDZ directly below the waste canister. Figure 1.13 shows this to persist, until the moisture begins to disperse when the decay heat diminishes.

Figure 1.15 clearly shows the asymmetry between the top and bottom of the waste canister. The liquid moisture dries out below the canister between about 1 to 3 years, coinciding with the hottest waste canister temperatures. The gas phase at the top of the canister is mostly water vapor owing to the evaporation. The high permeability in the backfill facilitates the transport of air via the gas flow away from the waste canister, resulting in high concentrations of water vapor near the canister. The waste begins to cool after about 10 years, and the moisture content rises both above and below. The increased moisture content in the backfill is a result of dewatering of the EDZ region, as indicated by a volume integral of the moisture in the backfill and EDZ.
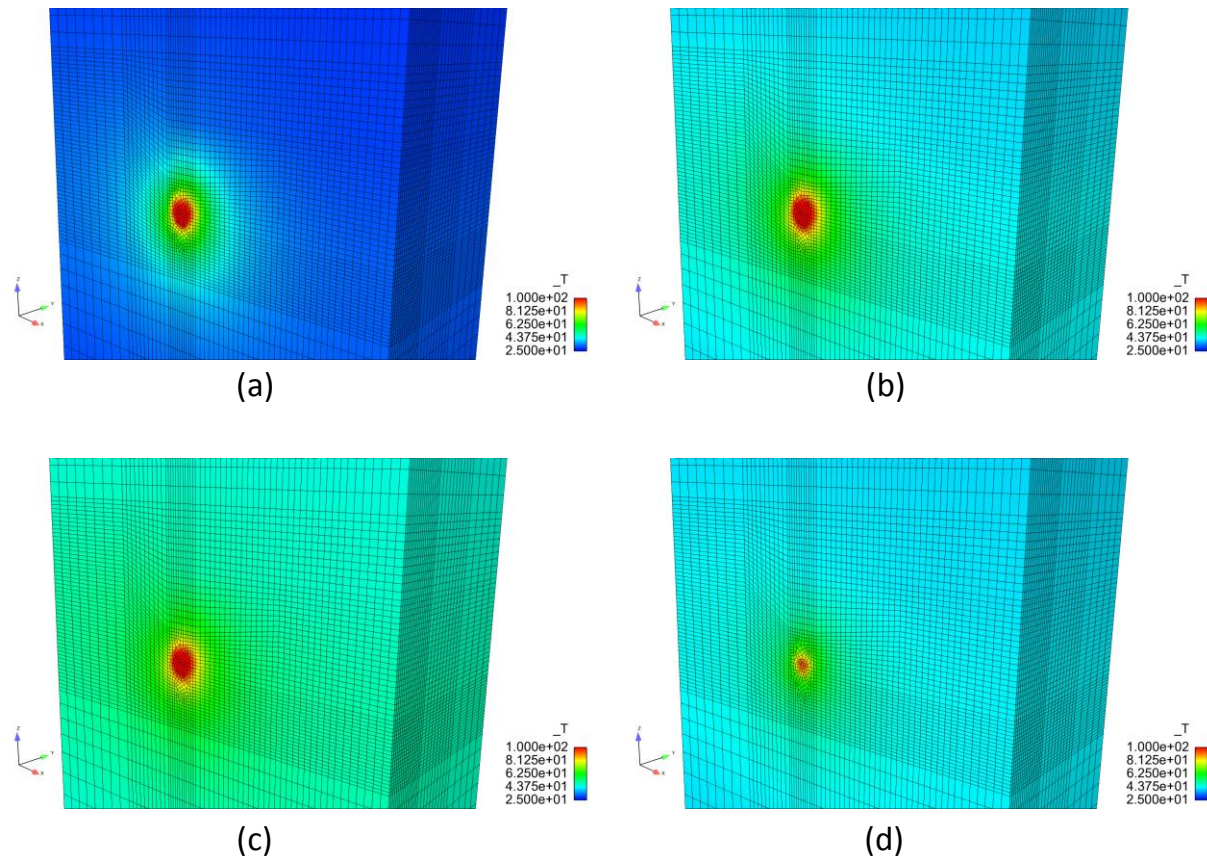
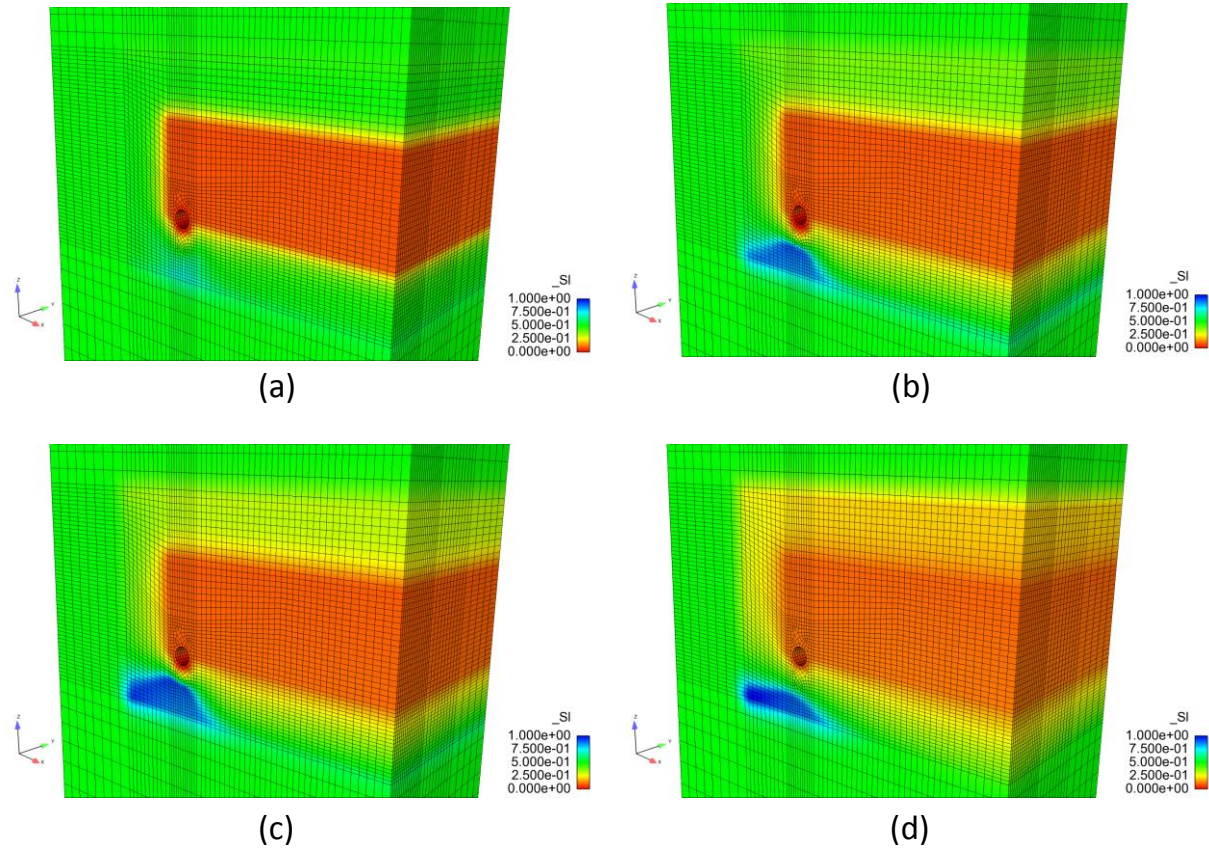**Figure 1.12. Distribution of temperature at (a) 1, (b) 5, (c) 10, and (d) 30 years.**

Figure 1.13. Distribution of liquid saturation at (a) 1, (b) 5, (c) 10, and (d) 30 years.
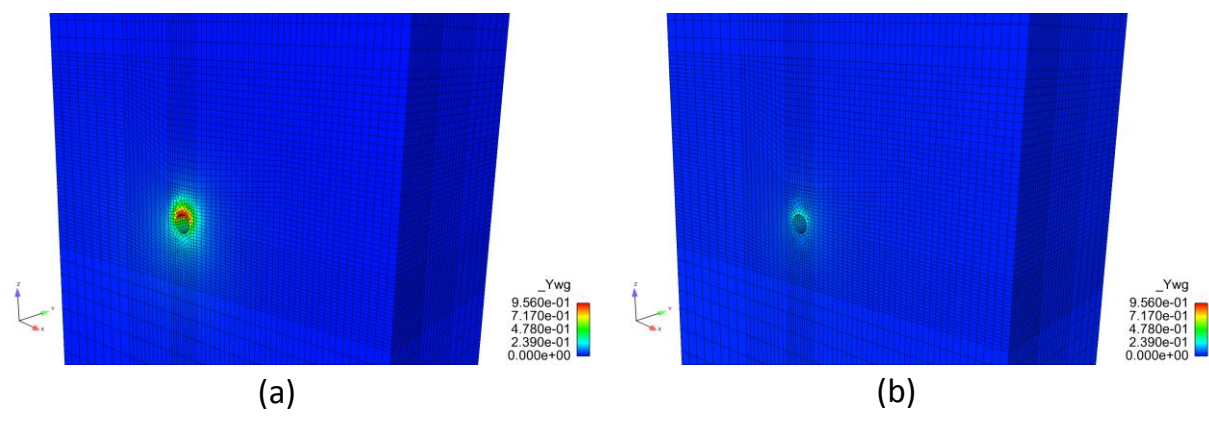

Figure 1.14. Distribution of the mass fraction of water vapor at (a) 1 and (b) 30 years.
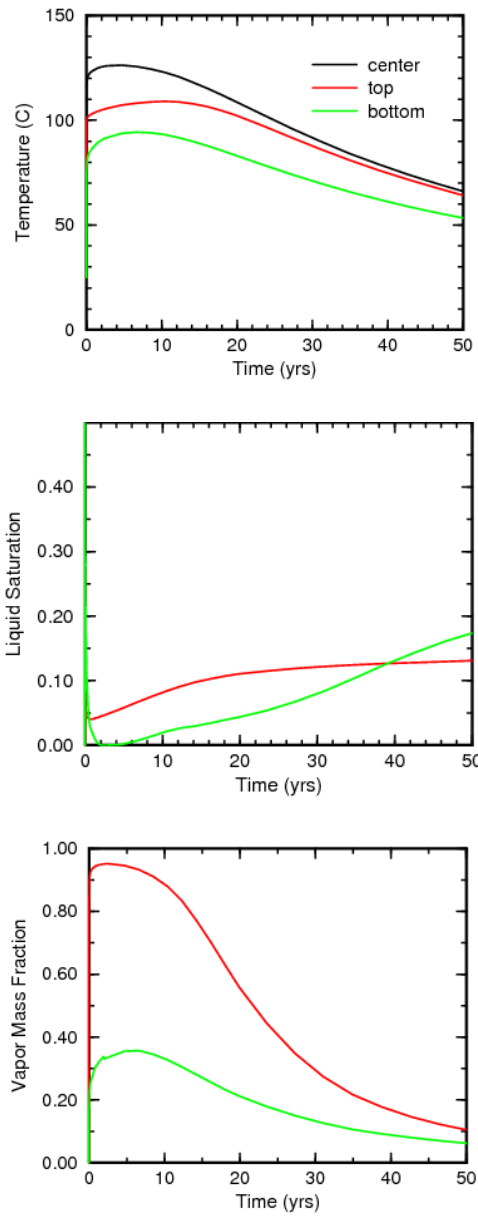
Figure 1.15. Temperature, liquid saturation, and vapor mass fraction histories at the center (temperature only), top and bottom of the waste canister.

Table 1.20. Material Properties in the TH calculations

Property	Intact Salt	EDZ Salt	Crushed Salt	Waste Package
Porosity	0.01	0.014	0.35	-
Permeability (m^2)	10^{-21}	10^{-17}	10^{-13}	-
S_{lr}	0.05	0.05	0.01	
Grain density (kg/m^3)	2190	2190	2190	2200
Specific heat (J/kg K)	931	931	931	840
Thermal Conductivity (W/m K)	5	5	1	2

2. Conclusions

3D Coupled thermo-mechanical (TM) calculations of a generic salt repository involving heat generating waste have been conducted using the Sandia National Laboratories (SNL) Sierra codes. Similarly, two-phase 3D thermo-hydrological (TH) calculations have been conducted to evaluate moisture transport dynamics near the heating waste canister and throughout the disposal room. THM data for salt have been compiled from literature sources associated to various repository research programs. This information is used to constraint the inputs to the models considered in this study. A summary of the salient results obtained in this modeling study:

- The 3D TM analyses provide time estimates for the crushed salt backfill to consolidate at levels near that of intact salt.

- Moisture has a strong influence on crushed salt backfill consolidation on the time needed to approach intact salt characteristic density or porosity. The adopted Callahan constitutive model for crushed salt implicitly captures the chemical effects of pressure solution and compaction on granular salt material.

- Comparison between 2D (plane strain) and 3D calculations of consolidation rates highlights the necessity for using a 3D numerical representation accounting for the alcove and access drifts geometries defined in these simulations.

- Moisture transport (albeit decoupled from TM) indicates the asymmetric distribution of liquid saturation and vapor mass fraction near the heat generating waste canister and its evolution with time. TH modeling results indicate how moisture is trapped in low permeability regions adjacent or at the EDZ.

2.1 Rest of FY12 and FY13 activities

Remainder of FY12 THM modeling activities on salt:

- Checks and test of code related couplings:
  - o Check that the code coupling is working correctly. We must ensure that the porosity and volumetric strain rates are properly accounted for in the conservation equations for mass and energy in Aria.
  - o Check functionality in Aria for evaluation of capillary phenomena across a material interface (e.g. saturation discontinuities).

- Conduct THM simulations to examine the effect of initial saturation conditions for intact salt and EDZ regions on the overall consolidation response.

Anticipated FY13 THM modeling activities on salt:

- Study the influence of moisture in the crushed salt backfill. Moisture appears to have a significant impact on the time needed for the salt backfill to approach intact salt density or porosity. It is expected that the water content will be non-uniform throughout the salt backfill. Regions near the waste package will be drier and thus slower to consolidate. This effect should be considered in future modeling to understand how strongly it affects the backfill consolidation rate.

- Explore expansion of the TM modeling to capture the evolution of damage and healing in salt and its coupling with hydraulic modeling through permeability/porosity changes. The constitutive model for intact salt employed in the current modeling activity does not account for excavation induced damage. The region of damaged salt would have higher permeability than non-damaged material due to the presence of microcracks in the salt. Eventually the inward creep of the host rock will compact the backfill and the resulting backstress from the backfill will close or heal the microcracks.

3.   References

Bechthold, W., Rothfuchs, T., Poley, A., Ghoreychi, M., Heusermann, S., Gens, A., and Olivella, S., 1999, BackBackfilling and Sealing of Underground repositories for Radioactive Waste in Salt (BAMBUS Project), Nuclear Science and Technology, Project report, European Commission, EUR 19124 EN.

Bechthold, W., Smailos, E., Heusermann, S., Bollingerfehr, W., Bazargan Sabet, B., Rothfuchs, T., Kamlot, P., Grupa, J., Olivella, S., and Hansen, F.D., 2004, Backfilling and Sealing of Underground Repositories for Radioactive Waste in Salt (BAMBUS II Project), Final Report EUR 20621, Nuclear Science and Technology, Luxembourg.

Callahan, G.D., 1999, Crushed Salt Constitutive Model. Sandia National Laboratories, Albuquerque, NM. SAND98-2680, Prepared by RESPEC, Rapid City, SD, for Sandia National Laboratories, Albuquerque, NM.

Callahan, G. D. and Hansen, F. D., 2002, Crushed Salt Constitutive Model. Proceedings, Fifth Conference on the Mechanical behavior of Salt, University of Bucharest, Bucharest, Romania, August 9-11, N. D. Cristescu; J. R. Hardy, Jr.; and R. O. Simionescu (eds.), A. A. Balkema, Netherlands, p. 239-252.

Carmichael, R. S., 1984, *CRC Handbook pf Physical properties of Rocks*. Boca Raton FL.: CRC Press. Inc. Vol. III.

Clayton, D.J., 2010, *Parameter Summary Report: CRA-2009 Performance Assessment Baseline Calculation*. ERMS 552889. Carlsbad, NM: Sandia National Laboratories.

Clayton, D.J., 2010, Thermal Analyses of a Generic Salt repository with High-Level Waste-10429, Waste management 2010 Conference, March 7-11, 2010, Phoenix, AZ.

Clayton, D., Freeze, G., Hadgu, T., Hardin, E., Lee, J., Prouty, J., Rogers, R., Nutt, W.M., Birkholzer, J., Liu, H.H., Zheng, L., and Chu, S., 2011, Generic Disposal System Modeling Fiscal Year 2011 Progress Report, Fuel Cycle Research and Development, Used Fuel Disposition, USDOE (SAND2011-5828P)

Hansen, F. D., Mellegard, K. D., and Senseny, P. E., 1984, Elasticity and Strength of Ten Natural Rock Salts, The Mechanical Behavior of Salt, Proceedings of the First Conference, edited by H. Reginald Hardy, Jr. and Michael Langer, Trans Tech Publications.

Hansen, F. D., Pfeifle, T. W., and Lord, D. L., 2003, Parameter Justification report for DRSPALL, SAND2003-2930.

Hardin, E., Clayton, D., Jove-Colon, C.F, Zheng, L., Rutqvist, J., Houseworth, J., Davis, J., Tinnacher, R., Li, L., Liu, H.H, Sutton, M., Tayne, A. and Wolery, T., 2011, Repository Science THMC Coupled Processes Investigations FY11, FCRD-USED-1011-000288 Rev.0, Prepared for U.S. Department of Energy Office of Used Fuel Disposition.

Helton, J.C., Bean, J.E., Berglund, J.W., Davis, F.J., Economy, K., Garner, J.W., Johnson, J.D., MacKinnon, R.J., Miller, J., O'Brien, D.G., Ramsey, J.L., Schreiber, J.D., Shinta, A., Smith, L.N., Stoelzel, D.M., Stockman, C., and Vaughn, P., 1998, Uncertainty and Sensitivity Analysis Results Obtained in the 1996 Performance Assessment for the Waste Isolation Pilot Plant. SAND98-0365, Sandia National Laboratories, Albuquerque, NM.

Langer, M. and Wallner, M. 1998. Evaluation of Repository Concepts for the Disposal of Spent Fuel on the Basis of Geotechnical Safety Indicators and Exploration Data. Radioactive Waste Management and Disposal, *Nuclear Technology*, Vol. 121, p. 199-211.

Liang, W., Yang, C., Zhao, Y., Dusseault, M. B., and Liu, J. 2007. Experimental Investigation of mechanical Properties of bedded Salt Rock, *International Journal of Rock Mechanics and Mining Sciences*, vol. 44, p. 400-411.

Martinez, M.J., Stone, C.M., Notz, P.K., et al., 2011, "Computational thermal, chemical, fluid and solid mechanics for geosystems management. Tech. Rept., SAND2011-6643, Sandia National Laboratories, Albuquerque, NM.

Munson, D.E. and Dawson, P.R., SAND79-1853, *Constitutive Model for the Low Temperature Creep of Salt (With Application to WIPP)*, Sandia National Laboratories Albuquerque, NM, 1979.

Munson, D.E., Fossum, A.F., and Senseny, P.E., 1989, Advances in Resolution of Discrepancies between Predicted and Measured WIPP In-situ Room Closures. Sandia National Laboratories, Albuquerque, NM. SAND88-2948.

Munson, D. E., Devries, K. L., and Callahan, G. D., 1990, "Comparison of Calculations and In Situ Results for a Large, Heated Test Room at the Waste Isolation Pilot Plant (WIPP)", Proceedings, 31st U.S. Symposium on Rock Mechanics, Colorado School of Mines, Golden, CO, June 18–20, W. A. Hustrulid and G. A. Johnson (eds.), A. A. Balkema, Rotterdam, p. 389–396.

Olivella, S. and Gens, A., 2002, A constitutive model for crushed salt, Int. J. Numer. Anal. Meth. Geomech., 26, p. 719–746.

Olivella, S., Castagna, S., Alonso. E. E., and Lloret, A., 2011, Porosity variations in Saline Media Induced by temperature Gradients: Experimental Evidences and Modelimg, Trans Porous Media, 90, p. 763-777.

Pudewills, A. and Droste, J., 2003, Numerical Modeling of the Thermomechanical Behavior of a Large-Scale Underground Experiment. *Computers and Structures*, vol. 81, p. 911-918. Elsevier Science Ltd.

Notz, P. K., Subia, S.R., Hopkins, M.M., Moffat, H.K., and Noble, D., 2007, *Aria 1.5: User Manual,* SAND2007-2734. Albuquerque, NM: Sandia National Laboratories,

Rothfuchs, T., Droste, J. and D Feddersen, H-K., 1998, Special Safety Aspects of Drift Disposal – The Thermal Simulation of the Drift Storage Experiment. Radioactive Waste Management and Disposal, *Nuclear Technology*, Vol. 121, p. 189-198.

Scherzinger, W. M. and Hammerand, D.C., 2007, *Constitutive Models in LAME,* SAND2007-5873. Albuquerque, NM: Sandia National Laboratories.

Spencer, B. W. et al. (2011) *Adagio 4.20 User's Guide*, SAND2011-1825. Albuquerque, NM: Sandia National Laboratories.

Spiers, C.J. and Brzesowsky, R.H., *Densification Behaviour of Wet Granular Salt: Theory vs. Experiment*, Seventh Symposium on Salt, Kyoto, Japan, April 6-9, 1992, Eds. H. Kakihana, H.R. Hardy, Jr., T. Hoshi, and K. Toyokura. Amsterdam; New York: Elsevier. Vol. 1, 83-92, 1993.

U.S. Department of Energy, 1988. Site Characterization Plan, Deaf Smith County Site, Texas, Volume 1, Nuclear Waste Policy Act (Section 113).